TECNUN - Universidad de Navarra
School of Engineering

Design, modeling and characterization of lattice structures for orthopedic implant applications

by

Markel Alaña Olivares

July, 2022

Supervised by
Aitziber López de Arancibia
Sergio Ruiz de Galarreta Moriones

Dissertation submitted for the Degree of Doctor of Philosophy of Universidad de Navarra.

TECNUN - Universidad de Navarra
Donostia - San Sebastián
Spain

This dissertation is the end of a journey that started in 2018, when I knew that I wanted to work in research, but had little idea how to make it happen. I would like to express my deepest gratitude to TECNUN and Universidad de Navarra for giving me the opportunity and showing me the path into the academic world. I am also very grateful to Juan Carlos Ramos, head of the Department of Mechanical Engineering and Materials, and Nere Gil-Negrete for the continuous support I received during this process.

I could not have undertaken this challenge without my doctorate supervisors Aitziber López de Arancibia and Sergio Ruiz de Galarreta. I am deeply grateful for their invaluable advice and encouragement, and the freedom they gave me to explore the limitless world of lattice structures. Within such freedom, their guidance has been central in my learning. I would also like to give special thanks to Naiara Rodríguez for the knowledge, energy and initiative she brought to the group.

I would also like to extend my sincere thanks to Brecht Van Hooreweder and Antonio Cutolo, from KU Leuven, for welcoming me as a visiting researcher. Their knowledge and experience have helped me to have a broader vision of my research field, and our fruitful collaboration has been essential in my work.

Thanks should also go to Asier López and Juan Villarón for their valuable contribution in all the experimental set ups and to Iñigo Ordoñez for manufacturing all sorts of lattice structures and parts. Their willingness to give advice and the nice atmosphere in their office made it always so easy to ask for the much needed help.

I also would like to mention the PhD students or colleagues I have shared my journey with: Jorge, Julio, Ignacio, Dima, Leire, Javi, Alaine, Reduan, Alex, Fabian, Guillermo, María, etc. Special thanks to Irati and Unai for all the support and the nice chats that made the days shorter.

I also owe a word of gratitude to the family and friends that have been by my side during this journey, celebrating the good moments and offering their hand in the bad ones.

This work would have been much more difficult without a place in Donosti out of my hometown in Bilbao. I must thank Julene, Ibone, Laura and Itsaso for creating a warm home to come back to, a nice space to share our daily lives. I also want to thank Javi and Leire for all the nice evenings that have made my life in Donosti something I will definitely miss.

Besides, I want to thank the friends in the 'cuadrilla', for the great moments we shared, and for their kindness and empathy. I want to especially thank Josu, Ibai, Koldo and Sergio for being incredible flatmates and friends, Asier for being present in the distance, and Ibane for always checking up on me. I am so grateful to Nerea for believing in me even more than myself. And last but not least, I want to thank my parents Maite and Patxi, and my brother, Bittor, without them all the rest would have been impossible.

Abstract

Interest in lattice structures has soared in recent years thanks to the advances in the field of additive manufacturing, which has led to increasingly complex designs and the production of parts which was impossible up to not long ago. These advances enabled the consistent manufacturing of smaller and smaller features, reaching submilimetric scales and opening a path to create structures that mimic the cellular solids of nature. This possibility attracted broad attention due to its applicability in the aerospace and biomedical industries. On the one hand, lattice structures allow to create parts with outstanding stiffness to weight ratios. On the other hand, these structures can be designed to have predefined stiffness and strength values, which enables the production of parts with engineered mechanical properties.

This is especially useful in the design of novel orthopedic implants. Traditionally, the implants have been monolithic parts of biocompatible metals such as Ti6Al4V, CoCr, pure Ti, etc. One problem of this concept is the mismatch between the stiffness of the host bone and the metallic implant, which creates the so called stress shielding. Stress shielding occurs when the bone adjacent to the implant does not have to withstand the main physiological loads because the much stiffer implant bears them in its place. Bone is a living tissue, which is created or resorbed (diluted in blood) depending on the loads to optimize its functionality. Thus, the stiffness mismatch between bone and the implant leads to the bone resorption due to the lack of mechanical stimuli on the host bone. The bone surrounding the implant loses density and weakens, which causes pain to the patient, affects implant stability, and may lead to the loosening of the implant.

Lattice structures offer the possibility to create porous implants with tailored mechanical properties to match the stiffness of the surrounding bone, thus avoiding stress shielding and subsequent bone loss. Furthermore, lattice structures form porous parts with high surface to volume ratios, and this porosity enables the bone ingrowth within the implant, improving its fixation and long-term stability.

Research of lattice structures for load bearing applications has been mainly devoted to understand their mechanical properties and to explore design possibilities that were not available with solid materials. This work is devoted to the development of tools to design lattice structures with controlled mechanical properties, as well as to deepen into the factors that affect such properties. Thus, the main purpose of this dissertation is to create lattice structures that mimic bone stiffness and could be implemented in orthopedic implants to avoid the stress shielding. In addition, orthopedic implants must withstand millions of load cycles throughout the lifetime of the patients, thus the fatigue behavior of the structures was also studied in this thesis. Finally, the small feature sizes required to implement such structures in orthopedic implants requires to reach the manufacturing limits of current additive manufacturing technologies, which induces important deviations from the actually designed geometry and in turn the mechanical properties. Another goal of this work is to understand the impact of such manufacturing deviations on the stiffness of the structures.

The obtained results show that there are different possibilities to design structures with stiffness levels comparable to bone. The developed analytical or semi-analytical models predict and enable to design the mechanical properties of the structures for different topologies. These models can be used with personalized bone data to mimic the bone stiffness of each patient, and the modeling of the complete stiffness matrix enables to implement such structures in optimization algorithms. Furthermore, the anisotropy of the structures can also be controlled to adapt it to the complex loads that arise in various anatomical sites. Regarding dynamic loads, fatigue life prediction tools in literature were compared and adapted to improve their applicability, and a fatigue failure surface was developed to easily predict the fatigue life of the structures. Moreover, it was concluded that hot isostatic pressing enhanced the fatigue strength of the structures. Finally, the manufacturing deviations were studied, developing a methodology to consider the proximity to the nodes in the analysis of the imperfection level, and to include such imperfections in a numerical model that predicts the change of anisotropy in the structure.

Contents

List of Figures

List of Tables

Chapter 1

Introduction

This introductory chapter gives a brief overview of what lattice structures are. First, the chapter introduces the cellular solids, to give context and to better understand the origin of the lattice structure designs. In addition, some examples of such structures and their classification are presented. Afterwards, a literature review is carried out to have an idea of the current state of the research on lattice structures and the main topics and challenges.

1.1 Lattice structures

Cellular solids are defined as an assembly of cells with solid edges or faces, packed together so that they fill space. Cellular solids are very common in nature, and can be found in very different environments [1]. Some good examples of such natural materials are wood, cork, bone, or sponge (see Figure 1.1).

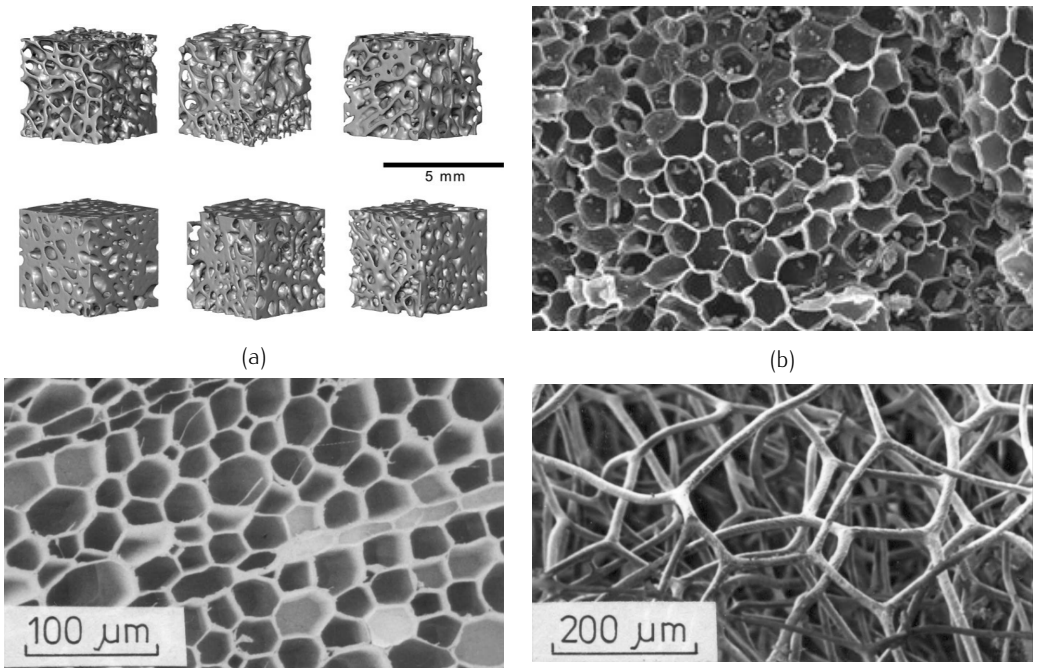

(a) (b) (c) (d)

Figure 1.1: a) cancellous bone [2], b) structure of cork [3], c) balsa wood [1] and d) sponge [1].

Additive manufacturing (AM) is the process of joining materials to make objects from 3D model data, usually layer upon layer, as opposed to subtractive manufacturing methodologies [4]. The advances in AM in recent years have enabled the manufacturing of parts with increased complexity and smaller feature sizes, mimicking some of the functionalities of cellular solids with mesoscale structures. Mesoscale structures are cellular solids small enough to be modeled as an homogeneous continuum from the macroscopic point of view, therefore creating a metamaterial whose mechanical properties depend on the architecture of the structure. Thus, the higher control over the geometry has resulted in a new paradigm, bringing the possibility to rationally design mesostructures that can be used as metamaterials.

These metamaterials can be considered composites made of a constituent material and void, and they offer the possibility to design mechanical properties out of range of their constituent materials [5]. These might include negative Poisson's ratio [6, 7, 8] or negative thermal expansion coefficient [9, 10]. Furthermore, these structures also enable to tailor mechanical properties with a high stiffness to weight ratio, while implementing functionally graded metamaterials that can be adjusted according to specific loads [11, 12]. This has led to a growing interest in cellular structures in various fields such as biomedical or aerospace, among others [13]. Figure 1.2 depicts some examples of their applications.

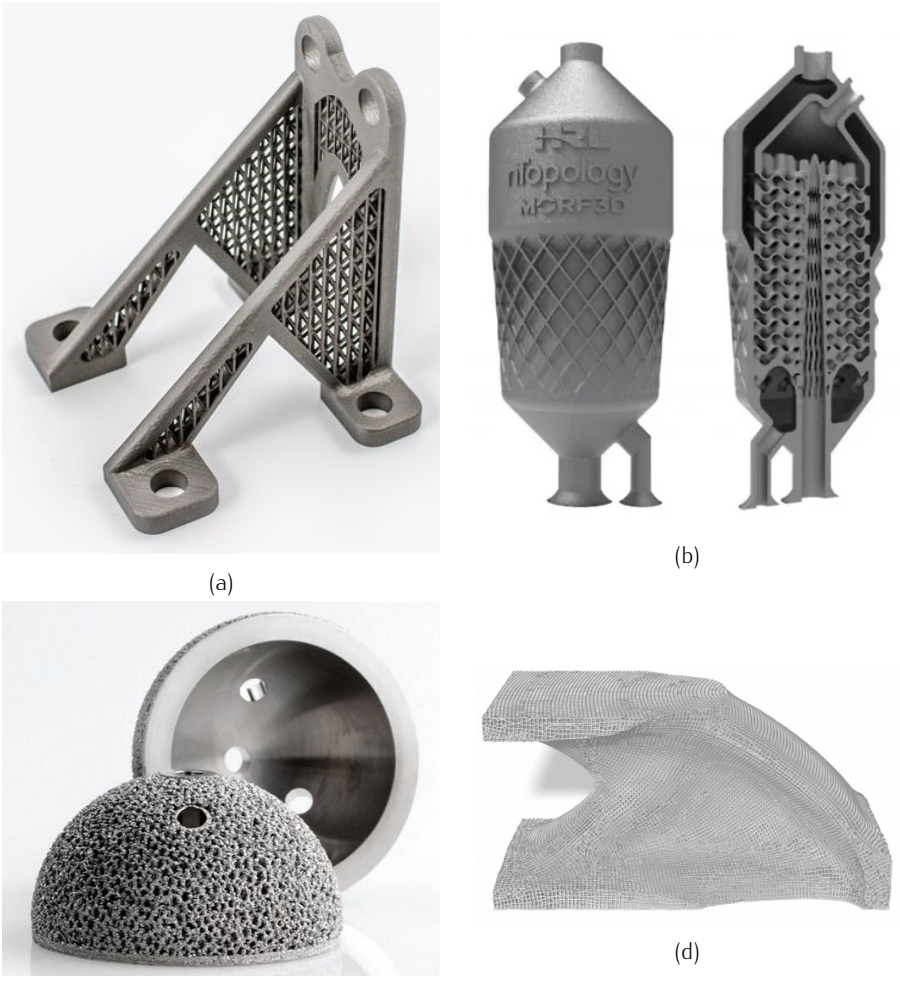

(a) (b) (c) (d)

Figure 1.2: a) Titanium aerospace part (Materialise) [14], b) heat exchanger (Ansys) [15], c) acetabullar cup [16] and d) cantilever beam [17].

Cellular solids are commonly referred to as lattice structures in literature when they are engineered features for technological applications. Lattice structures can be classified according to two different criteria: periodicity and constituent element type. Lattice structures can be divided by the following constituents:

- Struts: The structures are formed by beams called struts, which connect node pairs to form the structure.
- Shells: The structures are formed by a 3D shell with low thickness that fills the space.
- Plates: Intersecting plates in different orientations form the lattice structure.
- Skeletal: Structures formed by elements that do not fit in the previous categories, such as an equation that describes the parts of the structure filled with material, or natural bone-like structures.

On the other hand, according to their periodicity, lattice structures can be divided in two groups:

- Stochastic: These structures do not follow a clear pattern in 3D space, but are formed by stochastic patterns.
- Periodic: The structures are formed by a unit cell that is repeated in the 3D space to create the structure.

Table 1.1 depicts some unit cells corresponding to periodic 3D lattice structures.

Struts	Shells	Plates	Skeletal
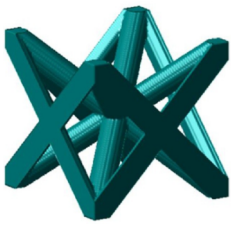	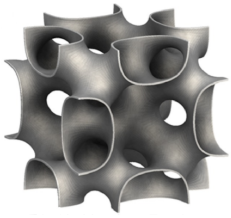		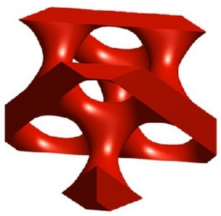

Table 1.1: Periodic lattice structure types based on their constituent features [18, 19, 20, 21].

This work focuses on periodic lattice structures based on struts due to their capacity to mimic the mechanical properties of various types of bones, making them suitable for orthopedic implant designs. On the other hand, the design of strut based structures is simpler than for other types, due to the complex nature of trigonometric functions used to define shell based and skeletal structures. In addition, they are also easier to manufacture compared to the plate based structure because of the open pores of strut based structures. Figure 1.3 depicts some strut based unit cells which repeat in space to form structures. These were were studied as metamaterials.

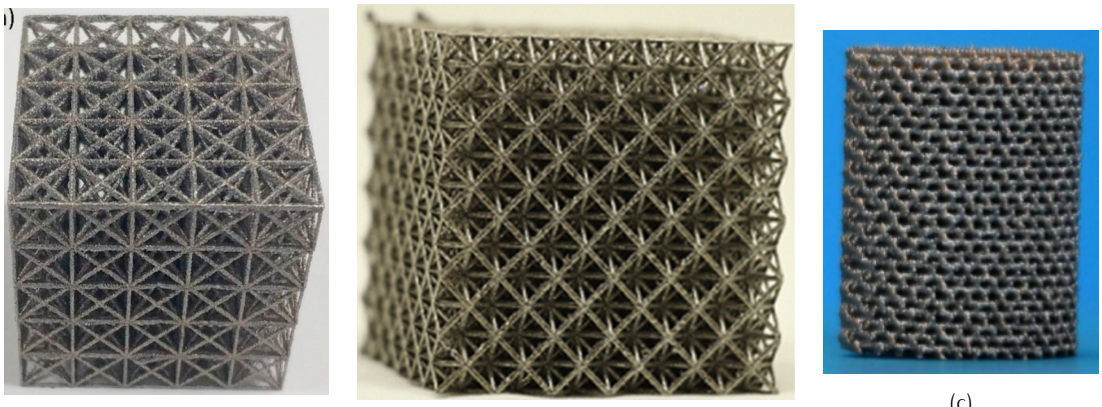

(a) (b) (c)

Figure 1.3: Lattice structures manufactured by SLM [22, 23, 24].

1.2 Literature review

This section is devoted to analyze many of the aspects that influence lattice structures and their applicability in bone tissue engineering. Firstly, the use of AM is discussed to produce lattice structures, including the analysis of different types of AM technologies. Afterwards, the manufacturing deviations that commonly arise in AM are presented, as well as their impact on the accuracy of the structure geometry. Furthermore, some general considerations about the quasi-static and fatigue mechanical properties of strut based lattice structures are analyzed, along with different modeling approaches to predict such properties. This is the basis to understand the main contributions of this work. Finally, the architecture of bone, its mechanical properties, and the challenges of orthopedic implants are presented to understand the potential of lattice structures in the field of bone tissue engineering.

1.2.1 Additive manufacturing of lattice structures

AM consists in manufacturing a three-dimensional part layer by layer, so that each layer is a thin slice containing a cross-section of the part, which is obtained from the CAD model [25, 26]. This additive nature of the manufacturing process, in contrast to subtractive manufacturing (e.g. milling, cutting) or formative manufacturing (e.g. forging, injection molding), enables to produce more complex parts, as it is the case of lattice structures. Moreover, the digital workflow from design to manufacturing allows to automate the design process of complex systems for mass-customization, and the efficient use of material reduces the waste and material cost even for very complex geometries. On the other hand, digital files can be easily shared globally, reducing lead-time and transport costs [27].

Figure 1.4 shows a representation of the unit cost for traditional manufacturing (TM) and AM, under the simplified assumption that the unit cost for AM is independent from production volume and product complexity. There are two possible scenarios in which the unit cost is lower for additively manufactured parts: Small production volumes, for which manufacturing of specific tooling is not cost effective, or highly complex parts, such as topologically optimized geometries, functional systems, or lattice structures [27].

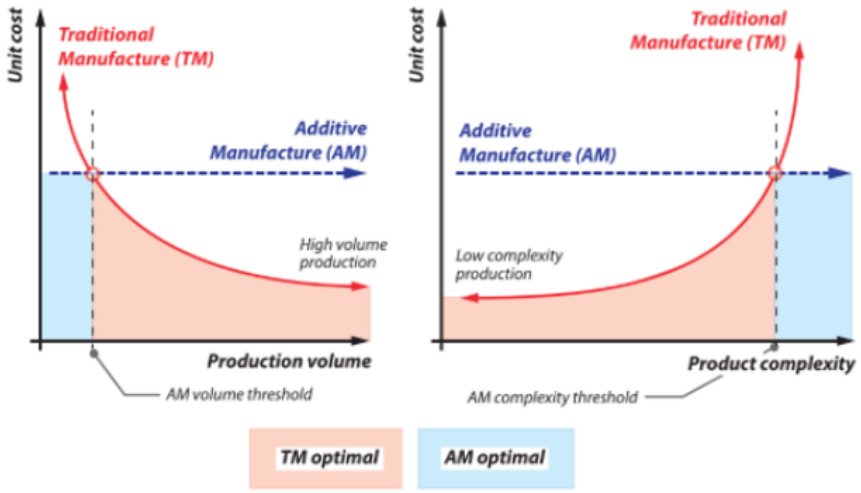

Figure 1.4: AM and TM unit cost as a function of production volume and product complexity [27].

The general process from the design to manufacture a part with an AM technique is described in Figure 1.5 [26]:

1. CAD: Design of the part geometry in a CAD modelling software.

2. STL convert: Transform the external closed surface of the part to STL format, and fix the errors the STL might arise in the creation of the file. The STL format is the basis for the calculation of the slices.

3. File transfer to machine: STL file is transferred to the machine, and some manipulation might be needed for correct size, position and orientation part. Orientation is critical for the final mechanical performance of the part and the support structures.

4. Machine setup: manufacturing parameters like material constraints, energy source, layer thickness, timing, etc. must be specified.

5. Build: automated process of the actual layer by layer manufacturing. Nonetheless, supervision is recommended to ensure correct function.

6. Remove: removing the parts from the machine should be done ensuring temperature is sufficiently low. Afterwards, the part should be detached from the build plate and support material must be removed. Depending on the AM technology EDM may be necessary to detach the part from the build plate.

7. Post-process: parts might need post-treatments before they are ready to use. These treatments can be heat-treatments to change the microstructure of the material, surface treatments, machining to ensure tolerance compliance, etc. If required, support structures should be removed.

8. Application: Parts are ready to use, and they may require to be assembled with other components or parts.

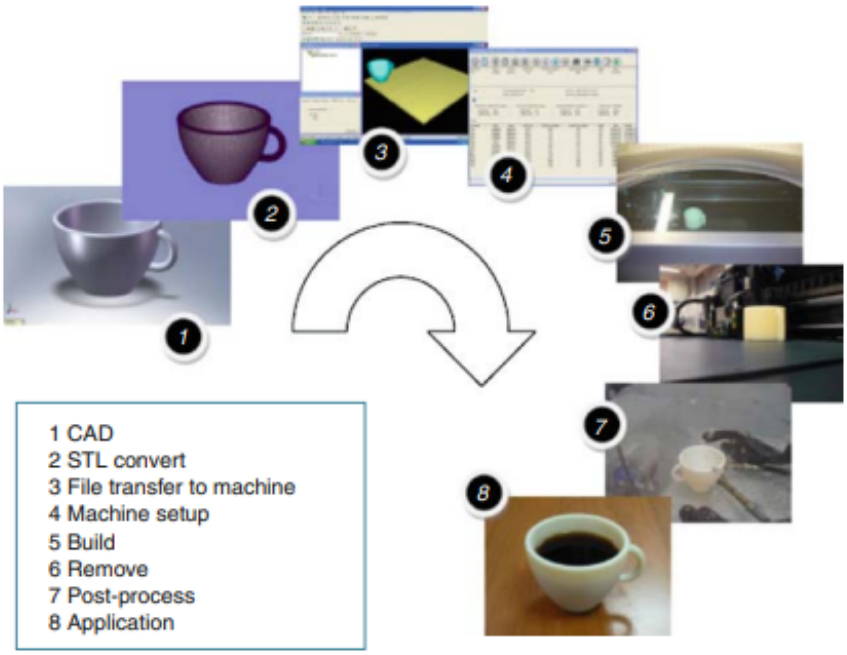

Figure 1.5: Different steps of AM from design phase to final part [26].

There are many different types of AM technologies, but this work is focused on powder bed fusion (PBF) technology because it offers the highest resolution, and it is the most suitable for the manufacture of metallic lattice structures [28]. However, other technologies can also be used for metal AM, such as Binder Jetting and direct energy deposition (DED), and are reviewed below.

Binder Jetting uses a liquid-based binding agent to selectively join the material in a powder bed [29]. Two dimensional layers are stacked to build the part. For that, a layer of powder is spread on the build plate by means of a roller, and afterwards the print-head jets the liquid to bind the powder particles together [30]. This process is repeated until the completion of the part, and the result is named green part (Figure 1.6a depicts the building process). This part has to be post-processed for its final use: excess powder has to be removed, binder is decomposed upon heating, and sintering of the particles results in a densified and strong part. This densification process also contracts the part, which makes it more difficult to control its final geometry.

DED melts the material at the same time as it is being deposited layer by layer (see Figure 1.6b). In this process, a deposition head is used to deliver the material in a substrate, which can be done in powder or wire format. The laser and material feeding nozzles are usually integrated in the head, as well as inert gas protection of the molten metal before solidification. This enables the use of this technology as a tool in CNC milling machines [26]. However, the manufacturing of lattice structures with this technology is not always possible, specially for complex lattice structures.

In PBF the powder of the material is spread in thin layers, and it is exposed to an energy source that melts the slice according to the cross section of the part. Once a layer is melted, the building platform is lowered a certain amount, and a new layer of powder is placed on top of the melted layer, repeating the process (see Figure 1.7). This process allows the manufacturing of parts of very different materials, and various types of polymers, ceramics and metals can be produced.

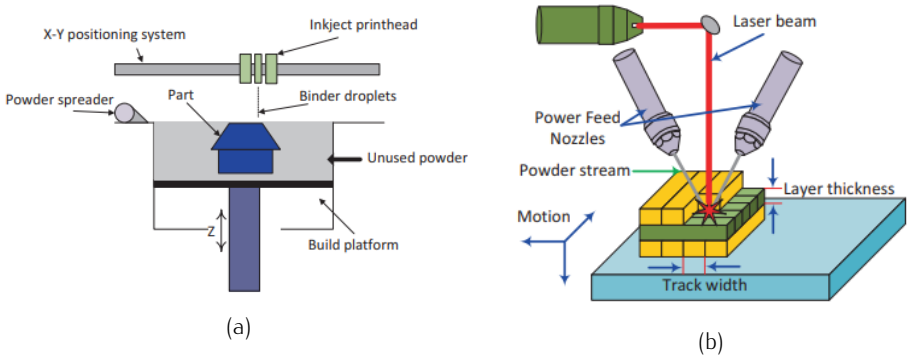

Figure 1.6: a) Binder Jetting and direct energy deposition simplified processes [26].

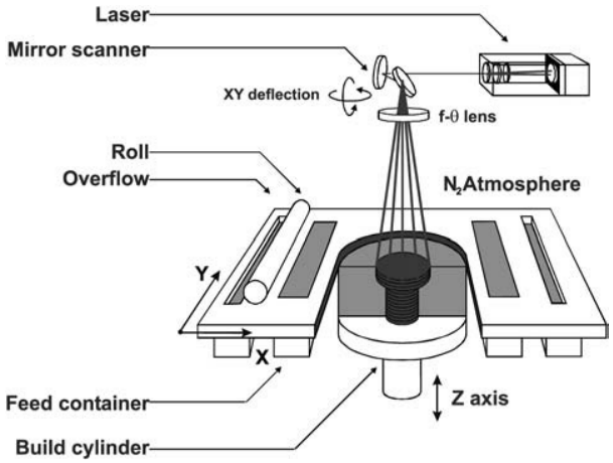

Figure 1.7: Layout of a SLM machine [31].

The energy source of PBF technologies can be a laser or an electron beam. The technology that uses a laser beam to melt the powder can be referred to as selective laser melting (SLM). In this process, the powder is contained in an inert atmosphere to prevent oxidizing. On the other hand, in electron beam melting (EBM) the powder absorbs the electron beams by transforming their kinetic energy into heat. EBM is carried out in a vacuum chamber, and the powder is preheated at much higher temperatures compared to the SLM process. As a result, the parts produced by EBM cool at much lower rate, leading to a coarser microstructure, with lower tensile strength and higher ductility, and lower residual stresses [28]. In both technologies the energy input as well as the scanning strategy and the layer thickness can be adjusted to optimize the structural integrity and the geometrical accuracy of the produced parts [32].

PBF allows to manufacture structures in many metallic materials such as titanium and its alloys, aluminum alloys, maraging steel, stainless steel, cobalt chrome, nickel super alloys, copper, magnesium and its alloys, precious metals, etc. [28, 33]. However, the metals used for orthopedic implants need to be biocompatible, and depending on their main constituent they can be divided in four groups: stainless steels, cobalt-based alloys, titanium-based alloys, and others [34]. This last group includes many recently developed materials such as NiTi, and alloys of Ta. Furthermore, recently biodegradable lattice structures of Mg, Fe and Zn alloys were developed [35], which are promising to treat large bone defects, since they promote bone ingrowth while degrading in human body, ideally at the same rate [36]. Nonetheless, this work will focus on the non-biodegradable alloys most commonly used in orthopedic implant applications.

The design freedom provided by AM enables the mass-customization of parts. This is very helpful to design parts that adapt to the anatomy and specific need of each patient in case of orthopedic implants. Moreover, this capacity can be combined with the use of lattice structures so that implants are optimized for better performance and osseointegration. Figure 1.8 shows some examples of orthopedic implants produced by AM and including lattice structures.

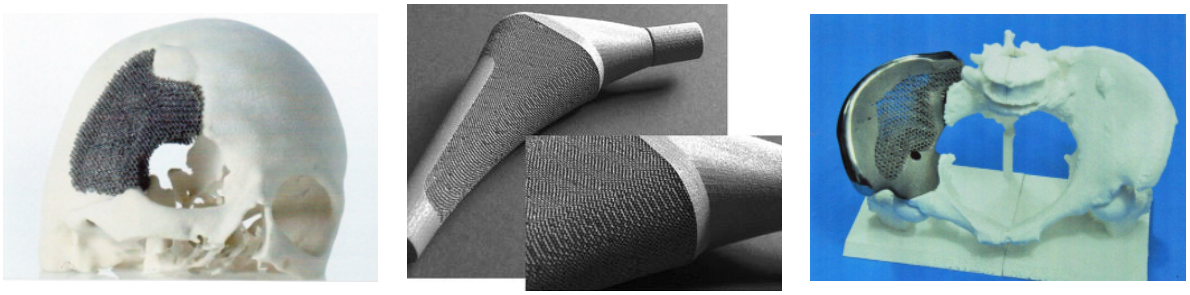

(a) (b) (c)

Figure 1.8: Orthopedic implants with lattice structures for a) skull [37], b) femoral stem [38] and c) hip [37].

1.2.2 Imperfections and manufacturing deviations

The parts produced by PBF commonly have a set of defects directly related to the manufacturing technology [39, 40, 41]:

- Porosity: voids can be formed during the process due to the gases trapped because of the high cooling rates, as depicted in Figures 1.9a and 1.9b.
- Lack of fusion: incomplete fusion can appear as a result of insufficient input energy, leaving unmelted powder in the part.
- Surface roughnes and stair step effect: parts produced by PBF have high surface roughness. Surfaces directly supported by the powder bed (down-skin surfaces) are more irregular, since the powder does not properly conduct heat, hindering the proper cooling of the part (dross formation). This is not the case for surfaces facing upwards (up-skin surfaces) because the heat is evacuated through the solidified part. Stair step effect is formed by discontinuities between layers, also increasing surface roughness (see Figure 1.9).
- Residual stresses: high thermal gradients create residual stresses that might affect the integrity of the part by creating cracks, delamination between layers or dimensional inaccuracies

The manufacturing of lattice structures with the required detail level in order to meet the design requirements entails a major challenge. The porosity and pore sizes that optimize osseointegration and vascularization of the scaffolds require feature sizes that both SLM and EBM technologies hardly achieve with the desired accuracy. Thus, the inspection of the manufactured structures has become as important as the design itself in order to predict their mechanical behavior, and a whole research topic has emerged from the analysis of the differences between the designed and produced structures, and their implications.

Strut based lattice structures may have different manufacturing deviation types as a result of the above mentioned effects, combined with the required small feature sizes:

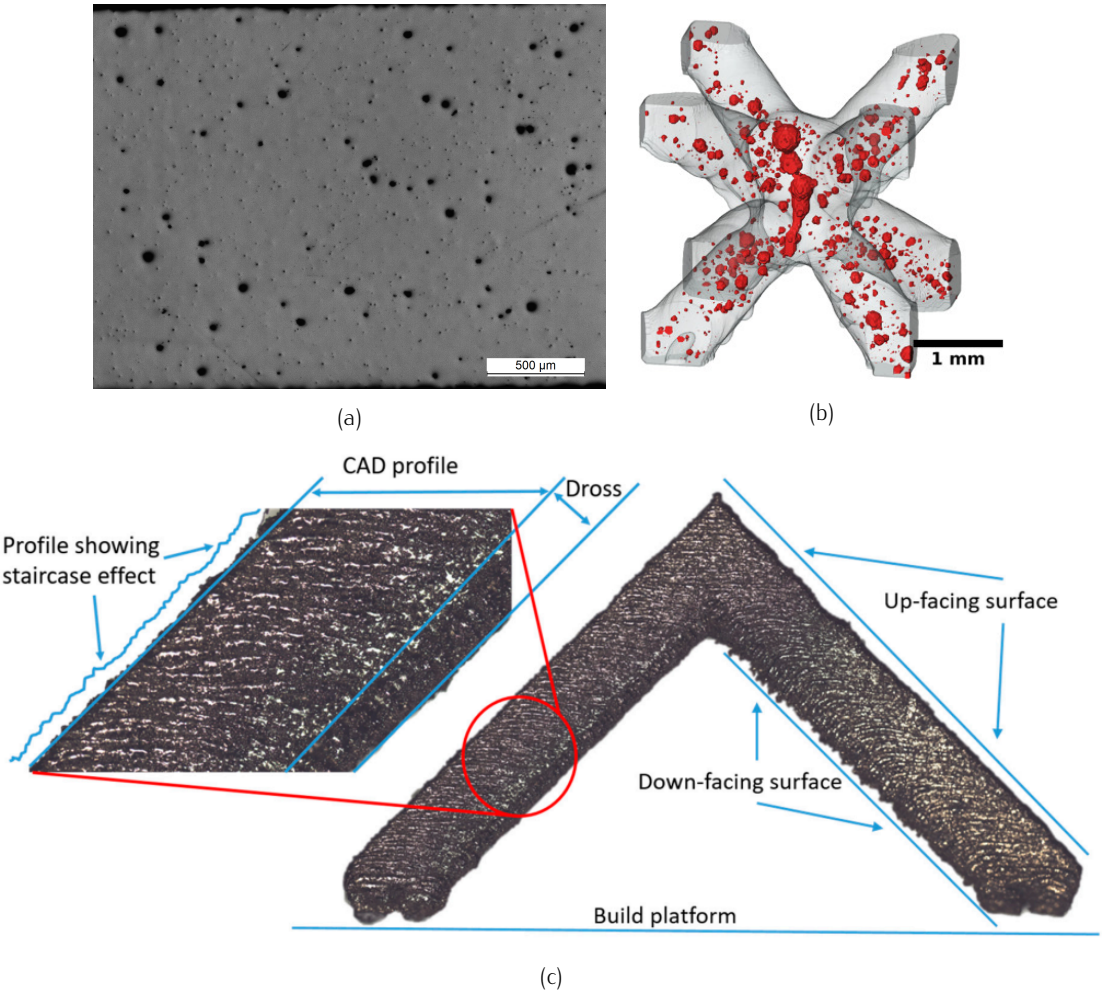

Figure 1.9: a) internal porosity of a Ti6Al4V part, b) porosities in a unit cell of a lattice structure [42], c) stair step effect and up-skin vs. down-skin surfaces [43].

- Strut diameter: manufacturing a strut with the given diameter is complicated, and deviations beyond 40% can be observed in many structures and across different studies in which the nominal diameter is below 1 mm [44, 45, 46]. For example, Figure 1.10a depicts a distribution of strut diameter deviations. The inaccuracy varies with the orientation of the strut, as depicted in Figure 1.10d: for vertical struts the deviation is the lowest, and the error increases as the angle with respect to the building platform reduces, reaching the highest imperfection levels in horizontal struts [47, 48, 49].
- Cross-section shape: the shape of the cross section does not remain as designed, since dross formation in down-skin surfaces commonly leads to elliptical cross sections [50]. This effect is observed in Figure 1.10c, which shows some superposed cross sections of a strut with elliptical cross-sections. This dross formation also depends on orientation of the strut with respect to the building plane, with horizontal struts having the worst quality.
- Strut waviness: the center of gravity of the strut does not follow a straight line along the strut, but it deviates from the nominal axis, as shown in Figure 1.10b [51].

The characterization of the above mentioned manufacturing deviations and imperfections can be carried out with different techniques. A very widely used method is to obtain a μ-CT model of the manufactured

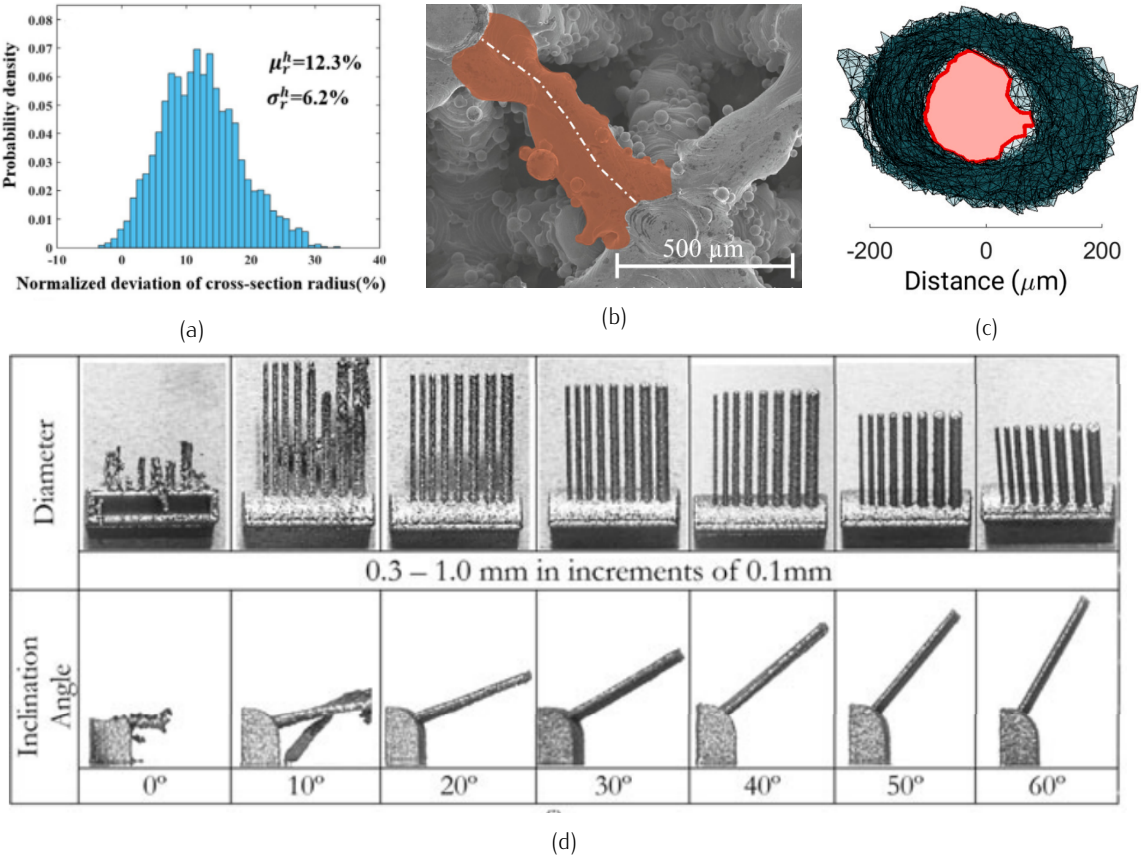

Figure 1.10: a) Relative deviation from the nominal strut diameter [48], b) strut waviness [51], c) axial view of a strut, with its core highlighted [49], d) manufactured struts for different diameters and angles [52].

structures, as done in [48, 49, 53, 50]. Depending on the resolution of the scan this method might be suitable to measure the internal porosity of the struts or to study the shape and waviness of the struts. This technique provides a lot of information about the actual quality of the structure, but it is costly and analyzing the large amount of obtained data is time consuming [39]. On the other hand, SEM and optical microscopy can also be used to easily obtain dimensional measurements and analyze the surface texture of the structures, providing valuable information. Finally, Archimedes' principle is commonly used to calculate the internal porosity of the structure, by comparing the weight difference of the structure in air and a fluid [54].

1.2.3 Mechanical properties of lattice structures

The use of lattice structures in orthopedic implants allows to tailor effective mechanical properties, being the Young's modulus and yield strength of the structures two of the most important parameters. It must be noted that the effective properties of a structure are not the actual properties of its constituent material, but instead they describe the behavior of the structure from the perspective of an homogeneous material. This process of modeling an heterogeneous medium with its equivalent effective properties is called homogenization [55].

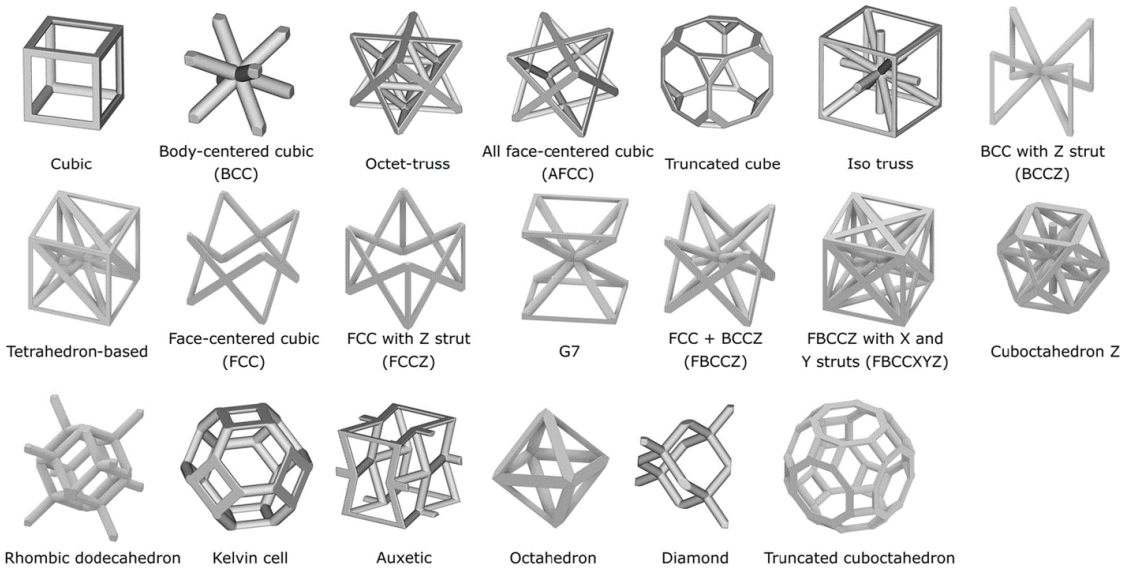

Figure 1.11: Some common strut based topologies used to design lattice structures [28].

The effective mechanical properties of lattice structures are mainly defined by the base material of the structure, strut topology and relative density:

- Base material: also named constituent material, is the material the structure is made of.
- Strut topology: the strut topology refers to the configuration of the struts, i.e., the number of struts, their orientation and how they are interconnected between each other. This gives name to the unit cell, and Figure 1.11 shows different common topologies of strut based lattice structures.
- Relative density: the relative density (ρ/ρ_s) of a structure is the proportion of actual mass in the space that the unit cell fills.

Once a topology is chosen for the lattice structure, the design parameters that define the structure's relative density are the diameter of the struts and unit cell size. From the definition of the relative density, it follows that it is a function of the ratio between the diameter of the struts and unit cell size: ($\rho/\rho_s = f(D/L)$). The unit cell size is defined as the length of the imaginary cube that each unit cell takes in space. Furthermore, it is possible to change the aspect ratio of the unit cell, i.e. change its dimension in some principal orientations, or to have different strut diameter values within the structure to better adapt the effective mechanical properties to certain loads.

Quasi-static mechanical properties

There is no clear consensus on how to characterize the effective mechanical properties of lattice structures. There are relatively few studies regarding the bending [56, 57], shear [46] or tensile [58, 59] properties of lattice structures, and uniaxial compression tests are by far the most commonly performed tests to obtain the quasi-static mechanical properties of any type of structure. Figure 1.12 shows some of the effective compressive stress-strain curves of lattice structures with different relative densities.

In order to obtain the stiffness of the structures, one option is to use the gradient of the linear part of the curve [60, 61, 62, 63]. On the other hand, the ISO 13314 [64] standard for porous metals also

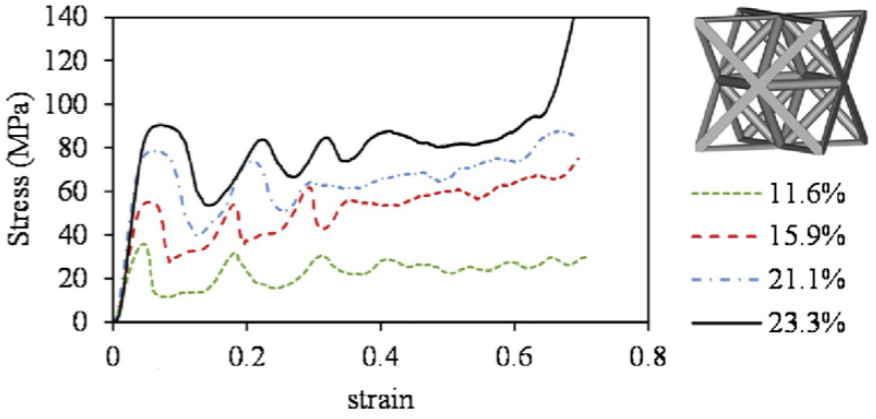

(a)

(b)

Figure 1.12: a) Effective stress versus effective strain curve of a octet-truss lattice structure with relative densities of 11.6%, 15.9%, 21.1% and 23.3% and b) compression process of the structure [22].

proposes to obtain the gradient by means of a hysteresis loop between the points at the 20% and 70% of the maximum stress level, and this approach was followed in [65]. Others [66, 67], also use the gradient between 20% and 70% without specifying if it was obtained in a hysteresis loop, or directly from monotonic compression.

Regarding the strength of the structures, yield strength is commonly defined as 0.2% offset stress as in solid materials [68, 69, 70], although 1% offset can also be found [65, 71]. Furthermore, some studies use yield strength and plateau stress indistinctly [72, 66]. Plateau stress is defined in the ISO 13314 standard as the mean stress between the 20% and 40% or between 20% and 30% strain rates [64]. These inconsistencies when defining the quasi-static mechanical properties of the structures hinder the comparison across different studies.

Lattice structures can be divided into bending dominated and stretch dominated [1]. Bending dominated lattice structures carry the load mainly by the bending of the struts, while in stretch dominated structures the load is carried axially along the struts. This is determined by the topology of the structures: Maxwell's number establishes the degrees of freedom of a pin jointed structure [73]:

$$M = b - 3j + 6 \tag{1.1}$$

In Equation 1.1 M represents the Maxwell's number, an equivalent to the degrees of freedom, j is the number of joints, and b is the number of struts. For structures with $M < 0$, mechanisms could be formed

with perfect pin joints, while $M \geq 0$ ensures that there are no degrees of freedom within the structure. For additively manufactured lattice structures the joints between struts are rigid, thus, with $M < 0$ the stiffness of the structure is dependent on the bending load at the joints to prevent rotation. Generally, this means that the structure is bending dominated, while $M \geq 0$ ensures the structure is stretch dominated.

Hashin and Shtrikman already established in 1963 the bounds of the elastic properties that isotropic heterogeneous materials should fulfill [74]. This established a theoretical maximum efficiency to carry load for any isotropic lattice structure, which is very related to the concept of relative density. Nonetheless, lattice structures are usually not isotropic, and their stiffness varies considerably depending on the load direction. Furthermore, in most of the cases it is not relevant to reach maximum stiffness to weight ratios in the design of orthopedic implants, since the design goal is to mimic the stiffness of the bone tissue. Therefore, although they are a good reference to measure the efficiency of the structures, Hashin-Shtrikman bounds are not critical in the design process.

Gibson and Ashby [1] thoroughly studied cellular structures, and stated that stiffness and strength of lattice structures can be described by a power law of their relative density, such that:

$$\frac{E}{E_s} = C_n \left(\frac{\rho}{\rho_s} \right)^n \tag{1.2}$$

$$\frac{\sigma}{\sigma_s} = C_m \left(\frac{\rho}{\rho_s} \right)^m \tag{1.3}$$

In Equations 1.2 and 1.3, E and σ are the stiffness and strength of the structure, while E_s and σ_s correspond to the stiffness and strength of the constituent material, and ρ/ρ_s is the relative density. Thus, the equations describe the stiffness and strength of a structure with respect to the values corresponding to the solid material the structure is made of. Apart from the described variables, C_n, n, C_m and m vary with the topology of the structure.

Since stretch dominated structures are more efficient, the exponent n in Equation 1.2 is close to 1, whereas for bending dominated structures n tends to take values close to 2 (note that $\rho/\rho_s < 1$). Several lattice structures have been widely studied, and their Gibson-Ashby curves are already known. Among the bending dominated, body-centered cubic (BCC) [75], diamond [67] and rhombic dodecahedron [56] are common. For the stretch dominated structures, simple cubic (SC) [72] and octet truss [76] are the most representative examples.

Figure 1.13 depicts the Gibson-Ashby curves of several lattice structures with different relative densities, unit cell types and constituent materials. This shows the high variability of the stiffness and strength of the structures, which is very useful for the design of metamaterials. Furthermore, in order to reduce the uncertainty arising from different experimental results, and to have a comprehensive data set associated to each unit cell and its possible design spaces, Hanks et al. [77] gathered a very extensive set of experimental data and simulations for 18 different unit cell topologies.

Nonetheless, the Gibson-Ashby curves will strongly depend on the load direction. For example, SC is considered stretch dominated because it is usually loaded vertically, which only creates axial loads in the vertical struts. If loaded in another direction, such as [111] using Miller indices, the Gibson Ashby curve would be close to other bending dominated curves. The opposite occurs with the BCC structure, commonly regarded as bending dominated.

In general, the stiffness and strength of the lattice structures vary depending on the orientation of the load. Xu et al. [78] numerically obtained the directional stiffness of a set of unit cells (depicted in Figure 1.14a), and also developed some combinations of unit cells that resulted in an isotropic elastic

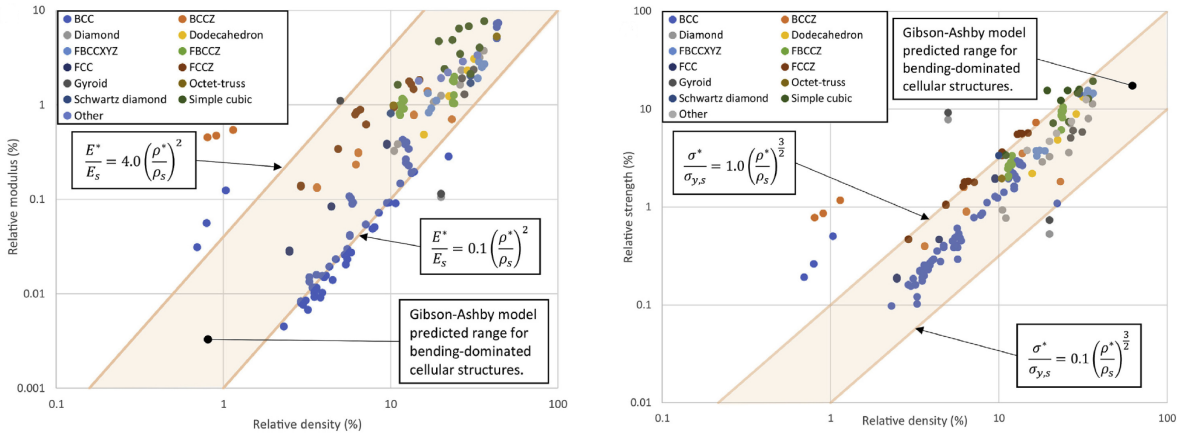

(a) (b)

Figure 1.13: a) Effective Young's moduli, and b) effective yield strength of several representative lattice structures and comparison to Gibson-Ashby predictions [13].

behavior. On the other hand, Munford et al. [71] developed an experimental method to better describe the anisotropy of a lattice structure (Figure 1.14b). Isotropy has been a design objective in several studies [19, 79, 80]. Furthermore, Tancogne-Dejean and Mohr [81] analytically described the necessary conditions that isotropic strut based lattice structures should fulfill.

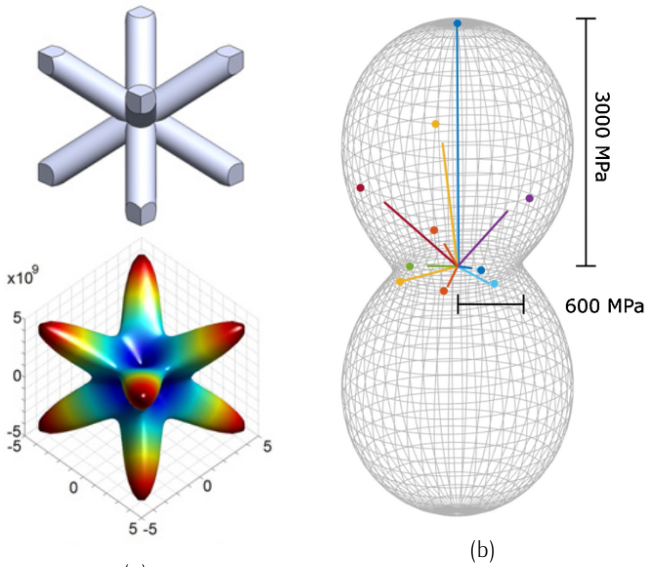

(a) (b)

Figure 1.14: a) Effective stiffness of a BCC structure depending on the load direction [78] obtained numerically, and b) approximation of effective stiffness of a stochastic structure based on 10 experimental points [71].

Nevertheless, bone tissue is generally anisotropic, since it is oriented with respect to the load it withstands in order to optimize its morphology [82, 83]. This suggests that the lattice structures to be used as bone substitutes can also be anisotropic, and the lower strength and stiffness in unloaded directions can

be beneficial to reduce the weight of the implant and increase its permeability and material transportation capabilities.

Fatigue mechanical properties

Orthopedic implants must withstand millions of cycles of stress [84] every year as a result of the everyday activity of the patients. For permanent implants, the scaffolds should endure tens of years [5], therefore, the study of lattice structures under fatigue loading conditions is of utmost importance.

Most of the musculoskeletal loads are compressive loads. Fatigue under compressive loads is not a problem for solid metals, but due to the complex geometries of the lattice structures tensile loads arise in scaffolds even under pure compression. This has a very negative effect on the fatigue strength of lattice structures, and thus the fatigue strength of the scaffolds is far below their solid non-porous counterparts [85].

Compression-compression fatigue has been widely studied for several lattice structures and materials [24, 86, 87, 88, 89, 90, 91, 92, 93, 94, 95, 96]. These works try to understand the fatigue behavior of lattice structures to predict the fatigue life under different load levels. This is based on the S-N curves as shown in Figure 1.15a, where the fatigue life is plotted against the maximum stress. The so called S-N curves are obtained from a regression similar to the Basquin's law [97], where σ represents the either stress amplitude or maximum stress of the cycle, N corresponds to the number of cycles, and A and B are the fitting parameters:

$$\sigma = AN^B \tag{1.4}$$

The compression-compression or tension-tension tests in literature induce a mean stress on the sample ($\sigma_{mean} = (\sigma_{max} + \sigma_{min})/2$) with a ratio R, defined in Equation 1.5 [98].

$$R = \frac{\sigma_{min}}{\sigma_{max}} \tag{1.5}$$

The type of unit cell greatly affects the fatigue behavior of the structures (see Figure 1.15a), since it determines the stress distribution within the lattice. The fatigue life of the structures is mainly driven by the tensile stresses that arise under global compression stress [89, 88]. In the case of the SC unit cell, the endurance limit is above the 80% of the yield strength of the structure, since no tensile stress is developed under global compression [89]. On the other hand, the relative density also determines the fatigue behavior of the structures as shown in Figure 1.15b. Furthermore, the S-N curves of the same unit cell for different relative densities are commonly normalized with the yield strength of the structure, as depicted in Figures 1.15c and 1.15d. In some cases, this allows to obtain an approximation of the fatigue life of a structure regardless the relative density, and based on quasi-static mechanical properties, which are easier to obtain (Figure 1.15d). Nevertheless, the normalized curves are not always consistent, as the normalized fatigue strength increases with relative density for some unit cell types (Figure 1.15c) [24, 93]. This occurs because fatigue failure is a phenomenon locally driven by the tensile stress concentration sites, while the obtained yield strength is related to more global plastic deformation.

To overcome this problem, Van Hooreweder et al. [99] developed a local stress method to predict the fatigue failure of a structure. In this method the maximum tensile stress of the structure is analytically obtained with an Euler-Bernoulli beam model of the strut, and the tensile stress is used as a predictor of the failure of the structure, that is, S_1 as depicted in Figure 1.16.

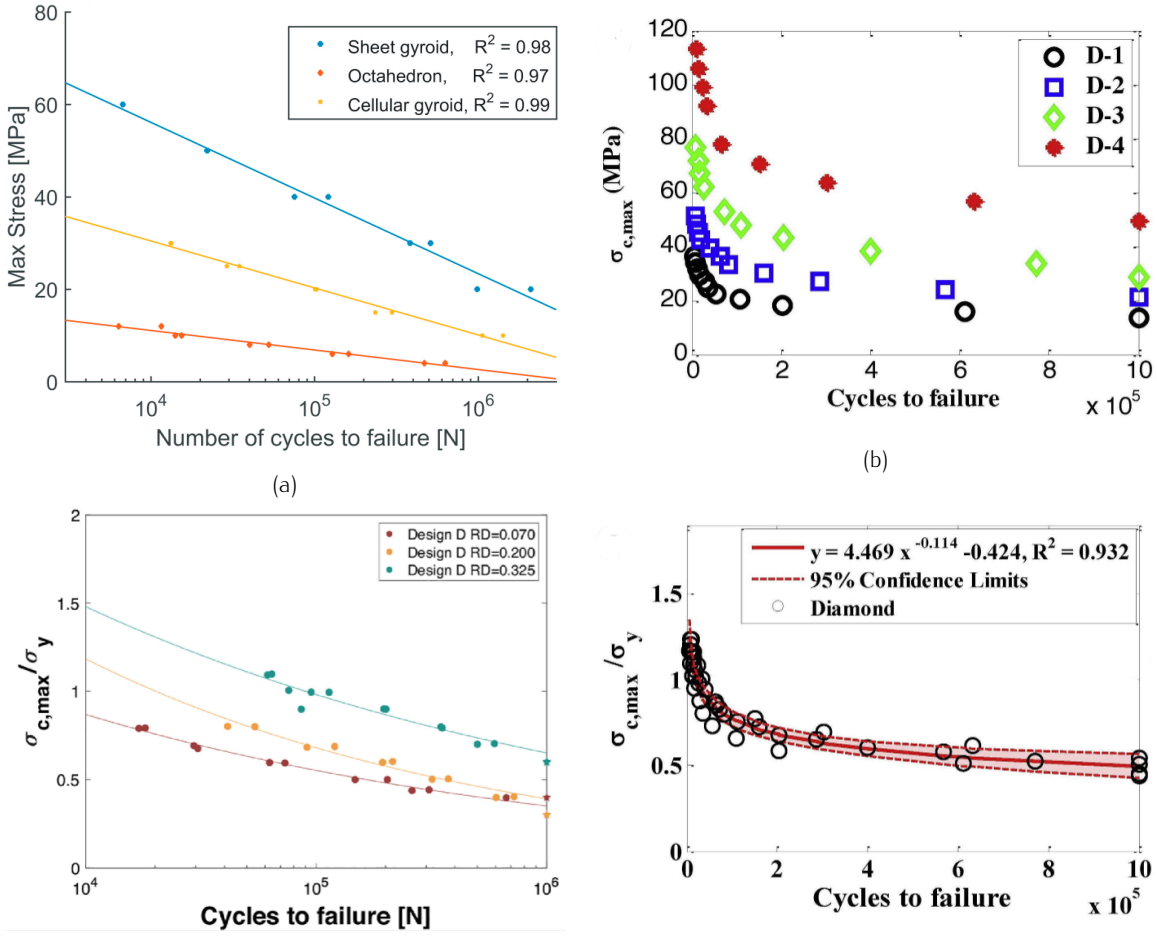

Figure 1.15: a) Global S-N curves of different NiTi unit cell types [86], b) global S-N curves of Ti6Al4V diamond unit cell with different relative densities (relative density increases from D-1 to D-4 specimens) [24], c) normalized S-N curves of Ti6Al4V auxetic metamaterial [93], d) normalized S-N curve of Ti6Al4V diamond unit cell [24].

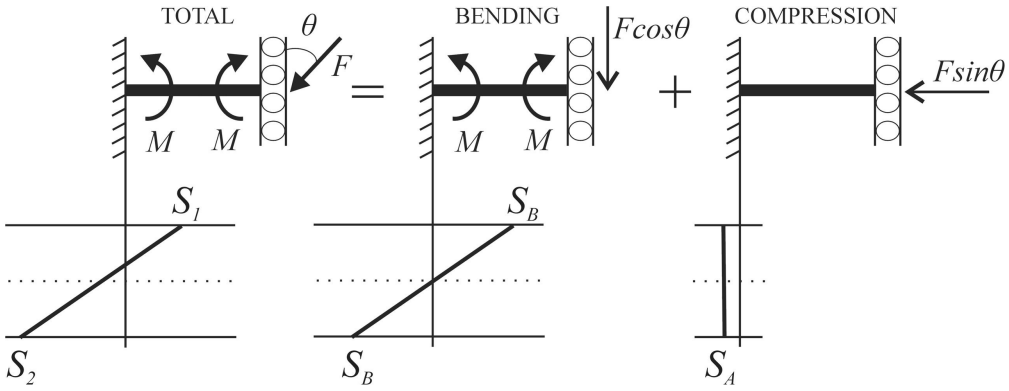

Figure 1.16: Beam model of a strut and its stress diagram for a bending and compression combination.

With this approach the S-N curves depict the maximum tensile stress according to the beam model with the number of cycles, as in Figure 1.17. Therefore, structures can be compared by observing their strength under the local tensile loads that actually cause the fatigue failure. This is particularly useful to compare different types of post processing techniques or load cases.

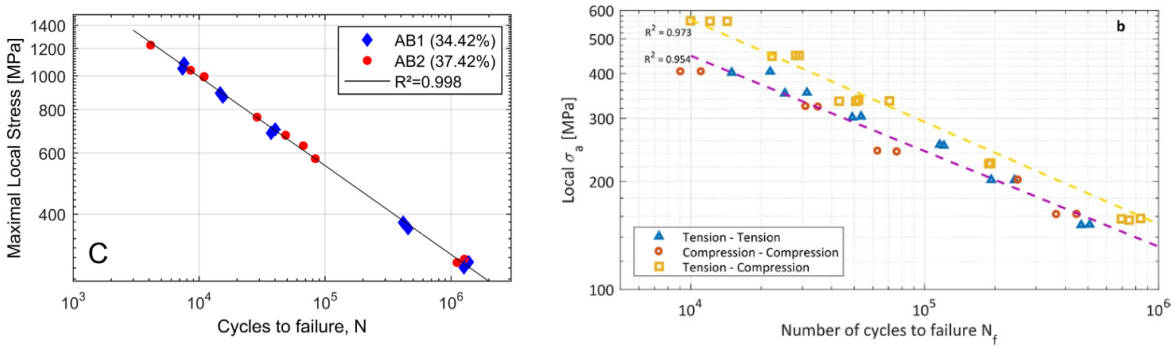

(a) (b)

Figure 1.17: S-N curves obtained from local stress method to compare a) two different relative densities [99] and b) different load cases [100].

Furthermore, it has been found that the material of the structure does not only affect the global S-N curve, but it also has a great influence on the normalized S-N curves. In fact, the material has a greater influence than the unit cell type for normalized S-N curves [24], contrary to what occurs in normalized quasi-static mechanical properties, which are more affected by the topology of the structures rather than by the material [69]. This might be explained by the different response to the surface roughness and crack tip plasticity for different material types, and thus, this difference is greater for high cycle fatigue. As a consequence, the endurance limit of AM lattice structures may vary between $< 20\%$ and $\approx 60\%$ of their yield strength [24].

This also means that for the same material, fatigue life is greatly influenced by post-treatments. In general, hot isostatic pressing (HIP) or heat treatment (HT) processes change the microstructure of the specimens, creating a more ductile material [101]. In the case of Ti6Al4V, the martensitic α' is replaced with a $\alpha + \beta$ microstructure [102]. In addition, HIP process also closes some pores due to the high pressure, reducing its internal porosity. The increased ductility has beneficial effects in the fatigue life of the structures [99, 87, 95], even if the added effect of the pressure in the HIP does not increase the fatigue strength compared to HT [103]. This might occur because of the importance of the surface geometrical imperfections, which dilutes the effect of the reduced internal porosity. In order to capture this benefit, HIP has to be combined with some sort of surface treatment [103]. Regarding the fatigue of other metals suitable for orthopedic implant such as CoCr [91, 104] among others [105, 106, 86, 107], the evidence is scarce compared to Ti6Al4V, and more studies are required.

Surface treatments, such as chemical etching, sand blasting, or electrochemical polishing, usually remove the attached powder particles and reduce the surface roughness, which is beneficial for the fatigue properties of the structures [99, 91, 108, 109]. Moreover, sand blasting also generates local plastic deformation on the surface, retarding micro-crack nucleation and growth [90, 87]. Figure 1.18 shows the isolated and combined effects of some different post-treatment options for enhancement of fatigue life in lattice structures.

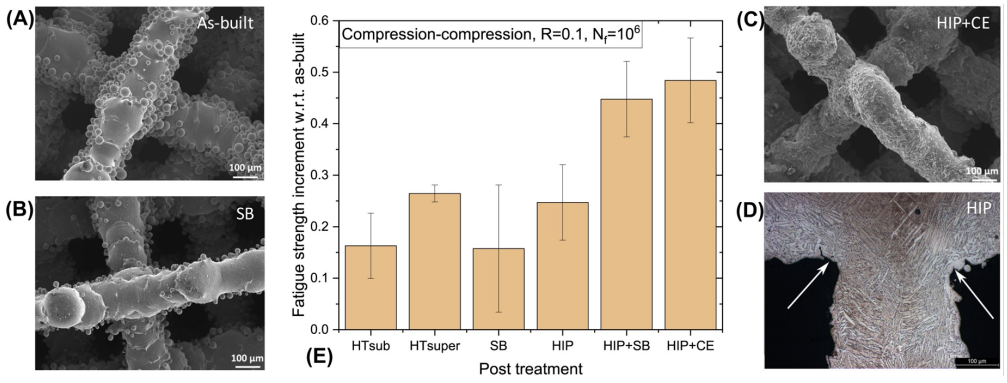

Figure 1.18: Effect of post-treatments on the compression-compression fatigue strength for 10^6 cycles of Ti6Al4V lattice structures. SEM micrographs of (A) as-built, (B) sand-blasted, and (C) HIPed and chemichal etched diamond lattice. (D) Microstructure of HIPed lattice. HTsub and HTsuper: heat treatment below and above β-transus, respectively. SB: sand-blasting. HIP: hot isostatic pressing. HIP+SB: HIP followed by sand blasting. HIP+CE: HIP followed by chemical etching. Figure obtained from [103].

1.2.4 Modeling of lattice structures

In order to design the properties of a lattice structure it is very useful to use models that describe the mechanical behavior of the structures. These models can be analytical or numerical, and offer the possibility to analyze the impact of the design parameters on the resulting mechanical properties of the structures before their manufacturing.

Analytical models

Analytical models are the simplest method to predict the mechanical properties of the structures, avoiding computational or experimental costs. These models can describe the stiffness and strength of lattice structures in any direction, and can be easily implemented in optimization algorithms. Furthermore, they have proved to be useful in determination of fatigue life.

Analytical models offer a good approximation for structures with slender struts, thus for structures with low relative densities. While experimentally obtained data is dependent on variables such as the material of the structure, the building quality, the size of the structure, etc., the analytical models offer an objective tool to compare the properties of different structure topologies.

These models are commonly based on Euler or Timoshenko beam theory [110], and the axial and bending loads of the struts are modeled, as depicted in Figure 1.19. Timoshenko beam theory considers shear deformation of the struts, in contrast to Euler beams, which makes the Timoshenko beam more accurate for higher relative densities, when struts are not as slender [110].

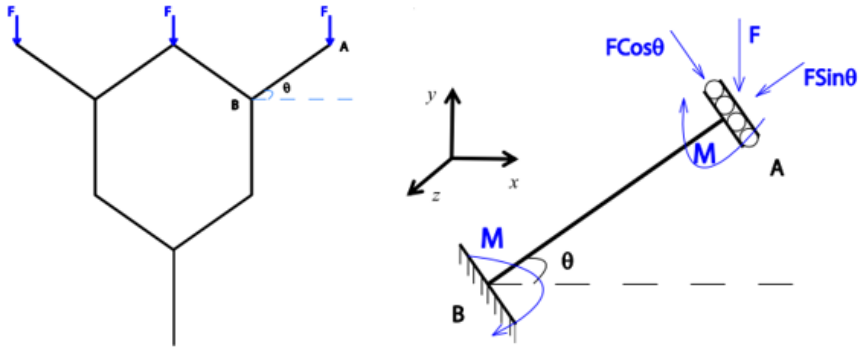

Figure 1.19: Beam model of a diamond unit cell, adapted from [67].

Analytical models were developed for a wide range of structures: the BCC structure [111], diamond unit cell [67], rhombic dodecahedron [112], truncated cuboctahedron [113] and truncated cube [114]. Furthermore, Zadpoor and Hedayati collected many of the models for different structures in a review article [110], which also includes buckling analysis, and these models are depicted in Figure 1.20.

The analytical models obtained in literature can be limited to the stiffness of the structures in one principal direction, or can also include the yield strength of the structures or the Poisson's ratio. Furthermore, in some cases it is relevant to obtain these parameters for different load orientations. This is done in some studies for BCC and its variations [115, 116] and rhombic dodecahedron [116].

Apart from Timoshenko and Euler beam models, for some stretch dominated structures the bending of the struts can be neglected, and thus the struts can be modeled as simple truss elements [76]. This was done by Tancogne-Dejean and Mohr [81], who modeled the struts as simple truss elements and obtained the stiffness matrix of any stretch dominated elastically isotropic lattice structure (Equation 1.6) as a function of the relative density (ρ^*) and the Young's modulus of the material (E_s), provided that the bending of the beams could be neglected. Moreover, Messner et al. [117] developed an analytical yield surface for stretch dominated lattices with Eq. 1.7, which relates the axial stress in each strut ($\sigma^{(i)}$) with the Young's modulus of the material, the compliance matrix of the structure ($\underline{\underline{\underline{\underline{S}}}}$), the direction of the strut ($\underline{\boldsymbol{n}}^{(i)}$) and macroscopic stress ($\underline{\underline{\boldsymbol{\sigma}}}$).

$$\mathbf{C} = \frac{\rho^* E_s}{15} \begin{bmatrix} 3 & 1 & 1 & 0 & 0 & 0 \\ & 3 & 1 & 0 & 0 & 0 \\ & & 3 & 0 & 0 & 0 \\ & & & 1 & 0 & 0 \\ & sym & & & 1 & 0 \\ & & & & & 1 \end{bmatrix} \tag{1.6}$$

$$\sigma^{(i)} = E_s \varepsilon^{(i)} = E_s \left[\underline{\underline{\underline{\underline{S}}}} : (\underline{\boldsymbol{n}}^{(i)} \otimes \underline{\boldsymbol{n}}^{(i)}) \right] : \underline{\underline{\boldsymbol{\sigma}}} \tag{1.7}$$

Finite Element models

Finite element (FE) models enable a more accurate representation of the lattice structures compared to the analytical models. Instead of a unit cell, the whole structure can be simulated and compared to the experimental values to validate the numerical model. Furthermore, manufacturing deviations can be

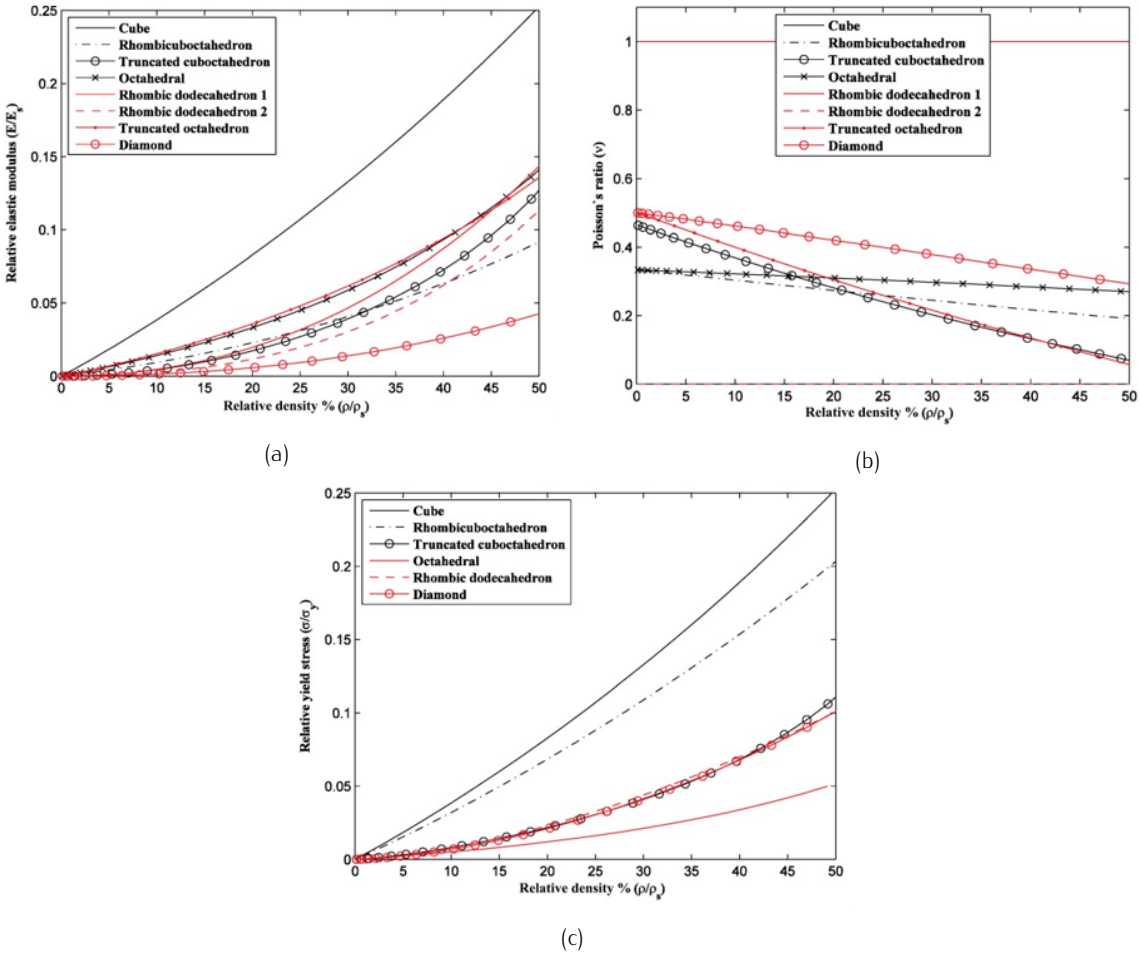

Figure 1.20: Analytical models of lattice structures with different unit cell topologies based on Euler-Bernoulli beams for a) relative stiffness, b) Poisson's ratio, and c) relative yield strength [110].

included in the models, and other variables such as stress concentrations, material plasticity, contact and time dependent properties can be implemented for a more comprehensive study of the mechanical behavior of the structures. FE models can be made of beam elements or 3D continuum elements.

Beam models have very low computational cost due to their reduced degrees of freedom. However, beam models do not consider overlapping volume domains at the nodes, or the excess of material at nodes [118]. Nonetheless, the low computational costs of beam elements enable to simulate entire structures with hundreds of unit cells, as it is usually the case with experimental specimens. This allows to include boundary effects in the simulation. Boundary effects arise in the free surfaces of the structures, and on the contact surface of the structure with the clamps, creating a nonuniform stress state. Minimizing such effects is necessary to obtain the effective macroscopic properties of the structures accurately [52].

The beam models can be implemented as-designed, with increased thickness at the nodes or including the aforementioned manufacturing imperfections. The accuracy of as-designed beam models (see Figure 1.21a) varies across different works: while in some studies the numerical models agree with the experimental data [119, 67], in others the experimental stiffness and strength are below the numerical values [114, 113, 120], or even the opposite [111].

One method to account for the higher stiffness of strut intersections is to artificially increase the diameter of the numerical beams at both ends [121, 122, 123], as shown in Figure 1.21b. Nevertheless, the increase in thickness to match the experimental values is arbitrary, and therefore it is not suitable for the prediction of mechanical properties previous to manufacturing.

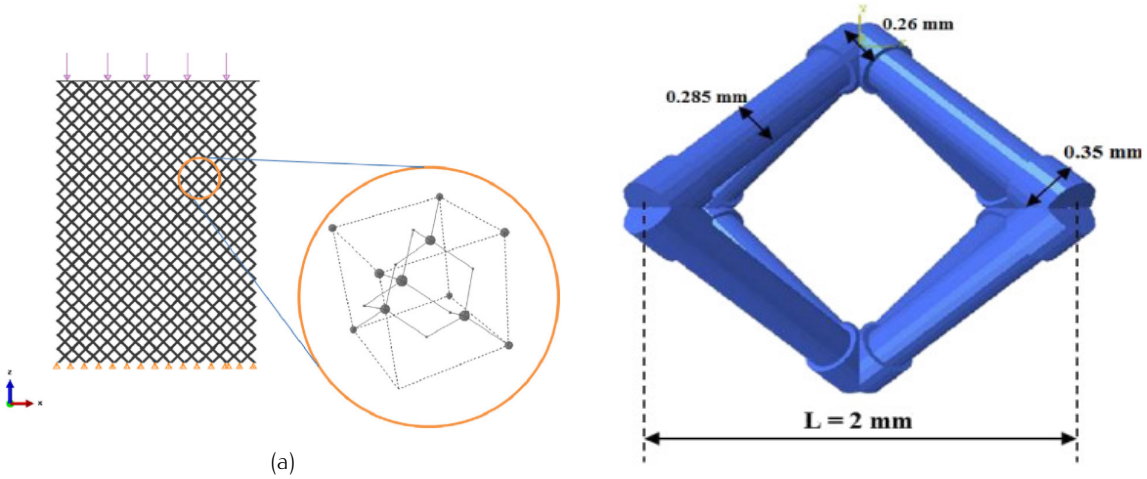

(a) (b)

Figure 1.21: a) Beam model structure of diamond unit cell [67] and b) modified beam model of BCC unit cell to account for the effect of strut intersection at the nodes [121].

One of the sources of the discrepancies between the numerical and experimental values is the use of ideal struts. As already stated, there can be very significant manufacturing deviations in the produced lattice structures, and including these imperfections in the FE beam models improves their accuracy. This can be done by using a μ-CT to measure the actual shape of the struts, as well as their waviness. Different levels of imperfections can be introduced:

- Variation of strut diameter: different strut diameters can be assigned to each element along the strut, as done in [124, 125, 126] (see Figure 1.22a).
- Variation of strut diameter and waviness: apart from the cross-section variation, the center of gravity of each node along the strut is displaced according to previously measured statistical data, as in [48, 53, 23] (see Figure 1.22b).

One advantage of the beam models is that they are suitable to create models for fatigue prediction. The rapid computation time allows to create algorithms that simulate the degradation process of the structure by introducing the failure of individual struts. Thus, the simulations are carried out again and again considering the damage of previous cycles to capture loss of stiffness of the whole structure, until the total collapse. This approach was used by Hedayati et al. [127] with ideal struts, while Zargarian et al. [128] also included manufacturing imperfections.

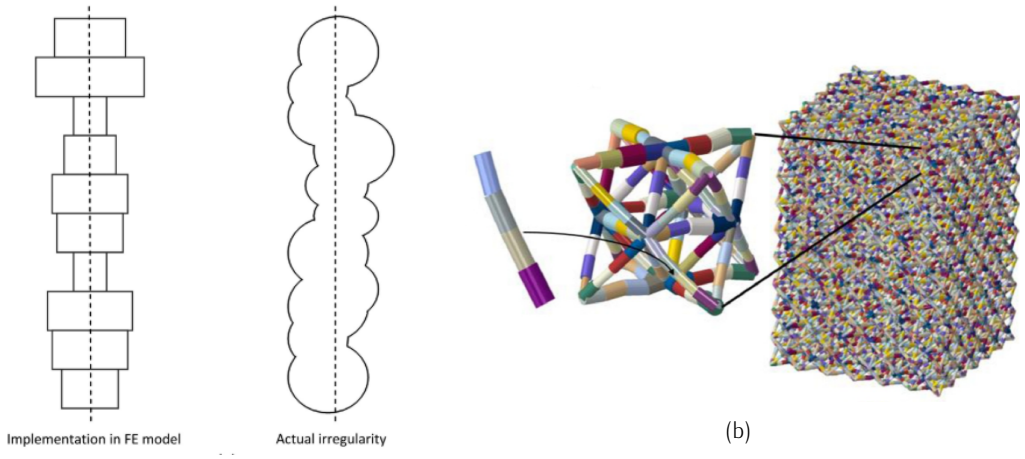

(a) (b)

Figure 1.22: a) Beam model with variable diameter along its length [125], and b) reconstructed beam model of an octet-truss structure including diameter variation and waviness [48].

The use of 3D elements allows a more precise representation of the actual geometry for any relative density, including the strut intersections and any manufacturing deviations. Nevertheless, the computational cost is much higher due to the great number of degrees of freedom of the models. FE models are mostly used to simulate the monotonic unidirectional compression experiments, as done in [129, 61], rather than to fully characterize the effective mechanical properties of the structures. Therefore, commonly the FE model of the experiment consists of the structure and two rigid plates as in Figure 1.23a. Some studies focus on the effect of boundary conditions, and the minimum amount of unit cells required to dilute the boundary effects and obtain the Young's modulus and yield strength at the minimal computational cost [130, 131]. Compression tests can be simulated establishing a frictionless contact between the struts and the platens [123], giving a friction coefficient [130], or completely restricting the lateral displacement of both ends of the specimen [89].

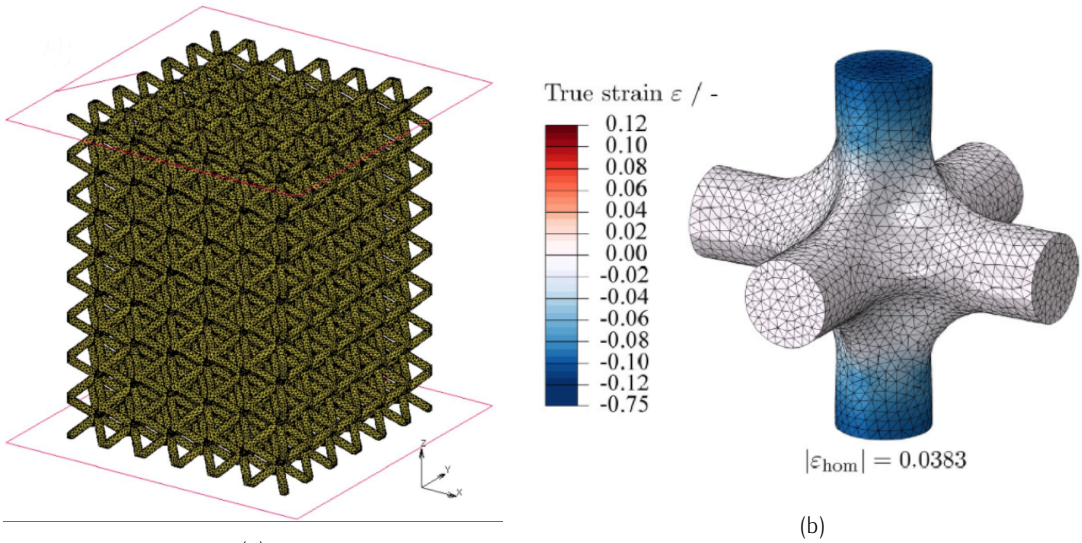

(a) (b)

Figure 1.23: a) FE model of a BCC structure with tetrahedral elements [123] and b) FE model of a unit cell with PBC [59].

One way to reduce the size of the model is to simulate a single unit cell and apply periodic boundary conditions (PBC), as done in Figure 1.23b. PBC establish constraints in the displacement fields of opposite faces of a unit cell, imposing a periodicity that simulates an infinite continuum formed by periodical arrays of the unit cell [132]. This is a very computationally cost effective method, since a single unit cell represents the whole structure, and is especially used to obtain the effective stiffness matrix of the structures as in [116, 78, 133]. Even if boundary effects can not be modeled by this approach, these models offer a good approximation of the behavior of the actual structures [131, 59].

Nevertheless, as for beam elements, the modeling of the manufacturing imperfections plays a key role in reducing the difference between the simulations and experiments. In this case one option is to simulate a numerical model directly obtained from the μ-CT data. The FE model can be built by using an STL file that defines the surface of the structure, as in [134, 42, 48, 53], or by creating a voxel mesh [135] and using efficient finite cell methods as in [136, 137]. Another option is to build a FE model based on statistical data of the strut measurements [51, 138, 48]. Figure 1.24 depicts some of the models generated by using such methods.

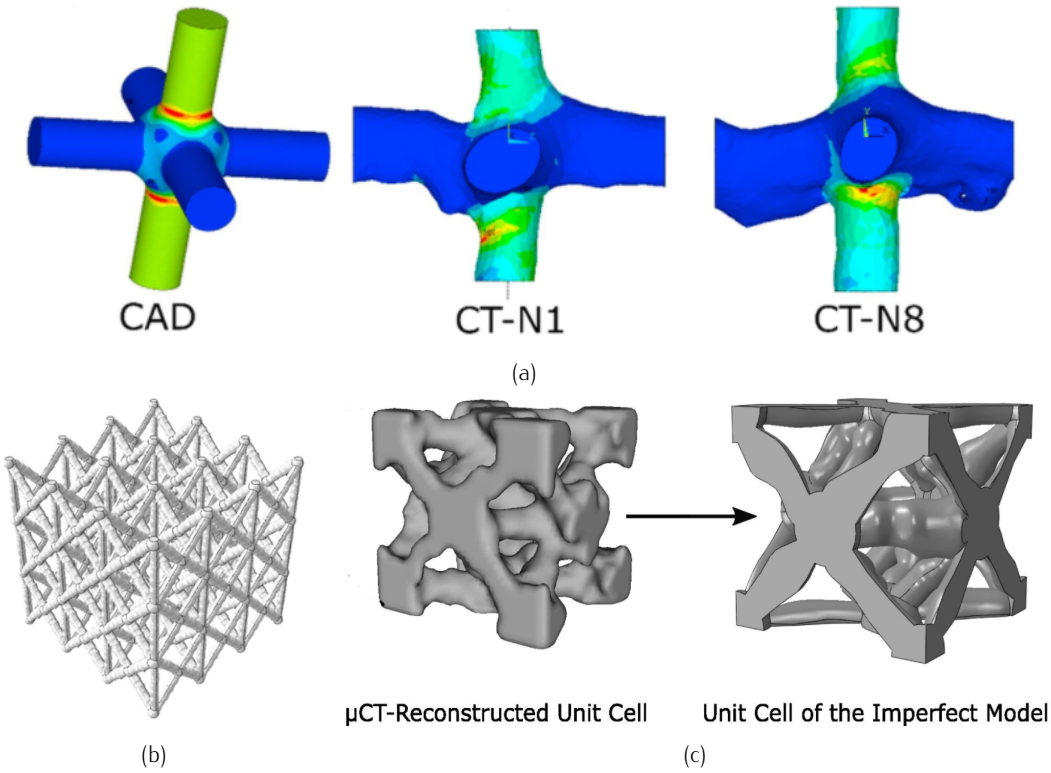

Figure 1.24: a) The CAD model and two manufactured unit cells of a SC unit cell [53], b) 3x3x3 lattice structure of reconstructed struts [138] and c) reconstruction from μ-CT scan to imperfect CAD model [51].

Even if these methods include the manufacturing deviations of the structures, their capability of effectively mimicking the experimental mechanical properties is limited, and depends on many factors such as the dimensions of the structure, the surface roughness, or the internal porosity, which are difficult or very inefficient to take into account in a single model. As an example, Doroszko et al. [139] showed that the resolution of the CT scan has an important effect on the capability to capture the actual behavior

of a lattice structure: a resolution of 127μm clearly overestimated the mechanical properties, whereas a 2.94μm resolution offered an accurate estimate, as shown in Figure 1.25.

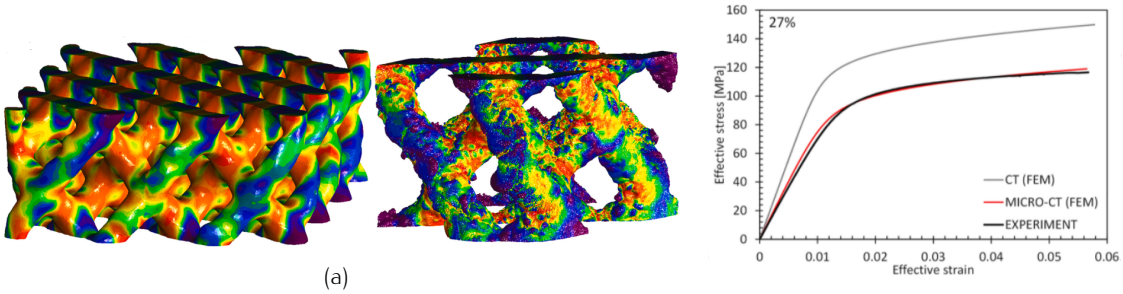

Figure 1.25: a) Stress of CT scanned FE models with 127μm (left) and 2.94μm (right) resolutions and b) stress strain curves of the FE models compared to the experimental curve.

One method to implicitly include the manufacturing deviations in the numerical analysis without modeling the actual complex geometry of the structure is to reduce the stiffness and strength values of the constituent material. In some studies individual struts were manufactured and tested, showing much lower mechanical properties than for the bulk material [130, 140, 141]. These material properties were then assigned to FE models to improve the accuracy of the simulations.

1.2.5 Lattice structures for orthopedic implants

The use of lattice structures in orthopedic implants has a promising prospect, and interest has grown in recent years in this research field. Lattice structures, together with AM, enable the patient-specific design of implants. This means that the bone replacement can be adjusted to the patient anatomy, considering the precise geometry of the bone defect. In addition, lattice structures are capable of mimicking the mechanical properties of bone they are substituting, which avoids the problematic major disruptions in the stress and strain fields of the adjacent bone.

Bone is a natural composite, formed by two main phases: collagen and hydroxyapatite (HA) crystals [142]. The HA crystals give the bone its strength and toughness, while the collagen holds the structure together and gives flexibility [143]. With this basis, bone is formed in a hierarchical structure, organized from macroscopic scale to sub-nanoscale, as depicted in Figure 1.26. From the macroscopic point of view, bone can be divided in trabecular bone and cortical bone. Trabecular bone, also named cancellous bone, is a bone structure with high porosity (between 50% and 90%) to leave space for bone marrow. Cortical bone is highly dense, leaving only 3-5% porosity for osteocytes, canaliculi, blood vessels, etc [143]. Furthermore, bone continuously adapts its structure to ensure optimal functionality with minimal metabolic cost [144, 145, 146]. The functional adaptation of bone is achieved by morphology variations that depend on the strain stimulus of the bone [145]. The mature or damaged bone tissue can be resorbed (bone tissue is broken down to release its minerals to the blood [147]) by osteoclasts and new bone tissue is created by osteoblasts, in a continuous process to ensure optimal morphology according to the load.

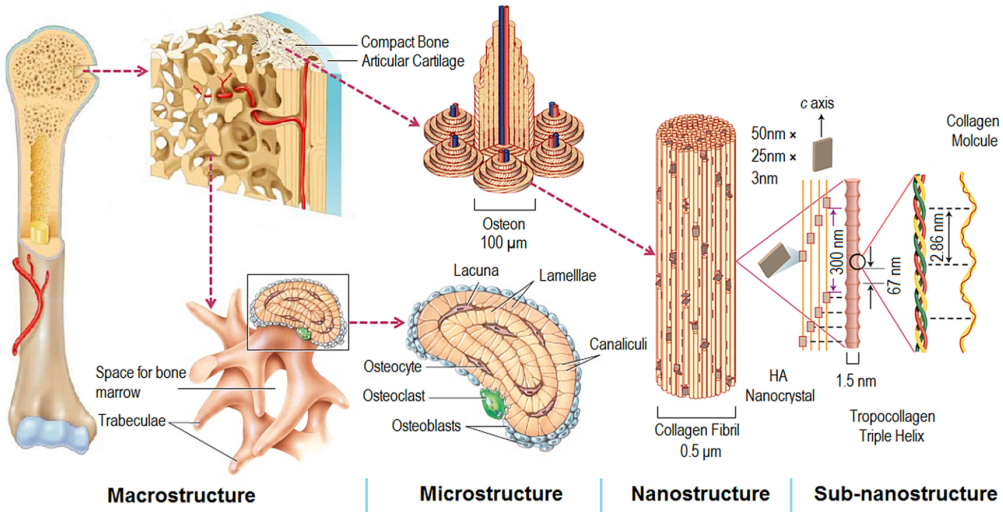

Figure 1.26: Hierarchical structure of trabecular and cortical bone [143].

Both trabecular bone and cortical bone have different properties depending on anatomical site, age, sex, physical activity level, etc [148]. The mechanical properties of bones are still a field of study, and the elastic modulus is the main studied variable due to its importance in characterizing bone pathologies and in implants development [143]. The strength of bones is the other major variable, which is also important in the design of orthopedic implants. Figure 1.27 shows some values for bone in different sites, and according to different studies. The high variablity can be attributed to the aforementioned variables that determine bone properties.

The mean stiffness of trabecular bone is in the range between 22 MPa [152] and 1091 MPa [149], with strength values varying between 0.37 MPa [151] and 5.83 MPa [149]. On the other hand, cortical bone is much stiffer and stronger due to its compact nature, with Young's modulus between 6 GPa [158] and 22.4 GPa [107], and compressive yield strength between 83 MPa and 225 MPa [158]. Apart from the variability between bone locations and studies, Figure 1.27 also shows the high anisotropy of bone tissue. Cortical bone is usually considered a transversely isotropic material [154, 160], i.e. its stiffness is higher in the axial direction aligned with osteons (see Figure 1.26), and has a lower isotropic stiffness in the transverse plane perpendicular to the osteons. On the other hand, trabecular bone also has variable levels of anisotropy, as a result of the functional adaptation to the complex physiological loads in each bone site.

As mentioned above, bone is a natural tissue that is able to reconstruct itself when a bone defect is induced. This bone defect can occur as a fracture with bone loss, high energy trauma, blast injuries, infection requiring debridement of bone or resection of bone tumors [161]. A critical size defect (CSD) is a defect that bone is not able to reconstruct by itself due to its size [162]. Autogenous bone grafts (autografts) are bone pieces of the same patient taken from other anatomical sites, and used to fill these CSD, enabling the reconstruction of bone [163]. This procedure is considered the gold standard to treat CSD, but it is complicated and has drawbacks like donor site morbidity, limited graft volume, anesthesia time or need for additional surgical resources [162]. One alternative is to use implants to substitute the absent bone. Furthermore, implants are also used in joint replacements such as ankle, knee or hip, and can be also used for spinal fusion, among others [164, 165]. Figure 1.28 shows some examples of implants that also have lattice structures.

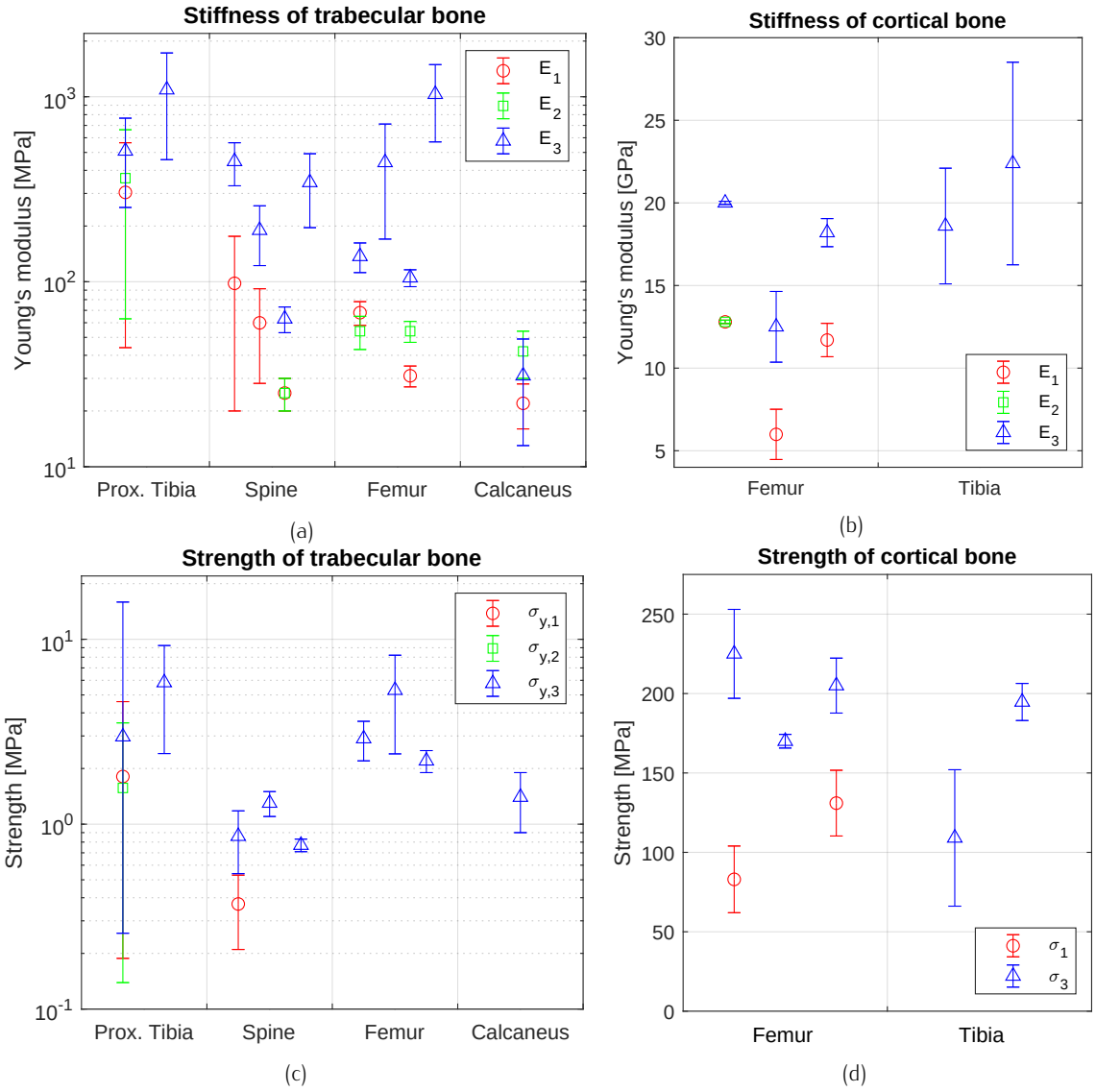

Figure 1.27: Literature values in various bone sites for a) stiffness of trabecular bone, b) stiffness of cortical bone, c) strength of trabecular bone, and d) strength of cortical bone. Obtained from [71, 149, 150, 151, 152, 153, 154, 155, 156, 157, 158, 107, 159].

Traditional metallic orthopedic implants are made of bulk parts, based on alloys of titanium, stainless steel or cobalt, among others [169]. Nonetheless, these dense implants are at least one order of magnitude stiffer than the hosting bone. As a result of this mismatch of stiffness, the mechanical stimulus in the bone adjacent to the implant is reduced, as the implant carries most of the load. This phenomenon is referred to as stress shielding. The lack of long term strain stimulus caused by the stress shielding can result in bone resorption in areas adjacent to the implant, as it is depicted in Figure 1.29 [170, 171]. Moreover, the vascularization (creation of blood vessels) is more difficult in areas surrounding solid implants, leading to a deficit of nutrients for the bone [172]. The loss of bone density can result in the implant loosening from the bone, which in turn affects to the fixation and longevity of the implant. In fact, stiff metal devices lead to additional and more extensive revision surgery [173, 171].

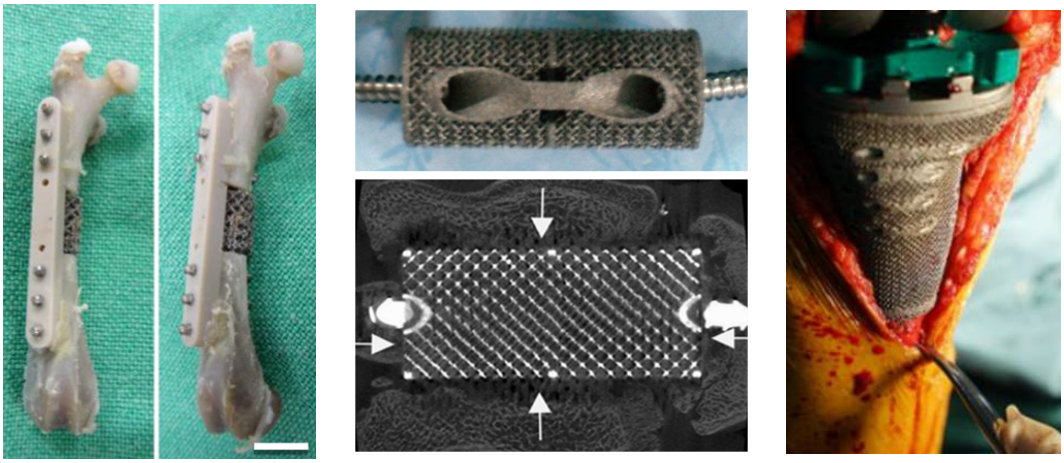

(a) (b) (c)

Figure 1.28: Lattice structures in orthopedic implants for a) a segmental bone defect in rat femur [166], b) vertebral implant for spinal fusion in sheep [167] c) proximal tibia in knee replacement [168].

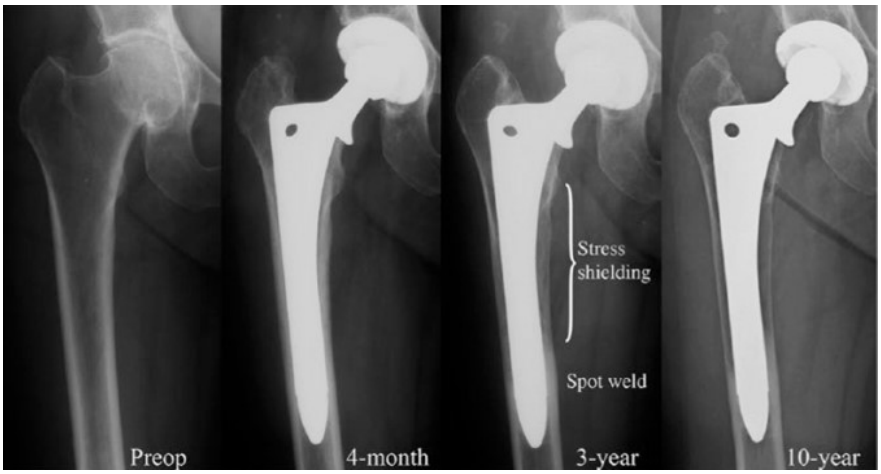

Figure 1.29: Bone resorption caused by the stress shielding after 10 years of total hip arthroplasty [174].

Moreover, the pores of open-cell lattice structures can host new bone tissue [169], while also allowing vascularization and mass transport [175], promoting bone ingrowth. The shape and size of the pores, as well as the porosity, determine the extent to which the structure can support the creation of new bone tissue [176, 177]. Two mechanisms compete in the creation of new bone tissue. On the one hand, small pore size and higher specific surface allow a higher initial cell attachment on the structure, while larger pores enhance vascularization and transport of nutrients to the implant, resulting in a better osteogenesis after the initial stage [177]. In general, pore sizes higher than 300μm are recommended for full osseointegration, and some studies also set optimum upper bounds around 600 or 800μm, although there is not a clear consensus in literature [172, 178, 176, 179].

Overall, lattice structures provide a set of properties that makes them suitable as alternative to conventional solid implants. Through the topology design, structures with an effective Young's modulus close to the one of the hosting bone can be obtained to mechanically stimulate hosting bone, and thus

mitigate stress shielding [180]. In this way, apart from providing structural support, the lattice structure can also guide the formation of new bone tissue due to its porous nature, improving the osseointegration of the implant and bone healing capacity [171]. Furthermore, the geometrical as well as the mechanical properties of the structures can be tuned and graded within the implant depending on the properties of the adjacent bone tissue and patient specific data, thus enabling the design of novel metamaterials for bone substitutes and orthopedic implants [181].

Chapter 2

Objectives

Lattice structures have the potential to improve the existing monolithic orthopedic implants by reducing the stress shielding and promoting osseointegration, hence leading to more durable implants that reduce the number of revision interventions. Nevertheless, the available knowledge of this type of structures is still scarce. The main motivation of this dissertation is to expand the available knowledge on the mechanical properties of additively manufactured lattice structures under static and dynamic loads and the modeling of these structures to provide new possibilities for the design of orthopedic implants. To this end, three main objectives were defined:

Develop analytical models to define the elastic response under different loads of lattice structures that can potentially be implemented into orthopedic implants

As discussed above, one of the main problems of current orthopedic implants is the stress shielding-effect due to the mismatch between bone and implant stiffness. Bone properties might be very different depending on patient characteristics (gender, aging or skeletal pathologies) and the implant site, thus the implants should be able to adapt to a wide range of mechanical properties. To experimentally determine the optimal structure for the implant is costly and time consuming, and numerical simulations are not a rapid tool to design the mechanical properties of the structures. In contrast, analytical models are fast and they can be implemented into optimization algorithms to design implants that adapt to each load type.

Hence, the first objective of this work is to develop novel analytical models that describe the mechanical properties of lattice structures. Since the loads of an implant can be complex, the analytical models can also be a design tool to efficiently adapt the morphology of the structures to such loads. This includes controlling the isotropy or anisotropy of the structures for optimal load carrying capacity.

Characterize the fatigue behavior of lattice structures

Orthopedic implants will be subjected to dynamic loads during daily activities, therefore the fatigue life and endurance limit of these structures is of utmost importance. The fatigue behavior of the structure will depend on the structure topology, material, post-build treatment and relative density. The second objective of this work is to study the fatigue behavior of lattice structures considering the effect of post-build treatment and the relative density. This information will in turn be used to develop tools that effectively predict the fatigue life of the structures.

Study the effect of manufacturing deviations on the mechanical properties of the structures

The development of additive manufacturing opens the possibility to produce complex lattice structures with very small features suitable for orthopedic implant applications. However, there are some imperfections intrinsic to the manufacturing process such as dross formation, waviness, or strut shape and diameter variation that affect to the resulting mechanical properties of the structures. Therefore, another objective of this work is to study the manufacturing deviations that arise when producing such small meso-structures, and to develop a numerical framework that is capable of simulating the quasi-static mechanical properties of lattice structures while considering such deviations within the model. This enables a faster design process of new structures and a more precise analysis of the response of the implant under physiological loads.

Chapter 3

Structure

This dissertation encloses four research papers, namely **Paper A**, **Paper B**, **Paper C** and **Paper D**, and each work contributes to the stated objectives in a different manner.

Paper A is entitled 'Analytical model of the elastic behavior of a modified face-centered cubic lattice structure'. This work analyses a modified face-centered cubic (FCCm) unit cell, and the analytical expression of the stiffness matrix was obtained based on geometric variables of the structure. In addition, this model was validated through a FE model of beam elements. Thus, the analytical model is a tool to tailor specific mechanical properties to mimic bone stiffness by adjusting its geometric parameters, contributing to objective 1. The stiffness of the unit cell was also compared to other analytical models in the literature, to have a better insight on the similarities and differences with the FCCm structure, and a study of the pore size was also carried out due to its importance for the osseointegration of the structure.

Paper B is entitled 'Influence of relative density on quasi-static and fatigue failure of lattice structures in Ti6Al4V produced by laser powder bed fusion'. This work also studies the FCCm unit cell, but takes a more experimental approach. Manufactured FCCm structures with different relative densities were tested under quasi-static and fatigue uniaxial compression. The Gibson-Ashby curves were obtained for macroscopic stiffness and strength of the structures, contributing to objective 1. The experimental values were compared to the numerical simulation of a solid FE model with periodic boundary conditions (PBC) to assess the prediction capacity of the FE model and to study the relationship between macroscopic and mesoscopic stress phenomena.

Furthermore, a fatigue analysis was carried out to assess the durability of the structures. A stiffness based failure criterion was proposed, and an analytical expression was developed to relate the cyclic load, fatigue life and relative density of the structures. In addition, other methods for fatigue life prediction in literature were assessed and modified to increase their accuracy. Thus, this paper also contributes to objective 2 of this dissertation.

Paper C is entitled 'Additively manufactured lattice structures with controlled transverse isotropy for orthopedic porous implants'. This paper presents a set of unit cells that have elastic transverse isotropy in one plane, and a higher stiffness in the direction perpendicular to the plane. One particular unit cell was chosen due to its suitability for additive manufacturing, and the numerical and experimental validation of the analytical model were carried out. Transversely isotropic lattice structures offer the possibility to better mimic the anisotropy of some bone tissue in locations where the load is primarily oriented in a single direction. Thus, this paper contributes to objective 1.

Paper D is entitled 'Understanding elastic anisotropy in diamond based lattice structures produced by laser powder bed fusion: Effect of manufacturing deviations'. In this work the anisotropy of the diamond structure was analyzed considering the manufacturing deviations, which corresponds to the objective 3.

The isolated and combined effects of the errors in diameter, cross-section shape and waviness were studied and compared to the ideal stiffness of the diamond structure. Furthermore, a method was developed to analyze the manufacturing imperfections along the strut and to include such deviations in a FE model.

Chapter 4

Publications

This Chapter encloses the four publications made along this thesis, which are the main contributions of this work to the field of lattice structures.

4.1 Paper A

This article is entitled 'Analytical model of the elastic behavior of a modified face-centered cubic lattice structure'. It develops an analytical model of the stiffness of a modified face-centered cubic structure (FCCm) based on Timoshenko beam theory. These are the main contributions of this work:

- The struts were modeled considering their axial elongation, bending and torsion, thus, a perfect correlation between the model and numerical simulations with beam elements can be guaranteed.
- The complete stiffness matrix was modeled to identify stiffer and more compliant directions, and to enable the implementation of the analytical model in optimization algorithms.
- A variable height to width ratio (R) of the unit cell was included to expand the design possibilities and to adjust the anisotropy of the structure.
- The design space of the FCCm unit cell is explored to mimic the stiffnss of bone, and a pore size analysis is included to assess the osseointegration capability of the structure.

Journal of the Mechanical Behavior of Biomedical Materials 98 (2019) 357–368

Contents lists available at ScienceDirect

Journal of the Mechanical Behavior of Biomedical Materials

journal homepage: www.elsevier.com/locate/jmbbm

Analytical model of the elastic behavior of a modified face-centered cubic lattice structure

Markel Alaña*, Aitziber Lopez-Arancibia, Ainara Pradera-Mallabiabarrena, Sergio Ruiz de Galarreta

Universidad de Navarra, TECNUN Escuela de Ingenieros, Paseo Manuel de Lardizabal, 13, 20018, San Sebastin, Spain

ARTICLE INFO

Keywords:
Porous biomaterials
Lattice structures
Analytical model
Additive manufacturing
Mechanical properties
Homogenization

ABSTRACT

As result of the advances made in additive manufacturing in recent years, the design of porous materials with controlled mechanical properties has gained importance due to their capability to offer case-specific solutions in multiple applications. In terms of biomaterials, the use of lattice structures provides a considerable variety of mechanical and geometric properties that can enhance osseointegration and reduce stress shielding. In this paper, the elastic response of a modified face-centered cubic (FCC) unit cell was studied, and analytical expressions for macroscopic effective Young's moduli, shear moduli and Poisson's ratios were obtained, thus providing the necessary parameters for the homogenization of the unit cell. The analytical expressions of the homogenization parameters open the possibility for implementation in other research fields, such as topology optimization. Timoshenko beam theory was used to model the struts of the modified FCC unit cell and a finite element analysis using shear flexible beam elements was performed to assess the accuracy of the analytical expressions. In addition to modelling the bending of the beams, axial and torsional displacements were also considered for a more detailed analysis. It can be concluded that the expressions obtained represent the elastic behavior of the modified FCC unit cell with high accuracy. Finally, the elastic response was further analyzed by introducing variability in the aspect ratio in order to enable the design of unit cells with controlled anisotropy.

1. Introduction

Advances in the field of additive manufacturing (AM) in recent years have enabled the development of cost-effective applications for additively manufactured parts in several research fields due to the high flexibility and low fixed costs of AM (Merkt et al., 2015). One of the main advantages AM offers is the possibility of manufacturing lightweight and high-porosity lattice structures, which are built from connected struts that repeat a geometric pattern (Ashby, 2006).

Lattice structures are of interest to researchers due to their superior specific mechanical properties (Crupi et al., 2017; Kadkhodapour et al., 2017; Carlton et al., 2017; Wadley et al., 2003). They are also relevant because of their energy absorption properties (Brennan-Craddock et al., 1088; Mines et al., 2013; Maskery et al., 2017; Tancogne-Dejean et al., 2016; Al-Saedi et al., 2018), and their capacity to act as heat exchangers (Wong et al., 2009) and noise reducers, and to transmit vibrations (Wang et al., 2018; Matlack et al., 2016). These properties greatly depend on their relative density and the geometry of the space-filling unit cells, which can form stretching or bending dominated lattice structures (Deshpande et al., 2001a).

Lattice structures have also become relevant in the design of biomaterials due to their porous nature and the adaptability of their mechanical and geometric properties, which enables the design of metamaterials that reduce stress shielding while considering other parameters such as permeability (Ali and Sen, 2017; Montazerian et al., 2017; Zhang et al., 2018a). This makes it possible to design metamaterials that avoid bone resorption and at the same time promote bone ingrowth. Therefore, lattice structures offer considerable promise for creating optimal biomaterials for bone replacement (Zhang et al., 2018b; Wang et al., 2017).

Due to the importance and variety of applications of lattice structures in health, civil and aerospace industries, among others, recent research has focused on understanding the mechanical behavior of many unit cells, both experimentally and numerically. Such research is focused on static behavior (Crupi et al., 2017; Leary et al., 2016), energy absorption (Al-Saedi et al., 2018; Tancogne-Dejean et al., 2016), deformations (Carlton et al., 2017; Kadkhodapour et al., 2017), fatigue (Ahmadi et al., 2018; Zhao et al., 2016; Lietaert et al., 2018; Amin

* Corresponding author.
E-mail address: malana@tecnun.es (M. Alaña).

https://doi.org/10.1016/j.jmbbm.2019.05.043
Received 1 February 2019; Received in revised form 8 May 2019; Accepted 28 May 2019
Available online 22 June 2019
1751-6161/

Yavari et al., 2015), dynamic properties (Xiao et al., 2017) and the effect of imperfections (Amani et al., 2018; Takano et al., 2017; Liu et al., 2017; Campoli et al., 2013), among other features.

However, experiments are costly and time consuming. Therefore, analytical models are also required in order to make it easy to predict the mechanical behavior of lattice structures prior to their fabrication. For this reason, much of the research is focused not only on studying the lattice structures numerically and experimentally, but also on obtaining analytical models that can predict their mechanical properties. Thus, several analytical models have been developed for many unit cells: cubic (Gent and Thomas, 1963), body-centered cubic (BCC) and its variations (Smith et al., 2013; Ushijima et al., 2011a, 2011b; Tancogne-Dejean and Mohr, 2018a; Gümrük and Mines, 2013; Zhang et al., 2018c), diamond (Ahmadi et al., 2014), rhombic dodecahedron (Babaee et al., 2012; Zhang et al., 2018c), truncated cuboctahedron (Hedayati et al., 2016a), truncated cube (Hedayati et al., 2016b), octet-truss (Deshpande et al., 2001b), truncated octahedron (Roberts and Garboczi, 2002), octahedron (Hedayati et al., 2017). Additionally, Tancogne-Dejean et al. (Tancogne-Dejean and Mohr, 2018b) calculated the mechanical properties of elastically isotropic truss-lattices.

Some of the existing literature is limited to analyzing the Young's moduli of the unit cells, excluding shear moduli or Poisson's ratios, and for analytical studies the mechanical responses are simplified, thereby neglecting torsion or potential axial deformations in the struts. The present work analyzes the elastic behavior of a modified FCC unit cell by taking into consideration bending, axial and torsion deformations, which results in a very high correlation between the finite elements analysis and the analytical solutions. Moreover, the unit cell was homogenized by obtaining 9 parameters that correspond to the effective Young's and shear moduli, and the Poisson's ratios of an orthotropic material and their analytical expressions were obtained. Furthermore, an additional geometric parameter was introduced: the aspect ratio of the unit cell. This parameter defines the ratio between the height and width of the unit cell, thus allowing the type of load in the struts (axial or bending) to be adjusted for a given external load and enabling control over the degree of anisotropy in the unit cell. This analytical model was then validated with FE analyses.

2. Materials and methods

2.1. Geometry of the FCC lattice

The FCC unit cell is formed by 12 struts crossing at the center of each face of the unit cell. The analyzed FCC was modified and the struts corresponding to two parallel faces were eliminated. For the sake of clarity, the modified FCC unit cell is referred to as FCCm in the text. Both geometries are illustrated in Fig. 1.

In order to analytically calculate the elastic response of the unit cell, the best representative volume element (RVE) must be chosen so that the forces and moments of adjacent unit cells are considered in the analysis. For the convenience of a mechanical analysis, an appropriate RVE is taken from the lattice structure, as shown in Fig. 2. In addition, as previously stated, the aspect ratio R represents the fraction between the height and the width of the unit cell.

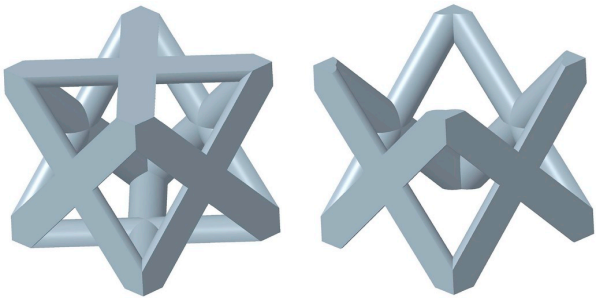

Fig. 1. FCC unit cell (left) and FCCm unit cell (right).

In contrast with the BCC unit cell, in the FCCm unit cell some nodes are connected to 8 struts, while others are connected to just 4. This results in a more compliant unit cell and a different arrangement of the pores, which allow bigger pore sizes than in BCC unit cells, as shown in Fig. 3.

The length of each strut, denoted by l', depends on the width of the unit cell (L) and its aspect ratio (R), as shown in Fig. 2 and defined in Eq. (1). The angle ϑ of the struts with respect to the global Cartesian coordinates can also be determined with parameter R (Eqs. (2) and (3)). The struts considered for the analysis were modelled as beams of a circular cross section of diameter D.

$$l' = \frac{L}{2}\sqrt{1+R^2} \tag{1}$$

$$\sin\vartheta = \frac{\frac{RL}{2}}{l'} = \frac{R}{\sqrt{1+R^2}} \tag{2}$$

$$\cos\vartheta = \frac{\frac{L}{2}}{l'} = \frac{1}{\sqrt{1+R^2}} \tag{3}$$

Equation (4) determines the relative density of the FCCm unit cell, which was calculated by integrating the volume of the struts and dividing it by the total volume of the unit cell. The relative density, as a function of D/L and R, is illustrated in Fig. 4.

$$\frac{\rho}{\rho_s} = \frac{\sqrt{1+R^2}}{R}\pi\left(\frac{D}{L}\right)^2 - \frac{2}{3}\left(\frac{D}{L}\right)^3\left[\frac{1+R^2}{R}(1+\sin\phi) + \frac{\sqrt{1+R^2}}{R}(1+\cos\phi)\right] \tag{4}$$

$$\text{where, } \phi = \arctan\frac{\sqrt{1+R^2}}{R} \tag{5}$$

2.2. Analytical model

The aim of this section is to determine the equations that relate the elastic response of the FCCm unit cell with the elastic modulus (E_s) and Poisson's ratio (ν_s) of the matrix material and the FCCm unit cell geometry. It is assumed that the FCCm is a repeating unit cell of a larger structure, and therefore it is useful to homogenize its mechanical behavior by describing it in terms of effective Young's moduli, shear moduli and Poisson's ratios. In this case, the FCCm is considered orthotropic, and thus, nine variables are needed to define its elastic response.

The Timoshenko beam model, which is shear flexible, was used to calculate the elastic response of the FCCm unit cell. The behavior of the beam was modelled with 12 degrees of freedom, corresponding to the three displacements and the three rotations of both beam ends in the three components of the local coordinate system. The material was considered isotropic and linear elastic, thus $G_s = E_s/[2(1+\nu_s)]$ holds for the matrix material. Moreover, as previously stated, the cross section of the struts was considered circular.

Fig. 5 shows a simple cantilever beam under several loads applied at the end of the beam. The deformations caused by these loads are also given under the assumption that there are small deformations, and the principle of superposition was applied to calculate the displacements and rotations under combined load states. I represents the second moment of inertia of the cross section, A is the area of the cross section, E_s corresponds to the Young's modulus of the matrix material, I_p is the polar moment of inertia of the section, G_s is the shear modulus of the matrix material, and k is the correction factor for shear deformation ($k = 6(1+\nu_s)/(7+6\nu_s)$ for circular cross section (Cowper, 1966)). Note that in the case of the force F, the shear deformation is also included in the expression of the δ_F displacement.

The equivalent Young's and shear moduli are determined as the

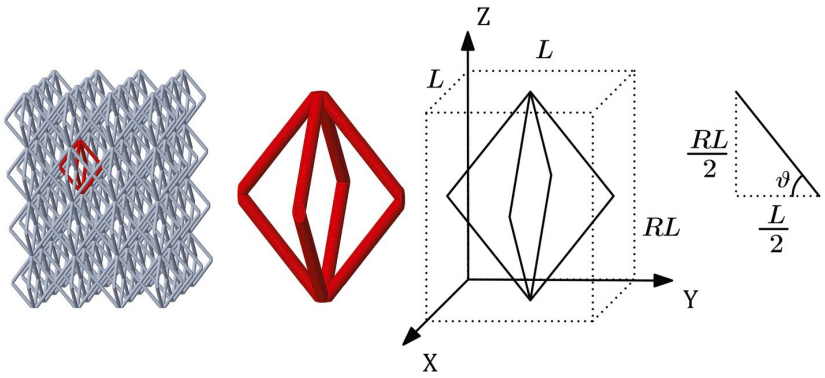

Fig. 2. FCCm unit cell with $R = 1.25$.

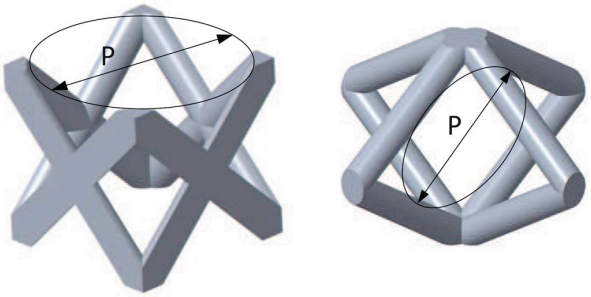

Fig. 3. Location of biggest pore for the FCCm unit cell with $R = 1$ (left) and for BCC unit cell (right).

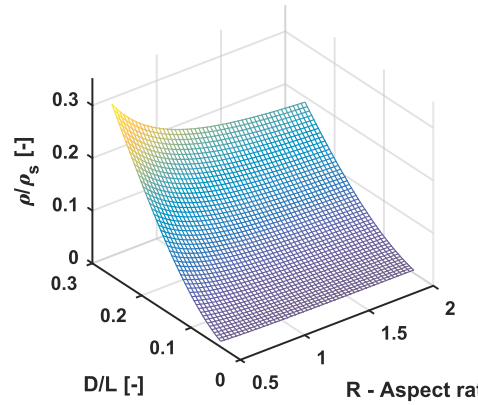

Fig. 4. Relative density of the FCCm unit cell as function of D/L and R.

relation between the force applied to the upper vertices and the cross section area of the chosen RVE. This means that the total area considered in the RVE is much larger than the actual cross section of the beams, and therefore the equivalent stress is not the real one of the beams. Nonetheless, these equivalent material parameters make it easier to compare between different lattices and the implementation of lattice structures in other fields. In addition, the equivalent Poisson's ratios correspond to the ratio between the displacements of the vertices located at the outer surfaces of the RVE.

The displacements in Fig. 6 can be related to the macroscopic strains by assuming periodic boundary conditions, thus obtaining the following relationships:

$$\varepsilon_x = \frac{2u_x}{L},\ \varepsilon_y = \frac{2v_y}{L},\ \varepsilon_z = \frac{2w_z}{RL} \tag{6}$$

$$\gamma_{xy} = \frac{v_x}{L/2} + \frac{u_y}{L/2},\ \gamma_{xz} = \frac{w_x}{RL/2} + \frac{u_z}{L/2},\ \gamma_{yz} = \frac{w_y}{RL/2} + \frac{v_z}{L/2} \tag{7}$$

The axial and bending stiffness (K_a and K_f respectively) are defined so that the total energy of a strut can be defined as $U_{strut} = \frac{1}{2}K_a\delta_a^2 + \frac{1}{2}K_f\delta_f^2$:

$$K_f = \frac{F}{\delta_f} = \frac{1}{\frac{l^3}{3E_sI} + \frac{l'}{kAG_s} - \frac{M}{F}\frac{l^3}{2EI_s}} \tag{8}$$

$$K_a = \frac{N}{\delta_a} = \frac{E_sA}{l'} \tag{9}$$

Depending on the load case, factor M varies because of the different boundary conditions that the unit cell is subjected to.

2.2.1. Strain energy under normal stress

Each strut of the FCCm unit cell can be modelled as a clamped strut in order to describe its loads and deformations. Fig. 7 models such a

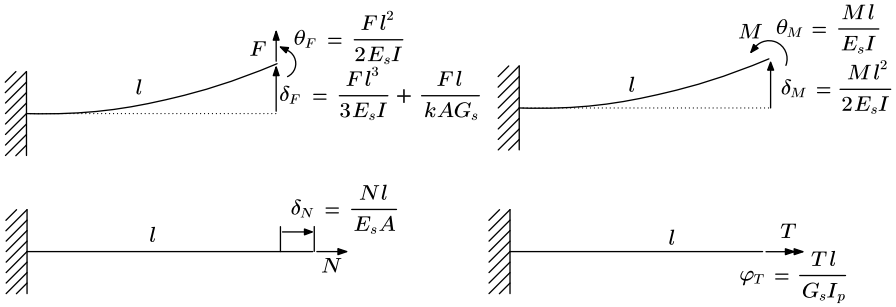

Fig. 5. Deformation under several simple loading conditions.

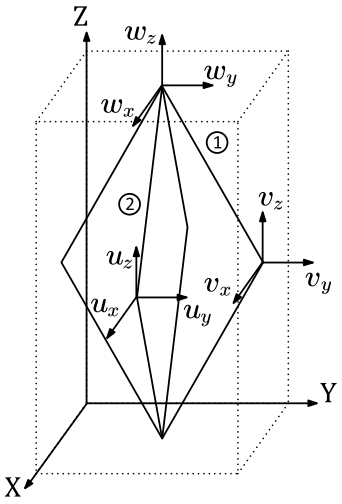

Fig. 6. Global displacements of the nodes.

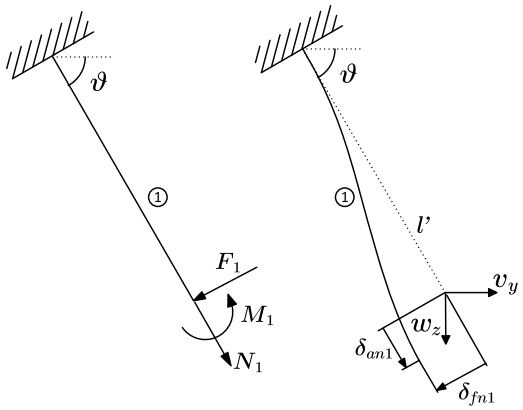

Fig. 7. Loads and deformation of strut 1 under normal macroscopic stress.

beam, and it also shows the relation between the bending and axial deflections and the global deformations w_z and v_y. Under normal stresses there is no rotation at the joints of the beams, which means that $M = Fl'/2$. By introducing this moment in Eq. (8), the bending stiffness can be obtained for a normal stress:

$$K_{fn} = \frac{1}{\frac{l^3}{12E_sI} + \frac{l'}{kAG_s}} \tag{10}$$

In order to relate the local deformations of the beam (δ_{an1} and δ_{fn1}) with the macroscopic stress and strains, first the local deformations must be expressed as a function of the global displacements:

$$\delta_{an1} = \frac{Rw_z + v_y}{\sqrt{1+R^2}},\ \delta_{fn1} = \frac{w_z - Rv_y}{\sqrt{1+R^2}} \tag{11}$$

Analogously, the same can be done for strut 2:

$$\delta_{an2} = \frac{Rw_z + u_x}{\sqrt{1+R^2}},\ \delta_{fn2} = \frac{w_z - Ru_x}{\sqrt{1+R^2}} \tag{12}$$

By considering the number of struts in the unit cell and its volume, the strain energy density can be obtained as:

$$U_{0-n} = \frac{2}{RL^3}[K_{fn}(\delta_{fn1}^2 + \delta_{fn2}^2) + K_a(\delta_{an1}^2 + \delta_{an2}^2)] \tag{13}$$

Note that this expression depends on the macroscopic normal strains

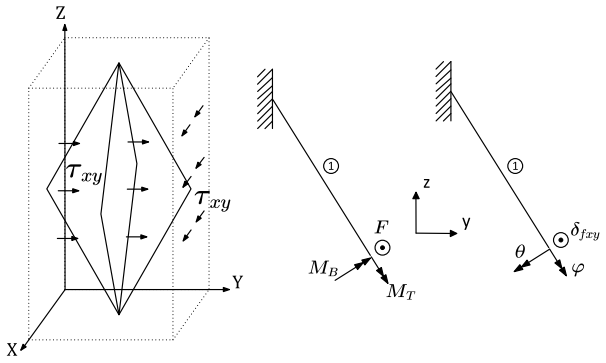

Fig. 8. Model of a cantilever beam under XY shear stress.

defined in Eq. (6).

2.2.2. Strain energy under shear stress in XY

In this case the beams can be modelled as being clamped at one end, while allowing some degree of rotation at the other end. This rotation is limited by the bending of adjacent beams, which in turn also causes torsion in the modelled beam. Fig. 8 shows the loads and displacements of the beam.

From these diagrams the bending moment at the beam end (M_B) can be defined as a function of F. Note that the rotation of the beam on the Y axis must be restricted for pure shear in XY.

$$RM_T = M_B,\ \theta R = \varphi \tag{14}$$

$$M_B = Fl'\frac{R^2G_s}{2R^2G_s + E_s} \tag{15}$$

Therefore, the bending stiffness can be defined as follows:

$$K_{fxy} = \frac{1}{\frac{l^3}{3E_sI} + \frac{l'}{kAG_s} - \frac{l^3}{2E_sI}\frac{R^2G_s}{2R^2G_s + E_s}} \tag{16}$$

Also, the deflection of the beam end is related to the macroscopic strains in Eq. (7), since $\delta_{fxy} = v_x = u_y$. Therefore, the strain energy density associated with the shear stress in XY is the following:

$$U_{0-xy} = \frac{4}{RL^3}K_{fxy}\delta_{fxy}^2 \tag{17}$$

2.2.3. Strain energy under shear stress in YZ and XZ

The stress in YZ causes two different stress states and deformations in struts 1 and 2. The problem is solved for stress in YZ, and XZ can be obtained analogously.

The loads and deflections of strut 1 are shown in Fig. 9. The deformations of the figure can be related to the macroscopic strain deformations as follows:

$$\delta_{fyz1} = \frac{v_z - Rw_y}{\sqrt{1+R^2}} + \alpha l',\ \delta_{ayz} = \frac{Rv_z + w_y}{\sqrt{1+R^2}} \tag{18}$$

The loads of each strut are depicted in Fig. 10 and by means of force and moment equilibria the following equations can be obtained:

$$\sum F_{z(a)} = T_1 - 2N_1\sin\vartheta - 2F_1\cos\vartheta = 0 \tag{19}$$

$$\sum F_{y(b)} = T_2 + 2F_1\sin\vartheta - 2N_1\cos\vartheta - 2F_2 = 0 \tag{20}$$

$$\sum M_{x_1=x_2=0} = M_{x_1} = M_{x_2} = M_2 \tag{21}$$

$$M_2 = \frac{RL}{2}F_2 \tag{22}$$

From Eq. (19)–(22) and considering that $RT_2 = T_1$ must hold for

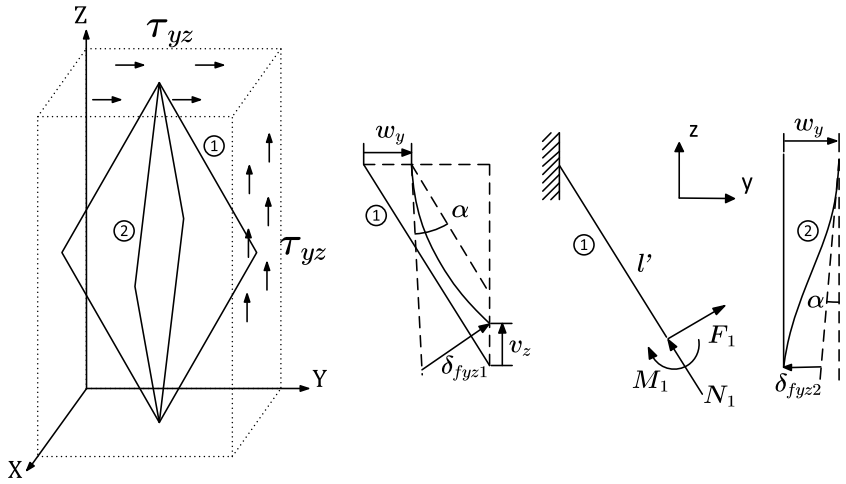

Fig. 9. Shear loading in YZ plane, deformation of strut 1 and cantilever beam model of strut 1.

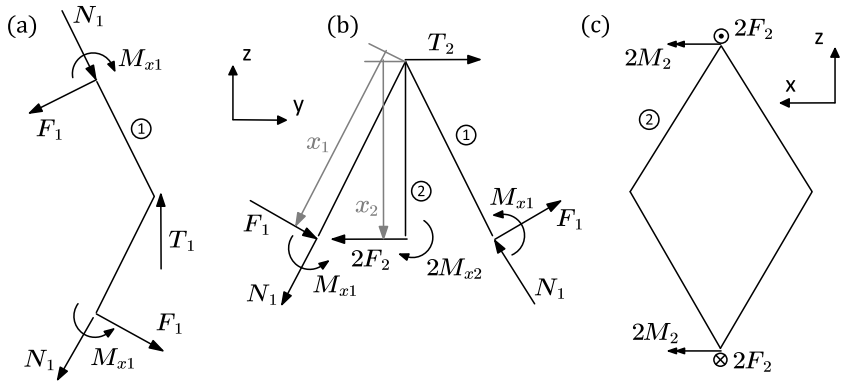

Fig. 10. Free body diagrams of struts under YZ shear stress.

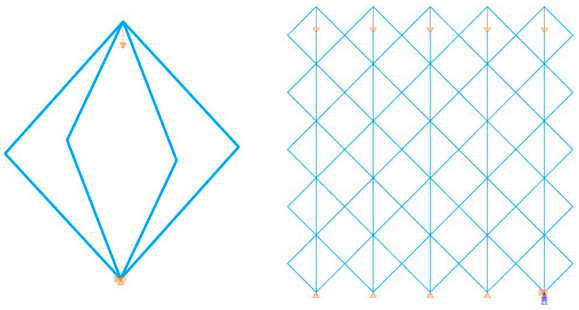

Fig. 11. Singe unit cell (left) and lattice structure (N = 5) for finite element analysis (right).

equilibrium, it is concluded that $M_1 = 0$. Therefore, the bending stiffness of the strut 1 under shear stress in YZ is:

$$K_{fyz1} = \frac{1}{\frac{l^3}{3E_s I} + \frac{l'}{kAG_s}} \tag{23}$$

Furthermore, if a uniform shear strain is considered, that is $w_y = Rv_z$, the energy of strut 1 is defined as:

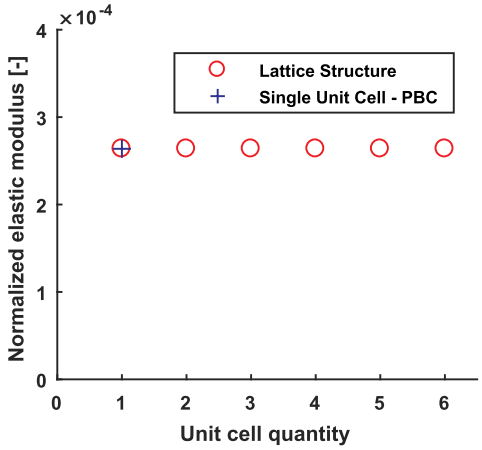

Fig. 12. Normalized E_z of FCCm lattice structures and FCCm unit cell with PBC.

$$U_1 = \frac{1}{2}K_a\frac{4R^2}{1+R^2}v_z^2 + \frac{1}{2}K_{fyz1}\left(\frac{1-R^2}{\sqrt{1+R^2}}v_z + \alpha l'\right)^2 \tag{24}$$

For strut 2, the loads are analogous to the ones for the stress in XY, as illustrated in Fig. 8. The difference in this case is that instead of there being no rotation in the Y axis, there is no rotation in the Z axis. Thus,

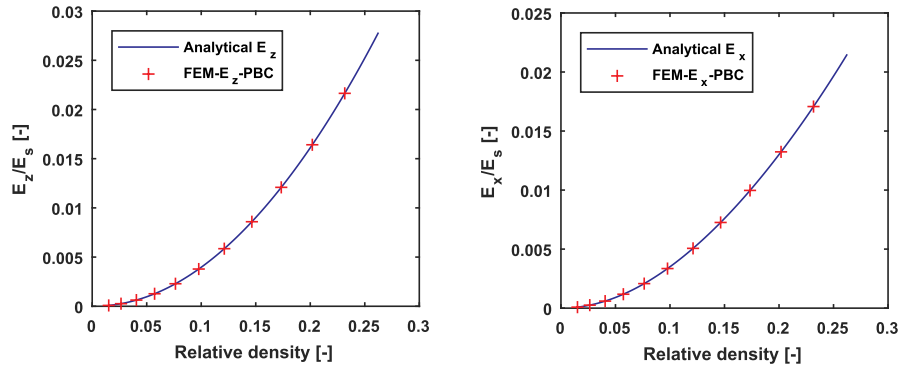

(a) (b)

Fig. 13. Comparison between analytical model and FEM of FCCm unit cell with R = 1 for Young's moduli in Z (a) and X or Y (b).

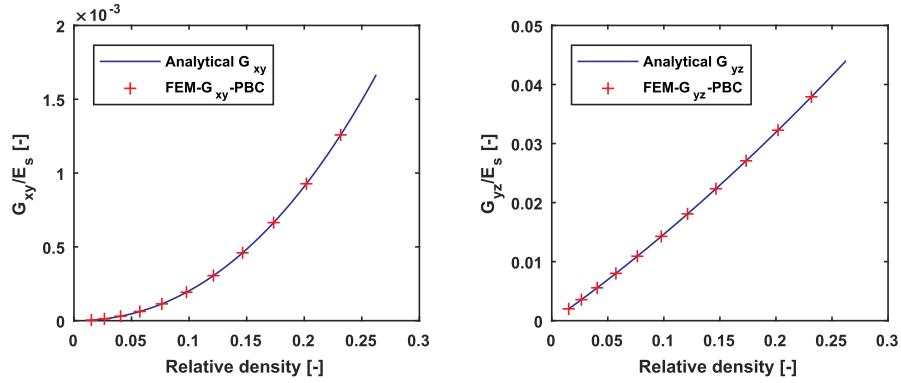

(a) (b)

Fig. 14. Comparison between analytical model and FEM of FCCm unit cell with R = 1 for shear moduli in XY (a) and YZ or XZ (b).

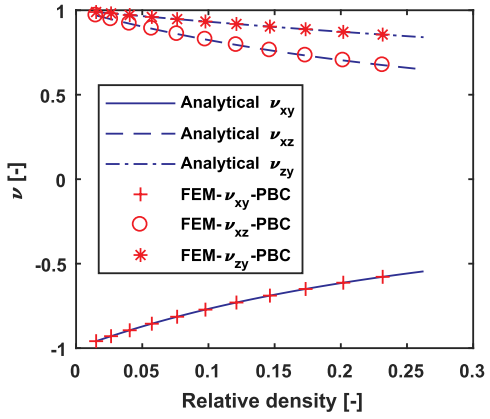

Fig. 15. Comparison between analytical model and FEM of FCCm unit cell with R = 1 for Poisson's ratios.

the bending moment M_B can be calculated as a function of F_2:

$$\theta = R\varphi, \quad RM_B = M_T \tag{25}$$

$$M_B = F_2 l' \frac{G_s}{E_s R^2 + 2G_s} \tag{26}$$

The bending stiffness and energy of strut 2 can then be defined as:

$$K_{fyz2} = \frac{1}{\frac{l^3}{3E_s I} + \frac{l'}{kAG_s} - \frac{l^3}{2E_s I}\frac{G_s}{E_s R^2 + 2G_s}} \tag{27}$$

$$U_2 = \frac{1}{2} K_{fyz2} \delta_{fyz2}^2 \tag{28}$$

In addition, deflections δ_{fyz1} and , as well as rotation α, need to be related to global displacements w_y and v_z. Fig. 9 illustrates the relationship between displacement w_y of strut 2 and its deformations, and taking into account Equations (19), (20) and (29) and that $w_y = Rv_z$:

$$w_y = \alpha \frac{RL}{2} + \delta_{fyz2} \tag{29}$$

$$\alpha = \frac{\frac{2}{L} - \frac{2(1-R^2)}{R^2 L}\frac{K_{fyz1}}{K_{fyz2}}}{1 + \frac{2l'}{R^2 L}\frac{1+R^2}{\sqrt{1+R^2}}\frac{K_{fyz1}}{K_{fyz2}}} v_z \tag{30}$$

Now the energy of struts 1 and 2 can be calculated exclusively as a function of w_y and v_z, and therefore related to the macroscopic strain γ_{yz}. The total strain energy density in this case will be:

$$U_{0-yz} = \frac{2}{RL^3}(K_a \delta_{ayz}^2 + K_{fyz1}\delta_{fyz1}^2 + K_{fyz2}\delta_{fyz2}^2) \tag{31}$$

2.2.4. Elastic moduli and Poisson's ratios

The total strain energy density is the sum of all the calculated values, which can be expressed as a function of the macroscopic strains as:

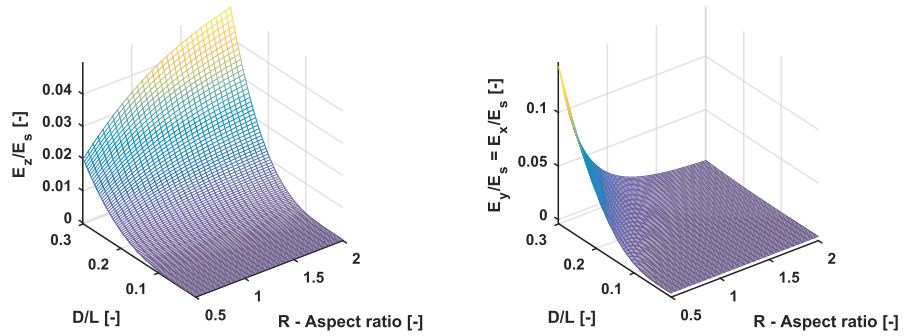

Fig. 16. Normalized effective Young's moduli of FCCm unit cell as a function of D/L and R. E_z in (a) and $E_x = E_y$ in (b).

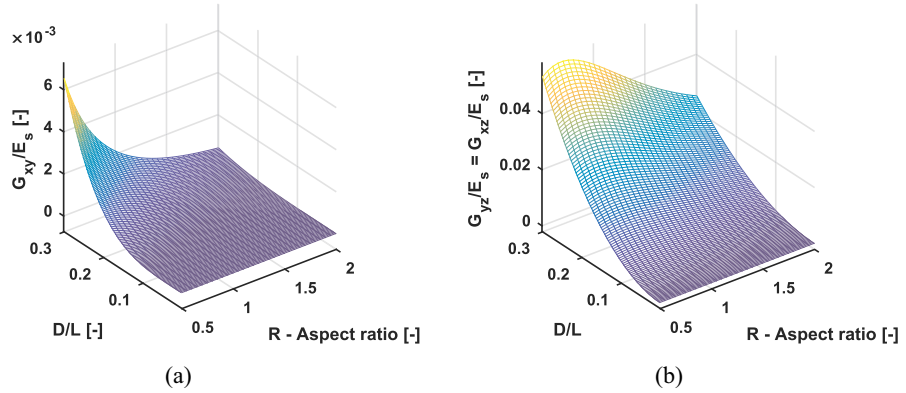

Fig. 17. Normalized effective shear moduli of FCCm unit cell as a function of D/L and R. G_{xy} in (a) and $G_{yz} = G_{xz}$ in (b).

$$U_0 = \frac{1}{2RL(1+R^2)}\{K_a[(\varepsilon_x + R^2\varepsilon_z)^2 + (\varepsilon_y + R^2\varepsilon_z)^2] + K_{fn}R^2[(\varepsilon_x - \varepsilon_z)^2 + (\varepsilon_y - \varepsilon_z)^2]\} + \frac{1}{4LR}K_{fxy}\gamma_{xy}^2 + \frac{R\left[K_aK_{fyz1}(1+R^2) + K_{fyz2}\left(K_{fyz1} + R^2K_a\right)\right]}{2L(1+R^2)\left[K_{fyz1}(1+R^2) + K_{fyz2}R^2\right]}\left(\gamma_{xz}^2 + \gamma_{yz}^2\right) \tag{32}$$

The effective stiffness tensor can be defined by differentiating the strain energy density with respect to the macroscopic strains.

$$C = \begin{bmatrix} \frac{\partial^2 U_0}{\partial \varepsilon_x^2} & \frac{\partial^2 U_0}{\partial \varepsilon_x \partial \varepsilon_y} & \frac{\partial^2 U_0}{\partial \varepsilon_x \partial \varepsilon_z} & 0 & 0 & 0 \\ & \frac{\partial^2 U_0}{\partial \varepsilon_y^2} & \frac{\partial^2 U_0}{\partial \varepsilon_y \partial \varepsilon_z} & 0 & 0 & 0 \\ & & \frac{\partial^2 U_0}{\partial \varepsilon_z^2} & 0 & 0 & 0 \\ & & & \frac{\partial^2 U_0}{\partial \gamma_{yz}^2} & 0 & 0 \\ & sym & & & \frac{\partial^2 U_0}{\partial \gamma_{xz}^2} & 0 \\ & & & & & \frac{\partial^2 U_0}{\partial \gamma_{xy}^2} \end{bmatrix} \tag{33}$$

The elastic moduli and Poisson's ratios can then be calculated from the stiffness matrix elements.

$$E_x = E_y = \frac{2(1+R^2)K_aK_{fn}(R^2K_{fn} + K_a)}{LR[(K_aR + K_{fn}R)^2 + 2K_aK_{fn}(1+R^4)]} \tag{34}$$

$$E_z = \frac{2K_aK_{fn}R(1+R^2)}{L(K_{fn}R^2 + K_a)} \tag{35}$$

$$G_{xy} = \frac{K_{fxy}}{2LR} \tag{36}$$

$$G_{xz} = G_{yz} = \frac{R[K_aK_{fyz1}(1+R^2) + K_{fyz2}(K_{fyz1} + R^2K_a)]}{L(1+R^2)[K_{fyz1}(1+R^2) + K_{fyz2}R^2]} \tag{37}$$

$$\nu_{xy} = \nu_{yx} = \frac{-R^2(K_a - K_{fn})^2}{R^2(K_a + K_{fn})^2 + 2K_aK_{fn}(1+R^4)} \tag{38}$$

$$\nu_{xz} = \nu_{yz} = \frac{(K_{fn}R^2 + K_a)(K_a - K_{fn})}{R^2(K_a + K_{fn})^2 + 2K_aK_{fn}(1+R^4)} \tag{39}$$

$$\nu_{zx} = \nu_{zy} = \frac{R^2(K_a - K_{fn})}{K_{fn}R^2 + K_a} \tag{40}$$

2.3. Finite element analysis

A finite element analysis was performed to check the accuracy of the obtained model. Simulations were run in commercial software (Abaqus, 2018; Dassault Systems), each strut was discretized with 10 shear flexible quadratic beam elements (B32 elements), and the same RVE as the one used for the analytical model was chosen here in order to obtain a better comparison. The material properties were those from the Ti6Al4V-ELI alloy, with E_s = 122.3 GPa and ν_s = 0.342, as in (Hedayati et al., 2016b).

The effect of the quantity of simulated unit cells was studied in order to determine the influence of the free surface in the overall behavior of a FCCm lattice structure. In order to do that, lattice structures of NxNxN unit cells were built, where N represents the number of unit cells in each orthogonal direction, and their elastic behaviors were analyzed. In all the simulations, engineering strains of 0.1 were applied for the load cases studied in Section 2.2. Then, the sums of reaction

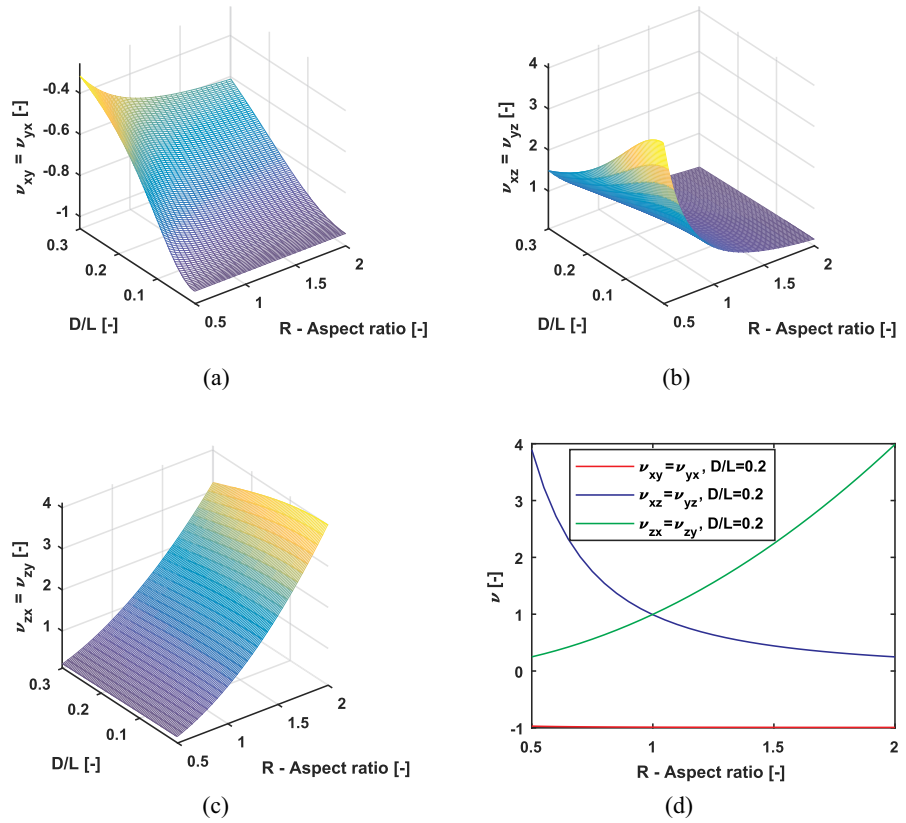

Fig. 18. Poisson's ratios of the FCCm unit cell as a function of D/L and R. $\nu_{xy} = \nu_{yx}$ (a), $\nu_{xz} = \nu_{yz}$ (b), $\nu_{zx} = \nu_{zy}$ (c) and variability of Poisson's ratios with R (d).

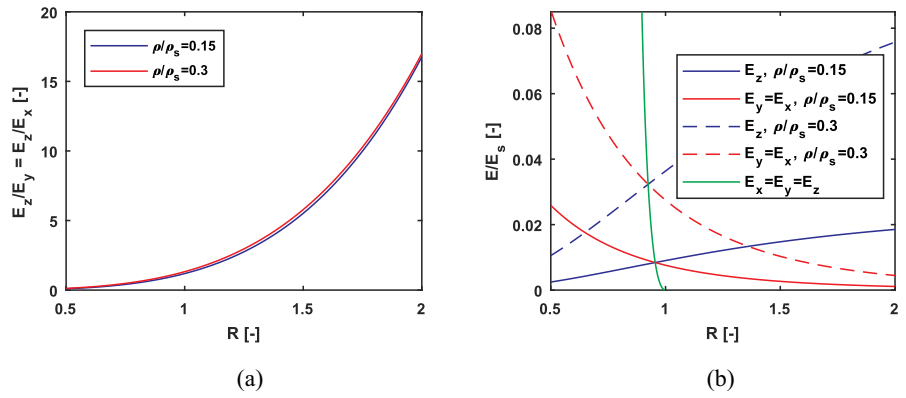

Fig. 19. $E_z/E_y = E_z/E_x$ ratio with variable R (a) and Young's moduli with variable R (b) for two different ρ/ρ_s ratios.

forces were divided by the total cross section area of the structure to obtain the effective Young's and shear moduli. From these analyses the Poisson's ratios were also measured. Moreover, a single unit cell was studied by applying Periodic Boundary Conditions (PBC). To that end, the Python script presented by Omairey (Omairey et al., 1007) was adjusted for the FCCm unit cell.

Finally, the accuracy of the obtained analytical models was studied by comparing the analytical expressions and the results obtained from the FE analysis (see Fig. 11).

3. Results

3.1. Influence of the number of unit cells

Fig. 12 represents the normalized elastic modulus for different numbers of unit cells. The results show that E_z is independent of how many unit cells are simulated (difference below 0.1%). The unit cell with PBC is also represented in the diagram, and, as can be seen, no difference is observed. The same results were obtained for $E_y = E_x$, G_{xy}, $G_{yz} = G_{xz}$, $\nu_{xy} = \nu_{yx}$, $\nu_{xz} = \nu_{yz}$ and $\nu_{zx} = \nu_{zy}$. Therefore, it can be concluded that the selected RVE represents the elastic behavior of an FCCm structure regardless of the number of unit cells. Furthermore, it has

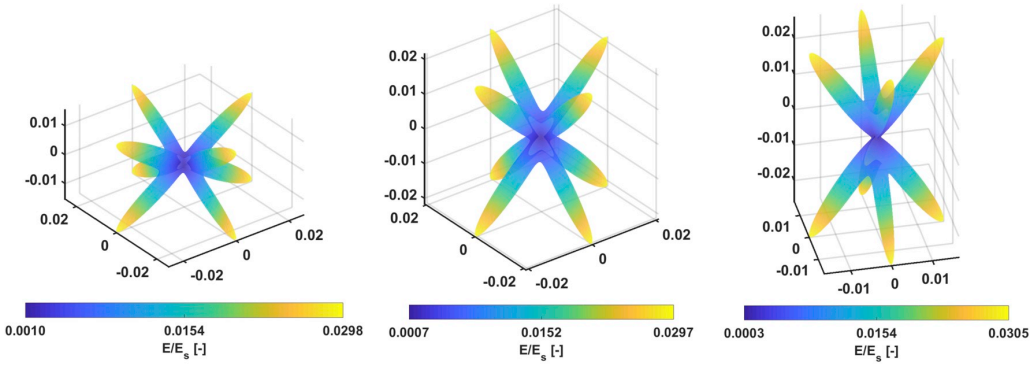

Fig. 20. Young's modulus surface for FCCm lattices with $\rho/\rho_s = 0.1$ and $R = 0.6$ (a), $R = 1$ (b) and $R = 1.5$ (c).

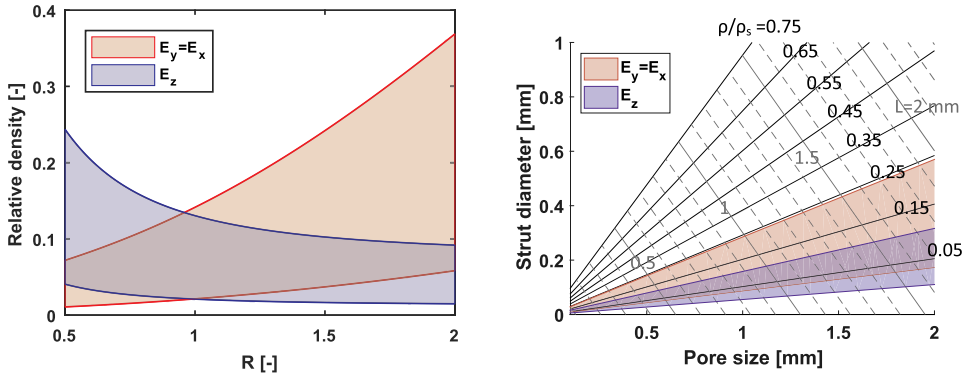

Fig. 21. Aspect ratio and relative density of FCCm for Young's modulus between 20 MPa and 830 MPa (a), and design space as in (Arabnejad et al., 2016) of FCCm unit cell for $R = 1.5$ with the relative densities that equal the cancellous bone stiffness (b).

been found that for the selected RVE there is no significant difference between applying and not applying the PBC. As a result, the accuracy of the analytical model was tested by comparing it with the FE analysis of a single unit cell with PBC.

3.2. Comparing the analytical model and numerical results

As Figs. 13–15 show, the numerical analysis shows very good agreement with the developed analytical curves for any of the calculated moduli or Poisson's ratios. The models with different aspect ratios (R = 0.5, R = 2) were also compared, yielding similar results.

4. Discussion

The main contribution of this work is a set of analytical solutions for a modified FCC unit cell with variable geometry in order to easily predict its mechanical behavior. The analytical solutions determine the elastic moduli, shear moduli and Poisson's ratios in the 3 directions of the FCCm unit cell, and the obtained expressions show very good correlation with numerical studies. Although the analytical model was not experimentally validated, other works (Gümrük and Mines, 2013; Ahmadi et al., 2014; Hedayati et al., 2016a, 2016b) have already shown the high correlation between the Timoshenko beam model and experimentally obtained values for different unit cells.

4.1. Variability of elastic behavior

Having ensured the correlation between the analytical and the FE models, the obtained expressions can be further analyzed. The two geometric factors affecting the elastic properties of the FCCm unit cell are D/L and aspect ratio R. Both factors have a significant influence on the Young's moduli in the Z and the X or Y directions, as can be observed in Fig. 16. As expected, while increasing the D/L term, the Young's modulus increases in all cases, and the variation of R affects whether the struts withstand an axial or bending load depending on the direction in which the effective stress is applied. Therefore, the increase of R has variable effects depending on the loading direction.

Regarding the shear moduli for the XY plane, a small R benefits the shear stiffness. In contrast, for the XZ and YZ planes, the shear modulus is at its maximum when R is close to but below 1, since the struts are axially loaded in this configuration. This also results in a much higher shear moduli in the XZ and YZ planes than in the XY plane for the same D/L and R, as shown in Fig. 17.

The effective Poisson's ratios also present high variability when D/L and R are modified. In general, the increase of D/L always brings the Poisson's ratios closer to zero. On the other hand, the variability is different with respect to R for every Poisson's ratio, as shown in Fig. 18. Both ν_{xy} and ν_{xz} decrease with the increase of R, while ν_{zx} increases. Nonetheless, since ν_{xy} is negative its decrease supposes that the magnitude of the displacement in the perpendicular cross section is actually increasing. Thus, it makes more sense to note that for any given D/L, if R increases it is only ν_{xz} that tends to zero, while ν_{xy} and ν_{zx} increase

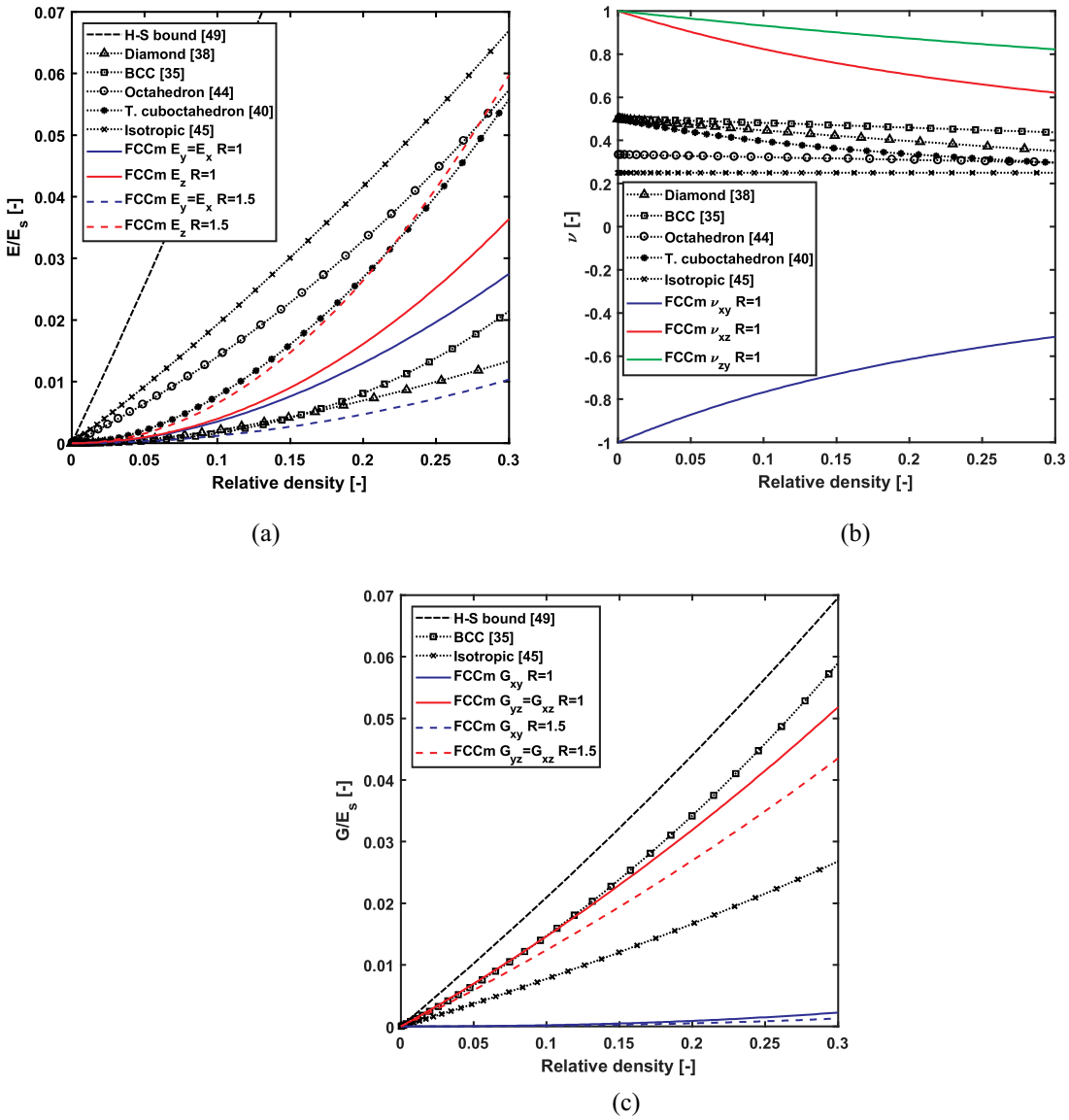

Fig. 22. Comparison of analytical Young's modulus (a), Poisson's ratio (b) and shear modulus (c) of FCCm unit cell and other unit cells, as well as Hashin-Shtrikman bounds.

their absolute values, the variability of ν_{xy} being much smaller than the variability of ν_{zx}.

Fig. 19a shows how E_z/E_y varies with respect to R for two different values of ρ/ρ_s. Thus, the change of relative density has a minimal effect on the E_z/E_y ratio, while R has a major influence. Moreover Fig. 19b shows that it is possible to design a FCCm unit cell fulfilling $E_x = E_y = E_z$ for a range of different ρ/ρ_s values.

Using the obtained parameters, the elastic behavior of the FCCm unit cell can be represented in space and the 3D effective Young's moduli can be analytically calculated. Fig. 20 shows how the variability of R affects the overall shape of the effective Young's modulus. For any R, the anisotropy of the FCCm unit cell is very high, as the struts change from bending to axial loads with the direction of the macroscopic load, as is also the case in other unit cells such as BCC and Simple Cubic.

4.2. FCCm as bone replacement

In order to avoid the stress shielding effect, it is crucial that the elastic properties of the materials used in load bearing bone replacements are close to the ones of the bone being replaced. The mechanical properties of bones show great variability depending on the type and location of the bone, and other factors, such as age or gender, also have an influence. The elastic modulus of the cancellous bone varies between 20 MPa and 830 MPa, while for the cortical bone the elastic modulus is between 13.6 GPa and 35.3 GPa (Zhang et al., 2018b).

The FCCm unit cell can adjust its elastic properties by changing the diameter to cell size ratio or the aspect ratio. Therefore, for a given range of Young's moduli, there is a range of relative densities of the unit cell for every aspect ratio matching these elastic properties. Fig. 21a shows the possible relative density values for every aspect ratio that matches the stiffness range of the human cancellous bone.

Once the aspect ratio is fixed, the geometry of the unit cell is defined, and the relative density and cell size can then be related to the pore size and strut diameter, while considering the upper and lower bounds of the prescribed limits for the Young's modulus, as in Fig. 21b.

4.3. Comparison with other unit cells

The obtained results were compared with the analytical expressions of other unit cells. Although Euler-Bernoulli beams are widely used to model the elastic behavior of similar bending dominated unit cells, in order to ensure the validity of the comparison, only those modelled as Timoshenko beams were taken into account. This limits the number of unit cells to compare, especially in the case of shear moduli. In addition to the bending dominated unit cells, an isotropic unit cell was also considered from (Tancogne-Dejean and Mohr, 2018b), which models the beams of a stretch dominated unit cell as trusses. Fig. 22 shows the elastic parameters of different unit cells, as well as the Hashin-Shtrikman bounds (Hashin and Shtrikman, 1963), as a function of the relative density, including the FCCm unit cell with two different aspect ratios ($R = 1$ and $R = 1.5$).

Fig. 22a shows that the Young's moduli of FCCm are in the range of other bending dominated unit cells for $R = 1$. Nevertheless, as R changes, the axial load of each strut also varies depending on the load case, which increases the difference between $E_x = E_y$ and E_z. This variability, although noticeable, is slightly lower for the shear moduli. The biggest difference with respect to other unit cells can be seen in the Poisson's ratio (Fig. 22b), where there are much higher values compared to the rest of the studied unit cells, and even a negative ν_{xy}. This particularity of the behavior of the Poisson's ratios occurs because some nodes are connected to 4 struts, while others are connected to 8 struts, which results in different elastic responses lacking cubic symmetry.

5. Conclusions

The mechanical properties of lattice structures made of a modified FCC unit cell were studied and the analytical expressions can predict the elastic moduli, shear moduli and Poisson's ratios in the 3 directions as a function of the bulk material properties and 2 geometric parameters: the D/L ratio and aspect ratio R of the unit cell. This can be of paramount importance in designing biomaterials with the prescribed mechanical properties and for some applications such as topology optimization, where the analytical calculation of the compliance matrix for different relative densities decreases the computational cost.

Parameter R makes it possible to regulate not only the elastic modulus, but also the degree of anisotropy of the lattice structure, and thus it is possible to design a FCCm unit cell such that $E_x = E_y = E_z$.

The modelling of the shear and torsion deformation, apart from axial and bending displacements, increases the accuracy of the analytical expressions, which show a very high correlation with the FEM calculations of beam elements.

Acknowledgements

This research did not receive any specific grant from funding agencies in the public, commercial or not-for-profit sectors.

References

Ahmadi, S.M., Campoli, G., Amin Yavari, S., Sajadi, B., Wauthle, R., Schrooten, J., Weinans, H., Zadpoor, A.A., 2014. Mechanical behavior of regular open-cell porous biomaterials made of diamond lattice unit cells. J. Mech. Behav. Biomed. Mater. 34 (106–115). https://doi.org/10.1016/j.jmbbm.2014.02.003. ISSN 17516161.

Ahmadi, S.M., Hedayati, R., Li, Y., Lietaert, K., Tümer, N., Fatemi, A., Rans, C.D., Pouran, B., Weinans, H., Zadpoor, A.A., 2018. Fatigue performance of additively manufactured meta-biomaterials: the effects of topology and material type. Acta Biomater. 65, 292–304. https://doi.org/10.1016/j.actbio.2017.11.014.

Al-Saedi, D.S., Masood, S., Faizan-Ur-Rab, M., Alomarah, A., Ponnusamy, P., 2018. Mechanical properties and energy absorption capability of functionally graded F2BCC lattice fabricated by SLM. Mater. Des. 144, 32–44. https://doi.org/10.1016/j.matdes.2018.01.059. ISSN 02641275.

Ali, D., Sen, S., 2017. Finite element analysis of mechanical behavior, permeability and fluid induced wall shear stress of high porosity scaffolds with gyroid and lattice-based architectures. J. Mech. Behav. Biomed. Mater. 75 (July), 262–270. https://doi.org/10.1016/j.jmbbm.2017.07.035. ISSN 18780180.

Amani, Y., Dancette, S., Delroisse, P., Simar, A., Maire, E., 2018. Compression behavior of lattice structures produced by selective laser melting: X-ray tomography based experimental and finite element approaches. Acta Mater. 159 (395–407). https://doi.org/10.1016/j.actamat.2018.08.030. ISSN 13596454.

Amin Yavari, S., Ahmadi, S.M., Wauthle, R., Pouran, B., Schrooten, J., Weinans, H., Zadpoor, A.A., 2015. Relationship between unit cell type and porosity and the fatigue behavior of selective laser melted meta-biomaterials. J. Mech. Behav. Biomed. Mater. 43, 91–100. https://doi.org/10.1016/j.jmbbm.2014.12.015.

Arabnejad, S., Burnett Johnston, R., Pura, J.A., Singh, B., Tanzer, M., Pasini, D., 2016. High-strength porous biomaterials for bone replacement: a strategy to assess the interplay between cell morphology, mechanical properties, bone ingrowth and manufacturing constraints. Acta Biomater. 30, 345–356. https://doi.org/10.1016/j.actbio.2015.10.048. ISSN 18787568.

Ashby, M.F., 2006. The properties of foams and lattices (1838). Phil. Trans. Math. Phys. Eng. Sci. 364, 15–30. https://doi.org/10.1098/rsta.2005.1678. ISSN 1364503X.

Babaee, S., Jahromi, H., Ajdari, A., Nayeb-Hashemi, H., Vaziri, A., 2012. Mechanical properties of open-cell rhombic dodecahedron cellular structures. Acta Mater. 60, 2873–2885. https://doi.org/10.1016/j.actamat.2012.01.052.

J. Brennan-Craddock, D. Brackett, R. Wildman, R. Hague, The design of impact absorbing structures for additive manufacture Related content, J. Phys. Conf. Ser. 382, doi:10.1088/1742-6596/382/1/012042.

Campoli, G., Borleffs, M.S., Amin Yavari, S., Wauthle, R., Weinans, H., Zadpoor, A.A., 2013. Mechanical properties of open-cell metallic biomaterials manufactured using additive manufacturing. Mater. Des. 49, 957–965. https://doi.org/10.1016/j.matdes.2013.01.071. ISSN 18734197.

Carlton, H.D., Lind, J., Messner, M.C., Volkoff-Shoemaker, N.A., Barnard, H.S., Barton, N.R., Kumar, M., 2017. Mapping local deformation behavior in single cell metal lattice structures. Acta Mater. 129, 239–250. https://doi.org/10.1016/j.actamat.2017.02.023. ISSN 13596454.

Cowper, G.R., 1966. The shear coefficient in timoshenko's beam theory. J. Appl. Mech. 33 (2), 335. https://doi.org/10.1115/1.3625046.

Crupi, V., Kara, E., Epasto, G., Guglielmino, E., Aykul, H., 2017. Static behavior of lattice structures produced via direct metal laser sintering technology. Mater. Des. 135, 246–256. https://doi.org/10.1016/j.matdes.2017.09.003. ISSN 18734197.

Deshpande, V.S., Ashby, M.F., Fleck, N.A., 2001a. Foam topology: bending versus stretching dominated architectures. Acta Mater. 49 (6), 1035–1040.

Deshpande, V.S., Fleck, N.A., Ashby, M.F., 2001b. Effective properties of the octet-truss lattice material. Tech. Rep.

Gent, A., Thomas, A., 1963. Mechanics of foamed elastic materials. Rubber Chem. Technol. 36 (3), 597–610.

Gümrük, R., Mines, R.A.W., 2013. Compressive behaviour of stainless steel micro-lattice structures. Int. J. Mech. Sci. 68, 125–139. https://doi.org/10.1016/j.ijmecsci.2013.01.006.

Hashin, Z., Shtrikman, S., 1963. A variational approach to the theory of the elastic behaviour of multiphase materials. J. Mech. Phys. Solids 11 (2), 127–140.

Hedayati, R., Sadighi, M., Mohammadi-Aghdam, M., Zadpoor, A.A., 2016a. Mechanical behavior of additively manufactured porous biomaterials made from truncated cuboctahedron unit cells. Int. J. Mech. Sci. 106 (38), 19. https://doi.org/10.1016/j.ijmecsci.2015.11.033. ISSN 00207403.

Hedayati, R., Sadighi, M., Mohammadi-Aghdam, M., Zadpoor, A.A., 2016b. Mechanical properties of regular porous biomaterials made from truncated cube repeating unit cells: analytical solutions and computational models. Mater. Sci. Eng. C 60, 163–183. https://doi.org/10.1016/j.msec.2015.11.001.

Hedayati, R., Sadighi, M., Mohammadi-Aghdam, M., Zadpoor, A.A., 2017. Analytical relationships for the mechanical properties of additively manufactured porous biomaterials based on octahedral unit cells. Appl. Math. Model. 46, 408–422. https://doi.org/10.1016/j.apm.2017.01.076.

Kadkhodapour, J., Montazerian, H., Darabi, A.C., Zargarian, A., Schmauder, S., 2017. The relationships between deformation mechanisms and mechanical properties of additively manufactured porous biomaterials. J. Mech. Behav. Biomed. Mater. 70 (28–42). https://doi.org/10.1016/j.jmbbm.2016.09.018. ISSN 17516161.

Leary, M., Mazur, M., Elambasseril, J., Mcmillan, M., Chirent, T., Sun, Y., Qian, M., Easton, M., Brandt, M., 2016. Selective laser melting (SLM) of AlSi12Mg lattice structures. Mater. Des. 98, 344–357. https://doi.org/10.1016/j.matdes.2016.02.127.

Lietaert, K., Cutolo, A., Brecht, Hooreweder, V., 2018. Fatigue life of additively manufactured Ti6Al4V scaffolds under tension-tension, tension-compression and compression-compression fatigue load OPEN. Sci. Rep. 8, 4957. https://doi.org/10.1038/s41598-018-23414-2.

Liu, L., Kamm, P., García-Moreno, F., Banhart, J., Pasini, D., 2017. Elastic and failure response of imperfect three-dimensional metallic lattices: the role of geometric defects induced by Selective Laser Melting. J. Mech. Phys. Solids 107, 160–184. https://doi.org/10.1016/j.jmps.2017.07.003. ISSN 00225096.

Maskery, I., Hussey, A., Panesar, A., Aremu, A., Tuck, C., Ashcroft, I., Hague, R., 2017. An investigation into reinforced and functionally graded lattice structures. J. Cell. Plast. 53 (2), 151–165. https://doi.org/10.1177/0021955X16639035. ISSN 15307999.

Matlack, K.H., Bauhofer, A., Krödel, S., Palermo, A., Daraio, C., 2016. Composite 3D-printed metastructures for low-frequency and broadband vibration absorption. Proc. Natl. Acad. Sci. Unit. States Am. 113 (30), 8386–8390. https://doi.org/10.1073/pnas.1600171113. ISSN 0027-8424.

Merkt, S., Hinke, C., Bültmann, J., Brandt, M., Xie, Y.M., 2015. Mechanical response of

TiAl6V4 lattice structures manufactured by selective laser melting in quasistatic and dynamic compression tests, Citation. J. Laser Appl. 27, 17006. https://doi.org/10.2351/1.4898835.
Mines, R., Tsopanos, S., Shen, Y., Hasan, R., McKown, S., 2013. Drop weight impact behaviour of sandwich panels with metallic micro lattice cores. Int. J. Impact Eng. 60, 120–132. https://doi.org/10.1016/J.IJIMPENG.2013.04.007. ISSN 0734-743X.
Montazerian, H., Zhianmanesh, M., Davoodi, E., Milani, A., Hoorfar, M., 2017. Longitudinal and radial permeability analysis of additively manufactured porous scaffolds: effect of pore shape and porosity. Mater. Des. 122, 146–156. https://doi.org/10.1016/j.matdes.2017.03.006. ISSN 02641275.
S. L. Omairey, P. D. Dunning, S. Sriramula, Development of an ABAQUS plugin tool for periodic RVE homogenisation, Eng. Comput. doi:10.1007/s00366-018-0616-4.
Roberts, A.P., Garboczi, E.J., 2002. Elastic properties of model random three-dimensional open-cell solids. J. Mech. Phys. Solids 50 (1), 33–55.
Smith, M., Guan, Z., Cantwell, W., 2013. Finite element modelling of the compressive response of lattice structures manufactured using the selective laser melting technique. Int. J. Mech. Sci. 67, 28–41.
Takano, N., Takizawa, H., Wen, P., Odaka, K., Matsunaga, S., Abe, S., 2017. Stochastic prediction of apparent compressive stiffness of selective laser sintered lattice structure with geometrical imperfection and uncertainty in material property. Int. J. Mech. Sci. 134, 347–356. https://doi.org/10.1016/j.ijmecsci.2017.08.060. ISSN 00207403.
Tancogne-Dejean, T., Mohr, D., 2018a. Stiffness and specific energy absorption of additively-manufactured metallic BCC metamaterials composed of tapered beams. Int. J. Mech. Sci. 141, 101–116.
Tancogne-Dejean, T., Mohr, D., 2018b. Elastically-isotropic truss lattice materials of reduced plastic anisotropy. Int. J. Solids Struct. 138, 24–39. https://doi.org/10.1016/j.ijsolstr.2017.12.025. ISSN 00207683.
Tancogne-Dejean, T., Spierings, A.B., Mohr, D., 2016. Additively-manufactured metallic micro-lattice materials for high specific energy absorption under static and dynamic loading. Acta Mater. 116, 14–28. https://doi.org/10.1016/J.ACTAMAT.2016.05.054. ISSN 1359-6454.
Ushijima, K., Cantwell, W., Mines, R., Tsopanos, S., Smith, M., 2011a. An investigation into the compressive properties of stainless steel micro-lattice structures. J. Sandw. Struct. Mater. 13 (3), 303–329.
Ushijima, K., Cantwell, W.J., Chen, D.H., 2011b. Estimation of the compressive and shear responses of three-dimensional micro-lattice structures. Procedia Eng. 10, 2441–2446. https://doi.org/10.1016/j.proeng.2011.04.402. ISSN 18777058.
Wadley, H.N.G., Fleck, N.A., Evans, A.G., 2003. Fabrication and structural performance of periodic cellular metal sandwich structures. Compos. Sci. Technol. 63, 2331–2343. https://doi.org/10.1016/S0266-3538(03)00266-5.
Wang, Z., Wang, C., Li, C., Qin, Y., Zhong, L., Chen, B., Li, Z., Liu, H., Chang, F., Wang, J., 2017. Analysis of factors influencing bone ingrowth into three-dimensional printed porous metal scaffolds: a review. J. Alloy. Comp. 717 (271–285). https://doi.org/10.1016/J.JALLCOM.2017.05.079. ISSN 0925-8388.
Wang, X., Zhang, P., Ludwick, S., Belski, E., To, A.C., 2018. Natural frequency optimization of 3D printed variable-density honeycomb structure via a homogenization-based approach. Addit. Manuf. 20, 189–198. https://doi.org/10.1016/j.addma.2017.10.001. ISSN 22148604.
Wong, M., Owen, I., Sutcliffe, C.J., Puri, A., 2009. Convective heat transfer and pressure losses across novel heat sinks fabricated by Selective Laser Melting. Int. J. Heat Mass Transf. 52, 281–288. https://doi.org/10.1016/j.ijheatmasstransfer.2008.06.002.
Xiao, L., Song, W., Wang, C., Tang, H., Fan, Q., Liu, N., Wang, J., 2017. Mechanical properties of open-cell rhombic dodecahedron titanium alloy lattice structure manufactured using electron beam melting under dynamic loading. Int. J. Impact Eng. 100, 75–89. https://doi.org/10.1016/j.ijimpeng.2016.10.006. ISSN 0734743X.
Zhang, X.-Y., Fang, G., Xing, L.-L., Liu, W., Zhou, J., 2018a. Effect of porosity variation strategy on the performance of functionally graded Ti-6Al-4V scaffolds for bone tissue engineering. Mater. Des. 157, 523–538. https://doi.org/10.1016/j.matdes.2018.07.064. ISSN 02641275.
Zhang, X.Z., Leary, M., Tang, H.P., Song, T., Qian, M., 2018b. Selective electron beam manufactured Ti-6Al-4V lattice structures for orthopedic implant applications: current status and outstanding challenges. Curr. Opin. Solid State Mater. Sci. 22 (3). https://doi.org/10.1016/j.cossms.2018.05.002. 75–99, ISSN 13590286.
Zhang, M., Yang, Z., Lu, Z., Liao, B., He, X., 2018c. Effective elastic properties and initial yield surfaces of two 3D lattice structures. Int. J. Mech. Sci. 138–139 (158), 146. https://doi.org/10.1016/J.IJMECSCI.2018.02.008. ISSN 0020-7403.
Zhao, S., Li, S., Hou, W., Hao, Y., Yang, R., Misra, R., 2016. The influence of cell morphology on the compressive fatigue behavior of Ti-6Al-4V meshes fabricated by electron beam melting. J. Mech. Behav. Biomed. Mater. 59 (251–264). https://doi.org/10.1016/J.JMBBM.2016.01.034. ISSN 1751-6161.

4.2 Paper B

The title of the **Paper B** is 'Influence of relative density on quasi-static and fatigue failure of lattice structures in Ti6Al4V produced by laser powder bed fusion'. The article continues with the analysis of the FCCm structure, and its mechanical behavior is analyzed in more depth both numerically and experimentally:

- FCCm structures were manufactured with different relative densities and hot isostatic pressing (HIP) was applied, while keeping some as-built structures to study the effect of HIP.
- Gibson-Ashby curves of FCCm structures were obtained, and comparison with numerical simulations was carried out to study the failure under quasi-static load.
- S-N fatigue curves were obtained for different relative densities, and fatigue failure of the structures was studied based on stiffness evolution, establishing a restrictive failure criterion.
- Fatigue failure prediction methods from literature were compared and modified to improve their fatigue life prediction capabilites.
- A fatigue failure surface was proposed to explicitly include relative density in the cyclic load prediction.

Influence of relative density on quasi-static and fatigue failure of lattice structures in Ti6Al4V produced by laser powder bed fusion

Markel Alaña [1,*], Antonio Cutolo[2], Sergio Ruiz de Galarreta[1], and Brecht Van Hooreweder[2,3]

[1]Department of Mechanical Engineering and Materials, Universidad de Navarra, TECNUN Escuela de Ingenieros, Paseo Manuel de Lardizabal, 13, 20018 San Sebastian, Spain
[2]KU Leuven Department of Mechanical Engineering, Celestijnenlaan 300, 3001 Leuven (Heverlee), Belgium
[3]Members Flanders Make, Leuven, Belgium
[*]malana@tecnun.es

ABSTRACT

Lattice structures produced by additive manufacturing have been increasingly studied in recent years due to their potential to tailor prescribed mechanical properties. Their mechanical performances are influenced by several factors such as unit cell topology, parent material and relative density. In this study, static and dynamic behaviors of Ti6Al4V lattice structures were analyzed focusing on the criteria used to define the failure of lattices. A modified face-centered cubic (FCCm) lattice structure was designed to avoid the manufacturing problems that arise in the production of horizontal struts by laser powder bed fusion. The Gibson-Ashby curves of the FCCm lattice were obtained and it was found that relative density not only affects stiffness and strength of the structures, but also has important implications on the assumption of macroscopic yield criterion. Regarding fatigue properties, a stiffness based criterion was analyzed to improve the assessment of lattice structure failure in load bearing applications, and the influence of relative density on the stiffness evolution was studied. Apart from common normalization of S-N curves, a more accurate fatigue failure surface was developed, which is also compatible with stiffness based failure criteria. Finally, the effect of hot isostatic pressing in FCCm structures was also studied.

Introduction

Additive manufacturing (AM), and laser powder bed fusion (LPBF) of metals specifically, enables the production of exceptionally complex parts in a cost-effective manner, including architected lattice structures[1]. These structures offer a set of mechanical property combinations unavailable until few decades ago. Lattice structures can be considered as metamaterials when analyzed at macroscopic level[2,3]. These metamaterials can be formed by a three dimensional pattern of a repeating unit cell (UC), or by stochastic arrangements of structural units that fill a certain space to form a part[4].

The large amount of available configurations makes lattice structures interesting for diverse applications, ranging from structural components as well as in energy absorption, heat exchanger devices, vibration attenuators or for catalytic purposes[5–8]. In terms of load carrying applications, the freedom that AM offers regarding the manufacturability of geometries enables the design of lattice structures tailoring specific mechanical properties that meet specific needs[9,10].

Lattice structures can be categorized in stretching or bending dominated structures depending on the configuration of their struts[11]. Along with the topology of the structures, relative density is an important driving factor of their mechanical properties, defined by the proportion of the parent material within a Representative Volume Element (RVE) of the lattice structure.

The influence of relative density on the quasi-static lattice mechanical properties has been studied for different structures like BCC[12], diamond[13], octet truss[14], FCC[15], rhombic dodecahedron[16] or cubic[17], among others[18], covering a wide range of stiffness and strength levels. Yield strength or plateau stress are in turn used to better predict the fatigue properties of those structures, because they implicitly include the effect of variables such as material, microstructure, surface roughness, relative density or manufacturing deviations[17]. Ahmadi et al.[19] concluded that the accuracy of this approach was highly dependent on the material and the unit cell topology. On the other hand, Van Hooreweder et al.[20] developed a Local Stress Method (LSM) to predict the fatigue behavior of lattice structures based on a beam model, and considering only local tensile stresses. In addition,

the effect of heat and surface treatments was also extensively studied, concluding that a combination of surface treatments like chemical etching or sand blasting with Hot Isostatic Pressing (HIP) sensibly improves the lattice structures fatigue life[20–22].

Most of the experimental work in fatigue is conducted under uniaxial compression-compression loads due to the simplicity of the test configuration[23], and as far as the authors know there is no standard failure criterion that defines the lattice specimen failure in fatigue tests. Nevertheless, it is common to consider the failure of a specimen when it loses most or all of its stiffness[22,24–26], e.g. 90% of stiffness reduction, or permanent displacement drops[20,21,27]. These criteria imply the loss of the load carrying capacity of the specimen, yet in the case of parts integrating lattices for load bearing applications, the changes in stiffness or deformations on the lattice might lead to the increase of stresses in the part. Thus, it is useful to consider other criteria to determine the failure of lattice structures, as done by Boniotti et al.[28], where a 10% stiffness loss failure criterion was used to analyze the fatigue of AlSi7Mg lattice structures.

Horizontal struts produced by LPBF have an overall lower quality than inclined or vertical struts, with higher strut porosity levels and lower dimensional accuracy[29]. This has significant effects on the mechanical properties of lattice structures, and limits their capability to perform under certain load orientations[30]. In this work, a modified FCC lattice structure (FCCm) was designed by removing the horizontal struts of the FCC unit cell. Lattice structures of several relative densities were produced with LPBF Ti6Al4V. The fatigue behavior was studied for the different relative densities, analyzing the evolution of the stiffness of the specimens, and assessing a stiffness based failure criterion for fatigue. A new method to predict the fatigue life of lattice structures for a wide range of relative densities is also proposed, which can be used along with stiffness based failure criteria. Furthermore, the interaction between the mesoscopic stress state and macroscopic metamaterial properties were numerically investigated to explore in depth in the assumption of the 0.2% offset stress as the macroscopic yield strength of lattice structures. Finally, a batch of as-built FCCm lattices was also produced to analyze the effect of heat treatment on the quasi-static and fatigue properties of the FCCm structures.

Materials and Methods

Design and production of lattice structures

Lattice structures were designed based on the FCCm unit cell, which is formed by 6 nodes and 8 struts forming an angle of 45º with respect to the build plate as in Figure 1. A unit cell size of 1.5mm was used, and structures of two different sizes were produced. Lattices of 10%, 20% and 30% relative densities - referred as RD01, RD02 and RD03 - were designed using the formula developed in Alaña et al.[31], with diameters of 0.24 mm, 0.36 mm and 0.46 mm respectively, and a width of 15 mm and height of 19.5 mm (left in Figure 1). These structures were HIP treated at 920°C for two hours with a pressure of 1000 bar after production. On the other hand, structures of 12 mm size were also designed based in the same unit cell, and with a prescribed relative density of 20% (right in Figure 1). These structures were not treated after production and are named AB (as-built). All the samples were produced in Ti6Al4V by LPBF on a Mlab machine (Concept Laser).

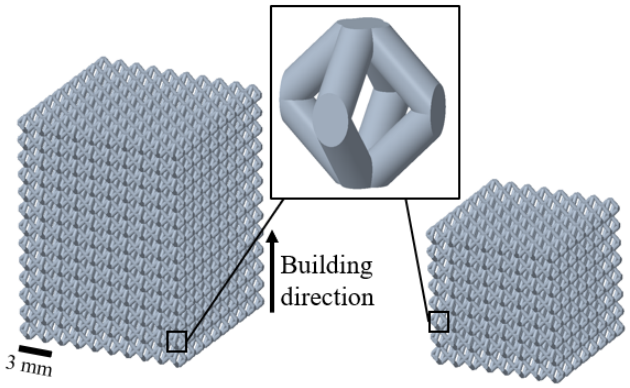

Figure 1. Specimen geometry for 20% relative density design for HIP (left) and as-built (right) conditions.

Morphological characterization and mechanical testing

For each of the produced specimens, the relative density of the structures was measured by dry weighing. The total volume of the specimen was calculated from caliper measurements, and a theoretical density of 4.42 g/cm^3 was assumed for Ti6Al4V. Furthermore, the strut density was also measured by means of Archimedes method, submerging the specimens in ethanol.

Quasi-static compression tests were carried out on an Instron 3360 with a 30 kN load cell. A crosshead velocity of 0.9 mm/min was used, and Teflon sheets of 0.2 mm were used to reduce the friction between the specimen and the compression plates. The strain was measured using the Instron Video Extensometer AVE2. For the RD03 structures an Instron 5982 was used with a 100 kN load cell due to their higher strength. In this case, the crosshead displacement was measured, and strain was calculated by compensating the compliance of the machine.

Load controlled compression-compression fatigue tests were performed on an Instron Electropuls E10000 machine, with a frequency of 15 Hz and a load ratio (R) of 10. Tests were stopped when collapse of the specimen occurred, or after reaching 10^6 cycles. Furthermore, the stiffness of the samples was measured every 1000 cycles. After compensating the stiffness of the machine, an additional failure criterion was established at 10% stiffness loss of the sample. Due to the high strength of the RD03 specimens a Schenck equipped with a load cell of 160 kN was used for fatigue testing. The fatigue strength (FS) of the structures at 10^6 cycles was obtained by means of the staircase method[32]. An arbitrary stress is applied to the specimen (σ_n), and after the prescribed number of cycles is reached ($N_{limit} = 10^6$) the stress level is increased and the same specimen is tested again. The FS is obtained by means of Eq. 1.

$$\sigma_{FS} = \sigma_{n-1} + \frac{N_{failure}}{N_{limit}}(\sigma_n - \sigma_{n-1}) \tag{1}$$

Numerical models

In order to understand the effect of the relative density on the macroscopic properties of the FCCm lattice a Finite Element (FE) analysis was carried out. The simulations were also performed to study the relationship between the lattice macroscopic properties and the bulk material as the relative density varies.

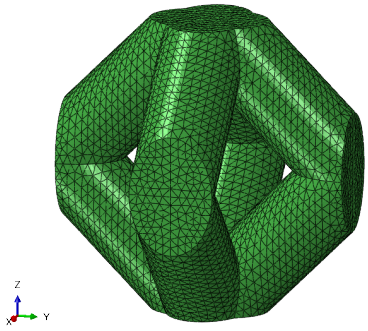

Figure 2. FE model of a unit cell of the RD02 specimen.

The FE models were constructed with a single unit cell (Figure 2) with Periodic Boundary Conditions (PBC)[33]. On the one hand, FE models were built with relative densities corresponding to the values obtained by dry weighing, in order to compare directly with the experiments. Therefore, a part of the manufacturing deviation was already accounted for. On the other hand, several numerical models with relative densities between 5% and 40% were also designed in order to analyze the interaction between macroscopic and mesoscopic stress levels and their variability for different relative densities. Abaqus 2020 was used for the analyses, with second order tetrahedral elements (C3D10) after conducting a sensitivity analysis, and the element size was designed to be ten times smaller than the strut diameter for each model. Linear elasticity was assumed, and J2 plasticity was used to model plastic behavior. The material was assigned a Young's modulus of 129 MPa, a Poisson ratio of 0.342 and a yield strength of 921 MPa.

Normalization of fatigue curves

For each relative density the fatigue experimental data were used to derive specific S-N curves. These curves were normalized with the global 0.2% offset stress obtained from the quasi-static compression tests to assess the variability of the normalized curves for different relative densities and to analyze the effect of the HIP.

Moreover, the Local Stress Method (LSM) developed by Van Hooreweder et al.[20] was implemented in the FCCm structures. This normalization is based on a Timoshenko beam model of the struts, and considers only the tensile stress of the beam model to assess the fatigue life of the structures. In order to apply the LSM for a wide range of relative densities the method was modified to consider the variability of strut length (l_{strut}) apart from diameter (d) changes. Thus, this equation gives the analytical tensile stress across the FCCm struts:

$$\sigma_{LSM} = F\left(\frac{16 l_{strut}\cos\theta}{\pi d^3} - \frac{4\sin\theta}{\pi d^2}\right) \tag{2}$$

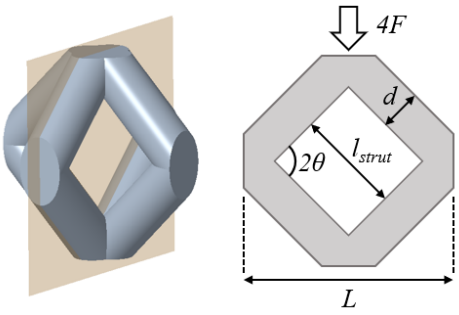

Figure 3. Parameters to obtain the maximum tensile stress in each strut by using the Local Stress Method.

In which F is force applied on the single strut and θ is the angle between the strut axis and the horizontal plane, as shown in Figure 3. For FCCm structures $\theta = 45°$. The relation between the strut diameter and the relative density for FCCm structures is given by Eq. 3, where L represents unit cell size.

$$\rho_{rel} = \alpha\left(\frac{d}{L}\right)^3 + \beta\left(\frac{d}{L}\right)^2, \quad \text{with } \alpha = -3.91 \text{ and } \beta = 4.44 \tag{3}$$

Fatigue failure surface

The S-N curves were used to define a S-N-ρ_{rel} surface, which expresses the fatigue properties of the FCCm lattice structures for a given relative density range. This surface is a result of two subsequent nonlinear regression fits, which were obtained by means of the Curve Fitting Toolbox of MATLAB (2020a, MathWorks, USA). Firstly, an S-N curve was generated for each tested relative density with the form of Eq. 4.

$$S = C_1 N^{C_2} \tag{4}$$

Once C_1 and C_2 values were obtained for the three batches, those values were used to fit two different exponential curves, one for each variable. Hence, the relative density is explicitly introduced as the function variable to define C_1 and C_2. In this case an offset was included in order to increase the flexibility of the variables.

$$C_1 = a\rho_{rel}^b + c, \quad C_2 = d\rho_{rel}^e + f \tag{5}$$

By introducing the expressions of Eq. 5 into Eq. 4, the next equation is obtained:

$$S = C_1 N^{C_2} = \left(a\rho_{rel}^{b} + c\right) N^{\left(d\rho_{rel}^{e} + f\right)} \tag{6}$$

Eq. 6 describes the S-N-ρ_{rel} surface that contains the fatigue life of the FCCm lattices, explicitly including the relative density in the equation of S-N curves.

Results and discussion

Manufacturing

The relative density of the scaffolds and their strut density are given in Table 1. For all the manufactured samples, the measured relative densities were always higher than designed, with the deviations between 2.39% and 7.72%.

The internal porosity of the struts is significantly lower in the RD01 specimens compared to the other samples. Even for the HIPed samples RD02 and RD03, the strut porosity is similar to as-built samples AB, indicating that the HIP process could not close the internal pores of the struts.

	RD01	RD02	RD03	AB
Designed relative density [%]	10	20	30	20
Manufactured relative density [%]	12.39 ± 0.34	27.72 ± 0.31	37.11 ± 0.27	26.59 ± 0.2
Strut density [%]	99.57 ± 0.10	97.28 ± 0.18	97.18 ± 0.46	97.52 ± 0.16

Table 1. Designed and manufactured relative densities.

Quasi-static compression

The values obtained from the quasi-static compression tests are given in Table 2, including the standard deviation.

	Quasi-elastic gradient [GPa]	0.2% offset stress [MPa]	Strain at stress offset [%]	Maximum stress [MPa]	Strain at maximum stress [%]
RD01	0.75 ± 0.01	17.95 ± 1.32	2.78 ± 0.25	23.94 ± 0.84	6.84 ± 0.32
RD02	4.96 ± 0.41	100.09 ± 0.35	3.15 ± 0.16	124.00 ± 0.65	7.77 ± 0.48
RD03	9.07 ± 0.60	181.79 ± 2.99	2.87 ± 0.05	234.43 ± 2.46	11.23 ± 0.53
AB	5.38 ± 0.39	121.00 ± 0.79	3.64 ± 0.23	138.40 ± 0.44	5.29 ± 0.29

Table 2. Experimental values of tested FCCm lattice structures.

Effect of relative density

Figure 4a shows the stress-strain curves of the HIP treated FCCm samples for different relative densities. The shaded area corresponds to the 95% confidence interval, which was obtained by combining the curves of the tested samples in each batch.

The scatter of the curves is very low in the elastic and beginning of plastic regions, and it increases in the stiffness drop region and afterwards. Moreover, even if the variability of the curves is rather small for RD01 and RD02, in the case of RD03 the curves of the samples show important differences, which leads to the wide shaded area of 95% confidence interval.

The fluctuation of the stress-strain curves varies depending on the relative density, and denser structures show a lower number of peaks and valleys for the same compression level of the sample. This indicates that the higher relative density favors a more homogeneous behavior of the structures, which do not collapse layer by layer or strut by strut, but more as a compact material. This effect can be better observed in Figure 4b, which depicts the stress-strain curves normalized by the macroscopic yield strength of each of the structures. The figure also indicates that the stiffness drop of RD03 occurs at higher strain levels, and is more progressive than for RD01 and RD02.

The stiffness and strength of the structures increase exponentially with the relative density, and the Gibson-Ashby curves of the FCCm lattices exhibit the typical bending dominated behavior. Figure 5 depicts the quasi-elastic gradient and macroscopic yield strength of the FCCm lattice structure and other bending dominated topologies under a wide range of relative densities, and the FCCm denotes superior stiffness and strength for the analyzed cases. These results are limited to a single load orientation, and can be explained by the different angle of the struts with respect to the load in the case of the FCCm lattice.

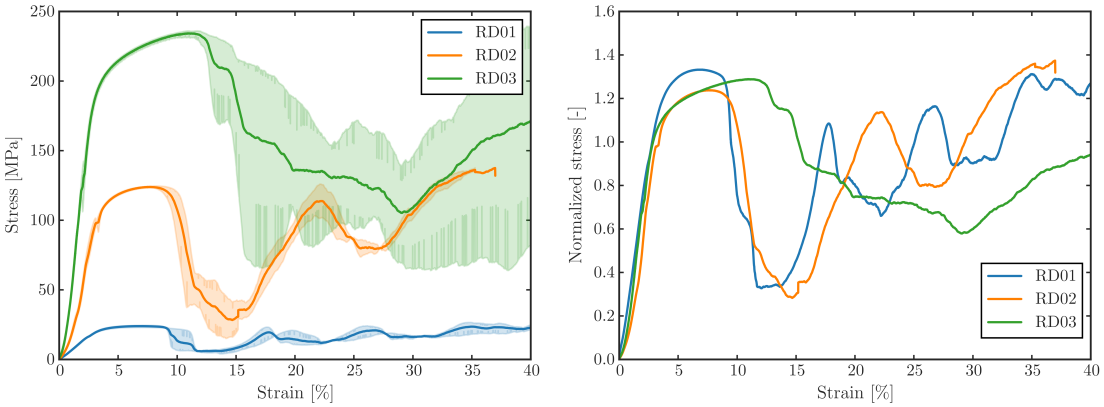

Figure 4. Stress strain curves of FCCm structures with different relative densities for a) macroscopic stress and b) normalized macroscopic stress.

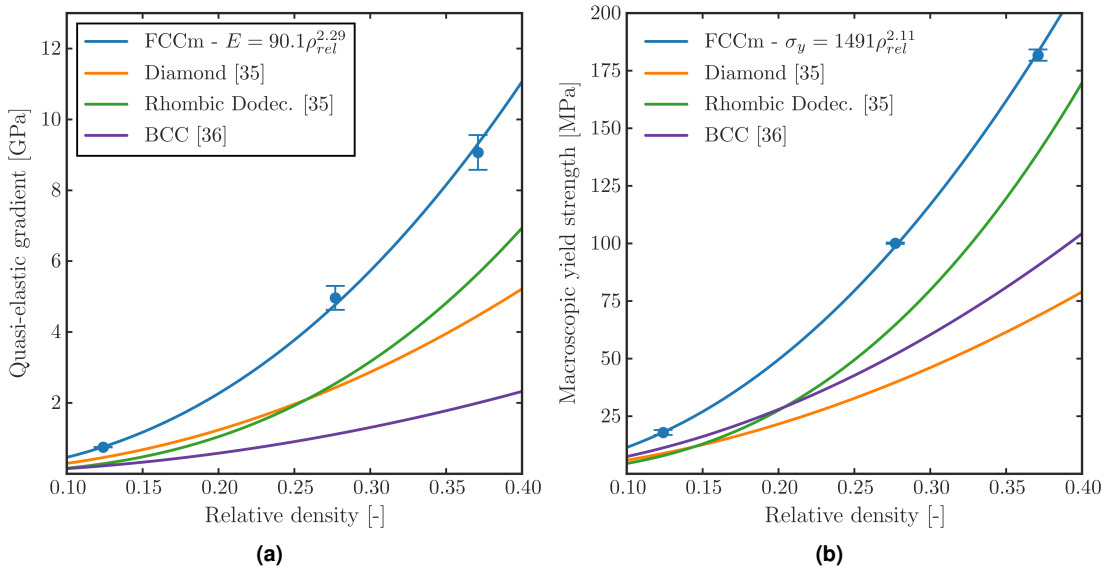

Figure 5. Gibson Ashby curves of FCCm and other bending dominated unit cells made of Ti6Al4V obtained from[34] and[35].

Effect of heat treatment

The HIP process has a strong influence on the structures' mechanical properties. As reported in several studies, HIP treatment of LPBF Ti6Al4V samples leads to residual stress relief, potential material porosity reduction and also a transition from the more brittle martensitic α' material structure to a more ductile $\alpha - \beta$ structure[20,25]. Figure 6 shows the difference between AB and HIP conditions. The AB samples have higher maximum stress, and a slightly higher quasi-elastic gradient. Nonetheless, the fracture of the structure is brittle, and occurs at lower strains compared to the samples after HIP treatment.

After the first stress drop, the HIPed structure is able to continue absorbing energy, while for the AB structure, the fracture plane divides the structure in several parts with the consequent loss of the structural integrity needed to carry load and absorb energy as shown in Figure 7. The difference in geometry between both structures may also play a role in this behavior, since the AB samples have fewer unit cells in each direction, making the structure more unstable after the slip plane appears. Figure 7

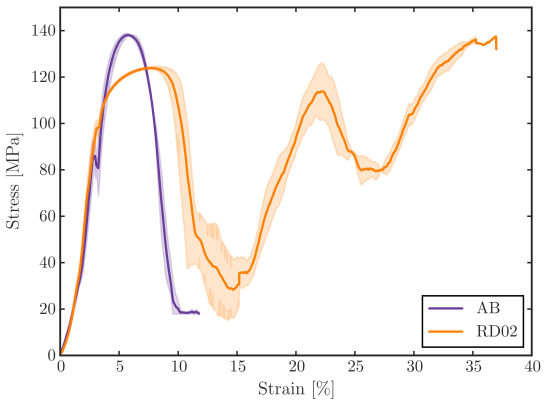

Figure 6. Stress strain curve of AB and RD02 structures.

also shows that the slip plane corresponds to the [111] orientation, which is a common property of the FCCm unit cell regardless the relative density and heat treatment, under uniaxial load in [001] direction.

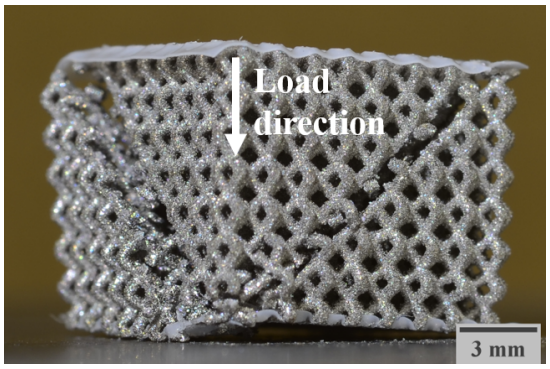

Figure 7. Fracture plane of the AB structure under compression load in [001].

Numerical simulation

The quasi-static mechanical properties of the numerical models are given in Table 3. The numerical model is capable of predicting the strength of the FCCm structures consistently, with a maximum relative error of 12% in the case of the RD01 structure. Nevertheless, the quasi-elastic gradients of the numerical models are far from the experimental values obtained. It is common to have significant differences between numerically and experimentally obtained mechanical properties of lattice structures, since numerical models neglect many imperfections that reduce the stiffness of lattices, and can even cause changes in their anisotropy[36,37]. These imperfections include the dross formation, the waviness of struts, the surface roughness, internal porosity, among others, and were not considered in the numerical models.

	RD01		RD02		RD03	
	Exp.	FE	Exp.	FE	Exp.	FE
Quasi-elastic gradient [GPa]	0.75	1.54	4.96	10.45	9.07	20.89
0.2% offset stress [MPa]	17.96	20.16	100.09	98.5	181.79	174.88

Table 3. Designed and manufactured relative densities.

Yield stress of structure and design criteria

The 0.2% offset stress is a widely used stress criterion to assess the strength of lattice structures, and often referred to as yield strength[10,34]. Nevertheless, this criterion should be used with caution if applied to lattice structures. Whereas the yield strength usually establishes the stress limit above which plastic deformation of the material begins, for lattice structures high plastic deformations may occur in large regions before reaching the macroscopic yield strength. This phenomenon is caused by the non-uniform stress fields that arise as the scaffolds are deformed.

Figure 8 depicts the distribution of the Von Mises stress for the numerical models corresponding to the tested specimens. The macroscopic stress applied to each model corresponds to the half of the macroscopic yield strength, obtained as 0.2% offset stress. The Von Mises stress corresponds to the actual stress of the bulk material within the structure, that is, the mesoscopic stress. The effect of relative density can be observed in the different shape of the distributions. For low relative densities, the proportion of low stress regions is much larger. The higher slenderness of the struts results in a more beam like load distribution, with large regions of the struts under low stress levels. As the relative density increases, the probability distribution covers a wider span of the stresses, and a larger proportion of the structure withstands higher stress levels for the same proportional macroscopic stress. The exponential growth of the Gibson Ashby curves can be explained by this evolution of the load carrying mechanism.

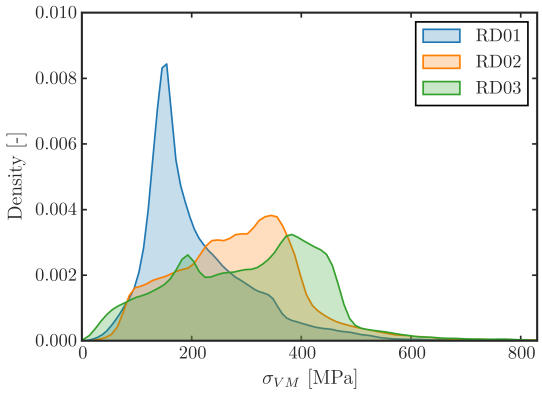

Figure 8. Probability distribution of Von Mises stress of the numerical models under same normalized macroscopic stresses.

The different stress distributions have significant implications when considering design criteria based on macroscopic stresses, such as macroscopic yield strength. If the stress state of the numerical models is analyzed for different macroscopic stress levels and different relative densities, it can be observed that the proportion of plastic deformation that occurs before the macroscopic yield strength is highly dependent on relative density, as indicated in Figure 9a. The Figure depicts the percentage of the bulk material of the lattice structures above yield stress, and the ratio between the applied macroscopic stress and the macroscopic yield strength. $\sigma/\sigma_y = 1$ corresponds to the 0.2% offset stress, considered the macroscopic yield stress for each model, after which macroscopic plastic deformation is assumed (blue area in Figure 9a).

Figure 9b indicates the percentage of the yielded volume of each structure at the macroscopic yield stress level corresponding to the 0.2% offset stress. As the relative density increases, the proportion of regions with plastic deformation is larger at the macroscopic yield stress level. For the FCCm lattice structures with relative density of 40%, above one quarter of the structure is undergoing plastic deformation before reaching the macroscopic yield criterion.

This information should be considered when designing parts that include lattice structures in case the bulk material is supposed to work only within the elastic region. Furthermore, the irregularities of the surface and manufacturing deviations were not accounted for in these simulations. These effects increase the stress level of the lattice structures, thus enhancing the probability to develop plastic strains before expected in the design process.

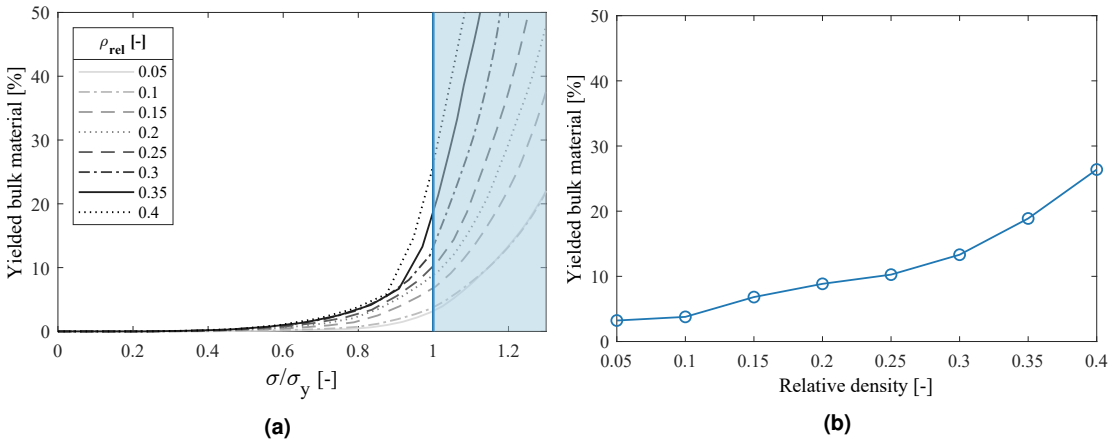

Figure 9. a) Evolution of bulk material yielding for different relative densities, b) proportion of yielded bulk material at macroscopic 0.2% offset yield stress for different relative densities.

Fatigue properties

Global S-N curves

Figure 10 depicts the S-N curves obtained from the experiments, including experimental data obtained using both the failure criteria of 10% stiffness drop and collapse of the structure. The experimental points were adjusted to Basquin's exponential curves $S = C_1 N^{C_2}$ and the obtained coefficients are given in Table 4.

The variation of the relative density comprises a very wide range of fatigue resistance values for the FCCm structure, across different orders of magnitude. This variability is suitable in order to tailor the mechanical properties of the structure considering the required fatigue performance under different load cases, or to design graded lattice structures with fatigue strength constraints. As expected, the HIP process significantly improves the fatigue life of the structures, even if in this case the HIP process was not able to close the internal pores of the struts. Therefore, the change in microstructure can be considered as the responsible for fatigue life enhancement[20].

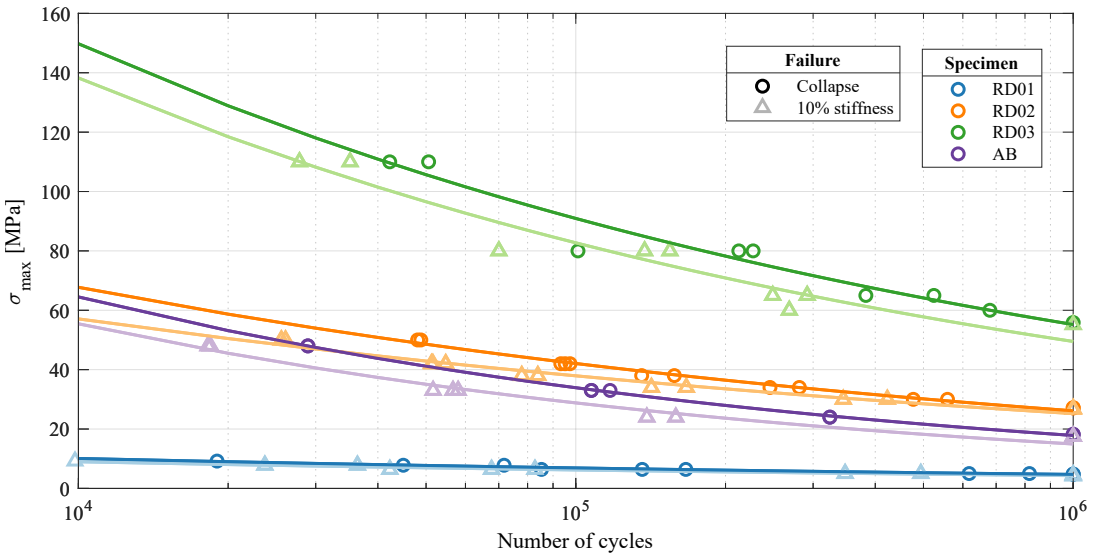

Figure 10. S-N curves of FCCm lattice structures for two different failure criteria.

	10% stiffness loss		Collapse failure	
	C_1	C_2	C_1	C_2
RD01	39.07	-0.160	46.24	-0.165
RD02	293.19	-0.178	455.32	-0.207
RD03	1078.7	-0.223	1102.6	-0.217
AB	761.35	-0.284	843.6	-0.279

Table 4. Coefficients for Basquin's exponential S-N curves of FCCm structures.

Evolution of stiffness and failure criteria

The loss of stiffness of lattice structures during fatigue loading is a progressive degradation process in which the damage, the failure or the local plastic deformation of each strut gradually reduces the macroscopic stiffness of the structure. This process is depicted in Figure 11 for the different relative densities of FCCm lattice structures. The legends include the proportion of maximum stress of the cycles with respect to the macroscopic yield strength of the structures.

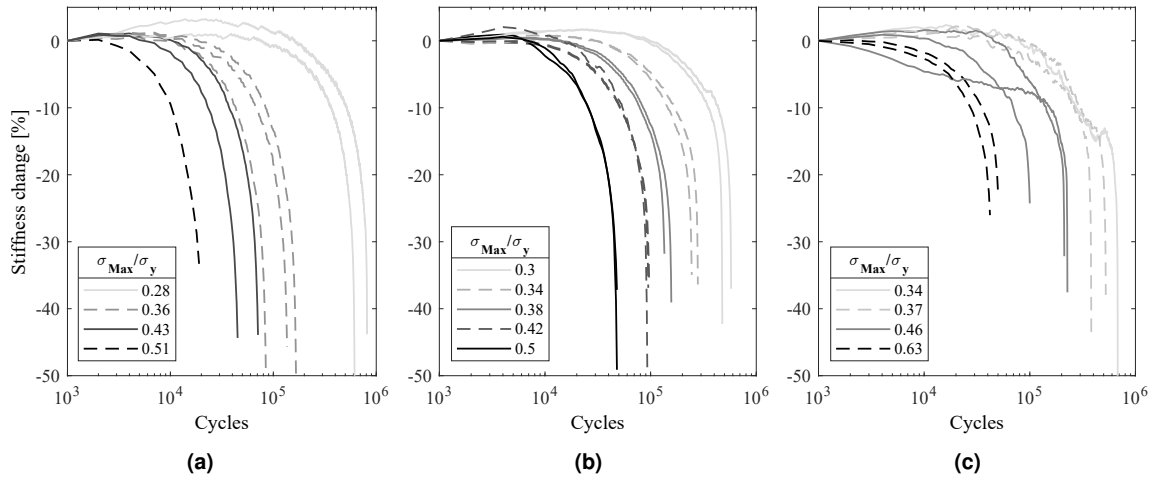

Figure 11. Evolution of stiffness under different loads and relative densities of a) 10%, b) 20% and c) 30%.

The damage that results in stiffness loss is accumulated at different rates depending on the load and the relative density. The highest stress levels induce more pronounced stiffness losses from the beginning of the test, with small regions of stable stiffness. Nonetheless, lower stress levels result in large stable stiffness regions before the accumulation of damage begins. This trend is observed for all the analyzed specimens, however, the rate of damage accumulation and its stability also depends on the relative density.

Establishing a fatigue criteria based on the 10% stiffness loss of the structure allows to guarantee the integrity of the lattice structure, as well as it hinders the excessive loading of parts adjacent to the lattice structure in load bearing applications. Nonetheless, it is important to notice that stiffness loss criteria for lattice structures imply different safety factors (SF) depending on the relative density. SF is defined by the ratio between the cycles until collapse and the cycles elapsed until the established fatigue criterion. Figure 12 presents the relationship between the elapsed cycles at the 10% stiffness loss, and the cycles left until total collapse of the structure, for each of the tested specimens. The two dashed lines in the figure correspond to SF=2 (y=x line) and to SF=1.5 (y=0.5x line) respectively.

In low cycle fatigue (LCF) there is a correlation between relative density and SF: the RD01 specimens coincide with the SF=2 line, the RD03 is in good agreement with the SF=1.5 line, and RD02 is between both lines, which means that a higher relative density implies a lower SF. It must be noted that the tendency of RD02 is not linear and presents higher variability with respect to the stress level compared to RD01 and RD03. On the other hand, for high cycle fatigue (HCF) the SF of RD01 and RD02 decreases with respect to LCF, whereas for RD03 the SF increases. The increase for RD03 samples above SF=1.5 line can be explained by the tendency change of the stiffness decrease as depicted in Figure 11c for the lowest stress levels. For the AB samples, the SF is similar to the HIPed samples, nevertheless, the decrease of stress level tends to increase the SF, which is

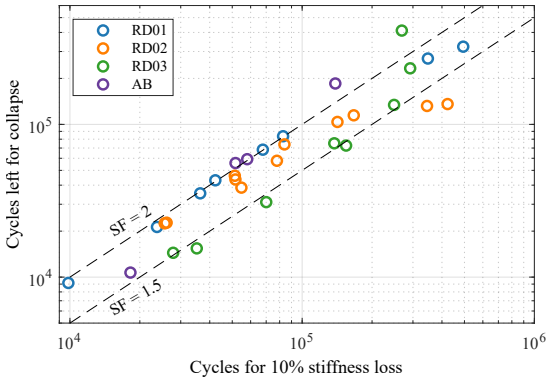

Figure 12. Cycles left until collapse for FCCm structures with different relative densities depending on cycles at 10% stiffness loss.

a tendency contrary to the one observed in the RD02 samples.

The ratio between the SF and stiffness loss enables the prediction of cycles left for FCCm lattice structures and thus a safer integration in load bearing applications. Furthermore, instead of establishing a certain stiffness drop as a failure criterion, it is also possible to use a certain SF as failure criterion, which can be implemented by calculating the stiffness drop corresponding to each relative density and stress level.

Strain accumulation must also be considered to consider the failure of the structure at 10% stiffness loss. For all the tested stress levels, the mean accumulated strain at 10% stiffness drop was 0.36%, 0.39% and 0.32% for RD01, RD02 and RD03 structures respectively, which ensures structural stability.

Normalization of S-N curves

Figure 13 shows the normalized S-N curves of the FCCm structures based on the final collapse failure criterion. Figure 13a depicts the S-N curves normalized with the macroscopic yield strength of each structure for different relative densities, and the fitted dashed line corresponds to all the HIPed samples. A clear difference can be observed between the studied relative densities, and the normalized fatigue strength increases with the relative density, which limits the fatigue prediction capability of this method. The effect of heat treatment can be observed with the AB curve below all the normalized curves after HIP, regardless the relative density.

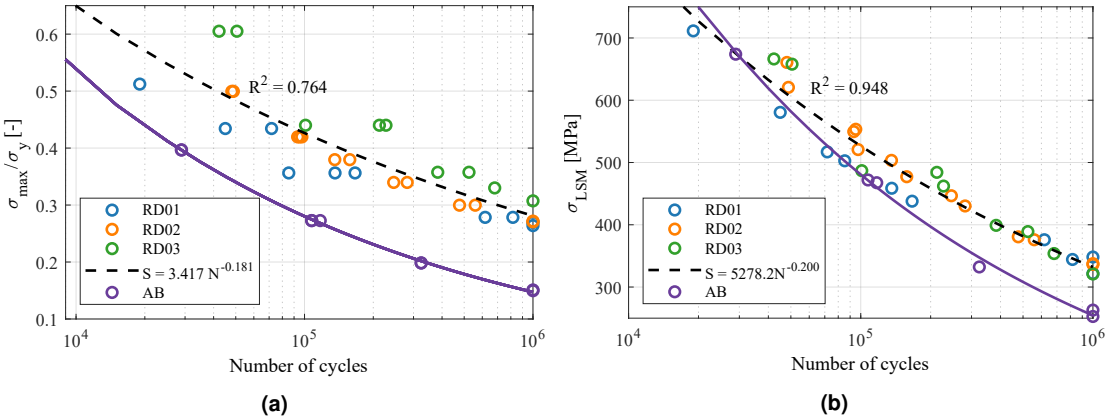

Figure 13. S-N curves of collapse of the structures normalized by a) yield strength and b) Local Stress Method.

It is common to normalize the S-N curves by dividing the stress with a quasi-static macroscopic property of the lattice structure being analyzed, e.g. the macroscopic yield strength or plateau stress[19,38]. The advantage of this approach is that

very different factors such as the variation of relative density, microstructure, or manufacturing defects can be accounted in an implicit manner, thus obtaining curves that enable the prediction of fatigue life. Nonetheless, the accuracy of this approach is variable across different works and studied unit cell types[19,39,40], and in the case of the FCCm unit cell it has only a limited reliability.

The normalization based on local tensile stresses of the beam models is given in Figure 13b, and it shows a very good agreement for all experimental data corresponding to HIPed specimens, regardless the relative density of the structures. The level of accuracy is higher in HCF, presumably because the assumption of elastic behavior is more valid in this region. The effect of heat treatment can also be observed in Figure 13b, indicating that the difference between AB and HIP increases from LCF to HCF.

It is worth noting that an analytical beam model considering the tensile stresses exhibits a higher accuracy than the normalization with the macroscopic yield strength, despite the latter implicitly considers more variables. This might be explained by the fact that the macroscopic yield of lattice structures is a compression driven phenomenon under macroscopic compression, while the fracture of struts and progressive damage accumulation is induced mainly by tensile stresses developed across each strut under compressive loads.

On the other hand, these methods to predict fatigue life are not as accurate if 10% stiffness loss criterion is used, as depicted in Figure 14. In the case of yield strength normalization, the R^2 is even lower than for collapse, and three different tendencies can be distinguished. Local Stress Method fits better, but the accuracy also decreases compared to Figure 13b. This loss of accuracy arises because of the fact that a prescribed stiffness loss corresponds to different SF for each relative density and stress level. Nonetheless, for a prescribed SF the normalization accuracy corresponds to the one in Figure 13. The fatigue failure surface was developed in order to have more flexibility in the prediction of fatigue life with various failure criteria.

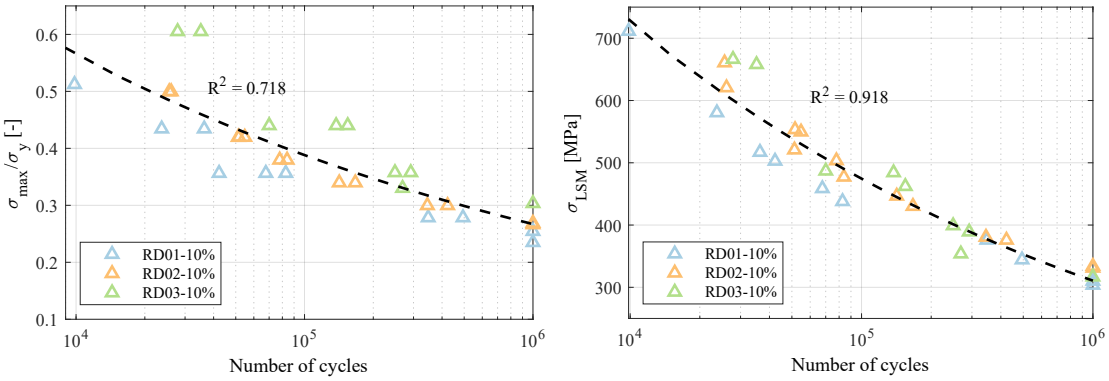

Figure 14. S-N curves of 10% stiffness loss criterion normalized by a) yield strength and b) Local Stress Method.

Fatigue failure surface

The constants resulting from the exponential fits described in Eq. 6 are given in Table 5. For each of the considered failure criteria a failure surface can be defined by introducing the constants in Eq. 6. The differences in sign for some constants for different failure criteria arise from the very different behavior of the evolution of stiffness after the 10% loss for each structure. This method provides an accurate tool ($R^2 = 0.991$ and $R^2 = 0.983$ for 10% stiffness loss and collapse criteria, respectively) to predict the fatigue life of FCCm lattice structures within a wide range of relative densities.

The failure surface of Figure 15a corresponds to the 10% stiffness loss of the structures, while the Figure 15b depicts the collapse of the structures for each relative density. As expected, the area corresponding to the 10% stiffness loss is smaller than for the collapse, since the former criterion is more restrictive.

The failure surface is a highly flexible tool to predict failure of lattice structures under several fatigue criteria. In this work the 10% stiffness loss was used apart from the collapse of the structure, but adopting any stiffness based criteria is also possible.

	10% stiffness loss	Collapse
a	118600	22940
b	4.77	3.07
c	33.51	8.53
d	-4.07	0.02
e	4.19	-0.74
f	-0.16	-0.26

Table 5. Constants from exponential fits for stiffness loss and collapse fatigue failure surfaces.

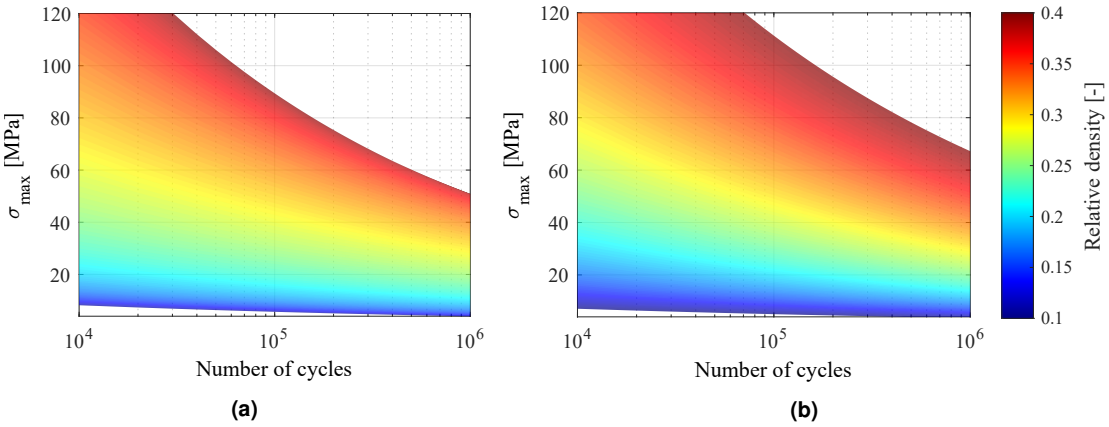

Figure 15. Failure surface after HIP for a) 10% stiffness loss and b) collapse of structure.

Furthermore, this method also allows considering different admissible stiffness loss values depending on the relative density: for lower relative densities, higher stiffness losses are admissible before collapse (Figure 12).

Fatigue strength at 10^6 ***cycles***

The resulting FS at 10^6 cycles for each of the tested structures is given in Figure 16. As expected, the fatigue strength varies with the relative density following an exponential curve as the quasi-static mechanical properties listed in Table 2. Moreover, the HIP treatment increases the FS of the structures as expected.

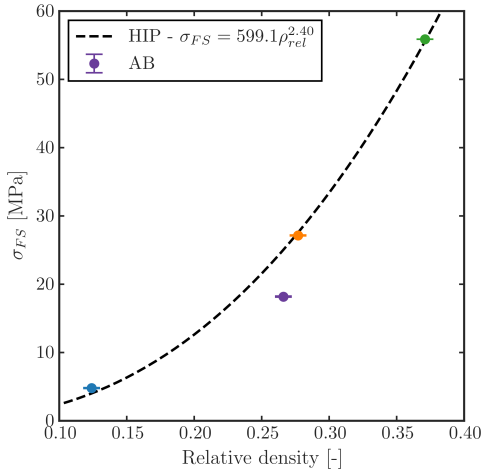

Figure 16. Fatigue strength at 10^6 cycles of FCCm structures for different relative densities and post treatments.

Figure 17 indicates the FS of each structure after normalization with macroscopic yield strength, and using the LSM

normalized by the yield strength of the bulk material. The normalized fatigue strength of HIPed samples increases slightly with relative density, from 0.27 to 0.31, while the AB sample has a normalized FS of 0.15. The FS at 10^6 for several bending dominated structures is reported to lay between 0.15 and 0.24 for AB condition[41]. The higher normalized FS for HIPed structures is in line with results reported in literature[42,43], and the LSM also indicates that HIP treatment increases the FS of the structures, regardless the relative density. This can be mainly attributed to the $\alpha + \beta$ microstructure of the HIPed samples compared to the α' of the AB condition.

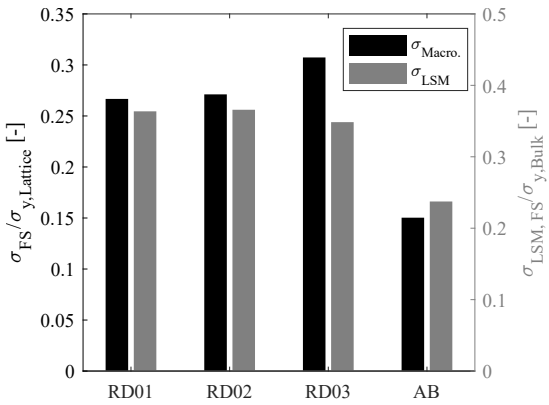

Figure 17. Normalization of fatigue strength with yield strength and local stress method.

Conclusions

The relative density of the lattice structures is one of the most relevant parameters that enables the control and design of their mechanical properties. This study analyzed the quasi-static and dynamic mechanical properties of lattice structures based on the FCCm unit cell with different relative densities, and the interaction between macroscopic and mesoscopic variables. The main conclusions are as follows:

- The quasi-static mechanical properties of FCCm lattice structures follow the expected exponential curve, and their quasi-elastic gradient and yield strength are above the ones of other bending dominated unit cells in the tested direction.
- Macroscopic 0.2% offset stress does not represent the transition from elastic to plastic deformation of the bulk material for lattice structures. In fact, the relative volume of the bulk material undergoing plastic deformation at macroscopic 0.2% offset stress varies with the relative density.
- The S-N curves of the FCCm unit cell made of HIPed Ti6Al4V were obtained under compressive load and R=10 for different relative densities.
- The Local Stress Method, which has proved valuable for diamond lattices, is also able to predict the fatigue life of FCCm structures within a very wide range of relative densities.
- A stiffness based fatigue failure criterion is presented to ensure structural integrity and load carrying capacity, showing that the Safety Factor depends on the relative density of the structures as well as on stress level.
- The developed fatigue failure surface method accurately describes the fatigue life of FCCm lattices, and its flexibility enables the use of stiffness based fatigue failure criteria.

References

1. Flores, I. *et al.* Implications of lattice structures on economics and productivity of metal powder bed fusion. *Addit. Manuf.* **31**, 100947, DOI: 10.1016/j.addma.2019.100947 (2020).
2. Fleck, N. A., Deshpande, V. S. & Ashby, M. F. Micro-architectured materials: past, present and future. *Proc. Royal Soc. A: Math. Phys. Eng. Sci.* **466**, 2495–2516 (2010).

3. Ashby, M. F. The properties of foams and lattices. *Philos. Transactions Royal Soc. A: Math. Phys. Eng. Sci.* **364**, 15–30, DOI: 10.1098/rsta.2005.1678 (2006).

4. Gibson, L. J. & Ashby, M. F. *Cellular solids structure and properties* (Pergamon Press, 1997).

5. Matlack, K. H. *et al.* Composite 3D-printed metastructures for low-frequency and broadband vibration absorption. *Proc. Natl. Acad. Sci.* **113**, DOI: 10.1073/pnas.1600171113 (2016).

6. Nagesha, B. K. *et al.* Review on characterization and impacts of the lattice structure in additive manufacturing. In *Materials Today: Proceedings*, vol. 21, 916–919, DOI: 10.1016/j.matpr.2019.08.158 (Elsevier Ltd, 2020).

7. Tancogne-Dejean, T., Spierings, A. B. & Mohr, D. Additively-manufactured metallic micro-lattice materials for high specific energy absorption under static and dynamic loading. *Acta Materialia* **116**, 14–28, DOI: 10.1016/J.ACTAMAT.2016.05.054 (2016).

8. Papetti, V. *et al.* Additive Manufactured open cell polyhedral structures as substrates for automotive catalysts. *Int. J. Heat Mass Transf.* **126**, 1035–1047, DOI: 10.1016/j.ijheatmasstransfer.2018.06.061 (2018).

9. Dong, G., Tang, Y., Li, D. & Zhao, Y. F. Design and optimization of solid lattice hybrid structures fabricated by additive manufacturing. *Addit. Manuf.* **33**, 101116, DOI: 10.1016/j.addma.2020.101116 (2020).

10. Barba, D., Alabort, E. & Reed, R. C. Synthetic bone: Design by additive manufacturing. *Acta Biomater.* **97**, 637–656, DOI: 10.1016/j.actbio.2019.07.049 (2019).

11. Deshpande, V. S., Ashby, M. F. & Fleck, N. A. Foam topology: Bending versus stretching dominated architectures. *Acta Materialia* **49**, 1035–1040 (2001).

12. Tancogne-Dejean, T. & Mohr, D. Stiffness and specific energy absorption of additively-manufactured metallic BCC metamaterials composed of tapered beams. *Int. J. Mech. Sci.* **141**, 101–116, DOI: 10.1016/j.ijmecsci.2018.03.027 (2018).

13. Ahmadi, S. M. *et al.* Mechanical behavior of regular open-cell porous biomaterials made of diamond lattice unit cells. *J. Mech. Behav. Biomed. Mater.* **34**, 106–115, DOI: 10.1016/j.jmbbm.2014.02.003 (2014).

14. Al-Ketan, O., Rowshan, R. & Abu Al-Rub, R. K. Topology-mechanical property relationship of 3D printed strut, skeletal, and sheet based periodic metallic cellular materials. *Addit. Manuf.* **19**, 167–183, DOI: 10.1016/j.addma.2017.12.006 (2018).

15. Ruiz de Galarreta, S., Jeffers, J. R. & Ghouse, S. A validated finite element analysis procedure for porous structures. *Mater. Des.* **189**, 108546, DOI: 10.1016/j.matdes.2020.108546 (2020).

16. Cao, X., Duan, S., Liang, J., Wen, W. & Fang, D. Mechanical properties of an improved 3D-printed rhombic dodecahedron stainless steel lattice structure of variable cross section. *Int. J. Mech. Sci.* **145**, 53–63, DOI: 10.1016/j.ijmecsci.2018.07.006 (2018).

17. Amin Yavari, S. *et al.* Relationship between unit cell type and porosity and the fatigue behavior of selective laser melted meta-biomaterials. *J. Mech. Behav. Biomed. Mater.* **43**, 91–100, DOI: 10.1016/j.jmbbm.2014.12.015 (2015).

18. Hanks, B., Berthel, J., Frecker, M. & Simpson, T. W. Mechanical properties of additively manufactured metal lattice structures: Data review and design interface. *Addit. Manuf.* **35**, 101301, DOI: 10.1016/j.addma.2020.101301 (2020).

19. Ahmadi, S. M. *et al.* Fatigue performance of additively manufactured meta-biomaterials: The effects of topology and material type. *Acta Biomater.* **65**, 292–304, DOI: 10.1016/j.actbio.2017.11.014 (2018).

20. Van Hooreweder, B., Apers, Y., Lietaert, K. & Kruth, J. P. Improving the fatigue performance of porous metallic biomaterials produced by Selective Laser Melting. *Acta Biomater.* **47**, 193–202, DOI: 10.1016/j.actbio.2016.10.005 (2017).

21. Karami, K. *et al.* Continuous and pulsed selective laser melting of Ti6Al4V lattice structures: Effect of post-processing on microstructural anisotropy and fatigue behaviour. *Addit. Manuf.* **36**, 101433, DOI: 10.1016/j.addma.2020.101433 (2020).

22. Ahmadi, S. *et al.* From microstructural design to surface engineering: A tailored approach for improving fatigue life of additively manufactured meta-biomaterials. *Acta Biomater.* **83**, 153–166, DOI: 10.1016/j.actbio.2018.10.043 (2019).

23. Benedetti, M. *et al.* Architected cellular materials: A review on their mechanical properties towards fatigue-tolerant design and fabrication, DOI: 10.1016/j.mser.2021.100606 (2021).

24. Yang, L. *et al.* Compression–compression fatigue behaviour of gyroid-type triply periodic minimal surface porous structures fabricated by selective laser melting. *Acta Materialia* **181**, 49–66, DOI: 10.1016/j.actamat.2019.09.042 (2019).

25. Lietaert, K., Cutolo, A. & Van Hooreweder, B. Fatigue life of additively manufactured Ti6Al4V scaffolds under tension-tension, tension-compression and compression-compression fatigue load. *Sci. Reports* **8**, 4957, DOI: 10.1038/s41598-018-23414-2 (2018).

26. Cutolo, A., Neirinck, B., Lietaert, K., de Formanoir, C. & Van Hooreweder, B. Influence of layer thickness and post-process treatments on the fatigue properties of CoCr scaffolds produced by laser powder bed fusion. *Addit. Manuf.* **23**, 498–504, DOI: 10.1016/j.addma.2018.07.008 (2018).

27. Mahmoud, D., Al-Rubaie, K. S. & Elbestawi, M. A. The influence of selective laser melting defects on the fatigue properties of Ti6Al4V porosity graded gyroids for bone implants. *Int. J. Mech. Sci.* **193**, 106180, DOI: 10.1016/j.ijmecsci.2020.106180 (2021).

28. Boniotti, L., Beretta, S., Patriarca, L., Rigoni, L. & Foletti, S. Experimental and numerical investigation on compressive fatigue strength of lattice structures of AlSi7Mg manufactured by SLM. *Int. J. Fatigue* **128**, 105181, DOI: 10.1016/j.ijfatigue.2019.06.041 (2019).

29. Dallago, M., Winiarski, B., Zanini, F., Carmignato, S. & Benedetti, M. On the effect of geometrical imperfections and defects on the fatigue strength of cellular lattice structures additively manufactured via Selective Laser Melting. *Int. J. Fatigue* **124**, 348–360, DOI: 10.1016/j.ijfatigue.2019.03.019 (2019).

30. Wauthle, R. *et al.* Effects of build orientation and heat treatment on the microstructure and mechanical properties of selective laser melted Ti6Al4V lattice structures. *Addit. Manuf.* **5**, 77–84, DOI: 10.1016/j.addma.2014.12.008 (2015).

31. Alaña, M., Lopez-Arancibia, A., Pradera-Mallabiabarrena, A. & Ruiz de Galarreta, S. Analytical model of the elastic behavior of a modified face-centered cubic lattice structure. *J. Mech. Behav. Biomed. Mater.* **98**, DOI: 10.1016/j.jmbbm.2019.05.043 (2019).

32. Maxwell, D. C. & Nicholas, T. A rapid method for generation of a Haigh diagram for high cycle fatigue. In *Fatigue and Fracture Mechanics: 29th Volume* (ASTM International, 1999).

33. Omairey, S. L., Dunning, P. D. & Sriramula, S. Development of an ABAQUS plugin tool for periodic RVE homogenisation. *Eng. with Comput.* **35**, 567–577, DOI: 10.1007/s00366-018-0616-4 (2018).

34. Hedayati, R. *et al.* Isolated and modulated effects of topology and material type on the mechanical properties of additively manufactured porous biomaterials. *J. Mech. Behav. Biomed. Mater.* **79**, 254–263, DOI: 10.1016/j.jmbbm.2017.12.029 (2018).

35. Crupi, V., Kara, E., Epasto, G., Guglielmino, E. & Aykul, H. Static behavior of lattice structures produced via direct metal laser sintering technology. *Mater. Des.* **135**, 246–256, DOI: 10.1016/j.matdes.2017.09.003 (2017).

36. Lozanovski, B. *et al.* Computational modelling of strut defects in SLM manufactured lattice structures. *Mater. Des.* **171**, DOI: 10.1016/j.matdes.2019.107671 (2019).

37. Alaña, M., Cutolo, A., Probst, G., Ruiz de Galarreta, S. & Van Hooreweder, B. Understanding elastic anisotropy in diamond based lattice structures produced by laser powder bed fusion: Effect of manufacturing deviations. *Mater. Des.* **195**, 108971, DOI: 10.1016/j.matdes.2020.108971 (2020).

38. Amin Yavari, S. *et al.* Fatigue behavior of porous biomaterials manufactured using selective laser melting. *Mater. Sci. Eng. C* **33**, 4849–4858, DOI: 10.1016/j.msec.2013.08.006 (2013).

39. de Krijger, J. *et al.* Effects of applied stress ratio on the fatigue behavior of additively manufactured porous biomaterials under compressive loading. *J. Mech. Behav. Biomed. Mater.* **70**, 7–16, DOI: 10.1016/j.jmbbm.2016.11.022 (2017).

40. Kolken, H. *et al.* Fatigue performance of auxetic meta-biomaterials. *Acta Biomater.* **126**, 511–523, DOI: 10.1016/j.actbio.2021.03.015 (2021).

41. Yánez, A., Fiorucci, M. P., Cuadrado, A., Martel, O. & Monopoli, D. Surface roughness effects on the fatigue behaviour of gyroid cellular structures obtained by additive manufacturing. *Int. J. Fatigue* **138**, DOI: 10.1016/j.ijfatigue.2020.105702 (2020).

42. Wu, M. W., Chen, J. K., Lin, B. H. & Chiang, P. H. Improved fatigue endurance ratio of additive manufactured Ti-6Al-4V lattice by hot isostatic pressing. *Mater. Des.* **134**, 163–170, DOI: 10.1016/j.matdes.2017.08.048 (2017).

43. Ren, D. *et al.* Fatigue behavior of Ti-6Al-4V cellular structures fabricated by additive manufacturing technique, DOI: 10.1016/j.jmst.2018.09.066 (2019).

Acknowledgements

The authors are grateful for the financial support for international movility of Fundación Bancaria "La Caixa" and to the "Interne Fondsen KU Leuven/Internal Funds KU Leuven".

Author contributions statement

M.A. and A.C conceived the experiments, M.A. and A.C. conducted the experiments, M.A and S.R analyzed the results, B.V.H supervised the work. All authors reviewed the manuscript.

Competing interest

The authors declare no competing interests.

4.3 Paper C

The title of this paper is 'Additively manufactured lattice structures with controlled transverse isotropy for orthopedic porous implants'. The article develops a semi-analytical model to create transversely isotropic lattices, and studies its applicability in bone tissue engineering, leading to the following contributions:

- The possible design space for transversely isotropic lattices is studied, obtaining a generalized stiffness matrix for any structure under certain assumptions, and proposing three different designs for transverse isotropy.
- The stiffness and strength of the so called VFCCBCC structure is analyzed semi-analytically and numerically, showing good correlation between both models.
- Quasi-static compression experiments with different load orientations were carried out to validate the model.
- The obtained model is able to mimic the anisotropy and stiffness levels of bone in various bone sites, which improves the osseointegration capability of the scaffold.

Additively manufactured lattice structures with controlled transverse isotropy for orthopedic porous implants

Markel Alaña[a,*], Aitziber Lopez-Arancibia[a], Shaaz Ghouse[b], Naiara Rodriguez-Florez[a,c], Sergio Ruiz de Galarreta[a]

[a]*Department of Mechanical Engineering and Materials, Universidad de Navarra, TECNUN Escuela de Ingenieros, Paseo Manuel de Lardizabal, 13, 20018 San Sebastian, Spain*
[b]*Department of Mechanical Engineering, Imperial College London, South Kensington, London SW7 2AZ, UK*
[c]*IKERBASQUE, Basque Foundation for Science, Plaza Euskadi 5, 48009, Bilbao, Spain*

Abstract

Additively manufactured lattice structures enable the design of tissue scaffolds with tailored mechanical properties, which can be implemented in porous biomaterials. The adaptation of bone to physiological loads results in anisotropic bone tissue properties which are optimized for site-specific loads; therefore, some bone sites are stiffer and stronger along the principal load direction compared to other orientations. In this work, a semi-analytical model was developed for the design of transversely isotropic lattice structures that can mimic the anisotropy characteristics of different types of bone tissue. Several design possibilities were explored, and a particular unit cell, which was best suited for additive manufacturing was further analyzed. The design of the unit cell was parameterized and in-silico analysis was performed via Finite Element Analysis. The structures were manufactured additively in metal and tested under compressive loads in different orientations. Finite element analysis showed good correlation with the semi-analytical model, especially for elastic constants with low relative densities. The anisotropy measured experimentally showed a variable accuracy, highlighting the deviations from designs to additively manufactured parts. Overall, the proposed model enables to exploit the anisotropy of lattice structures to design lighter scaffolds with higher porosity and increased permeability by aligning the scaffold with the principal direction of the load.

Keywords: Lattice structures- Transverse isotropy - Orthopedic implants - Additive manufacturing

1. Introduction

The advances in additive manufacturing (AM) in recent years paved the way for the manufacturing of lattice structures [1]. AM includes many different categories such as direct energy deposition (DED), material extrusion or powder bed fusion (PFB), among others [2]. PBF in general, and selective laser melting (SLM) in particular, offers the possibility to produce complex parts with very small feature sizes, which makes it ideal for the manufacturing of scaffolds for bone tissue engineering [3]. Lattice structures may be formed by stochastic patterns or by predefined unit cells that fill the space to form a part [4]. The mechanical properties of such parts can therefore be tuned by adjusting the topology of the lattice structures forming them [5].

This has brought the attention of several fields, including the biomedical [6, 7], since lattice structures may be used as meta-biomaterials for orthopedic implants or bone tissue scaffolds. Bulk metals used for orthopedic implants have an elastic modulus 1 or 2 orders of magnitude higher than host bone [8]. This mismatch of stiffness creates a stress shielding effect, which weakens the bone surrounding the implant, and might lead to implant loosening [8–10]. On the one hand, lattice structures prevent the stress shielding due to their lower stiffness level[11]; and on the other hand, they promote bone ingrowth within the implant due to the interconnected pore network, improving its fixation

*Corresponding authors
Email address: malana@tecnun.es (Markel Alaña)

and stability [12].

Bone tissue exhibits different levels of anisotropy depending on volume fraction and anatomical site [13–16]. Such anisotropy is highly influenced by the mechanoadaptation in bone, which reflects the complex loading environment the bone is subjected to. For example, it has been shown that anisotropy has a profound effect in peri-implant stress and strain in personalized mandibles [17] and maxillas [18], or in the biomechanical behavior of the acetabular cup implant [19]. Thus, matching not only the stiffness levels, but also anisotropy of host bone when designing a lattice structure has the potential to better mimic the mechanical behavior of bone [20]. On the other hand, for bone substitutes in a location where physiological load has a clear principal orientation (such as the proximal tibia [21], the spine [22] or the femur [23], where the loading is predominantly compressive and along the anatomical axis), anisotropy can be used to reduce the density of the lattice structure in the orientations other than the principal one, thus enhancing permeability and mass transport of the scaffold, while maintaining the strength and stiffness levels in the principal direction.

Many studies focus on the design of isotropic metamaterials [24–26], and numerical and experimental studies have been performed to determine the mechanical properties of different lattice structures. Nevertheless, most of the literature is focused on uniaxial load in a unique direction (commonly building direction), while this might not necessarily coincide with the main load direction of the implant. Challis et al. [27] and Xu et al. [28] studied the anisotropy of several lattice structures numerically, and developed some macroscopically isotropic structures. Cutolo et al. [29] and Munford et al. [30] tested different lattice structures in several directions to derive their directional stiffness, and Hossain et al. [31] also designed and tested isotropic stochastic structures. Some analytical models that define the permeability [32] and stiffness [33, 34] of lattice structures have also been developed in the literature. These models implemented together into optimization algorithms can be a powerful tool to design optimal implants considering both the mechanical performance and the fixation of the implant.

One way to obtain lattice structures with a unique principal direction is to develop transversely isotropic lattice structures, which also corresponds to bone tissue in certain locations [35, 36]. In this work a semi-analytical model is developed to design transversely isotropic stretch dominated lattice structures, with prescribed ratios of Young's moduli. This model can be used to design scaffolds that better mimic the patient bone properties to maintain physiological load transfer and to reduce the distortions in stress and strain caused by the implant. The model also enables the design of personalized implants optimized for the anatomical site and patient characteristics. The model was based on previous studies of Hutchinson and Fleck [37], Tancogne-Dejean and Mohr [25], and Messner et al. [24], which were modified to set transverse isotropy as design objective.

2. Materials and Methods

2.1. Semi-analytical model

2.1.1. Elastic behavior

In order to describe the mechanical behavior of a periodic lattice it was assumed that the structures are stretch dominated: the bending and torsion of the beams is neglected, and struts are considered to deform axially and rotate freely at the joints. Under this assumption, the stiffness matrix of any strut based lattice structure can be defined as done by Tancogne-Dejean and Mohr [25] and Messner et al. [24], with Eq. 1, where E_s is the Young's modulus of the constituent material, $l^{(i)}$ is the length of each strut, unit vector $\underline{\boldsymbol{n}}^{(i)}$ represents the strut direction, $A^{(i)}$ is the constant cross-section area of the strut, and V_0 defines the volume of the unit cell.

$$\underline{\underline{\underline{\underline{\boldsymbol{C}}}}} = E_s \sum_{i=1}^{N_{struts}} c^{(i)}\ \underline{\boldsymbol{n}}^{(i)} \otimes \underline{\boldsymbol{n}}^{(i)} \otimes \underline{\boldsymbol{n}}^{(i)} \otimes \underline{\boldsymbol{n}}^{(i)}, \quad \text{where } c^{(i)} = \frac{A^{(i)} l^{(i)}}{V_0} \tag{1}$$

This tensor can be represented in the common 6x6 matrix notation, with each component of the matrix defined as C_{ijkl} obtained from Eq. 1, and assuming an orthotropic material model. Fig. 1 defines the orthogonal directions used as subscripts of the stiffness matrix, together with some important directions defined with the Miller indices [100], [110], [101], [111] and [001], and the isotropic 1-2 plane.

$$\boldsymbol{C} = \begin{bmatrix} C_{1111} & C_{1122} & C_{1133} & 0 & 0 & 0 \\ & C_{2222} & C_{2233} & 0 & 0 & 0 \\ & & C_{3333} & 0 & 0 & 0 \\ & & & C_{2323} & 0 & 0 \\ & sym & & & C_{1313} & 0 \\ & & & & & C_{1212} \end{bmatrix} \tag{2}$$

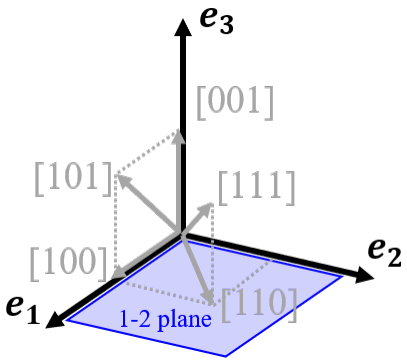

Figure 1: Coordinate system used to define 1, 2 and 3 orientations in the semi-analytical model, main directions according to the Miller indices ([100], [110], [101], [111] and [001]), and 1-2 isotropic plane.

Eq. 3 defines a relevant property of the stiffness matrix: for a stretch dominated lattice structure that fulfills the stated assumptions it can be stated that $C_{iijj} = C_{ijij}$. Thus, the equivalent homogenized metamaterial can be defined with a maximum of six independent material constants, instead of nine as in any generalized orthotropic material.

$$C_{jjkk} = E_s \sum_{i=1}^{N_{struts}} c^{(i)} (n_j^{(i)})^2 (n_k^{(i)})^2 = C_{jkjk} \tag{3}$$

On the other hand, Tancogne-Dejean and Mohr [25] show that under the stated assumptions, the sum of the stiffness matrix components equals the simple relative density (ρ_{simple}) of the structure multiplied by the Young's modulus of the material, as given in Eq. 4 (note that restrictions in Eq. 3 were included):

$$C_{1111} + C_{2222} + C_{3333} + 2C_{1122} + 2C_{1133} + 2C_{2233} = \rho_{simple} E_s \tag{4}$$

In Eq. 4 the parameter ρ_{simple} is defined as the total sum of relative densities of each individual strut, without considering the overlap at the nodes. A correction fit was applied with the form of an exponential curve to enhance the validity of the model, considering that the fraction of the mass at the nodes is not negligible. This fit relates the theoretical ρ_{simple} obtained from the simple sum of volume fractions, and ρ_{real}, which represents the real relative density of the structures:

$$\rho_{simple} = C_D (\rho_{real})^{n_D} \tag{5}$$

As stated above, the 1-2 plane is considered to be isotropic (see Fig. 1). This condition is enforced assuming that the elastic components in direction 1 are equal to the direction 2 ($C_{1111} = C_{2222}$ and $E_1 = E_2$), and that the elastic components in plane 1-3 are equal to the plane 2-3 ($C_{1133} = C_{2233}$, $G_{13} = G_{23}$ and $\nu_{13} = \nu_{23}$). Furthermore, the transverse isotropy condition must hold Eq. 6, which can be simplified by using Eq. 3:

$$C_{1111} - C_{1122} = 2C_{1212} \rightarrow C_{1111} = 3C_{1122} \tag{6}$$

With the imposed restrictions for transverse isotropy, the stiffness matrix can be defined as a function of the effective elastic constants of the structure (E_1, E_3, ν_{12}, ν_{13} and G_{13}) as done in Eq. 7. Note that for isotropy in 1-2

plane $G_{12} = E_1/2(1+\nu_{12})$ must be fulfilled. Thus, Eq. 7 relates the elastic constants with the effective stiffness matrix of the structure. Furthermore, Eq. 6 can also be rewritten in terms of elastic constants, as done in Eq. 8.

$$\boldsymbol{C} = \boldsymbol{S^{-1}} = \begin{bmatrix} \frac{1}{E_1} & \frac{-\nu_{12}}{E_1} & \frac{-\nu_{13}}{E_1} & 0 & 0 & 0 \\ & \frac{1}{E_1} & \frac{-\nu_{13}}{E_1} & 0 & 0 & 0 \\ & & \frac{1}{E_3} & 0 & 0 & 0 \\ & & & \frac{1}{G_{13}} & 0 & 0 \\ & sym & & & \frac{1}{G_{13}} & 0 \\ & & & & & \frac{2(1+\nu_{12})}{E_1} \end{bmatrix}^{-1} \tag{7}$$

$$4\frac{E_3}{E_1}\nu_{13}^2 + 3\nu_{12} - 1 = 0 \tag{8}$$

Equations 4 and 5 and the stiffness matrix symmetries for transverse isotropy can be introduced in Eq. 7 to obtain the stiffness matrix of any stretch dominated transversely isotropic lattice as defined in Eq. 9. Thus, the stiffness of the structures is defined as a function of the Young's modulus of the constituent material (E_s), the ratio between stiffness in principal direction 3 and the transverse plane (E_3/E_1), the Poisson's ratios ν_{12} and ν_{13} (note that Eq. 8 should also be fulfilled), the relative density of the structure (ρ_{real}), and the parameters C_D and n_D.

$$\boldsymbol{C} = \frac{3C_D(\rho_{real})^{n_D}E_s}{4[2+\frac{E_3}{E_1}(1-\nu_{12}+4\nu_{13})]} \begin{bmatrix} 1 & 1/3 & \frac{4}{3}\frac{E_3}{E_1}\nu_{13} & 0 & 0 & 0 \\ & 1 & \frac{4}{3}\frac{E_3}{E_1}\nu_{13} & 0 & 0 & 0 \\ & & \frac{4}{3}\frac{E_3}{E_1}(1-\nu_{12}) & 0 & 0 & 0 \\ & & & \frac{4}{3}\frac{E_3}{E_1}\nu_{13} & 0 & 0 \\ & sym & & & \frac{4}{3}\frac{E_3}{E_1}\nu_{13} & 0 \\ & & & & & 1/3 \end{bmatrix} \tag{9}$$

For a given ρ_{real} and E_3/E_1 ratio, there are infinitely many possible configurations that fulfill the transverse isotropy condition, depending on ν_{12} or ν_{13}. Fig. 2 depicts the directional stiffness for different values of ν_{12}, with constant ρ_{real} and E_3/E_1.

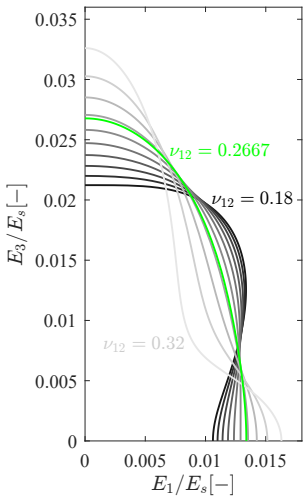

Figure 2: Directional stiffness for constant ρ_{real} and $E_3/E_1 = 2$, and varying ν_{12}.

The parameter ν_{12} was chosen so that the change of stiffness is as smooth as possible. Thus, the directional stiffness fits an ellipse in the 1-3 plane with axes E_1 and E_3, and an equivalent ellipsoid in 3D space (green curve in

Fig. 2). This was done by using the MATLAB Curve Fitting Toolbox, and the obtained results of ν_{12} for different E_3/E_1 ratios are shown in Table 1. Note that $E_3/E_1 = 1$ is a particular case of the model that corresponds to elastically isotropic behavior. The E_3/E_1 ratios were chosen to be of interest for bone substitutes in the proximal tibia, spine and femur [20, 30].

$\boldsymbol{E_3/E_1}$ [-]	1.0	1.25	1.5	1.75	2.0	2.25	2.5	2.75	3.0
$\boldsymbol{\nu_{12}}$ [-]	0.2500	0.2518	0.2560	0.2612	0.2667	0.2722	0.2775	0.2824	0.2870

Table 1: Values of ν_{12} obtained by linear least square approximation as a function of E_3/E_1.

2.1.2. Unit cell design

Eq. 9 defines the stiffness matrix of any transversely isotropic stretch dominated structure, while Eq. 1 relates the stiffness matrix with the geometric variables of the lattice structure: the orientation, length, and cross-section area of the struts ($\underline{\boldsymbol{n}}^{(i)}$, $l^{(i)}$ and $A^{(i)}$, respectively). This can be used to design a unit cell that actually fits in the imposed stiffness matrix. Before obtaining such geometric parameters it is necessary to define a strut configuration that might comply with the imposed restrictions. Furthermore, the parameters C_D and n_D are morphology dependent, and strut configuration must be known to define them. Fig. 3 depicts the process of the design of a transversely isotropic unit cell, with E_3/E_1, ρ_{simple}, Es and strut configuration as input values, and the diameters and aspect ratio (K) as output parameters. The parameter ρ_{real} is an input value once the C_D and n_D coefficients are obtained, but it also can be considered an output value needed to obtain such coefficients for a set of given ρ_{simple} values.

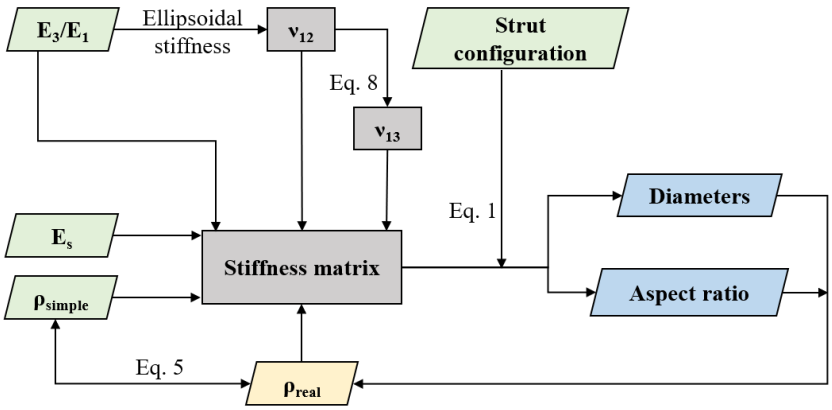

Figure 3: Design process of unit cells under the constraints of transversal isotropy.

Different combinations of well-known unit cells were used to build the structures, namely SC, BCC and FCC. Fig. 4 depicts those unit cells, while each color represents a different diameter value. Note that for SC and FCC two different diameters were assigned in each unit cell, whereas BCC has a unique diameter. These diameters are the design variables that allow the combined unit cells to comply with stiffness matrix in Eq. 9. Furthermore, another design parameter was included among the variables to widen the range of possible designs: the aspect ratio between the height and width of the unit cell, represented as K.

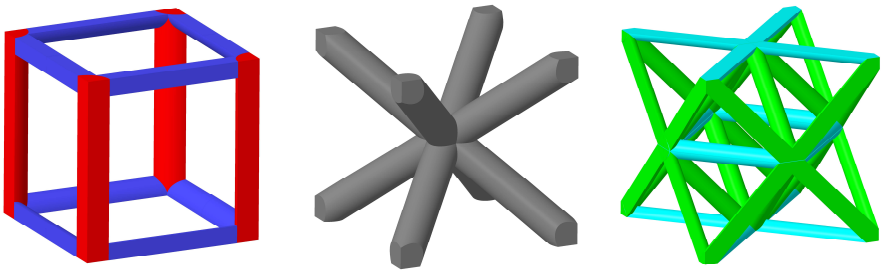

(a) (b) (c)

Figure 4: Basic unit cells to combine in order to form transversely isotropic lattices: a) SC, b) BCC, and c) FCC.

The arrangement of the diameter variables implicitly imposes $C_{1111} = C_{2222}$ and $C_{1133} = C_{2233}$. In addition, it can be proved that any unit cell needs at least 4 design variables to comply with a transversely isotropic stiffness matrix as defined in Eq. 9. Thus, the unit cells in Fig. 4 must be combined so that they offer 4 different design parameters. These are some of the possibilities:

- SC2BCC: SC with 2 diameters, and BCC with a unique diameter. Thus, a variable height to width ratio K is added to comply with transverse isotropy (Fig. 5a).
- SC2FCC2: A combination of SC and FCC unit cells, with two different diameters each (Fig. 5b).
- VFCCBCC: Combination of vertical struts (V), FCC struts out of the isotropic plane and BCC struts, also considering variable height to width ratio K (Fig. 5c).

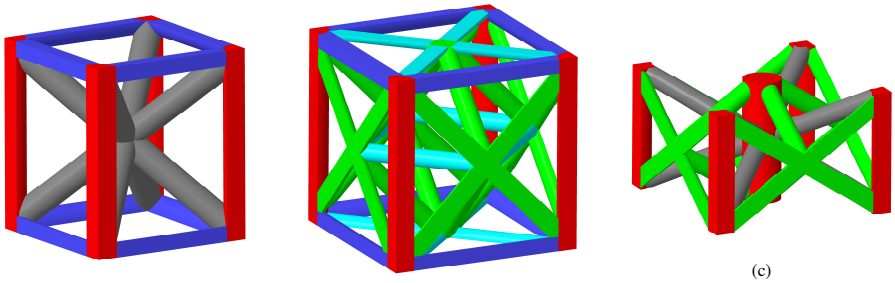

(a) (b) (c)

Figure 5: Unit cells of a) SC2BCC, b) SC2FCC2, and c) VFCCBCC, with each strut color representing a different cross-section variable.

It should be noted that one of the challenges of SLM technology is to fabricate horizontal struts (parallel to the building plate) that guarantee the required quality from a structural point of view. In order to overcome this limitation, the unit cell choice for this study was the VFCCBCC (Fig. 5c) which offers the possibility to orient the mass of the unit cell so that the orientation of the BCC and FCC struts compensate the lack of horizontal struts with their lower angle with respect to the building plane. Therefore, the VFCCBCC unit cell was chosen for the rest of the numerical validation and experimental analysis.

2.1.3. Elastic constants

For a given ρ_{real}, E_3/E_1, and ν_{12} (obtained as in Table 1, and provided that Eq. 8 holds), it is possible to analytically obtain the transversely isotropic stiffness matrix of any of the proposed unit cells, as well as the design parameters (diameters and K) that result in such elastic response.

The elastic behavior of the proposed model depends on the unit cell of the structures due to the adjustment between simple relative density (sum of volume of each strut) and actual relative density (Eq. 5). In order to derive C_D and n_D parameters, different VFCCBCC configurations were designed with different relative densities and E_3/E_1 ratios (it was observed that the latter could be neglected for the relative density adjustment).

Thus, the normalized elastic constants for the VFCCBCC lattice structure (also valid for the other unit cells) are obtained as a function of ρ_{real}, E_3/E_1, and ν_{12} as described below:

$$\frac{E_1}{E_s} = \frac{E_2}{E_s} = C_D(\rho_{real})^{n_D} \frac{(1+\nu_{12})}{4 + \frac{E_3}{E_1}[2(1-\nu_{12}) + 8\nu_{13}]} \tag{10}$$

$$\frac{E_3}{E_s} = C_D(\rho_{real})^{n_D} \frac{\frac{E_3}{E_1}(1+\nu_{12})}{4 + \frac{E_3}{E_1}[2(1-\nu_{12}) + 8\nu_{13}]} \tag{11}$$

$$\frac{G_{13}}{E_s} = \frac{G_{23}}{E_s} = C_D(\rho_{real})^{n_D} \frac{\frac{E_3}{E_1}\nu_{13}}{2 + \frac{E_3}{E_1}[(1-\nu_{12}) + 4\nu_{13}]} \tag{12}$$

The model is semi-analytical because the parameters C_D, n_D and ν_{12} are obtained by least square approximations.

2.1.4. Yield strength

The strength of an implant has to be sufficient to withstand the physiological loads of each bone site, and a predictive tool for the strength of the scaffolds is necessary for their application in orthopedic implants. Thus, a semi-analytical model was developed to define the effective yield strength of the VFCCBCC structure. The stress at each strut under an effective macroscopic stress was calculated using Eq. 13. In this equation the scalar values with superscript (i) correspond to parameters of each strut: $\sigma^{(i)}$ and $\varepsilon^{(i)}$ are the stress and axial strain of the strut (i), respectively, and $\underline{\boldsymbol{n}}^{(i)}$ defines the unit vector of the strut orientation. E_s is the Young's modulus of the constituent material, $\underline{\underline{\boldsymbol{S}}}$ defines the macroscopic compliance matrix of the structure and $\underline{\underline{\boldsymbol{\sigma_{eff}}}}$ corresponds to the macroscopic effective stress applied to the structure.

$$\sigma^{(i)} = E_s\varepsilon^{(i)} = E_s\left[\underline{\underline{\boldsymbol{S}}} : (\underline{\boldsymbol{n}}^{(i)} \otimes \underline{\boldsymbol{n}}^{(i)})\right] : \underline{\underline{\boldsymbol{\sigma_{eff}}}} \tag{13}$$

Thus, each strut of the unit cell will have a different stress level, and it will be proportional to the macroscopic effective stress ($\underline{\underline{\boldsymbol{\sigma_{eff}}}}$). The effective yield strength of the structure is calculated as the macroscopic stress that brings at least one strut to the yield strength of the constituent material ($\sigma_{y,s}$), that is $\sigma^{(i)}_{max} = \sigma_{y,s}$. As occurs with stiffness, the effective yield strength varies depending on the orientation of the load. To obtain the directional effective yield strength of the structures, denoted as $\sigma_{eff,y}$, a uniaxial $\underline{\underline{\boldsymbol{\sigma_{eff}}}}$ was applied in various orientations covering all the 3D space, and the magnitude $\sigma_{eff,y}$ was calculated to induce $\sigma_{y,s}$ stress level in the struts.

2.2. Numerical validation

The accuracy of the semi-analytical model and the effect of the relative density on the unit cell was studied with several numerical models built in Abaqus 2020 (Dassault Systems). 9 different unit cells were modeled for each E_3/E_1 ratio with relative densities varying from 1% to 30%, and E_3/E_1 ratios of 1.5, 2, and 3. The relative density of the structures was defined to ensure a high porosity range of the implants needed in scaffold design [38, 39]. Figure 6 depicts some of the analyzed structures with different relative densities. The models where meshed with second order tetrahedral elements and after conducting a mesh sensitivity analysis, the diameter/element size ratio was set to 5 for all the structures.

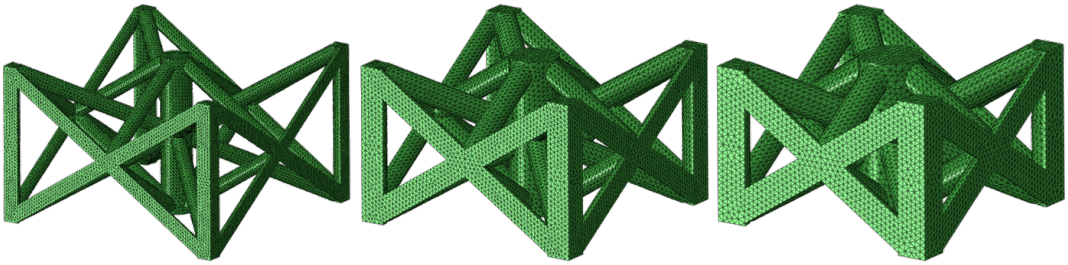

Figure 6: Numerical models of the VFCCBCC unit cell with $E_3/E_1 = 2$ and varying relative densities of 0.09, 0.2 and 0.3.

The material properties of 316L stainless steel were modeled as a bilinear material model, with values given in Table 2 [40].

Young's modulus [GPa]	Poisson's ratio [-]	Yield strength [MPa]	Tangent modulus [MPa]
190	0.3	453	260

Table 2: Material properties for FE model.

Periodic Boundary Conditions (PBC) were applied and the code of Omairey [41] was used to get the elastic constants of the VFCCBCC unit cell. Apart from the elastic and shear moduli, the accuracy of the semi-analytical model was also assessed by the E_3/E_1 ratio, as well as the Zener ratio in the 1-2 plane, which gives the measure of elastic isotropy:

$$Z_{12} = \frac{2C_{1212}}{C_{1111} - C_{1122}} \tag{14}$$

On the other hand, uniaxial stress was applied in directions [001], [110], [101], [111], [100] in the VFCCBCC unit cell with different relative densities, and under PBC to numerically calculate the yield strength of the structure.

The criteria to numerically determine the yield strength of the structure had to be adapted from the one used for the analytical model, where the struts were treated as axially loaded beams with a constant stress through the strut. Instead, the criteria to numerically determine the yield stress of the structure was to find the macroscopic stress value where the plastic dissipation energy exceeded 10% of the total energy of the structure, similarly to [25]. The results were compared to the semi-analytically obtained yield strength values.

2.3. Manufacturing

VFCCBCC structures were produced with $E_3/E_1 = 2$ and two different relative densities, 12.5% and 25%, to be tested in three different orientations, namely [100], [110] and [001]. To test 3 samples per density and load orientation, a total of 18 parts were manufactured. Unit cell size was 3mm, and the manufacturing orientation was the same in all cases to maintain the orientation of every strut with respect to the build plate and prevent unequal imperfection distributions between batches.

All specimens were manufactured on an AM250 metal powder bed fusion machine (Renishaw Plc.) under an inert argon atmosphere from Stainless Steel 316L directly onto a mild steel substrate. The parts were removed from the plate by electro discharge machining. Build files for the specimens were generated from an in-house piece of software, described previously in [42]. The software allows lattices to be defined in a beam format (start and end x,y,z positions) with a desired diameter. Based on the strut angle and desired diameter, laser parameters are assigned accordingly. Laser parameters were assigned to produce the struts of diameter described in Table 3.

The relative density of the produced specimens was measured by weighing the structures and dividing by the theoretical weight of a solid part with the external volume of the structures. On the other hand, to measure strut

		Diameters [mm]		
Structure	**Relative density [%]**	**Vertical (angle)**	**FCC (angle)**	**BCC (angle)**
A	12.5	0.47 (90.0)	0.22 (33.0)	0.23 (24.7)
B	25.0	0.70 (90.0)	0.33 (33.0)	0.35 (24.7)

Table 3: Diameters of manufactured structures for both relative densities.

density Archimedes method was used as done in other studies [43]. This method consists in measuring the weight difference of the part when submerged into ethanol compared to a dry environment (in air) to determine the proportion of internal pores. Eq. 15 defines the strut density (ρ_{strut}) as a function of the weight of the structure in air (w_{air}), the density of ethanol ($\rho_{ethanol}$), the density of 316L stainless steel (ρ_{316L}) and the weight of the structure in ethanol ($w_{ethanol}$).

$$\rho_{strut} = \frac{w_{air}\,\rho_{ethanol}}{\rho_{316L}\,(w_{air} - w_{ethanol})} \tag{15}$$

2.4. Mechanical testing

Compression tests were carried out as per ISO 13314:2011 [44] in an Instron 3360 with a load cell of 30kN except for the structure B in [001] orientation, which was tested in a Instron 5982 with a load cell of 100kN due to its higher strength. The tests were performed in three different orientations for each relative density: [001], [100] and [110]. For each relative density and orientation 3 specimens were tested. The strain was calculated after measuring the compliance of the machines. For each specimen quasi-elastic gradient and 0.2% offset stress (yield strength) was calculated.

3. Results

3.1. Semi-analytical model

Fig. 7 depicts the simple relative density (ρ_{simple}) of the VFCCBCC structure as a function of its real relative density (ρ_{real}). The ρ_{real} values were obtained from CAD measurements of models with different E_3/E_1 ratios. The C_D and n_D values derived by least square approximation ($R^2 = 0.999$) are 1.65 and 1.169, respectively. The values for the SC2BCC and SC2FCC2 are displayed in Table S1 (supplementary material).

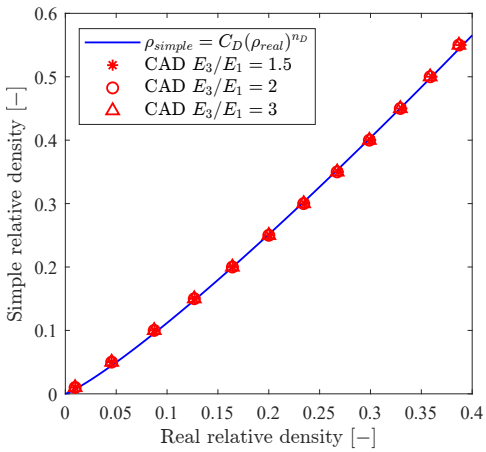

Figure 7: Designed VFCCBCC structures with different relative densities and E_3/E_1 values, and adjusted curve.

Fig. 8 shows the yield surface of VFCCBCC unit cells for uniaxial loads in any orientation. The surfaces for $E_3/E_1 = 1.5$, $E_3/E_1 = 2$, and $E_3/E_1 = 3$ are depicted, which are in the bone range (spine trabecular [22], proximal

tibia [21] or femur cortical bone [23]). Effective yield strength ($\sigma_{eff,y}$) is obtained from Eq. 13, and normalized with the density variable $C_D(\rho_{real})^{n_D}$ and the yield strength of the constituent material ($\sigma_{y,s}$). It can be observed that for any E_3/E_1 ratio, the structure is weaker in the directions that coincide with strut orientations, because the load is primarily carried by a single strut. On the contrary, in other orientations the load is more effectively distributed among struts. The effective strength in the transverse plane reduces with the increase of E_3/E_1 ratio, while the strength in [001] increases.

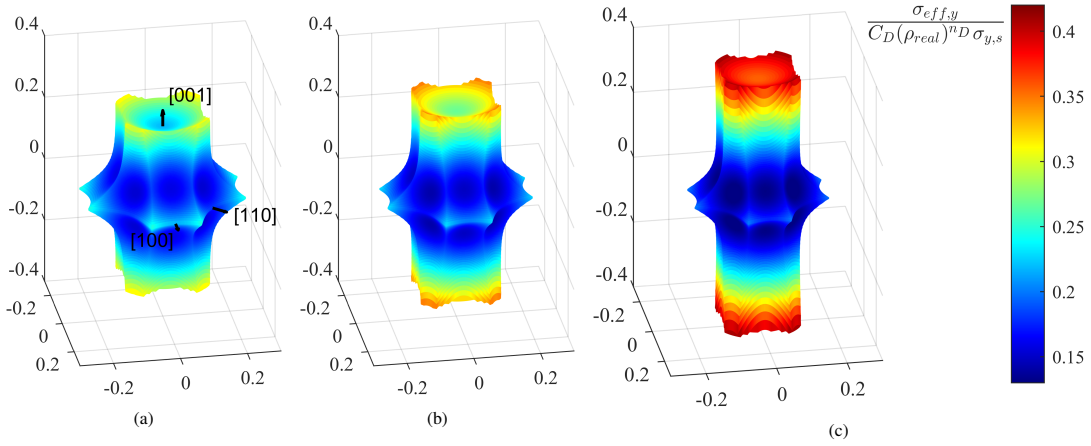

Figure 8: Semi-analytical yield surface of VFCCBCC in 3D space obtained from Eq. 13 with a) $E_3/E_1 = 1.5$, b) $E_3/E_1 = 2$, and c) $E_3/E_1 = 3$.

Fig. 9 depicts the values of normalized yield strength of VFCCBCC for different E_3/E_1 ratios, under [001] and [110] orientations, since the latter is the weakest orientation in the transverse plane. Thus, the effective yield strength of the structure can be directly calculated for any relative density by multiplying the normalized strength value with the yield strength of the constituent material. The strength ratio between the [001] and [110] plane is always lower than the E_3/E_1 ratio, with values of 1.21, 1.60 and 2.41 for E_3/E_1 of 1.5, 2, and 3, respectively.

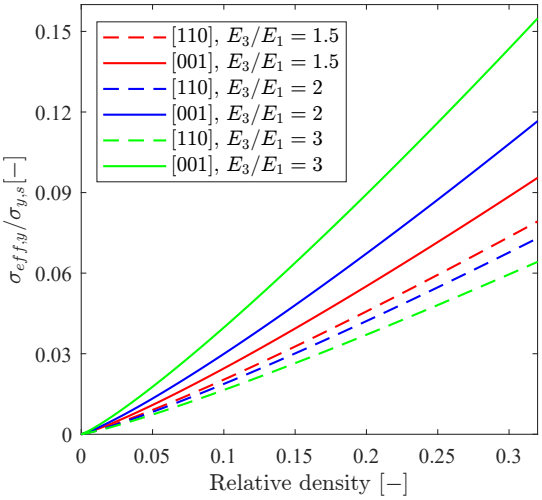

Figure 9: Yield strength of VFCCBCC for [110] (weakest orientation in transverse plane) and [001] orientations, for different E_3/E_1 ratios.

3.2. Finite element validation

3.2.1. Elastic behavior

The results of the numerical simulations of VFCCBCC unit cells with $E_3/E_1 = 1.5$, $E_3/E_1 = 2$, $E_3/E_1 = 3$ are depicted in Fig. 10, showing the elastic constants E_1, E_3, G_{12}, G_{13}, ν_{12}, and ν_{13}, and comparing the obtained values with the semi-analytical model obtained from Equations 8, 10-12. In general, a very good agreement between the FE analysis and the semi-analytical model can be observed, especially for low relative densities, and the error increases with the relative density.

In the case of effective Young's modulus, E_3 is more accurate than E_1 for any E_3/E_1 ratio. The R^2 coefficients for E_1 lay between 0.885 and 0.941, whereas for E_3 the R^2 values are higher than 0.989 for any E_3/E_1 ratio. This occurs because the assumption of pure axial stress is better fulfilled in [001] orientation due to the vertical struts of the VFCCBCC unit cell, while for [100] this assumption is not as valid for moderate relative densities. As a result, the maximum relative error arises for the highest studied relative density of 0.3. In this case, the maximum error of E_1 is 22.8% for $E_3/E_1 = 3$, and in the case of E_3 the maximum relative error is 7.8% for $E_3/E_1 = 1.5$.

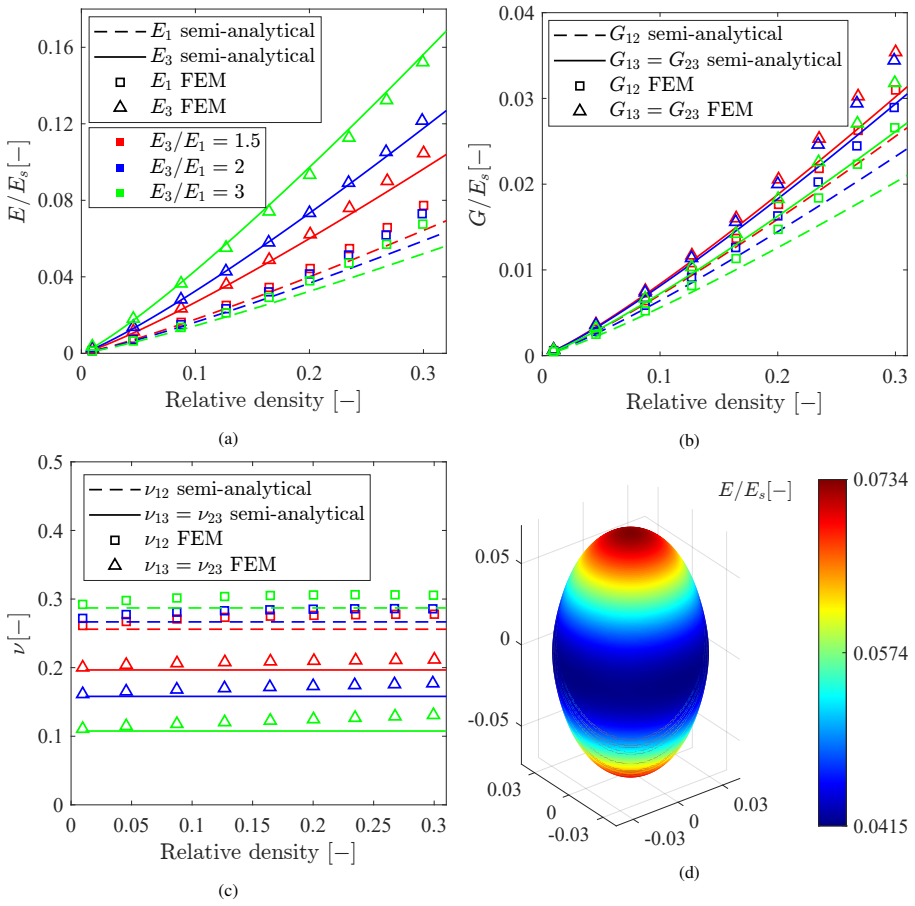

Figure 10: Semi-analytical and FEM comparison of the elastic behavior of VFCCBCC unit cell for $E_3/E_1 = 1.5$, $E_3/E_1 = 2$ and $E_3/E_1 = 3$: a) Young's moduli, b) shear moduli, c) Poisson's ratios. d) is the directional homogenized stiffness for $E_3/E_1 = 2$.

The accuracy of the shear moduli is lower than for Young's moduli. For G_{12} the R^2 value is between 0.878 ($E_3/E_1 = 3$) and 0.938 ($E_3/E_1 = 1.5$), while G_{13} has R^2 coefficients between 0.930 ($E_3/E_1 = 3$) and 0.954 ($E_3/E_1 = 1.5$). For $\rho_{real} = 0.3$, the maximum relative error for G_{12} is 23.8% and for G_{13} equals 17.7% ($E_3/E_1 = 3$ in both cases). For Poisson's ratios, the maximum error values of ν_{12} are 7.9%, 6.7% and 6.1% for $E_3/E_1 = 1.5$,

$E_3/E_1 = 2$ and $E_3/E_1 = 3$, respectively, and 7.2%, 10.7% and 17.8% for ν_{13}. Fig. 10d depicts the 3D stiffness of the FE model with a $\rho_{real} = 0.2$ and $E_3/E_1 = 2$. The directional stiffness has the expected ellipsoidal shape, the change in stiffness is smooth and the variability in the 1-2 plane is very small (below 0.1%).

As depicted in Fig. 11a, the accuracy of the E_3/E_1 ratio is very high for low relative densities, but decreases with increased relative density for any of the studied cases. This is a consequence of the bending that increases the stiffness more in direction [100] compared to [001], as also observed in Fig. 10a. Furthermore, as prescribed E_3/E_1 increases, the error of the semi-analytical model also increases. For $\rho_{real} = 0.3$, the relative errors of E_3/E_1 are 10.7%, 20% and 33.1% for $E_3/E_1 = 1.5$, $E_3/E_1 = 2$, and $E_3/E_1 = 3$ respectively. On the other hand, the Zener ratio in the 1-2 plane, which measures the elastic isotropy in the plane, and defined in Eq. 14, is depicted in Fig. 11b for the three E_3/E_1 ratios, showing that the transverse isotropy is maintained with a relative error below 2.8% for any studied relative density and E_3/E_1 ratio. This suggests that the stiffness added by the bending of struts acts uniformly in the 1-2 plane.

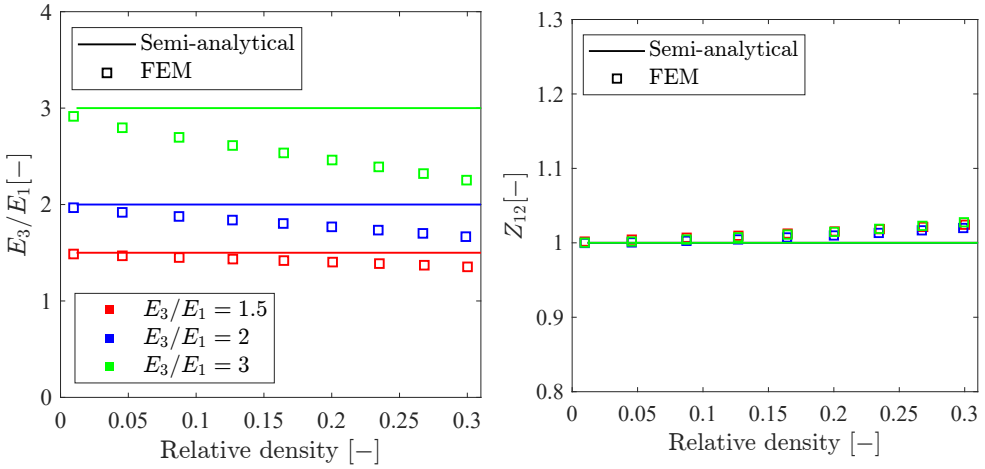

Figure 11: Semi-analytical and FEM comparison of the elastic behavior of VFCCBCC unit cell for $E_3/E_1 = 1.5$, $E_3/E_1 = 2$ and $E_3/E_1 = 3$: a) E_3/E_1 ratio, and b) Zener ratio.

Fig. 12 depicts the Von Mises stress of the VFCCBCC unit cell under pure shear load in the 1-2 plane for two relative densities. The stress of the loaded struts is closer to the assumption of uniaxial uniform stress for thin struts, while in thick struts the bending loads induce non-uniform stresses along the struts. Furthermore, the strut joints have more relevance for higher relative densities, and triaxial stress states arising there affect a larger part of the structure. This explains the gradual loss of accuracy as the relative density increases.

The relative importance of the bending load also depends on the load type and orientation: the loads or deformations aligned with struts result in lower bending loads, which explains the variability of the accuracy for different elastic constants and yield strengths for the same relative density.

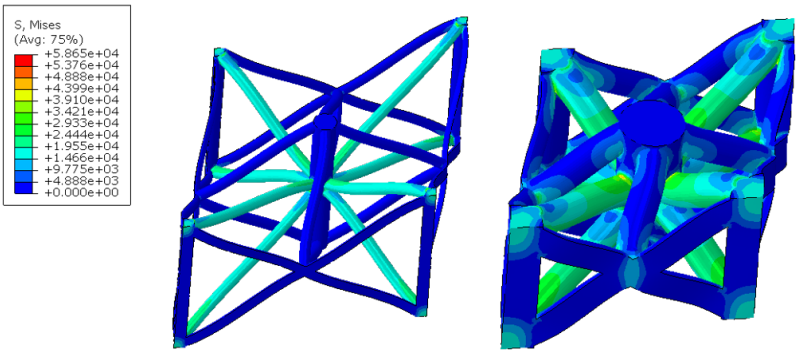

Figure 12: Von Mises stress of VFCCBCC unit cells with different relative densities under shear load in 1-2 plane.

3.2.2. *Yield strength*

The accuracy of the semi-analytical model (Eq. 13) to predict the yield strength of the VFCCBCC unit cell varies depending on the load orientation, the E_3/E_1 ratio and the relative density. Fig. 13 shows the yield strength for 5 different orientations, defined as in Fig. 1, and for $E_3/E_1 = 1.5$, $E_3/E_1 = 2$, and $E_3/E_1 = 3$. The semi-analytical yield model has the highest accuracy for [001] and [110] orientations, with R^2 values above 0.993 and 0.997, respectively, regardless E_3/E_1 ratios. In orientations [101] and [111] the semi-analytical model slightly underestimates the strength of the structures, but the R^2 coefficients indicate high correlation with minimum values of 0.969 for [101] and 0.955 for [111] for any E_3/E_1 stiffness ratio. On the other hand, the semi-analytical model overestimates the strength in [100] orientation, and the R^2 coefficient increases with E_3/E_1 ratio, with $R^2 = 0.888$ for $E_3/E_1 = 1.5$ and $R^2 = 0.919$ for $E_3/E_1 = 3$.

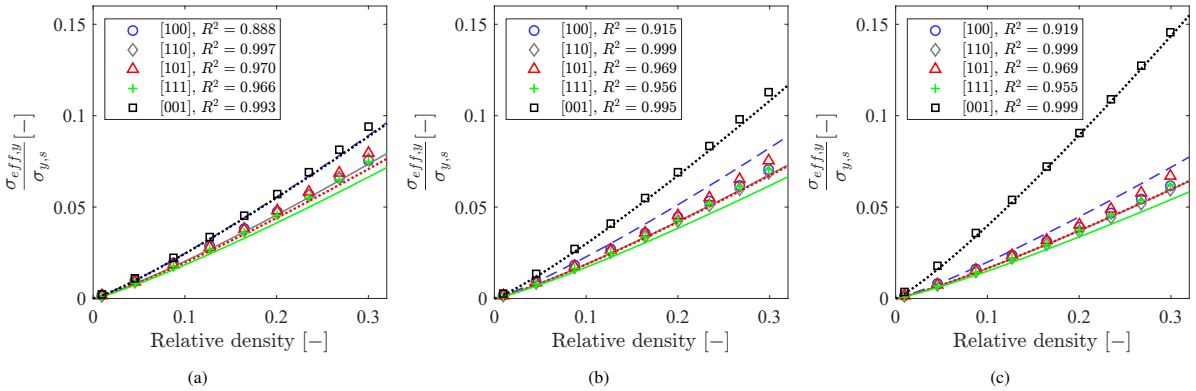

(a) (b) (c)

Figure 13: Effective yield strength of VFCCBCC unit cell in various orientations, normalized with constituent material yield strength, and for different E_3/E_1 ratios: a) $E_3/E_1 = 1.5$ b) $E_3/E_1 = 2$, c) $E_3/E_1 = 3$.

3.3. *Mechanical testing*

3.3.1. *Morphology of specimens*

Specimens of two prescribed relative densities were produced, 12.5% and 25%, and the resulting relative density and strut density properties are given in Table 4. The average differences between the designed and manufactured relative densities were of 2.2% in batch A and 7.3% in batch B. Even if the manufacturing parameters were the same within each batch, a significant variability (relative variability above 10% with respect to the designed value) of the produced relative densities can be observed in batch B. The strut density is above 98% in all cases, indicating some prevalence of internal pores.

Specimen	Relative density [%]	Strut density [%]
A-[001]	9.77 ± 0.46	98.67 ± 0.58
A-[100]	10.27 ± 0.40	98.45 ± 0.22
A-[110]	9.28 ± 0.40	98.63 ± 0.61
B-[001]	19.44 ± 0.06	99.15 ± 0.17
B-[100]	16.47 ± 0.27	98.88 ± 0.12
B-[110]	17.30 ± 0.69	98.98 ± 0.02

Table 4: Relative density and strut density values for produced specimens.

Fig. 14 depicts the actual morphology of the struts, indicating clear deviations from the designed CAD geometry. An important waviness can be observed, especially in the struts with lower angles with respect to the build plate. Moreover, in the thinnest struts the staircase effect that arises from the layer by layer manufacturing process is clearly visible, and this effect is enhanced by the fact that the struts were produced point by point.

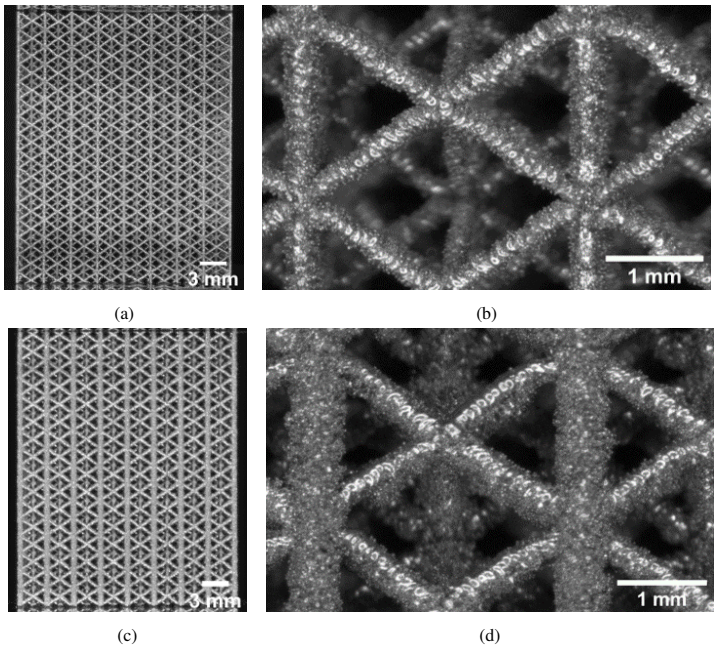

Figure 14: Manufactured specimens of VFCCBCC structures for loading in [001] corresponding to batch A a) and b), and batch B c) and d).

3.3.2. Quasi-static compression

The curves obtained from quasi-static compression tests are given in Fig. 15. Fig. 15a and 15b correspond to the batch A, and Fig. 15c and 15d depict the compression curves of batch B. The shaded areas in Figures 15a and 15c represent the 95% confidence interval, and Fig. 15b and 15d depict a close-up of the compression curves up to a strain of 0.06, in order to give a better insight into the elastic response of the structures. The stress-strain curves present a expected shape for ductile metals, with a linear region, followed by the yielding of the structures and an energy absorption process up to densification of the structures. The variability within each sample is much higher in the batch A as shown in Fig. 15a. Furthermore, its lower relative density results in a compression process dominated by buckling with more peaks and valleys.

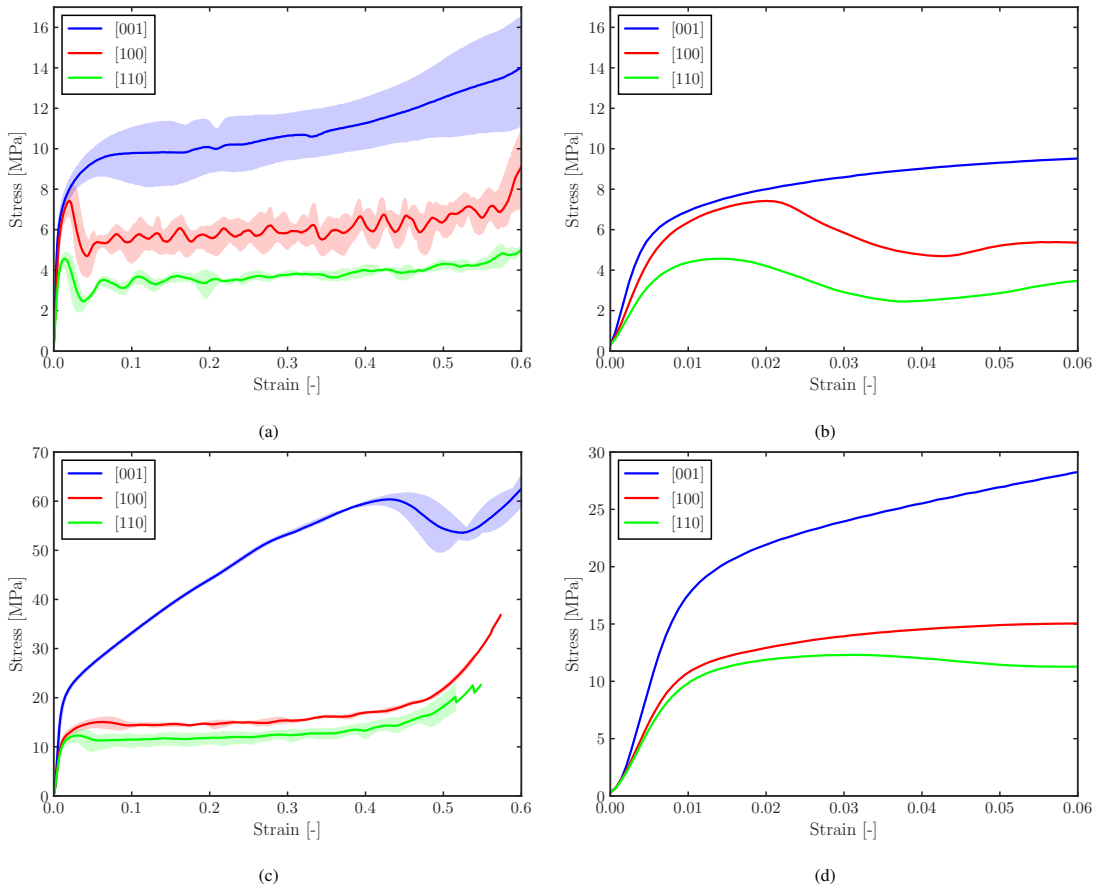

Figure 15: Stress-strain curves of specimens under [001], [100] and [110] load directions for batch A a) until densification and b) until $\varepsilon = 0.06$; and batch B c) until densification and d) until $\varepsilon = 0.06$.

	A			**B**		
	[001]	**[100]**	**[110]**	**[001]**	**[100]**	**[110]**
Quasi-elastic gradient [GPa]	1.55 ± 0.22	1.00 ± 0.07	0.70 ± 0.03	2.94 ± 0.28	1.51 ± 0.03	1.37 ± 0.05
σ_y [MPa]	6.04 ± 0.24	5.83 ± 0.39	3.83 ± 0.47	17.37 ± 0.2	10.64 ± 0.7	9.77 ± 0.8

Table 5: Results of quasi-static compression tests for batches A and B in directions [001], [100] and [110].

The obtained mechanical properties are listed in Table 5. For both relative densities the quasi-elastic gradient in direction [001] clearly exceeds the gradient in directions [100] and [110], as would be expected from the design of the structures.

Fig. 16 depicts the anisotropy characteristics of the semi-analytical and numerical models, compared to the experimental values in structures A and B. The E_{110}/E_1 and E_3/E_1 ratios are lower than the analytical values for both manufactured structures, nonetheless, the structure B is in good agreement with the prescribed values (relative error of 3% for E_3/E_1 and 10% for E_{110}/E_1). While the accuracy of the numerical model decreases with higher relative densities (see E_3/E_1 ratios in FEM), this also enables a reduced imperfection level of the manufactured structures,

thus reducing the error of the anisotropy with respect to the semi-analytical model (experimental E_3/E_1 and E_{110}/E_1 ratios).

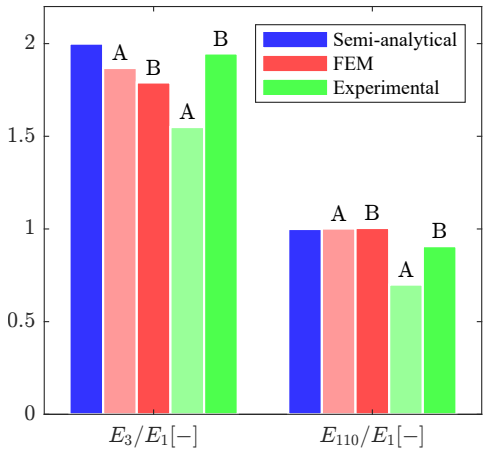

Figure 16: Elastic moduli ratios for semi-analytical model and numerical and experimental values of structures A and B.

4. Discussion

4.1. Validity of semi-analytical model

In this work a semi-analytical model was developed to design transversely isotropic porous structures. The model shows good correlation with numerical results, even if the overall accuracy decreases for higher relative densities and E_3/E_1 ratios. This deviation can be attributed to the arise of bending loads and stress triaxialities as the slenderness of the struts decreases.

Experimental tests were also carried out with structures A and B, but the absolute mechanical properties are not compared directly to the values predicted by the semi-analytical and numerical models, since the manufacturing imperfections of the VFCCBCC unit cell cause an important decrease of stiffness and strength. These imperfections include strut waviness, dross formation, surface roughness, etc. These types of deviations are more common when manufacturing thin struts or small unit cell sizes and their detrimental effect on mechanical properties has been broadly studied [45–47]. Moreover, these imperfections may change the anisotropy characteristics of the lattice structures [29, 48], as can be observed by comparing the A and B structures.

The similarity of the experimental anisotropy levels of structure B with designed values compared to the structure A might be attributed to lower imperfection levels due to larger strut diameters for structure B. This indicates that the semi-analytical model can be used to design unit cells with prescribed anisotropy. Furthermore, the good agreement between analytical and numerical models suggests that reducing the level of imperfection e.g. increasing unit cell size, the absolute mechanical properties of the structures can be better predicted.

4.2. Patient-specific scaffold design

The developed semi-analytical model enables to design scaffolds that mimic various stiffness ratios that appear in bone tissue. Thus, patient-specific bone volume fraction and anisotropy can be used as input values to design implants with equivalent stiffness in different directions, reducing peri-implant stress and strain distortions. Furthermore, with the obtained model, different elastic moduli can be achieved in the principal direction for a prescribed porosity by varying the E_3/E_1 ratio, while for regular lattice structures each porosity value corresponds to a unique value of elastic modulus (Gibson-Ashby model [49]).

This feature can be used to implement the model in the biomedical sector, specifically for the design of patient-specific implants. To show the utility of this model for implant applications, three case studies are depicted in Fig. 17: a) knee replacement in proximal tibia, b) spine cancellous bone, and c) load bearing cortical bone in different sites, such as femur. The colored surfaces represent the possible E_1 and E_3 values of the semi-analytical model for each value of relative density, while the grey areas correspond to the stiffness of bones in literature. A different parent material was chosen for each site to better match the target elastic properties, while also considering biocompatibility of the materials: Ti6Al4V for knee replacement, PEEK for spine cancellous bone, and CoCr for various cortical bones.

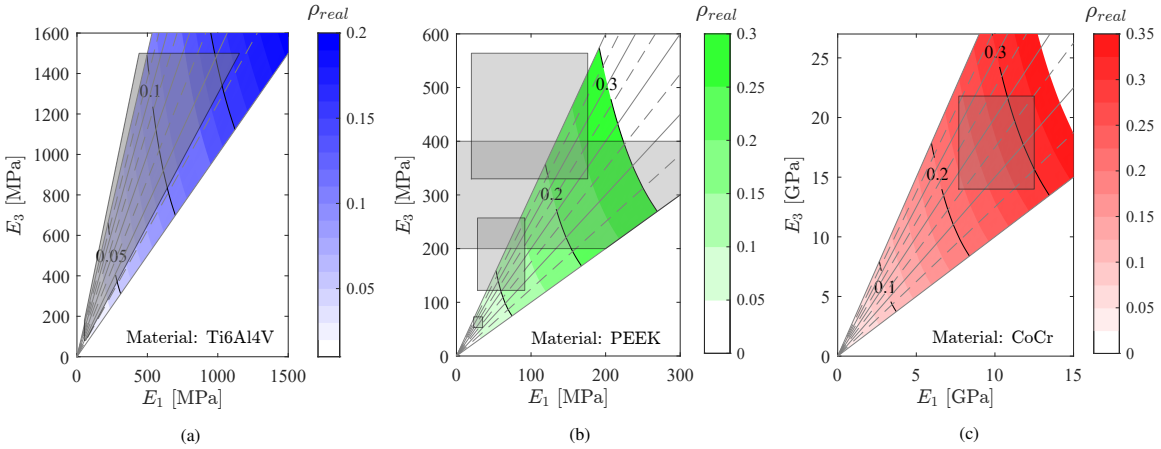

Figure 17: Stiffness values in main and transverse orientations in implants for a) proximal tibia [30], b) spine [16, 22, 50, 51], and c) load bearing cortical bone [9].

Knee replacements are in the increase due to the prevalence of osteoarthritis in the knee joint. The proximal tibia, which is replaced by this surgery, is mainly loaded in compression along the anatomical axis; thus, the design of knee implants should be based on bone elastic modulus in that direction (81 and 1500 MPa) with a degree of anisotropy ranging from 1.3 to 3.4 [21]. Fig. 17a shows the possible design space of the semi-analytical model to match the stiffness range of the proximal tibia in E_1 and E_3. The model covers a great part of the proximal tibia stiffness range, even if the manufacturing below relative densities of 0.1 can be challenging, and possibly larger unit cell sizes are required for such designs. It must be noted that a Young's modulus of 37.5 GPa was given to the Ti6Al4V parent material. This low modulus is a result of tensile tests of micro-struts to implicitly consider the manufacturing deviations of strut-based lattice structures [52].

The spine is also mainly loaded along its anatomical axis, and its cancellous bone can have a wide range of stiffness values according to different studies, with E_3/E_1 ratios as high as 7.3 [16, 22, 50, 51]. In this case, PEEK (E = 4 GPa) was chosen as parent material to match the elastic behavior of the spine. The design space of the semi-analytical model covers most of the E_3 stiffness ranges within relative densities between 0.1 and 0.3, as depicted in Fig. 17b. On the other hand, some of the E_3/E_1 ratios of the spine exceed the design space of the transversely isotropic model. In these cases it is possible to match the E_3 stiffness along the anatomical axis, at the cost of having a higher E_1 value in the transverse plane.

The cortical bone is transversely isotropic due to its microstructure, which is formed by aligned osteons that give superior stiffness along the diaphyseal axis, and inferior isotropic stiffness in the transverse plane [9, 23, 53]. For Fig. 17c CoCr (E=200 GPa) was assigned as parent material to enhance the stiffness of the design space of the semi-analytical model and mimic the elastic behavior of cortical bone. Thus, the model perfectly covers the E_3 and E_1 values found in literature, even if in some cases high relative densities above 0.3 are required. On the other hand, these stiffness values are expected for perfectly manufactured structures, which is rarely the case in additively manufactured scaffolds. The unit cell size should be increased to have larger features to be manufactured with a reduced

imperfection level to reach stiffness levels predicted by the model.

The transversely isotropic scaffolds aligned with the main load direction allow the design of lighter implants due to the reduced mass in the transverse direction. This also means that higher permeability can be achieved, enhancing bone ingrowth and vascularization within the implant while ensuring necessary stiffness and strength in the direction of the main load. This model could be implemented into optimization algorithms with other analytical models describing the permeability of the structure to design optimal and personalized implants based on the bone site and characteristics of the bone patient [32]. Moreover, the established relationship between the morphology of stretch dominated lattice structures and their orthotropic effective stiffness matrix enables optimization-based design to tailor the stiffness of different bone sites while also considering bone site specific anisotropy.

5. Conclusions

A semi-analytical model was developed to design transversely isotropic lattice structures with prescribed stiffness ratios between the longitudinal and transverse directions. Numerical and experimental analyses were performed to test the validity of the designs, and the main conclusions are as follows:

- The developed semi-analytical model effectively describes a transversely isotropic elastic behavior, with ellipsoidal directional stiffness, which enables the design of unit cells with prescribed anisotropy.
- The obtained semi-analytical model is capable of mimicking the stiffness and anisotropy of different bone sites such as proximal tibia, spine or femoral cortical bone. By correctly aligning the scaffold with the principal directions of the bone, a higher porosity of the scaffolds can be achieved compared to other isotropic counterparts.
- Many possible strut configurations are available to obtain a prescribed transverse isotropy. This work analyzed the VFCCBCC unit cell in more detail, and SC2BCC and SC2FCC2 were also presented as viable for transverse isotropy.
- The elastic constants obtained from numerical models of VFCCBCC unit cell are in good agreement with the semi-analytical model. The accuracy of the model decreases with an increase of relative density, and higher E_3/E_1 ratios also have a detrimental effect.
- Quasi-static compressive tests indicate that prescribed anisotropy can be achieved with the VFCCBCC unit cell, even if for lower relative densities the deviations from designed parameters increase due to the manufacturing defects.

Declaration of competing interest

The authors declare that they have no known competing financial interests or personal relationships that could have appeared to influence the work reported in this paper.

Acknowledgement

This research did not receive any specific grant from funding agencies in the public, commercial, or not-for-profit sectors.

References

[1] M. Leary, M. Mazur, J. Elambasseril, M. Mcmillan, T. Chirent, Y. Sun, M. Qian, M. Easton, M. Brandt, Selective laser melting (SLM) of AlSi12Mg lattice structures, Materials & Design 98 (2016) 344–357. doi:10.1016/j.matdes.2016.02.127.

[2] A. Azarniya, X. G. Colera, M. J. Mirzaali, S. Sovizi, F. Bartolomeu, M. k. St Weglowski, W. W. Wits, C. Y. Yap, J. Ahn, G. Miranda, F. S. Silva, H. R. Madaah Hosseini, S. Ramakrishna, A. A. Zadpoor, Additive manufacturing of Ti–6Al–4V parts through laser metal deposition (LMD): Process, microstructure, and mechanical properties, Journal of Alloys and Compounds 804 (2019) 163–191. doi:10.1016/J.JALLCOM.2019.04.255.

[3] I. Gibson, D. Rosen, B. Stucker, Powder bed fusion processes, in: Additive manufacturing technologies, Springer, 2015, pp. 107–145.

[4] Ashby M.F, The properties of foams and lattices, Philosophical Transactions of the Royal Society A: Mathematical, Physical and Engineering Sciences 364 (1838) (2006) 15–30. doi:10.1098/rsta.2005.1678.

[5] V. S. Deshpande, M. F. Ashby, N. A. Fleck, Foam topology: Bending versus stretching dominated architectures, Acta Materialia 49 (2001) 1035–1040. doi:10.1016/S1359-6454(00)00379-7.

[6] T. Maconachie, M. Leary, B. Lozanovski, X. Zhang, M. Qian, O. Faruque, M. Brandt, SLM lattice structures: Properties, performance, applications and challenges (dec 2019). doi:10.1016/j.matdes.2019.108137.

[7] H. Chen, Y. Liu, C. Wang, A. Zhang, B. Chen, Q. Han, J. Wang, Design and properties of biomimetic irregular scaffolds for bone tissue engineering, Computers in Biology and Medicine 130 (2021) 104241. doi:10.1016/J.COMPBIOMED.2021.104241.

[8] E. Davoodi, H. Montazerian, A. S. Mirhakimi, M. Zhianmanesh, O. Ibhadode, S. I. Shahabad, R. Esmaeilizadeh, E. Sarikhani, S. Toorandaz, S. A. Sarabi, R. Nasiri, Y. Zhu, J. Kadkhodapour, B. Li, A. Khademhosseini, E. Toyserkani, Additively manufactured metallic biomaterials, Bioactive Materials 15 (2022) 214–249. doi:10.1016/J.BIOACTMAT.2021.12.027.

[9] X. Wang, S. Xu, S. Zhou, W. Xu, M. Leary, P. Choong, M. Qian, M. Brandt, Y. M. Xie, Topological design and additive manufacturing of porous metals for bone scaffolds and orthopaedic implants: A review, Biomaterials 83 (2016) 127–141.

[10] R. S. Abass, M. Al Ali, M. Al Ali, Shape and topology optimization design for total hip joint implant, in: Proceedings of the World Congress on Engineering 2019, London, U.K., 2019.

[11] A. A. Zadpoor, Mechanical performance of additively manufactured meta-biomaterials, Acta Biomaterialia 85 (2019) 41–59. doi:10.1016/J.ACTBIO.2018.12.038.

[12] S. Ghouse, N. Reznikov, O. R. Boughton, S. Babu, K. C. Ng, G. Blunn, J. P. Cobb, M. M. Stevens, J. R. Jeffers, The design and in vivo testing of a locally stiffness-matched porous scaffold, Applied Materials Today 15 (2019) 377–388. doi:10.1016/J.APMT.2019.02.017.

[13] S. Li, E. Demirci, V. V. Silberschmidt, Variability and anisotropy of mechanical behavior of cortical bone in tension and compression, Journal of the Mechanical Behavior of Biomedical Materials 21 (2013) 109–120. doi:10.1016/J.JMBBM.2013.02.021.

[14] Z. Tabor, E. Rokita, Quantifying anisotropy of trabecular bone from gray-level images, Bone 40 (4) (2007) 966–972. doi:10.1016/J.BONE.2006.10.022.

[15] G. Maquer, S. N. Musy, J. Wandel, T. Gross, P. K. Zysset, Bone Volume Fraction and Fabric Anisotropy Are Better Determinants of Trabecular Bone Stiffness Than Other Morphological Variables, Journal of Bone and Mineral Research 30 (6) (2015) 1000–1008. doi:10.1002/JBMR.2437.

[16] P. Augat, T. Link, T. F. Lang, J. C. Lin, S. Majumdar, H. K. Genant, Anisotropy of the elastic modulus of trabecular bone specimens from different anatomical locations, Medical Engineering & Physics 20 (2) (1998) 124–131. doi:10.1016/S1350-4533(98)00001-0.

[17] S. H. Liao, R. F. Tong, J. X. Dong, Influence of anisotropy on peri-implant stress and strain in complete mandible model from CT, Computerized Medical Imaging and Graphics 32 (1) (2008) 53–60. doi:10.1016/J.COMPMEDIMAG.2007.09.001.

[18] Z. Gümrükçü, Y. T. Korkmaz, F. M. Korkmaz, Biomechanical evaluation of implant-supported prosthesis with various tilting implant angles and bone types in atrophic maxilla: A finite element study, Computers in Biology and Medicine 86 (2017) 47–54. doi:10.1016/J.COMPBIOMED.2017.04.015.

[19] V.-H. Nguyen, G. Rosi, S. Naili, A. Michel, M.-L. Raffa, R. Bosc, J.-P. Meningaud, C. Chappard, N. Takano, G. Haiat, Influence of anisotropic bone properties on the biomechanical behavior of the acetabular cup implant: a multiscale finite element study, Computer methods in biomechanics and biomedical engineering 20 (12) (2017) 1312–1325.

[20] J. Kang, E. Dong, D. Li, S. Dong, C. Zhang, L. Wang, Anisotropy characteristics of microstructures for bone substitutes and porous implants with application of additive manufacturing in orthopaedic, Materials and Design 191 (2020) 108608. doi:10.1016/j.matdes.2020.108608.

[21] M. Munford, U. Hossain, S. Ghouse, J. R. Jeffers, Prediction of anisotropic mechanical properties for lattice structures, Additive Manufacturing 32 (2020) 101041. doi:10.1016/j.addma.2020.101041.

[22] A. K. Aiyangar, J. Vivanco, A. G. Au, P. A. Anderson, E. L. Smith, H.-L. Ploeg, Dependence of anisotropy of human lumbar vertebral trabecular bone on quantitative computed tomography-based apparent density, Journal of Biomechanical Engineering 136 (9) (2014).

[23] S. Bernard, Q. Grimal, P. Laugier, Accurate measurement of cortical bone elasticity tensor with resonant ultrasound spectroscopy, Journal of the Mechanical Behavior of Biomedical Materials 18 (2013) 12–19. doi:https://doi.org/10.1016/j.jmbbm.2012.09.017.
[24] M. C. Messner, M. I. Barham, M. Kumar, N. R. Barton, Wave propagation in equivalent continuums representing truss lattice materials, International Journal of Solids and Structures 73 (2015) 55–66.
[25] T. Tancogne-Dejean, D. Mohr, Elastically-isotropic truss lattice materials of reduced plastic anisotropy, International Journal of Solids and Structures 138 (2018) 24–39.
[26] R. M. Latture, M. R. Begley, F. W. Zok, Design and mechanical properties of elastically isotropic trusses, Journal of Materials Research 33 (3) (2018) 249–263.
[27] V. J. Challis, X. Xu, L. C. Zhang, A. P. Roberts, J. F. Grotowski, T. B. Sercombe, High specific strength and stiffness structures produced using selective laser melting, Materials and Design 63 (2014) 783–788. doi:10.1016/j.matdes.2014.05.064.
[28] S. Xu, J. Shen, S. Zhou, X. Huang, Y. M. Xie, Design of lattice structures with controlled anisotropy, Materials & Design 93 (2016) 443–447. doi:10.1016/j.matdes.2016.01.007.
[29] A. Cutolo, B. Engelen, W. Desmet, B. Van Hooreweder, Mechanical properties of diamond lattice Ti–6Al–4V structures produced by laser powder bed fusion: On the effect of the load direction, Journal of the Mechanical Behavior of Biomedical Materials 104 (2020) 103656. doi:10.1016/j.jmbbm.2020.103656.
[30] M. Munford, U. Hossain, S. Ghouse, J. R. Jeffers, Prediction of anisotropic mechanical properties for lattice structures, Additive Manufacturing 32 (2020) 101041.
[31] U. Hossain, S. Ghouse, K. Nai, J. R. Jeffers, Controlling and testing anisotropy in additively manufactured stochastic structures, Additive Manufacturing 39 (2021) 101849.
[32] R. Asbai-Ghoudan, S. Ruiz de Galarreta, N. Rodriguez-Florez, Analytical model for the prediction of permeability of triply periodic minimal surfaces, Journal of the Mechanical Behavior of Biomedical Materials 124 (2021) 104804. doi:10.1016/J.JMBBM.2021.104804.
[33] M. Alaña, A. Lopez-Arancibia, A. Pradera-Mallabiabarrena, S. Ruiz de Galarreta, Analytical model of the elastic behavior of a modified face-centered cubic lattice structure, Journal of the Mechanical Behavior of Biomedical Materials 98 (2019). doi:10.1016/j.jmbbm.2019.05.043.
[34] M. Zhang, Z. Yang, Z. Lu, B. Liao, X. He, Effective elastic properties and initial yield surfaces of two 3D lattice structures, International Journal of Mechanical Sciences 138-139 (2018) 146–158. doi:10.1016/J.IJMECSCI.2018.02.008.
[35] A. A. Espinoza Orías, J. M. Deuerling, M. D. Landrigan, J. E. Renaud, R. K. Roeder, Anatomic variation in the elastic anisotropy of cortical bone tissue in the human femur, Journal of the Mechanical Behavior of Biomedical Materials 2 (3) (2009) 255–263. doi:10.1016/J.JMBBM.2008.08.005.
[36] S. W. Shore, P. E. Barbone, A. A. Oberai, E. F. Morgan, Transversely Isotropic Elasticity Imaging of Cancellous Bone, Journal of Biomechanical Engineering 133 (6) (jun 2011). doi:10.1115/1.4004231.
[37] R. G. Hutchinson, N. A. Fleck, The structural performance of the periodic truss, Journal of the Mechanics and Physics of Solids 54 (4) (2006) 756–782.
[38] V. Karageorgiou, D. Kaplan, Porosity of 3D biomaterial scaffolds and osteogenesis, Biomaterials 26 (27) (2005) 5474–5491. doi:10.1016/j.biomaterials.2005.02.002.
[39] C. Metz, G. N. Duda, S. Checa, Towards multi-dynamic mechano-biological optimization of 3D-printed scaffolds to foster bone regeneration, Acta Biomaterialia 101 (2020) 117–127. doi:10.1016/J.ACTBIO.2019.10.029.
[40] C. Elangeswaran, A. Cutolo, G. K. Muralidharan, C. de Formanoir, F. Berto, K. Vanmeensel, B. Van Hooreweder, Effect of post-treatments on the fatigue behaviour of 316L stainless steel manufactured by laser powder bed fusion, International Journal of Fatigue 123 (2019) 31–39. doi:10.1016/j.ijfatigue.2019.01.013.
[41] S. L. Omairey, P. D. Dunning, S. Sriramula, Development of an ABAQUS plugin tool for periodic RVE homogenisation, Engineering with Computers 35 (2) (2018) 567–577. doi:10.1007/s00366-018-0616-4.
[42] S. Ruiz de Galarreta, J. R. Jeffers, S. Ghouse, A validated finite element analysis procedure for porous structures, Materials and Design 189 (2020) 108546. doi:10.1016/j.matdes.2020.108546.
[43] X. Yan, Q. Li, S. Yin, Z. Chen, R. Jenkins, C. Chen, J. Wang, W. Ma, R. Bolot, R. Lupoi, Z. Ren, H. Liao, M. Liu, Mechanical and in vitro study of an isotropic Ti6Al4V lattice structure fabricated using selective laser melting, Journal of Alloys and Compounds 782 (2019) 209–223. doi:10.1016/J.JALLCOM.2018.12.220.
[44] ISO 13314:2011 - mechanical testing of metals – ductility testing – compression test for porous and cellular metals (2011).
[45] D. Melancon, Z. Bagheri, R. Johnston, L. Liu, M. Tanzer, D. Pasini, Mechanical characterization of structurally porous biomaterials built via additive manufacturing: experiments, predictive models, and design maps for load-bearing bone replacement implants, Acta Biomaterialia 63 (2017) 350–368. doi:10.1016/j.actbio.2017.09.013.
[46] D. Mahmoud, K. S. Al-Rubaie, M. A. Elbestawi, The influence of selective laser melting defects on the fatigue properties of Ti6Al4V porosity graded gyroids for bone implants, International Journal of Mechanical Sciences 193 (2021) 106180. doi:10.1016/j.ijmecsci.2020.106180.
[47] L. Xiao, S. Li, W. Song, X. Xu, S. Gao, Process-induced geometric defect sensitivity of Ti–6Al–4V lattice structures with different mesoscopic topologies fabricated by electron beam melting, Materials Science and Engineering A 778 (2020) 139092. doi:10.1016/j.msea.2020.139092.
[48] M. Alaña, A. Cutolo, G. Probst, S. Ruiz de Galarreta, B. Van Hooreweder, Understanding elastic anisotropy in diamond based lattice structures produced by laser powder bed fusion: Effect of manufacturing deviations, Materials and Design 195 (2020) 108971. doi:10.1016/j.matdes.2020.108971.
[49] M. F. Ashby, L. J. Gibson, Cellular solids: structure and properties, Press Syndicate of the University of Cambridge, Cambridge, UK (1997) 175–231.
[50] A. M. Arefin, M. Lahowetz, P. F. Egan, Simulated tissue growth in tetragonal lattices with mechanical stiffness tuned for bone tissue engineering, Computers in Biology and Medicine 138 (2021) 104913. doi:10.1016/J.COMPBIOMED.2021.104913.
[51] S. Dendorfer, H. J. Maier, D. Taylor, J. Hammer, Anisotropy of the fatigue behaviour of cancellous bone, Journal of biomechanics 41 (3) (2008) 636–641.
[52] U. Hossain, S. Ghouse, K. Nai, J. R. Jeffers, Mechanical and morphological properties of additively manufactured SS316L and Ti6Al4V micro-struts as a function of build angle, Additive Manufacturing 46 (2021) 102050. doi:10.1016/J.ADDMA.2021.102050.

[53] I. Sevostianov, M. Kachanov, Impact of the porous microstructure on the overall elastic properties of the osteonal cortical bone, Journal of Biomechanics 33 (7) (2000) 881–888.

4.4 Paper D

Paper D is entitled 'Understanding elastic anisotropy in diamond based lattice structures produced by laser powder bed fusion: Effect of manufacturing deviations'. This article is the follow-up of a previously published article, which analyzed the stiffness and strength of the diamond lattice structure under various orientations. In this work, the aim was to study the causes of the mismatch between the theoretical and actual anisotropy characteristics of the structures, considering the effect of the manufacturing deviations. These were the main studied aspects:

- A methodology was develop to analyze the imperfection level of the struts, while also considering the magnitude of such deviations along the struts.
- Different imperfection types were studied: the cross-section mismatch, the shape difference from circularity, and offset deviation of the center of gravity of the strut.
- A methodology was developed to create numerical models that included isolated and combined imperfection types.
- The combined effect of the studied imperfections led to a change in anisotropy that coincided with the experimental results.

Materials and Design 195 (2020) 108971

Contents lists available at ScienceDirect

Materials and Design

journal homepage: www.elsevier.com/locate/matdes

Understanding elastic anisotropy in diamond based lattice structures produced by laser powder bed fusion: Effect of manufacturing deviations

Markel Alaña [a,1,*], Antonio Cutolo [b,1,*], Gabriel Probst [b], Sergio Ruiz de Galarreta [a], Brecht Van Hooreweder [b,c]

[a] Department of Mechanical Engineering and Materials, Universidad de Navarra, TECNUN Escuela de Ingenieros, Paseo Manuel de Lardizabal, 13, 20018 San Sebastian, Spain
[b] KU Leuven Department of Mechanical Engineering, Celestijnenlaan 300, 3001 Leuven, Heverlee, Belgium
[c] Members Flanders Make, Leuven, Belgium

HIGHLIGHTS

- Manufacturing imperfections are aligned with the building direction and thus affect the anisotropy of the lattice structures.
- Probability distributions of the imperfections were obtained depending on the position of the cross-sections along the strut.
- The FE model with imperfections predicts the stiffest direction to change from [111] to [110] as reported in literature.
- The offset of the center of gravity of the strut cross section had the greatest effect in the anisotropy variation.

GRAPHICAL ABSTRACT

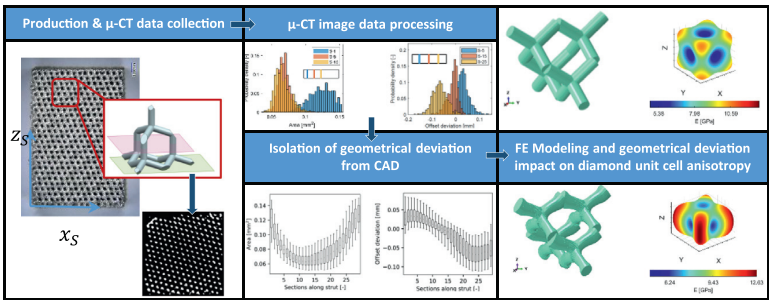

ARTICLE INFO

Article history:
Received 28 May 2020
Received in revised form 2 July 2020
Accepted 9 July 2020
Available online 16 July 2020

Keywords:
Laser powder bed fusion - Ti-6Al-4 V - lattice structures - anisotropy - FE modeling

ABSTRACT

Laser powder bed fusion (L-PBF) allows the production of metal lattice cellular structures with tailored mechanical properties. In order to generate the specific structural behavior it is of utmost importance to understand the response of the unit cells when different load conditions are considered. In this article the mechanical response of diamond based cellular structures has been investigated focusing on the impact of geometrical inaccuracy generated by the manufacturing process on the elastic anisotropy of the mentioned unit cell. The μ-CT analysis of the structures shows that the manufacturing deviations occur in certain orientations that depend highly on the building direction and proximity to nodes. The measured imperfection types were implemented in a finite element model in order to predict their single and combined effects in the elastic directional response. The results indicate that the L-PBF process can induce a significant change of elastic anisotropy in the diamond unit cells, including a substantial variation of the optimal orientation for minimal compliance. Methods are presented to calculate this anisotropy such that it can be taken into account when designing and using such lattice structures in real-life applications with multi-axial load conditions.

1. Introduction

Metal additive manufacturing (AM) refers to the production of metallic components in a layer by layer fashion from a specific computer-aided design (CAD) model. Among the AM processes the laser powder bed fusion (L-PBF) process uses a focused and computer controlled

* Corresponding authors.
E-mail addresses: malana@tecnun.es (M. Alaña), antonio.cutolo@kuleuven.be (A. Cutolo).
[1]Contributed equally to this work.

https://doi.org/10.1016/j.matdes.2020.108971

laser beam to selectively melt metal powder. This technique offers an attractive method for producing complex near net-shape geometries with an efficient material use [1]. One of the big advantages of using this AM technique is the possibility to produce parts with almost unlimited freedom in terms of geometrical design. This allows the integration of lattice structures in the design phase to target specific mechanical properties in designated locations while reducing the total weight of the component. Apart from their load bearing applications, lattice structures are also used in other fields for energy absorption, heat transfer devices, vibration attenuation or as cellular catalysts, among others [2–4].

Lattice structures are defined in this work as a class of cellular solids formed by beam like members named struts that connect nodes [5–7]. The struts are arranged in a fixed topology to generate the unit cell (UC) that is replicated in the 3D space to fill the volume of the structure.

According to Maxwell's stability criterion, UCs can be classified in stretching dominated and in bending dominated structures [8]. This paper will focus on the diamond unit cell, which is a bending dominated structure. The mechanical properties of lattice structures depend on several factors: (i) the type, size and topology of the UC; (ii) the relative density of the lattice structure defined as the quantity of material in the volume of the lattice structure; (iii) the parent material used for the production; and (iv) the material porosity and surface quality. Moreover, during recent years, in order to better integrate cellular lattice structures in load bearing applications, several authors have introduced the importance of understanding the UC elastic anisotropy behavior and the effect of load directions on static and dynamic properties of lattice structures [9–13].

In addition, some inherent geometrical imperfections may occur during the manufacturing process leading to deviations from the ideal structure. This phenomena can be more pronounced when the struts dimensions (length and/or diameter) approach the laser spot diameter [14]. Therefore it is essential to evaluate the impact of these geometrical imperfections on the structural response of the final component.

Several authors investigated the impact of geometrical imperfection on mechanical properties of metal lattice structures [15–17]. Dallago et al. [18] used micro X-ray computer tomography to measure and classify the types of morphological imperfections in terms of deviation from the CAD model of regular cubic Ti6Al4V cellular lattices. The authors highlighted that struts with a small angle with respect to the building platform are systematically affected by dross formation that increases the struts thickness and offsets the center of gravity of the cross-sections from the imaginary axis that connects the two nodes introducing a sort of "waviness". The data gathered from $\mu - CT$ were used to build different FE models with increasing level of complexity. From these simulations, Dallago et al. concluded that the higher thickness of the as-produced struts increased the overall stiffness of the cellular structure while the bending actions introduced by the waviness reduced the elastic stiffness. A comparable study with similar conclusions was made by Lei et al. [19] in which X-ray micro-computed tomography ($\mu - CT$) was employed to extract the geometrical deviations and to quantify the statistical distribution of strut diameter of two different unit cells, i.e. the BCC and the BCCZ produced with AlSi10Mg. The reconstructed models were used to analyze the impact of the distribution of the imperfections on the structure's response. Lozanovski et al. [20] followed a similar procedure to design very detailed geometrical models that included shape variation and "waviness" obtained from $\mu - CT$ scans.

On the other hand, Liu [21] and Xiao [22] simulated the mechanical properties of octet truss, rhombic dodecahedron and ideal rhombicuboctahedron along different directions, accounting for manufacturing deviations with respect to the ideal geometry. Liu and Xiao concluded that the manufacturing induced deviations had an important effect on the anisotropy of the studied lattices structures. Nevertheless, tests were performed with a fixed orientation between the load and the unit cell.

Wauthle et al. [9] were among the first researchers to investigate the elastic anisotropy of the cubic diamond UC produced with L-PBF in Ti6Al4V. However, due to the high level of internal defects generated during the manufacturing process i.e. pores and lack of fusion defects, the authors were not able to conclude on the effective anisotropic behavior of the diamond UC. Cutolo et al. [11] investigated the same topic highlighting a high level of elastic anisotropy of the diamond UC by testing the same lattice structure along different load directions. However, none of the above-mentioned studies included an investigation on the effect of the different morphological imperfections on the anisotropic behavior of the lattice structure.

The objective of the present study is to understand both the individual and combined impact of the different types of geometrical deviations on the elastic anisotropy response of Ti6Al4V diamond UC produced by L-PBF. In order to do so, a detailed analysis of the inherent geometrical imperfections was carried out. The morphology of the as produced lattice structures was reconstructed via $\mu - CT$ and different manufacturing imperfection types were classified in terms of deviation from the CAD model. The novelty of this research is that the deviation types were analyzed by considering their statistical distribution along the strut axis. From statistical analysis of $\mu - CT$ data, different beam FE models were created, with different levels of complexity to isolate the impact of the different types of geometrical deviations on the anisotropy of the diamond unit cells.

An overview of the methodology used to generate the different FE models is presented in Fig. 1. Experimental results obtained by Cutolo et al. that were reported in [11] show that the produced diamond based lattice structures have different anisotropy behavior with respect to the idealized UC model. The numerical results of this study are in line with the previous work by Cutolo et al., and indicate that the variation in the anisotropic response can be mainly attributed to the offset of the center of gravity of the struts cross-sections with respect to the ideal strut axis.

2. Materials and methods

2.1. Manufacturing

The samples considered in this investigation have been described in the recent work from Cutolo et al. [11] in which a diamond unit cell has been used for the creation of Ti6Al4V lattice structures to investigate the effect of load direction on the mechanical properties of diamond based cellular structures. A diamond unit cell can be described as an assembly of struts and nodes with an angle of 109.48 deg between each pair of struts connecting one node. From a manufacturing point of view, the main advantage of using this unit cell is that the strut angles with the build platform of the L-PBF machine is always 35.26 deg. This angle is high enough to guarantee a production of these struts via L-PBF without using support structures.

The studied samples were prisms with a square cross-section and with a side D of $10mm$ and height H of $15mm$. A unit cell size of $1mm$ was used with a prescribed relative density of 25%. The authors divided the samples in three batches according to the orientation between the load direction and UC orientation, i.e. [001], [111] and [011] as shown in Fig. 2. The orientation of all the diamond unit cells (X_U, Y_U, Z_U) with respect to the L-PBF base plate (X_L, Y_L) was chosen constant and equal for all samples, such that indeed all unit cell struts of all samples were at the same angle of 35.26 with respect to this base plate (X_L, Y_L). This guarantees equal unit cell quality and morphology for all samples. The orientation of the samples surrounding all unit cells (i.e. the lattice structures, X_S, Y_S, Z_S) with respect to the L-PBF base plate (X_L, Y_L) was varied as indicated in Fig. 2 to enable different load directions with respect to the unit cell orientation, and the obtained manufactured samples are shown in Fig. 3. A detailed description of sample design, production and testing is reported in [11].

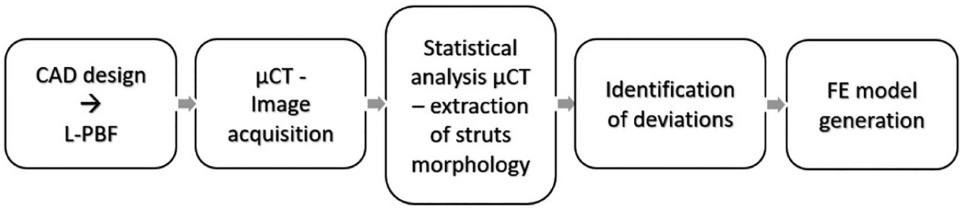

Fig. 1. Procedure for generating FE models.

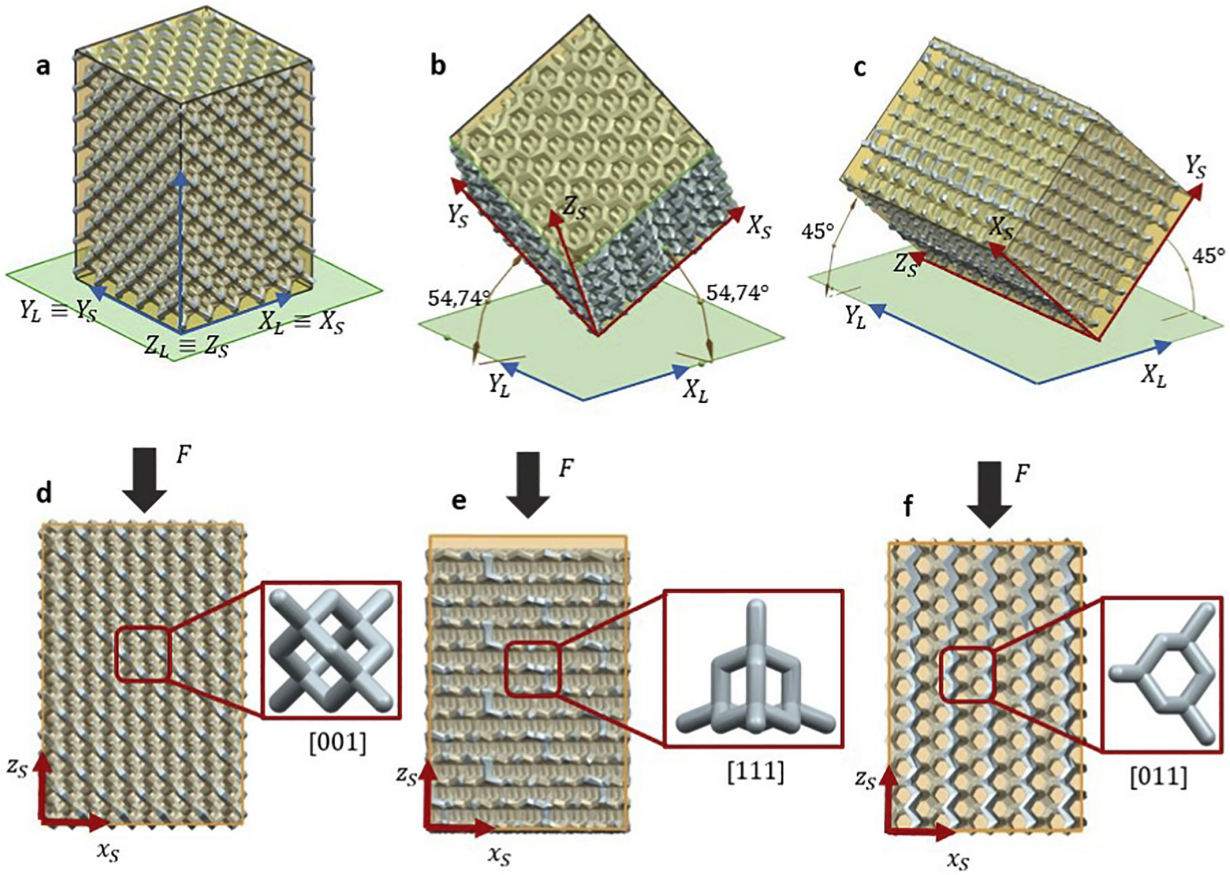

Fig. 2. Samples orientation with respect to the build platform X_L, Y_L for a) [001], b) [111], c)[011] orientation Force direction with respect to the UC for d) [001], e) [111], f) [011] orientation [11].

2.2. Analysis of manufactured structures

From each batch, two samples were analyzed with a Nikon XT H225 ST CT-system to evaluate the morphological differences between the CAD geometry and the produced samples. A *W* target and 1*mm* Cu filter were used during the scanning and the machine was set to a voltage of $[135 - 165]kV$ and a current of $[5070]\mu A$. The voxel size was $12\mu m$. $\mu - CT$ data were exported in terms of stacked images parallel to the X_S, Y_S plane of the samples with a frequency of 84 images per millimeter along the Z_S direction.

The morphological information extraction was performed using $\mu - CT$ scan data from the [111] oriented specimens. In this case, the resulting stacked images are perpendicular to 4 struts per unit cell (Fig. 2-e). The topology of the diamond unit cell and the fixed orientation of the unit cell with respect to the L-PBF build-platform, ensure strut-to-strut homogeneity in terms of morphology for all the specimens and thus the same distribution of imperfections can be considered.

For every sliced image, ImageJ software was used to extract the area and the center of gravity of each strut cross-section, as well as the best ellipse fit with the dimensions and orientation of the major and minor axes with respect to the X_S and Y_S axes, as shown in Fig. 4. These data were processed with Matlab to isolate the morphology of every single strut by means of the following procedure:

- each strut was identified by the position of its center of gravity;
- a deviation tolerance from the center of gravity was used to create a region of interest;

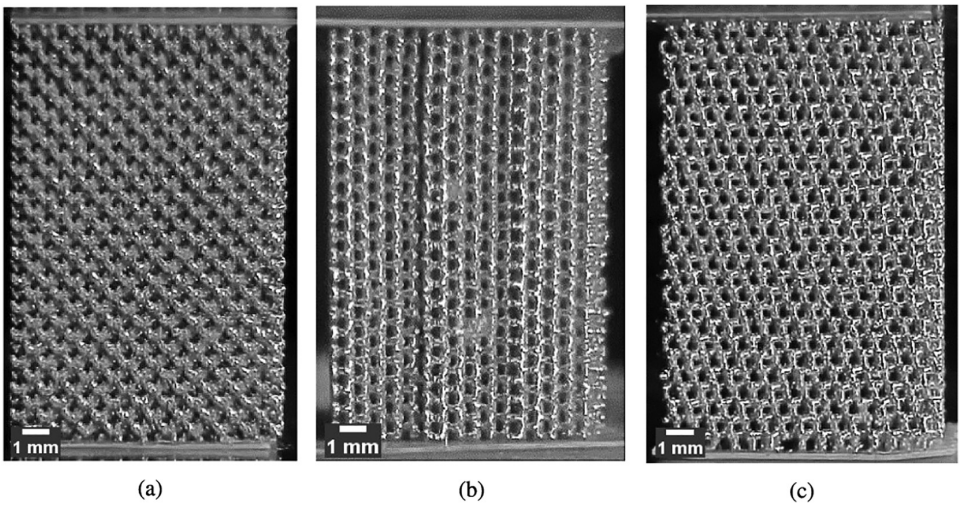

Fig. 3. Manufactured samples in (a) [001], (b) [011], (c) [111] orientations [11].

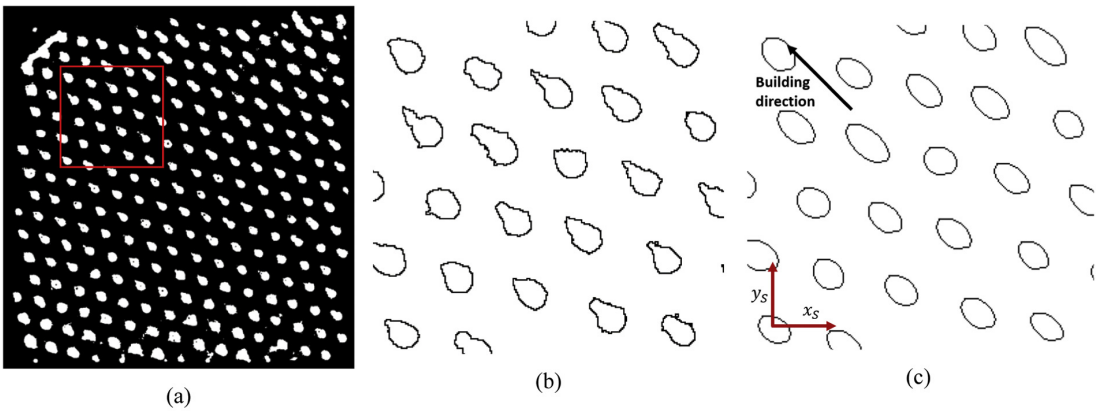

Fig. 4. (a) Stacked image from $\mu - CT$ scan, (b) detection of each cross-section, (c) best ellipse fit for every cross-section.

- all the strut cross-sections whose center of gravity reside in the defined region of interest were assigned to a single strut.

In this way, it was possible to isolate the evolution of the cross-section along the length of every strut. Three representative strut cross-sectional area distributions are presented in Fig. 5a.

Furthermore, in order to perform the statistical analysis, the isolated struts were transposed to a common reference system, as it is shown in Fig. 4-b for three representative struts. The use of this procedure allowed the analysis of the morphological evolution of more than 1000 struts along the strut axis with a robust and systematical procedure.

By using this procedure it was possible to isolate three morphological imperfection categories:

- Cross-section area: difference between the nominal cross-section and actual cross-sectional area
- Shape of the cross-section: cross-section deviation from the theoretical circular shape
- Offset from axis: distance between the center of gravity of the scanned cross-section and the axis of the designed strut

2.3. Finite Element modeling and homogenization

In order to study each type of deviation and their combined effects on the diamond UC anisotropic behavior, several finite element models were built. These models consist of beam elements generated using Abaqus 2019 (Dassault Systems). The material was modelled as linear elastic with typical AM Ti6Al4V properties: a Young's modulus of 113*GPa* and Poisson's ratio of 0.342 were considered. Each strut was modelled with 35 Timoshenko first order beam elements, to be consistent with the resolution of the $\mu - CT$ scan. From the distributions of the deviations along the struts, the mean values were used to model the deviation according to its position along the strut.

For each position along the strut axis the mean values of the imperfection distribution (i.e. variation in cross-section shape, area and offset) were extracted. These values were used to model beam elements along the strut axis. This process allowed the generation of strut FE models that reproduce the mean value trends of geometrical inaccuracy. However, the variability of the data was not considered in modeling (and thus also not in the simulations), and therefore all the lattice structure models were built using the same strut FE model.

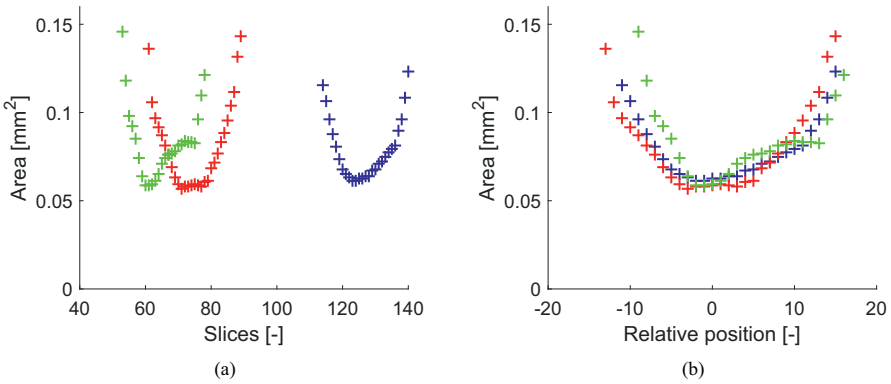

Fig. 5. (a) Absolute position of three struts (b) Relative positioning of struts along their axis.

The FE strut models were used to create 10×10×10 diamond unit cells with unit cell size of 1*mm*. Considering the type of imperfections, different models were built in order to assess both the isolated and combined effects of each type of deviation:

- Nominal: Circular and constant cross-sections, obtained as average of all mean values at each position along the strut.
- Variable Circular Cross-Section (VCCS): Circular cross-sections with variable area as measured in the $\mu - CT$.
- Constant Ellipse Cross-Section (CECS): Elliptical cross-section with constant area along the strut. The area corresponds to the average area of the ellipses.
- Constant Circular Offset Cross-Section (CCOCS): Circular and constant cross-sections as in Nominal model, in which every beam has an offset with respect to the theoretical strut axis.
- Variable Ellipse Cross-Section (VECS): Variable elliptical cross-section with values obtained from $\mu - CT$ scan.
- Variable Elliptical Offset Cross-Section (VEOCS): Elliptical cross-sections distribution as measured by the $\mu - CT$ scan, combined with the offset distribution from the strut axis. This model includes the combined effects of all measured imperfections (see Fig. 6).

The effects of the different imperfections on UC anisotropy were studied by homogenizing each FE model. This technique consists of treating each structure as if it was a homogeneous material and getting its equivalent mechanical properties. Periodic Boundary Conditions (PBC) are applied in order to analyze the behavior of the structures as if they were part of an infinite medium. In the PBC, the displacement of nodes in opposite faces of a representative volume element is constrained by relating the degrees of freedom to the mean macroscopic displacement (a detailed explanation can be found in [23]). Thus, effective elastic constants of the Eq. (1) can be obtained for each FE model according to Hooke's law for anisotropic bodies [24].

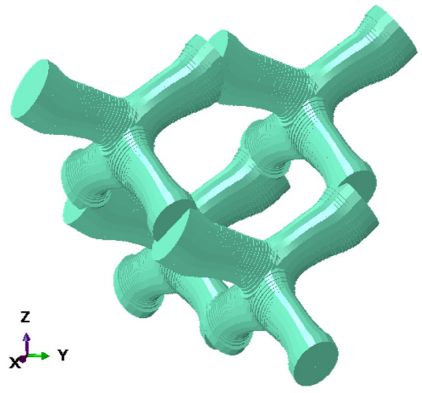

Fig. 6. VEOCS diamond unit cell model, with cross-sections scaled at 0.5.

$$\sigma = [C]\varepsilon \Rightarrow \begin{bmatrix} \sigma_1 \\ \vdots \\ \sigma_6 \end{bmatrix} = \begin{bmatrix} C_{11} & \cdots & C_{16} \\ \vdots & \ddots & \vdots \\ C_{61} & \cdots & C_{66} \end{bmatrix} \begin{bmatrix} \varepsilon_1 \\ \vdots \\ \varepsilon_6 \end{bmatrix} \tag{1}$$

A plugin developed by Omairey [23] was used to obtain the effective elastic constants of the simulated structures. This plugin applies six independent stress states, and for each case the resulting macroscopic strain tensor is obtained for the structure under PBC. As an example, for a normal macroscopic stress in direction 1, $\sigma = [\sigma_1 00000]^T$, and the resultant macroscopic strain matrix $\varepsilon = [\varepsilon_1 \varepsilon_2 \varepsilon_3 \varepsilon_4 \varepsilon_5 \varepsilon_6]^T$, the following elastic constants can be obtained for an orthotropic material:

$$E_1 = \frac{\sigma_1}{\varepsilon_1} \qquad \nu_{12} = -\frac{\varepsilon_2}{\varepsilon_1} \qquad \nu_{13} = -\frac{\varepsilon_3}{\varepsilon_1} \tag{2}$$

For shear stresses, if stress $\sigma = [00000\sigma_6]^T$ is applied, the shear modulus can be obtained as in Eq. (3), and the applied stresses and the equations are adjusted for each stress state and orientation.

$$G_{12} = \frac{\sigma_6}{\varepsilon_6} \tag{3}$$

Once the stiffness matrix $[C]$ is obtained for each FE model it is possible to evaluate the following ratios that can be used to compare the different levels of anisotropy:

$$\text{Young's modulus ratio} = \frac{E_3}{E_1} \tag{4}$$

$$\text{Poisson's coefficient ratio} = \frac{\nu_{13}}{\nu_{12}} \tag{5}$$

$$\text{Shear modulus ratio} = \frac{G_{13}}{G_{12}} \tag{6}$$

$$\text{Anisotropy coefficient 1} = A_{23} = \frac{4C_{44}}{C_{22} + C_{33} - 2C_{23}} \tag{7}$$

$$\text{Anisotropy coefficient 2} = A_{12} = \frac{4C_{66}}{C_{11} + C_{22} - 2C_{12}} \tag{8}$$

The anisotropy coefficients are a variation of the Zener ratio. Their use allows the evaluation of non-cubic stiffness tensors. In the context

of this research, the anisotropy coefficients are used to compare levels of isotropy in different planes. Thus, in this case, coefficient values of 1 are a necessary but not sufficient condition for isotropy. For actual isotropy $C_{ii} = C_{jj}$ must also hold for $i, j = 1,2,3$.

3. Results and discussion

3.1. Metrological analysis

In a previous work, Cutolo et al. [11] defined a novel sample preparation method with particular focus on orienting the unit cell coordinate system, the sample coordinate system and the L-PBF reference system. The authors fixed the UC coordinate system parallel to the L-PBF reference system. By changing the orientation of the samples with respect to the L-PBF base plate, the authors were able to investigate the anisotropic behavior of the diamond UC. Fixing the orientation of the diamond UC with respect to the L-PBF reference system ensures that each strut axis forms the same angle of 35.26 deg with the build platform and, consequently, a high level of strut-to-strut consistency in terms of strut dimensions is guaranteed. This has been confirmed by the results of the metrological analysis performed on the $\mu - CT$ data. Therefore, it can be assumed that all the struts in each unit cell of the lattice structure exhibits the same mechanical response.

Each strut has been isolated from the reconstructed model and sectioned with 35 planes perpendicular to the strut axis. From the cross-sectional analysis, several properties were extracted regarding the morphological differences with respect to the idealized strut.

The histograms in Fig. 7 show the distributions of morphological characteristics of the struts over 3 successive slices. A representation of the location of each cross-section along an ideal strut is also given in the figures: Slice 1 corresponds to the closest slice to the node, slice 8 is about the quarter of the strut length, and slice 15 is close to the center of the strut. Fig. 7a shows the very large difference in the cross-sectional area distribution along the different sections of the strut. Apart from the changes in the mean value, the data dispersion is also very different depending on the cross-section along the strut. As a result the data distribution type is not uniform and it would not be accurate to adjust all the cross-sectional area values to a single probability distribution.

Fig. 7b shows the eccentricity distribution across three sections. The eccentricity is the normalized distance between the center and the focus of an ellipse, and is defined as follows: $ecc = \sqrt{a^2 - b^2}/a$, with a and b being the major and minor semi-axes, respectively. For a circle, the focus and the center are the same ($ecc = 0$), which is the case of the designed lattice structure. Therefore, eccentricity indicates how close an ellipse is to circularity, and can be used to assess the struts cross-section shape quality.

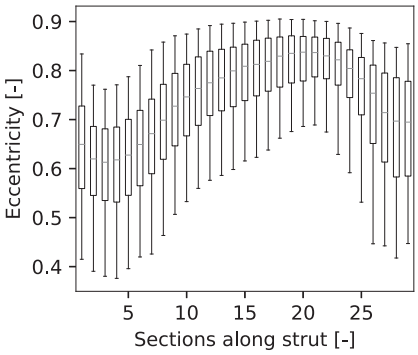

Fig. 8. Distribution of cross-section eccentricity along the strut.

Even if the cross-sectional area distributions of sections 8 and 15 are similar, Fig. 7b indicates that the eccentricity distributions have significant differences, which means that even in the regions where the area values are relatively stable, the shape of the cross-section changes.

Fig. 8 shows the evolution of the eccentricity along the strut axis. Each boxplot represents the statistical distribution of the eccentricity at the specific section, and the markers represent the 5th, 25th, 50th, 75th, and 95th percentiles. The eccentricity distributions indicate that the cross-section is not circular at any section along the strut. Furthermore, the circularity is higher close to the nodes, where the cross-sectional area deviates more from prescribed values. This means that the circularity is caused by the manufacturing deviations themselves rather than by the design.

Fig. 9 shows the probability distribution of the center of gravity offset of each cross-section. Contrary to the cross-sectional area, the offset data distribution types are quite uniform along the strut, although a clear difference in mean values can be noticed along the strut sections.

In Fig. 10 the cross-sectional area distributions are presented in terms of boxplots for each section along the strut axis. The most notable result is that the cross-sectional area decreases towards the middle of each strut indicating that less material is present in this region. On the other end, a cross-sectional area increase with a consequent mass increase can be observed approaching the two end nodes. From these data, it was possible to extract the equivalent radius distribution for each section. The VCCS strut model was generated using the mean value of the distributions presented in Fig. 10.

From the morphological analysis of the cross-section it has been noticed that the geometry of the strut cross-section deviates from the designed circular shape and tends to become elliptical. In Fig. 11 the distribution of the minor and major axis of the best fitting ellipses are

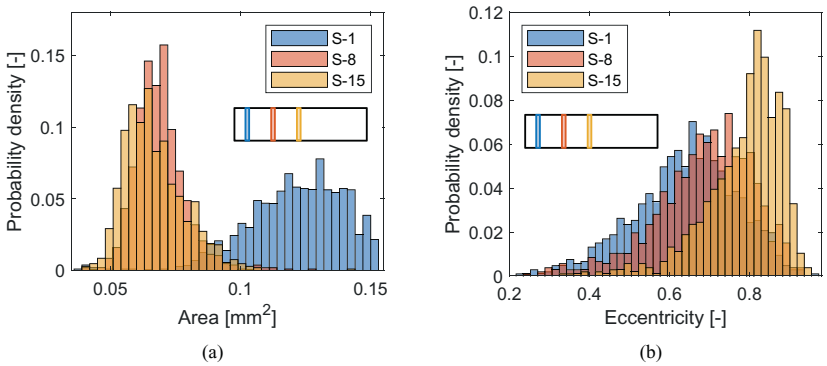

Fig. 7. Histogram of area distribution (a) and eccentricity (b) in three different sections along the strut.

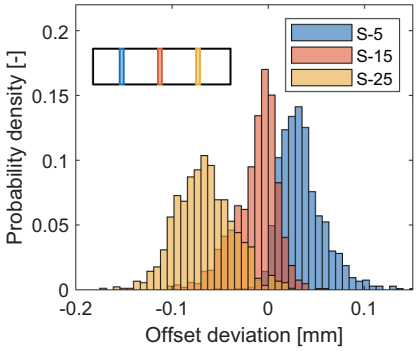

Fig. 9. Probability distribution of the offset of the center of gravity.

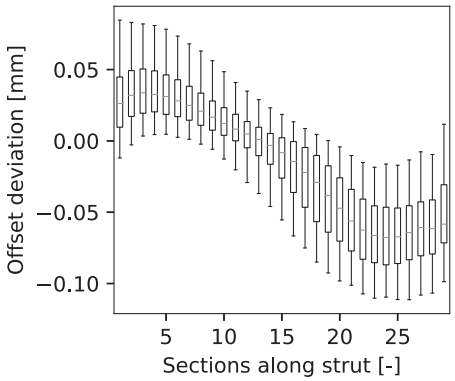

Fig. 12. Center of gravity deviation with respect the ideal strut axis.

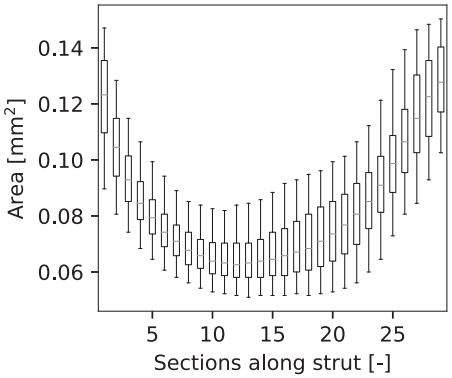

Fig. 10. Distributions of the cross-sectional area along the strut.

presented. Data are presented for each section along the strut axis in terms of boxplots. Both major and minor axes have a minimum value close to the center of the strut and higher values are reported for sections close to the nodes.

Another important feature extracted for each cross-section, was the orientation of the major and minor axis of the ellipses. From the analysis of the data it is shown that the major axis of each cross-section is oriented along the building direction. The elongated cross-section along the building direction indicates that this geometrical difference from the nominal circular shape is caused by the dross formation occurring underneath down-facing surfaces. It is also important to note that the dispersion of the data is much higher in the case of the major axis, which indicates that the dross formation is not uniform and has a high variability. The CECS FE model was created by assigning constant elliptical cross-section to the 35 Timoshenko beams for every strut. The area of the elliptical cross-section is equal to the mean value of the area distribution of Fig. 10. The VECS FE model was defined by including the information of Figs. 10 and 11 to account for the combined effect of the change in cross-section geometry and area along the strut axis.

The offset of the cross-sections follows a sort of wave distribution along the strut axis as indicated in Fig. 12. The center of gravities are shown for each section, and the 0 offset is assumed as the mean of 10 slices along the strut with lowest cross-sectional area. These cross-sections are less affected by the dross formation, and therefore their center of gravity is closer to the design values. For each strut the center of gravity offset results positive for the node that is closer to the built platform, decreasing along the strut longitudinal axis. This produces a lower strut inclination, leading to an angle between the horizontal plane and the axis of the strut smaller than 35.26 deg.

Fig. 13 shows the centers of gravity of each strut element projected on the plane perpendicular to the strut axis. It is interesting to notice that the drift of the center of gravity lies along a direction that is parallel to the building direction. With this information the CCOCS FE model was created consisting of 35 beam elements per strut, with circular cross-section. The centers of gravity were drifted following the distribution

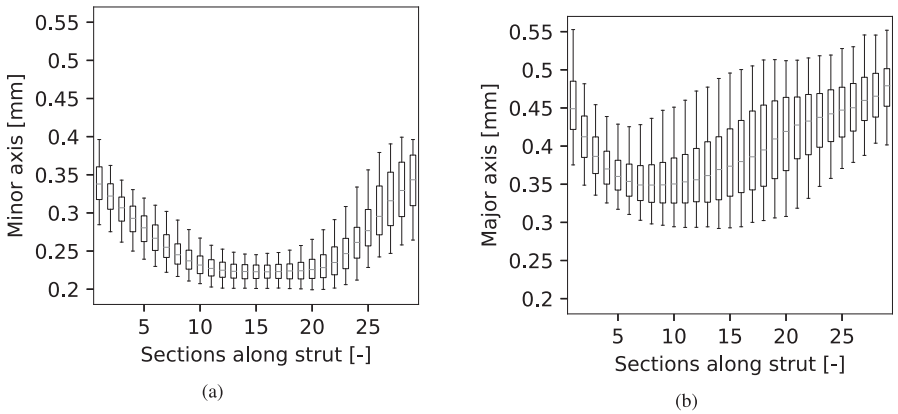

Fig. 11. Distribution of the (a) minor axis and (b) major axis of the elliptical cross-section along the strut axis.

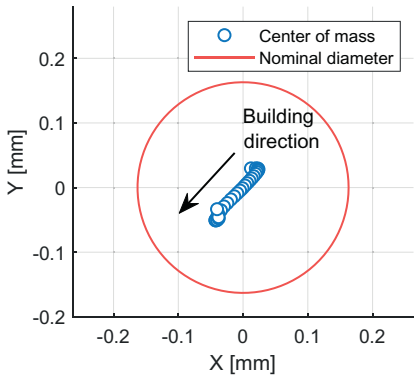

Fig. 13. Offset of the strut center of gravity along the length of the strut.

of mean values shown in Fig. 12. Combining the information of Figs. 10-12 the VEOCS FE model was generated.

3.2. FE results

The VCCS, CECS and CCOCS strut models were used to generate FE models of the diamond based lattice structure to evaluate the impact of a single geometrical imperfection on the anisotropic behavior of the diamond unit cell. The VECS and VEOCS strut models were used to evaluate the combined effect of the geometrical deviations on the anisotropic behavior of the diamond UC.

The homogenization process was performed on all the FE models generated to evaluate their directional stiffness and anisotropic coefficients from Eq. (2). Results of this analysis for different directions (i.e. [100], [001], [110], [011] and [111]) are reported in Fig. 14. Moreover, in order to visually express the impact of the different imperfections on the anisotropic behavior of the diamond unit cell, the homogenized Young's moduli were also plotted as 3 dimensional surfaces. These representations were used to clearly identify the strong and weak directions.

Fig. 15b plots the homogenized Young's modulus of the Nominal FE model showing the elastic anisotropy of the ideal diamond unit cell. The 3D surface plot clearly indicates a cubic anisotropic behavior, with shear directions (i.e.[111] directions) presenting the higher value of the Young's modulus and the orthonormal directions (i.e. [100], [010] and [001]) resulting the weaker directions. The principal planes XY and YZ present the same anisotropy. The high level of anisotropy is also indicated by the anisotropy coefficients A_{23} and A_{12}.

These results have been used as reference case and compared with the outcomes of the homogenization process performed on the other FE models. The comparisons have been made by means of polar plots obtained as indicated in Fig. 16: (i) the xy polar plot has been obtained intersecting the 3D directional stiffness surfaces with an ideal XY plane; (ii) the YZ polar plot has been obtained intersecting the 3D directional stiffness surfaces with an ideal YZ plane; (iii) the Ï€ polar plot obtained by intersecting the 3D directional stiffness surfaces with the plane formed by [111] and [110] directions.

3.3. Effect of change of cross-sectional area

The change of the cross-sectional area along the strut axis (Fig. 10) was used to generate the VCCS lattice structure. The homogenized Young's modulus surface presents a similar anisotropic behavior compared to the Nominal model. The polar plots shown in the first row of Table 1 indicate cubic anisotropy with equal stiffness in orthonormal directions and in shear directions. Comparing VCCS and Nominal results it can be noticed that VCCS presents higher stiffness along all the directions. The reason for this can be attributed to the fact that the nodes have bigger cross-section. As indicated by Van Hooreweder et al. [25], the maximum tensile and compressive stresses develop in regions close to the nodes of the struts. Higher dimensions of the cross-section in the nodal regions generate lower value of the nodal tensile and compressive stresses. Therefore, the distribution of the cross-section area along strut axis (Fig. 10) has a beneficial impact on the overall stiffness of the structure. Variation of the cross-sectional area also has an impact on the anisotropy of the diamond UC. As indicated in Fig. 13, the Young's, Poisson's and Shear ratios remain constant while A_{23} and A_{12} are reduced indicating a lower degree of anisotropy.

3.4. Effect of the constant elliptical cross-section

The homogenized Young's modulus surface of the CECS presents some difference with respect to the Nominal. The CECS doesn't present cubic anisotropy as the Nominal model. In fact, along the orthonormal directions different values of the Young's modulus are reported with [001] being stiffer than [100] direction as shown in Fig. 14a. The polar plots of the second row of Table 1 show that CECS possesses a lower stiffness and a lower anisotropy level across the YZ plane. This behavior is confirmed by the decrease of A_{23} coefficient and the increase of A_{12}.

The Poisson's and the shear ratios shown in Fig. 14b are systematically lower than the Nominal ones highlighting a shear stiffness transfer from YZ plane to XY plane.

These stiffness changes are the result of the change in cross-sectional shape. In fact the orientation of the major axis of the ellipse plays an

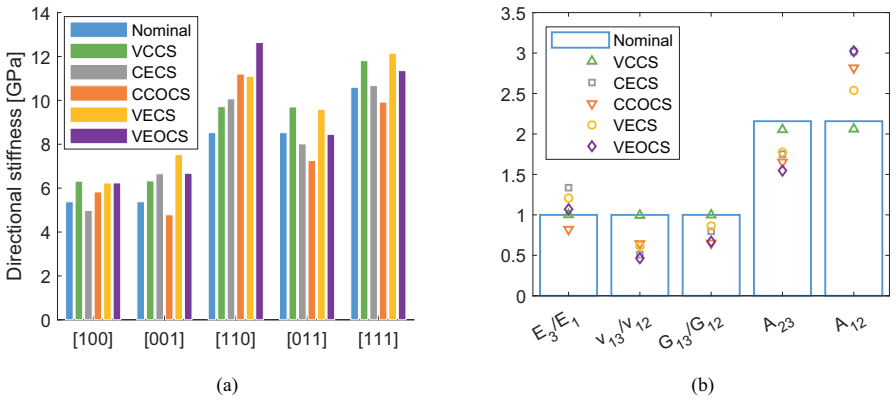

Fig. 14. (a) Directional stiffness along a particular direction (b) Anisotropic coefficients.

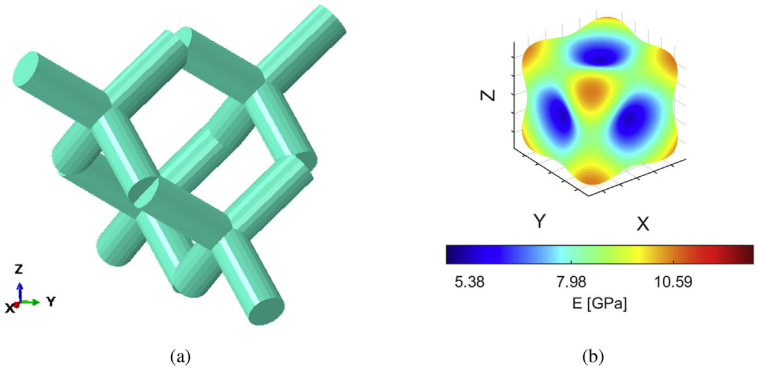

(a) (b)

Fig. 15. (a) Unit cell of Nominal FE model and (b) its directional stiffness.

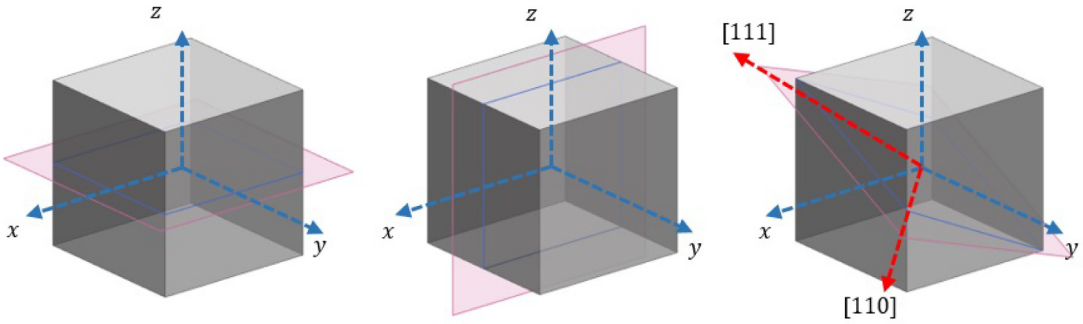

Fig. 16. Plane identification for (a) *XY* polar plot, (b) *XZ* polar plot, (c) π polar plot.

important role to explain this behavior. When the major axis is parallel to the load direction the structure is able to better absorb the external loads due to the higher inertia of the cross-section around the minor axis. On the contrary, if the load direction has the same orientation of the minor axis, the lower inertia makes the structure weaker.

3.5. Effect of the offset of the cross-section

The change in the position of the cross-section's centers of gravitiy has a significant impact on the mechanical properties of the lattice structure. The CCOCS directional stiffness of Fig. 13 and the polar plots of the third row in Table 1 indicate that this model does not present cubic anisotropy. The orthonormal directions perform differently with [001] direction being weaker than [100]. Moreover, the stiffer direction changes from the shear [111] direction to [110]. More information regarding the anisotropic characteristics of the CCOCS model can be extracted from Fig. 14. First of all, the decrease of A_{23} suggests higher isotropy on XZ and YZ planes whilst the increase of A_{12} indicates a higher level of anisotropy on XY plane. Secondly, ν_{13}/ν_{12} and G_{13}/G_{12} ratios suggest a stiffness transfer from plane YZ and XZ to XY plane.

The stiffness surface distribution of CCOCS differences with the nominal model can be attributed to the reduced inclination of the struts axis with respect to the building direction resulting from the wave distribution of the cross-sections offsets. According to the local stress method developed by Van Hooreweder et al. [25] for bending dominated diamond unit cells, the angle between the horizontal plane and the strut axis determine the stress distribution across the node. For diamond unit cells this angle is equal to 35.26 deg. A reduction of this angle causes a change of the distribution of the total load in axial and bending components. The axial load is a more efficient way to carry the loads, thus, the directions which maximize this component have a higher stiffness and lower bending stresses. The opposite happens for directions with a higher bending load component with respect to the nominal.

3.6. Combined effects: elliptical variable cross-section

The homogenized Young's modulus for the VECS model are shown in the fourth row of Table 1. The polar plots follow the same trend as the CECS indicating that the effect of the change in cross-section geometry largely impact the mechanical behavior of the diamond lattice structure. On the other hand, a general increase of the stiffness in all the direction can be observed. This is the result from the variability of the cross-sectional area.

The combined effect of the variable elliptical cross-section is also affecting the anisotropy coefficient expressed by Eq. (2). The anisotropy level across XZ and YZ planes decreases with respect to the nominal model as well as for the CECS model. On the contrary, the anisotropy level across XY plane increases but not as much as for the CECS model. This attenuation is due to the different stress distribution along the strut axis generated by the variation of cross-sectional area.

3.7. Combined effects: offset elliptical variable cross-section

The VEOCS homogenized stiffness presents the combined effect of the three different deviation typologies as shown in the last row of Table 1. The maximum directional stiffness is expressed by [110] directions and the weakest direction being [100] as effect of the offset of the cross-sections. The orthonormal stiffness are enhanced because of the effect of the change in cross-sectional area distribution. If compared with the nominal model, the VEOCS anisotropic behavior results

Table 1
Comparisons of VCCS, CECS, VECS, CCOCS and VEOCS directional stiffness with the Nominal.

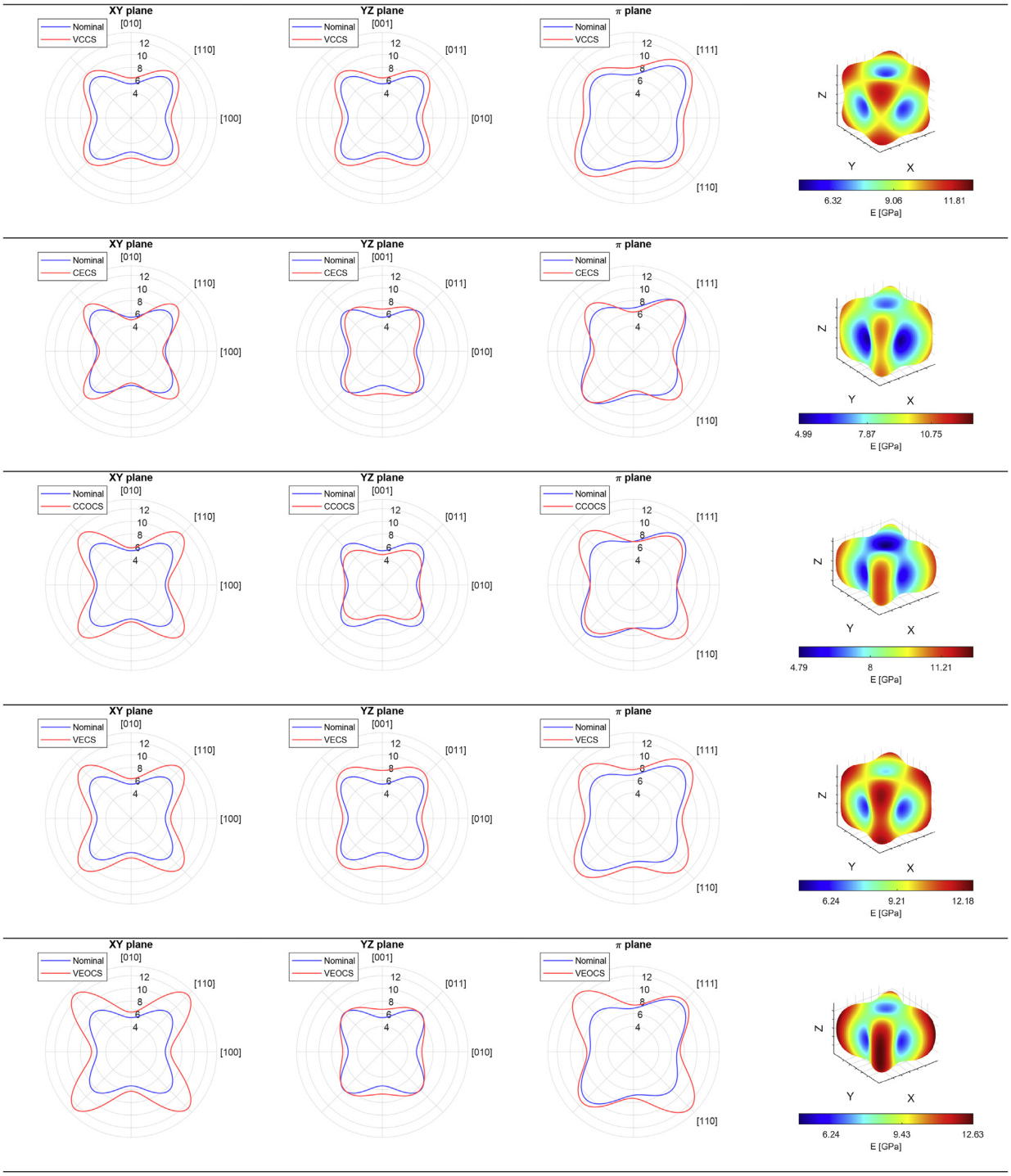

different: the YZ polar plot shows a very low degree of anisotropy, confirmed by the low value of A_{23}; on the other hand, XY and Ï€ polar plots indicate a very high anisotropic behavior. These two combined effects are the result of the lower struts inclination with respect to the horizontal plane superimposed to the change of the cross-sectional geometry.

3.8. Comparison with experimental results

Table 2 shows the homogenized stiffness evaluated for all the different FE models. Considering that the as-produced samples suffer from the three types of morphological imperfection, i.e. variation of cross-

Table 2
Comparison of the directional stiffness as predicted by different FE strategies.

	100	001	110	011	111
	(GPa)	(GPa)	(GPa)	(GPa)	(GPa)
Nominal	5,38	5,38	8,53	8,53	10,60
VCCS	6,32	6,33	9,72	9,70	11,81
CECS	4,98	6,66	10,07	8,02	10,67
CCOCS	5,83	4,79	11,20	7,26	9,92
VECS	6,24	7,53	11,10	9,59	12,15
VEOCS	6,24	6,68	12,64	8,45	11,36

sectional area, geometry and center of gravity, the FE model that better replicates the anisotropic behavior of the lattice structures is the VEOCS. In fact, the stiffest direction of the VCOCS structure changes from [111] in the ideal case to [110]. This result is in line with the experimental results presented in [8] in which [110] oriented structure was reported to have the highest stiffness.

This behavior is related to the combined effect of the center of gravity offsets and change in cross-sectional shape. These types of imperfections are mainly developed during the manufacturing process of the lattice structure due to dross formation underneath unsupported struts. As a matter of fact, during the L-PBF production of inclined struts, the laser tends to melt more powder than needed, elongating the strut cross-sectional shape along the build direction. Struts with small diameters and high diameter/length ratios, as the ones produced by Cutolo et al., are more affected by this phenomena. The change in cross-sectional shape produces also a change of the cross-section center of gravity with respect to the ideal case.

This phenomenon is not exclusive for Ti6Al4V nor for the diamond unit cell, and it can affect any lattice structure manufactured by L-PBF. Therefore, qualitatively similar effects are expected for other materials and unit cells, which are still to be studied. The procedure explained in this work can be used for other cases to assess the manufacturing deviations and predict their effect in the anisotropy by combining $\mu - CT$ data and FE simulations.

There are different approaches to overcome the morphological imperfections of these lattice structures: manufacturing parameters can be changed to try to reduce the dross formation in down-facing zones. On the other hand, the circularity of the cross-section can be improved by designing elliptical struts with reversed major and minor axes, in order to compensate the dross formation in manufacturing. Similarly, the cross-sectional area close to the nodes could be reduced in the design phase.

Finally, since these imperfections are more prevalent in small strut diameters, and with high diameter/length ratios, increasing the unit cell size while maintaining the relative density can be an option to obtain a lattice structure with equivalent mechanical properties and smaller deviations. Nonetheless, there are applications that require very small pore sizes, such as in the biomedical field. In this case, increasing unit cell size is not an option, and therefore, understanding the anisotropy of the lattice structures with small unit cell size and manufacturing deviations is of great importance.

4. Conclusions

Manufacturing imperfections have a significant impact on the anisotropy of lattice structures produced by L-PBF, and their effect is not limited to a uniform decrease of the stiffness and strength. These deviations change the elastic response of the lattice structure in a variable way depending on the load direction, and each of the studied imperfection types have a specific impact on the directional stiffness of the lattice structure.

The variation of the cross-sectional area increases the efficiency of the load carrying capacity for bending dominated lattice structures in any direction. This is caused by a higher bending load close to the nodes compared to the central part of the strut. On the other hand, the elliptical cross-section and the offset of the center of gravity have very direction dependent effects. The elliptical cross-section is especially significant in bending dominated lattice structures, since the directional stiffness change is driven by the higher inertia of the major axis compared to the minor axis. Regarding the offset of the center of gravity, the trend of the deviation is uniform enough to consider it as a change of the orientation of the strut axis and reduction of its angle with respect to the building plane. This varies the proportion of axial and bending load compared to the nominal structure. Thus, the anisotropy is affected because of the difference between the axial and bending stiffness of the beam.

Very clear trends can be observed on every deviation type depending on their proximity to the nodes. Therefore, it is necessary to take into account the position of the manufacturing deviations along the strut in order to explain their effect in the anisotropy. Moreover, these imperfections are highly dependent on the diameter to length ratio, unit cell size and relative density, as well as manufacturing parameters, and the observed trends are more significant when working closer to manufacturability limits.

The offset of the center of gravity has the most remarkable impact on the anisotropy because it changes the stiffest direction from [111] to [110], which can also be observed in experimental data. This has major implications when using this type of lattice structures in load bearing applications in which the structure needs to be oriented so as to minimize compliance.

Data availability

The raw and processed data required to reproduce these findings are available to download from: https://doi.org/10.5281/zenodo.3862128.

Declaration of Competing Interest

The authors declare that they have no known competing financial interests or personal relationships that could have appeared to influence the work reported in this paper.

Acknowledgement

The authors are grateful for the financial support for international movility of Fundación Bancaria “La Caixa” and to the “Interne Fondsen KU Leuven/Internal Funds KU Leuven”.

References

[1] J. Kruth, P. Mercelis, J. Van Vaerenbergh, L. Froyen, M. Rombouts, Binding mechanisms in selective laser sintering and selective laser melting, Rapid Prototyp. J. 11 (1) (2005) 26–36, https://doi.org/10.1108/13552540510573365.

[2] T. Maconachie, M. Leary, B. Lozanovski, X. Zhang, M. Qian, O. Faruque, M. Brandt, SLM lattice structures: properties, performance, applications and challenges, Mater. Des. 183 (2019) 108137, https://doi.org/10.1016/j.matdes.2019.108137.

[3] B. Nagesha, V. Dhinakaran, M.V. Shree, K.M. Kumar, D. Chalawadi, T. Sathish, Review on characterization and impacts of the lattice structure in additive manufacturing, Materials Today: Proceedings international Conference on Recent Trends in Nanomaterials for Energy, Environmental and Engineering Applications, 21, 2020, pp. 916–919, https://doi.org/10.1016/j.matpr.2019.08.158http://www.sciencedirect.com/science/article/pii/S2214785319331451.

[4] V. Papetti, P.D. Eggenschwiler, A.D. Torre, F. Lucci, A. Ortona, G. Montenegro, Additive manufactured open cell polyhedral structures as substrates for automotive catalysts, Int. J. Heat Mass Transf. 126 (2018) 1035–1047, https://doi.org/10.1016/j.ijheatmasstransfer.2018.06.061http://www.sciencedirect.com/science/article/pii/S0017931017355515.

[5] M. Ashby, The properties of foams and lattices, Philos. Trans. R. Soc. A Math. Phys. Eng. Sci. 364 (1838) (2006) 15–30, https://doi.org/10.1098/rsta.2005.1678.

[6] M.F. Ashby, Hybrids to fill holes in material property space, Philos. Mag. 85 (26) (2005) 3235–3257, https://doi.org/10.1080/14786430500079892.

[7] L. Gibson, M. Ashby, Cellular Solids: Structure and Properties, Pergamon Press, 1988.

[8] J. C. M. F.R.S, L. on the calculation of the equilibrium and stiffness of frames, Lond. Edinb. Dublin Philos. Mag. J. Sci. 27 (182) (1864) 294–299. doi:https://doi.org/10.1080/14786446408643668.

[9] R. Wauthle, B. Vrancken, B. Beynaerts, K. Jorissen, J. Schrooten, J.-P. Kruth, J. Van Humbeeck, Effects of build orientation and heat treatment on the microstructure and mechanical properties of selective laser melted ti6al4v lattice structures, Addit. Manuf. 5 (2015) 77–84, https://doi.org/10.1016/j.addma.2014.12.008http://linkinghub.elsevier.com/retrieve/pii/S2214860414000323.

[10] H. Soul, P. Terriault, V. Brailovski, The static and fatigue behavior of AlSiMg alloy plain, notched, and diamond lattice specimens fabricated by laser powder bed fusion, J. Manuf. Mater. Process. 2 (2) (2018) 25, https://doi.org/10.3390/jmmp2020025http://www.mdpi.com/2504-4494/2/2/25.

[11] A. Cutolo, B. Engelen, W. Desmet, B. Van Hooreweder, Mechanical properties of diamond lattice ti6al4v structures produced by laser powder bed fusion: on the effect of the load direction, J. Mech. Behav. Biomed. Mater. 104 (2020) 103656, https://doi.org/10.1016/j.jmbbm.2020.103656http://www.sciencedirect.com/science/article/pii/S1751616119314353.

[12] K. Lietaert, A. Cutolo, D. Boey, B. Van Hooreweder, Fatigue life of additively manufactured Ti6Al4V scaffolds under tension-tension, tension-compression and compression-compression fatigue load, Sci. Rep. 8 (2018) 4957, https://doi.org/10.1038/s41598-018-23414-2https://www.nature.com/articles/s41598-018-23414-2.

[13] L. Yang, C. Yan, H. Fan, Z. Li, C. Cai, P. Chen, Y. Shi, S. Yang, Investigation on the orientation dependence of elastic response in gyroid cellular structures, J. Mech. Behav. Biomed. Mater. 90 (2019) 73–85, https://doi.org/10.1016/j.jmbbm.2018.09.042http://www.sciencedirect.com/science/article/pii/S1751616118308506.

[14] S. Van Bael, G. Kerckhofs, M. Moesen, G. Pyka, J. Schrooten, J.P. Kruth, Micro-CT-based improvement of geometrical and mechanical controllability of selective laser melted ti6al4v porous structures, Mater. Sci. Eng. A 528 (24) (2011) 7423–7431, https://doi.org/10.1016/j.msea.2011.06.045http://www.sciencedirect.com/science/article/pii/S092150931100712X.

[15] H. Hassanin, Y. Alkendi, M. Elsayed, K. Essa, Y. Zweiri, Controlling the properties of additively manufactured cellular structures using machine learning approaches, Adv. Eng. Mater. 22 (3) (2020) 1901338 , arXiv:https://onlinelibrary.wiley.com/doi/pdf/10.1002/adem.201901338 https://doi.org/10.1002/adem.201901338https://onlinelibrary.wiley.com/doi/abs/10.1002/adem.201901338.

[16] C. Qiu, S. Yue, N.J. Adkins, M. Ward, H. Hassanin, P.D. Lee, P.J. Withers, M.M. Attallah, Influence of processing conditions on strut structure and compressive properties of cellular lattice structures fabricated by selective laser melting, Mater. Sci. Eng. A 628 (2015) 188–197, https://doi.org/10.1016/j.msea.2015.01.031http://www.sciencedirect.com/science/article/pii/S0921509315000453.

[17] C. Tan, S. Li, K. Essa, P. Jamshidi, K. Zhou, W. Ma, M.M. Attallah, Laser powder bed fusion of ti-rich tini lattice structures: Process optimisation, geometrical integrity, and phase transformations, Int. J. Mach. Tools Manuf. 141 (2019) 19–29, https://doi.org/10.1016/j.ijmachtools.2019.04.002http://www.sciencedirect.com/science/article/pii/S0890695519300392.

[18] M. Dallago, B. Winiarski, F. Zanini, S. Carmignato, M. Benedetti, On the effect of geometrical imperfections and defects on the fatigue strength of cellular lattice structures additively manufactured via selective laser melting, Int. J. Fatigue 124 (2019) 348–360, https://doi.org/10.1016/j.ijfatigue.2019.03.019http://www.sciencedirect.com/science/article/pii/S0142112319300957.

[19] H. Lei, C. Li, J. Meng, H. Zhou, Y. Liu, X. Zhang, P. Wang, D. Fang, Evaluation of compressive properties of SLM-fabricated multi-layer lattice structures by experimental test and Î¼-CT-based finite element analysis, Mater. Des. 169 (2019) 107685, https://doi.org/10.1016/j.matdes.2019.107685http://www.sciencedirect.com/science/article/pii/S0264127519301224.

[20] B. Lozanovski, M. Leary, P. Tran, D. Shidid, M. Qian, P. Choong, M. Brandt, Computational modelling of strut defects in SLM manufactured lattice structures, Mater. Des. 171 (2019) 107671, https://doi.org/10.1016/j.matdes.2019.107671http://www.sciencedirect.com/science/article/pii/S026412751930108X.

[21] L. Liu, P. Kamm, F. GarcÃ-A-Moreno, J. Banhart, D. Pasini, Elastic and failure response of imperfect three-dimensional metallic lattices: the role of geometric defects induced by selective laser melting, J. Mech. Phys. Solids 107 (2017) 160–184, https://doi.org/10.1016/j.jmps.2017.07.003http://www.sciencedirect.com/science/article/pii/S0022509616307608.

[22] L. Xiao, S. Li, W. Song, X. Xu, S. Gao, Process-induced geometric defect sensitivity of ti6al4v lattice structures with different mesoscopic topologies fabricated by electron beam melting, Mater. Sci. Eng. A 778 (2020) 139092, https://doi.org/10.1016/j.msea.2020.139092http://www.sciencedirect.com/science/article/pii/S0921509320301805.

[23] S.L. Omairey, P.D. Dunning, S. Sriramula, Development of an ABAQUS plugin tool for periodic RVE homogenisation, Eng. Comput. 35 (2) (2019) 567–577, https://doi.org/10.1007/s00366-018-0616-4.

[24] P. Vannucci, General Anisotropic Elasticity, 85, Springer Singapore, 2018 19–73, https://doi.org/10.1007/978-981-10-5439-6http://link.springer.com/10.1007/978-981-10-5439-6.

[25] B. Van Hooreweder, Y. Apers, K. Lietaert, J.-P. Kruth, Improving the fatigue performance of porous metallic biomaterials produced by selective laser melting, Acta Biomater. 47 (2017) 193–202, https://doi.org/10.1016/j.actbio.2016.10.005http://www.sciencedirect.com/science/article/pii/S1742706116305232.

Chapter 5

Discussion

Replacement surgery of the hip, knee or spine has not ceased to increase in recent years in OECD countries [182, 183, 182]. This increase is more pronounced in younger age groups (<65 years old), and the implants used in such interventions have only a limited lifespan [184]. This results in higher risk of revision surgery for younger age groups, and the combined trends of more interventions at earlier life stages is foreseen to greatly increase the number of revision surgery in years to come [185]. Therefore, novel implants are required to ensure longer durability.

The monolithic metallic implants used nowadays have stiffness values that are orders of magnitude higher compared to the bone stiffness. The result of this mismatch is the stress shielding effect, which occurs when the implant withstands most of the load, and causes bone resorption. This affects implant stability and osseointegration, which are essential for the durability of the implant. Furthermore, the lack of stability causes pain to the patient and may lead to the loosening of the implant or a fracture of bone. Replacing solid implants by porous ones enables the use of well-known biocompatible materials while drastically reducing the stiffness of the implant, avoiding the stress shielding and subsequent bone resorption. Thus, lattice structures offer the possibility to design such porous implants that can improve implant longevity.

While several challenges remain unsolved so far, continuous progress is being made in the applicability of additively manufactured lattice structures in orthopedic implants. This has enabled new design concepts that were unprecedented, and the research in manufacturing as well as in modeling techniques brings us closer to personalized scaffolds with tailored mechanical properties. The primary goal of this work is to contribute to this purpose by creating new tools to enable the design and manufacturing of suitable lattice structures with controlled mechanical properties. The three main issues that were planned to be covered in this thesis are:

- Develop tools that enable the optimal design of porous structures based on patient-specific bone requirements.
- Analyze the behavior of porous structures under cyclic loads.
- Understand the effect of manufacturing deviations on the mechanical properties of lattice structures.

Develop tools that enable the optimal design of porous structures based on patient-specific bone requirements

As explained above, lattice structures that match the bone properties reduce the stress shielding effect and have the potential to avoid bone resorption and the loss of long-term implant stability. DICOM

images and CT scans of the bone can be used to derive patient- and site-specific bone geometry and mechanical properties [181], and this data can be the starting point for the patient-specific implant design. This underlines the necessity of a design tool of lattice structures that enables to tune their mechanical properties according to bone data.

To do so, a more thorough analysis of the elastic behavior of the lattice structures must be carried out, by modeling the whole macroscopic stiffness matrix. Advanced analytical and numerical models are required to perform such an analysis, as well as experimental procedures necessary to validate such models.

The analytical and numerical models can be used to predict or to design the effective mechanical properties of lattice structures. Exhaustive analytical solutions can replicate the results of FE beam models, thus providing a useful tool for lattice structure design. Nonetheless, these expressions can be cumbersome to calculate, and their accuracy is limited in theory due to the reduced slenderness of the struts when the relative density increases, as the assumptions made in beam models do not hold.

Nevertheless, these analytical expressions are often closer to experimental stiffness values compared to other more complex numerical models, as it occurs in [67, 69, 186]. Even if analytical models do not consider the stiffness at the nodes and the struts are not slender enough to hold the assumptions of the Timoshenko beam model, the manufacturing deviations reduce the stiffness so that these two effects cancel each other.

In **Paper A**, a new analytical model was developed for a modified FCC unit cell, namely FCCm, accounting for beam stretching, bending and rotation. This enabled to obtain a very accurate orthotropic model with the elastic constants of the structure, so that its elastic behavior could be predicted in any orientation or under complex load conditions, which is the case in many anatomical sites.

In addition, the variability of its aspect ratio (unit cell height-width ratio) gives the designer some freedom to modify the mechanical properties of the structure depending on the load case, enabling to have the same stiffness in the three orthogonal directions, or some stiffer directions at the expense of the other counterparts. The FCCm structure was compared to other structures, showing a stiffness in the range of other bending dominated unit cells, and lower than for stretch dominated structures.

Transversely isotropic structures are another type of structures that may be of interest for implants design. Because of its architecture, cortical (dense) bone is stiffer and stronger along the anatomical axis of the bone, while it is more compliant and weaker in the transverse plane. On the other hand, trabecular bone in specific locations may also have a principal load orientation. As a result of the mechano-biological adaptation, the stiffness and strength in such direction are higher than in the transverse plane. Therefore, mimicking the transverse isotropy of bones can increase the efficiency of the lattice structure.

In **Paper C** a novel semi-analytical model was presented, which enables the tuning of the elastic behavior of some stretch dominated structures to be transversely isotropic. It is shown that the orthotropic stiffness matrix of any stretch dominated structure under affine deformation can be modelled with a maximum of 6 independent elastic constants. Some structures were proposed, and an ellipsoidal directional stiffness was set as a design objective, with a prescribed anisotropy ratio between the principal directions. Even if the stiffness matrix was the same for different topologies, the transverse isotropy was not fulfilled for strength, neither the strength ratios in the main orthogonal directions. The semi-analytical model was validated for the proposed VFCCBCC structure by means of numerical models, showing very good correlation of elastic constants for low relative densities, and the accuracy decreased for higher densities. On the other hand, the semi-analytical model predicted the strength of the structures consistently in [001], and [110], the accuracy was a bit lower in [100], [101] and [111].

Experiments were carried out, and specimens were compressed in directions [100], [110] and [001]. The absolute values of stiffness and strength were not comparable to the semi-analytical model due to the manufacturing defects of the specimens. Nevertheless, the transverse isotropy and the E3/E1 ratio were close to the designed values for one of the structures. Finally, the semi-analytical model was used to analyze the stiffness of the structures in different orientations and for three constituent materials, comparing them with the stiffness ranges of different bone sites.

Analyze the behavior of porous structures under cyclic loads

Increasing the fatigue life of porous scaffolds is one of the current challenges in AM, and the strength of the structures under cyclic loading is of paramount importance for their use in orthopedic implants. The surface roughness, internal defects and complex geometries of the scaffolds lead to complex stress states and stress concentrations that dramatically reduce the fatigue strength of lattice structures compared to their solid counterparts [103]. One method to increase the fatigue resistance of the structures is to apply post heat-treatments that reduce residual stress and internal porosity, and change the microstructure of the material. Therefore, the study of AM lattice structures under cyclic loads is also one of the objectives of this thesis. **Paper B** analyses the quasi-static and fatigue behavior of FCCm structures with different relative densities to study its effect. The effect of hot isostatic pressing (HIP) on the mechanical properties of the structures was also studied, and the stiffness based fatigue failure criterion is presented as a more useful criterion for load bearing applications, which is the case of orthopedic implants.

Furthermore, many different tools for fatigue life predictions were compared. In the literature, S-N curves are commonly normalized with the yield strength. However, in this work it was observed that this method is inaccurate as the normalized curves do not fit well into a single one. Thus, in this paper the fatigue life prediction based on the analytically obtained maximum tensile stress (local stress method) was modified from the literature to cover a wide range of relative densities and it shows very good agreement with the experimental data. Finally, a fatigue failure surface was presented to integrate the effect of relative density, stress level and elapsed cycles in a single expression, and it showed good correlation with the experiments.

Understand the effect of manufacturing deviations on the mechanical properties of lattice structures

As mentioned in the previous chapters, and discussed in more detail in the next section, a difference between numerical and experimental results can be found in this work in particular, and in literature in general. Some of the errors are due to the geometry deviations intrinsic to the current metal additive manufacturing process. The small features required to design meta-biomaterials push the limit of the SLM machines, and the restrictions imposed by the arising inaccuracies need to be addressed as a necessary step prior to the widespread application of this technology.

The **Paper D** focuses on the role of manufacturing deviations in the quasi-static mechanical properties of the lattice structures in different directions and is based on previous work by Cutolo et al. [63]. In their work, Cutolo et al. compressed diamond structures in [001], [110] and [111] directions, and they concluded that the [110] direction was the stiffest and strongest one for their structure. Nonetheless, it can be easily concluded from numerical analyses that the stiffest and strongest one should be the [111] orientation for an ideal diamond structure. To understand the underlying phenomena, the μCT scans of the structures were used to gather data of the cross-section of the struts and to create a beam finite element model of the manufactured structure.

Each cross-section was fitted to an ellipse, while also accounting for the deviation of the center of mass of the cross-section along each strut. The effect of each imperfection type was studied as well as the combined effects. It was observed that the major axis of the ellipse was aligned with the building direction of the structure, concluding that this lack of accuracy resulted from the dross formation in the down-skin surfaces. Furthermore, this deviation affected the position of the center of mass, so that the center of mass deviated also in the building direction. Another aspect of the manufacturing imperfections was that they greatly depended on their position along the strut: the closer to the nodes, the greater the deviation from the theoretical values. In addition, the shape of the statistical distribution of the imperfections was also dependent on the proximity to the nodes.

Due to their clear directionality, the elliptical cross-section and the offset from the center of gravity affected not only the absolute values of the mechanical properties, but also the anisotropy of the structure. The elliptical cross-section adds inertia in the building direction, which is particularly relevant in bending dominated structures. On the other hand, the offset from the center of gravity was so stable that could be compared to a change of the orientation of the strut, thus modifying the axial and bending load ratio, with great influence on anisotropy.

When all the deviations were considered and implemented in the finite element model, the stiffest direction changes from [111] to [110], as in the experiments of Cutolo et al. [63]. Therefore, the imperfections do not reduce the stiffness of the structures uniformly, but they affect their anisotropy, and thus these deviations should be studied to design lattice structures with tailored anisotropy. In the design process, this helps to identify stiffer and more compliant directions, and to orient the structure to better adjust to physiological loads.

5.1 Analytical vs Numerical vs Experimental results

As already stated, the differences between the analytical or numerical and experimental values are an important research topic for lattice structures. Apart from the mentioned manufacturing imperfections, analytical and numerical models have limitations to accurately describe the mechanical properties of the structures, and different possibilities are available with a wide range of complexity.

Analytical models for lattice structures are based on beam models, both Euler-Bernouilli and Timoshenko beam models. These models are commonly used for slender elements and they can be used to model lattice structures. In general, the struts are not too slender and shear deformations are not negligible, thus Timoshenko beam model is preferred. These analytical models can be accurate for low relative densities, but as the relative density of the lattice structure increases, the strut cannot be modeled as a beam anymore, and the models tend to underestimate the lattice structure stiffness.

When it comes to numerical models, beam FE models are equivalent to analytical models, with the possibility of increasing the complexity of the model to consider manufacturing deviations, or to study the energy absorption or the buckling of structures in more detail. Nevertheless, the limitations of the beam model concerning high relative densities and non-slender struts are equivalent to the analytical models. FE models with 3D elements, on the other hand, have the potential to predict the effective mechanical properties of lattice structures with greatest accuracy (specially for high relative densities), and can be useful to validate analytical models such as in **Paper C**.

It should be noted that many numerical and analytical models consider lattice structures with ideal geometries and properties. However, it is well known that the additively manufactured structures have some geometric errors which are intrinsic to the manufacturing process, and they do affect the mechanical

properties of the structures. In fact, one of the major challenges is to achieve the target relative density of the scaffolds. The imperfection types are various (discussed in **Paper D**), and highly dependent on manufacturing strategies. The final shape of the struts will be different if they are manufactured by melting a single point in each layer, as in VFCCBCC, in which some struts resemble to interconnected spheres rather than to a cylinder; or if the laser actually follows the contour of the cross-section of the strut, as in FCCm, in which a lot of excess energy created dross that unintentionally increased the relative density of the structure.

The imperfections potentially affect more to stretch dominated structures, because such deviations may change the loading type of the strut from pure axial load to combined axial and bending. If bending load appears in a supposedly pure axially loaded strut the stiffness loss is much higher than simply having lower bending stiffness due to manufacturing deviations in a bending dominated structure. Furthermore, since the main load of the structures are compressive, buckling plays an important role in the strength of the structures, and the imperfections in manufacturing can dramatically reduce the buckling load of stretch dominated structures.

The manufacturing deviations can also affect the anisotropy of the structures, as explained in **Paper D**, because the imperfections are usually orientation dependent. This issue also arises in **Paper C**, in which the anisotropy of structure A was different from structure B, which was closer to design values.

Furthermore, in **Paper B** very different outcomes were observed in the comparison between solid FE models and quasi-static experiments: while the stiffness values show bad correlation, the strength is predicted with acceptable accuracy. In addition, the development of plastic deformation was analyzed in the compression process, showing that plasticity appears way before the 0.2% offset stress criterion. This is the most used criterion in literature, and it must be considered that the concept of yield strength has different implications compared to solid materials. Hence, the acceptable macroscopic stress values might be lower than the calculated yield strength if plastic deformation is to be avoided.

Figure 5.1 shows the analytical, numerical and experimental results for the FCCm unit cell (**Paper A** and **Paper B**) and the VFCCBCC unit cell (**Paper C**). It can be appreciated in Figure 5.1a, that for low relative densities the analytical model is in good agreement with the solid finite element model, while for large relative densities the difference is greater. In theory, analytical models and beam FE models should be accurate for low relative densities , while for large relative densities solid FE models should be more accurate. However, solid FE models based on the designed geometry rather than in the manufactured one are not sufficiently accurate when comparing with experimental values as it can be observed in Figure 5.1a. This is due to the stiffness reduction of the experimental structures due to manufacturing imperfections. FE simulations can be considered a sort of upper bound of the stiffness for perfectly manufactured structures, while the analytical model gives a better approximation of the actual behavior.

However, the semi-analytical and numerical models of **Paper C** are not able to predict the experimental Young's moduli of the VFCCBCC structure, as depicted in Figure 5.1b. The semi-analytical model clearly overestimates the stiffness of the actual structures, as occurs with the solid FE model. Note that in this case, as opposed to Figure 5.1a, semi-analytical model is in good agreement with the solid FE model. This occurs because whereas in the semi-analytical model the relative density was adjusted to exclude the double counting of mass at the nodes, for FCCm the length of the struts was considered constant regardless the relative density.

Thus, the accuracy of the analytical model of the FCCm structure is based on the undesirable effect of the manufacturing imperfections, and this situation is expected to change as the manufacturing quality of lattice structures increases, limiting the use of the model for high relative densities. In addition, the

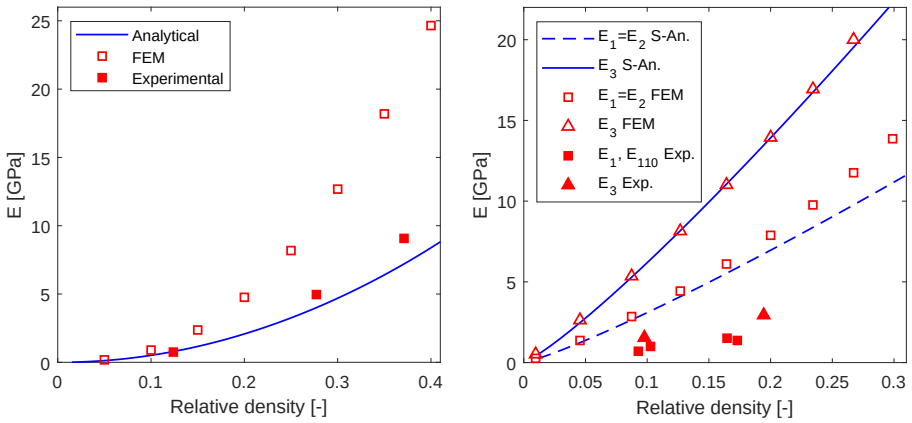

Figure 5.1: Young's moduli of a) FCCm and b) VFCCBCC structures for (semi) analytical and numerical models compared to experimental values.

semi-analytical model of VFCCBCC is only able to model the mechanical behavior of ideal structures, and the model will not be accurate as long as the manufacturing limitations are not overcome. Therefore, analytical models can be useful to design structures with prescribed elastic properties and orthotropic characteristics, but these models need to be adjusted according to an experimental validation process.

Regarding strength, the numerical model of VFCCBCC also overestimates the yield strength of the structure, while the numerical FCCm structure gives a good approximation of the yield strength. This might be explained because the manufactured structures do not have sharp edges at the intersections of the struts, which compensates the rest of the irregularities of the geometry.

In any case, the lack of robustness of as-designed numerical models present a significant challenge to design structures with tailored properties, and manufacturing and experimentation are necessary so far to confidently assess mechanical properties of the structures.

There are different methods to consider these imperfections in simulation tools to better predict the mechanical behavior of lattice structures. Methods that explicitly account for the actual shape of the structure are based on μCT data as in [139, 136, 124]. These methods are able to predict the actual behavior of the structures, but require costly equipment and handling of large sets of data. Moreover, it is difficult to use this information in the design phase to create scaffolds with tailored mechanical properties, and they are a mere sort of accurate descriptive tool for the structures.

On the other hand, it is possible to implicitly account for the manufacturing deviations by testing single struts and obtaining their E modulus and yield strength, which is much lower than that of the bulk material, as done in [187, 130, 188], and using those values as constituent material parameters. The advantage of this procedure is that the numerical models can be very simple, and it can be applied in the design process to predict and tailor the mechanical properties of the structure. Furthermore, the simplicity of the method enables its use in analytical models as done in the case study of the knee replacement with stiffness characteristics of proximal tibia of **Paper C**.

This method was applied in the models of Figure 5.1, assigning a Young's modulus of 37.5 GPa for Ti6Al4V (instead of 129 GPa) and 67.5 GPa for SS316L (instead of 190 GPa) [49]. The results for analytical and numerical models are depicted in Figure 5.2, compared with the same experimental values. For the FCCm structure (Figure 5.2a) the solid FE model is closer to the experimental values after the adjustment, at the expense of totally losing the accuracy of the analytical model for large relative densities. On the

other hand, in the case of VFCCBCC structure (Figure 5.2b) both the FE model and the semi-analytical model are closer to the experimental values compared to Figure 5.1b. In any case, it can be seen that even if numerical results are closer to the experiments, they are still not completely accurate, and obtaining the alternative stiffness values should be done considering strut dimensions and their manufacturing strategy. Another drawback of this method is the limitation to include anisotropy variations in the models, and assuming that all struts experience the same degradation of properties in manufacturing, regardless their orientation or diameter. Furthermore, the previous analysis of individual struts must be carried out, which adds complexity to the design process.

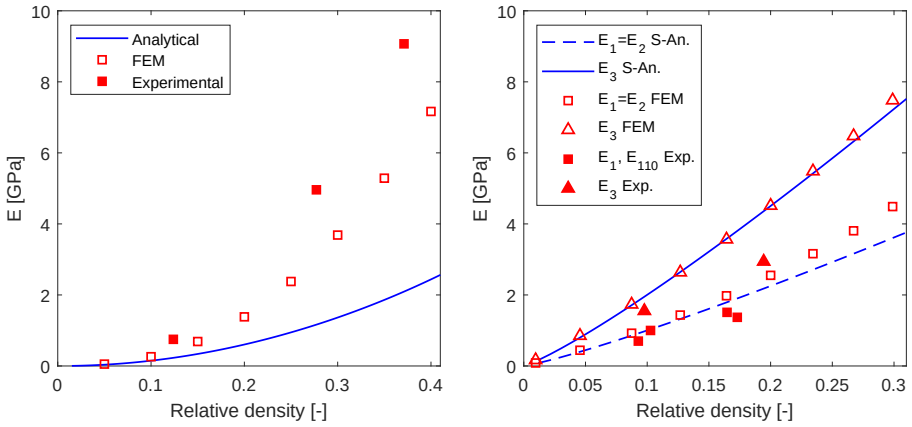

Figure 5.2: Young's moduli of a) FCCm and b) VFCCBCC structures for (semi) analytical and numerical models with adjusted Young's modulus from [49], compared to experimental values.

In summary, the numerical and analytical models give valuable information about the mechanical properties of lattice structures, even if the ideal models alone are not accurate enough. Therefore, it is still necessary to include the manufacturing deviations in such models to have a complete picture of the mechanical behavior of the structures and to design metamaterials with engineered mechanical properties.

As discussed, it is still a challenge to include the manufacturing deviations within the design process in a cost-effective manner while accounting for all the effects of such deviations on the mechanical properties of the structures. One alternative would be to reduce the impact of such imperfections by building larger unit cells, which has the cost of increasing the pore sizes within the structure, and this has a detrimental effect on the capacity of the bone to grow within the implant.

Another possible solution, which would be the optimal one, is to improve the lattice structure AM process to reduce the imperfections. The optimization of the parameters used in the manufacturing process, such as laser power, velocity, hatch distance or scan strategy are a necessary preliminary step to ensure quality and repeatability of the process. In addition, this optimization process should be specific not only for each unit cell, but also for each relative density, since the morphology has great variations in each case. This greatly increases the cost of the implementation of lattice structures in functional load bearing parts as the iterative process of manufacturing the structures, inspecting and assessing the accuracy, and adjusting manufacturing parameters is a very resource intensive process.

5.2 Lattice structures for orthopedic implants

The aim of this work is to propose lattice designs that can be used for bone tissue engineering, focusing on their mechanical properties to try to mimic bone tissue. The suitability of lattice structures as porous biomaterials depends on various aspects concerning the biocompatibility, capacity to promote bone ingrowth and vascularization, and mechanical properties of the scaffold. While biocompatibility can be ensured by using certain materials (pure titanium and its alloys, CoCr, SS316, tantalum, PEEK, etc.), depending on the bone site and its mechanical requirements, the optimal configuration to promote bone ingrowth and vascularization within the implant remains unclear. Nevertheless, it has been well documented that the relative density and pore size are key factors apart from permeability and curvature of the scaffold [189, 190].

The capacity of the structures for bone ingrowth and vascularization depends on the the pore size. Even if the literature is controversial on the topic, pore sizes between 300 μm and 800 μm are recommended to ensure nutrient transport within the scaffold [190, 179]. While smaller pores offer an improved cell attachment, larger pores avoid pore occlusion and enhance cell growth [191, 177].

In **Paper A**, due to manufacturability reasons, the pore sizes of the unit cells were above 1 mm. However, it must be said that the FCCm structure does not have a unique pore size, as depicted in Figure 5.3. Therefore, it can be considered as a hierarchical porous structure with different pore sizes, and considering only the biggest pore size (as done in **Paper A**) might be a simplistic approach to assess its bone ingrowth and vascularization capabilities. Regarding the VFCCBCC unit cell, the manufacturing constraints impose larger unit cell sizes than for FCCm to ensure manufacturability. Nonetheless, the high strut interconnection in the VFCCBCC structure results in smaller pores compared to the unit cell size (see Figure 5.3), and therefore they can be in the range suitable for bone formation.

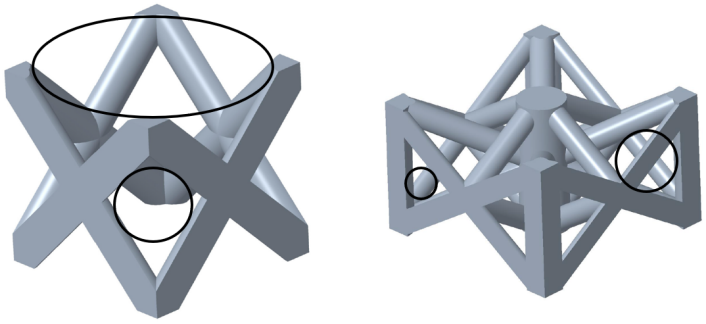

Figure 5.3: Pores of FCCm (left) and VFCCBCC (right) unit cells.

When it comes to the quasi-static mechanical properties of the scaffolds, it is known that matching implant stiffness to bone stiffness can reduce the stress-shielding effect. This work provides some solutions to match the stiffness of bone tissue in different sites, as already shown in **Paper A** and **Paper C**. Moreover, bone tissue is usually considered an orthotropic material [154, 71], with variable stiffness in different directions to optimize its functionality under the complex loads it withstands. The proposed structures do not have elastic cubic symmetry, which is the case of the commonly studied simple cubic, BCC, diamond, etc. Instead, the developed mechanical models of FCCm and VFCCBCC structures allow more variability of their mechanical behavior to adapt to different requirements.

Thus, a more detailed characterization of the elastic response of the lattice structures is provided to account for such variability, considering stiffness in various directions and obtaining the effective

orthotropic stiffness matrix of the unit cells. This is relevant for a more comprehensive analysis of the structures under realistic conditions, with complex loads of bone tissue in different sites. This thorough analysis is useful even for supposedly more simple unit cells such as diamond, which was proved not to have cubic symmetry of the elasticity due to manufacturing deviations.

Figure 5.4 shows the stiffness and yield strength values of the FCCm and VFCCBCC unit cells for different relative densities, as well as some other unit cells in the literature, comparing them with trabecular and cortical bone. The semi-analytical model of VFCCBCC was assigned different constituent materials as done in **Paper C**, with Young's modulus equal to 37.5 GPa for Ti6Al4V, 61.5 GPa for 316L stainless steel (implicitly considering manufacturing deviations), and 4 GPa for PEEK [192, 49]. The strength values are 610 MPa, 450 MPa and 70 MPa for Ti6Al4V, 316L stainless steel and PEEK, respectively [192, 49].

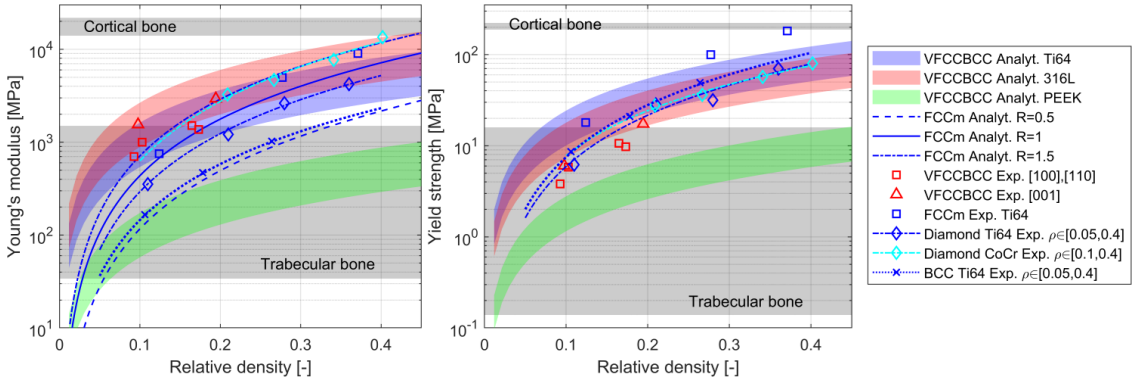

Figure 5.4: Young's modulus and yield strength of different unit cells in this dissertation and literature [69, 121], compared to bone range obtained from [152, 153, 71, 193, 143].

The semi-analytical model of VFCCBCC unit cell shows how different stiffness ranges can be achieved varying the constituent material. For Ti6Al4V and 316L the stiffness values are in general higher than trabecular bone, without reaching cortical bone stiffness. On the other hand, PEEK covers a wide range of stiffness of trabecular bone. For FCCm unit cell the analytical model of the stiffness in building direction (E_3) was included for 3 different aspect ratios (R=0.5, R=1, R=1.5), showing that R=0.5 can cover all the range of trabecular bone, and R=1.5 even reaches cortical bone stiffness for high relative densities (ρ^*>0.4). These results are in line with other structures and materials found in literature, with diamond CoCr reaching cortical bone stiffness, and BCC made of Ti6Al4V very close to FCCm with R=0.5.

Regarding strength, the analytical models of metallic VFCCBCC structures are stronger than trabecular bone in general, or at the upper part of the bone range, without reaching the cortical bone values. However, the experimental values of VFCCBCC are below the expected values, and fall within the trabecular bone strength. PEEK structures are in the range of trabecular bone. On the other hand, experimental FCCm structures are stronger than trabecular bone, and even reach the strength of cortical bone in denser structures. The yield strength values in literature have similar tendencies, with structures in the bone range for low relative densities, and above for intermediate and high relative densities.

Stiffness and strength must be considered together with design scaffolds for tissue engineering. The objective of the structures is to mimic the stiffness of the bone, while the strength needs to be equal or higher than the host bone to ensure structural integrity. Furthermore, these variables are highly dependent on bone site. Figure 5.5 depicts the stiffness and strength of various types of bone in the direction of their principal load, and compares them to the stiffness and strength of the FCCm and VFCCBCC structures, along with some other examples in the literature. Stiffness is represented in the X axis, and strength is

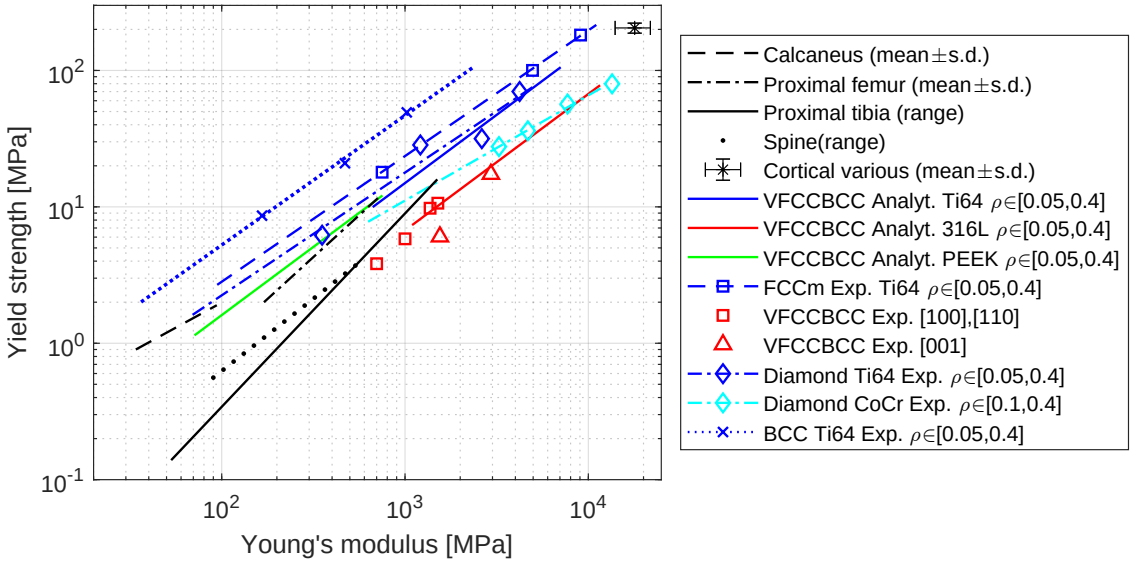

Figure 5.5: Associated stiffness and strength values for different unit cells studied in this dissertation and literature [69, 121]; and various bone sites [152, 153, 71, 193, 143].

given in Y axis. Thus, an ideal lattice structure for bone substitution should lay above the line in the figure.

The semi-analytical model of VFCCBCC shows how the suitability may change with base material. The strength/stiffness ratio of 316L stainless steel is lower than any trabecular bone site, which is not ideal for bone tissue engineering. Furthermore, the experimental strength/stiffness ratio is slightly below the analytical one (bear in mind that only corresponds to [001] orientation). On the contrary, the strength of the Ti6Al4V VFCCBCC structures is always above the bone strength for the same stiffness level, even if only a small portion of the bone stiffness is covered. PEEK is more suitable for bone sites with very low stiffness values, and the strength of the scaffold exceeds the one of any trabecular bone sites except the calcaneus. Therefore, Ti6Al4V and PEEK are better constituent materials compared to 316L stainless steel for stiffer and softer trabecular bone, respectively. On the other hand, the experimental values of the FCCm structure indicate that this structure is suitable for orthopedic implants due to its higher strength in stiffness levels corresponding to trabecular bone. Regarding other lattice structures in literature, BCC can be considered a suitable candidate for trabecular bone substitution. It must also be noted that the Ti6Al4V diamond lattice has a higher strength to stiffness ratio compared to its CoCr counterpart.

Apart from quasi-static yield strength, the strength of lattice structures under cyclic loads is a crucial parameter to assess the applicability of such structures in orthopedic implants. The use of 10^6 cycles as a measure for required fatigue strength is widely spread in literature, considering that the average patient walking activity is around 2 million cycles per year (52 weeks), and that the mean bone fracture is healed in around 16 weeks for healthy patients. Therefore, bone tissue is expected to grow within the implant before reaching 10^6 cycles [175, 194, 84].

The complex geometric features of strut based lattice structures create stress concentrations that greatly diminish the fatigue strength of structures compared to their constituent material. Thus, the fatigue strength of the FCCm structure lays between 27% and 31% of the yield strength of the structures, somewhat above most of the reported fatigue strength at around 20% [195] for Ti6Al4V strut based structures, even if it can be enhanced through different post-treatments [87]. Furthermore, Hedayati et al. [196] analyzed how the fatigue strength increased for lattice structures embedded in various resins, e.g. epoxy or polyurethane,

to simulate the joint strength of the structures with newly formed bone, and concluded that the fatigue strength increases up to 8 fold.

However, it is yet to be determined if new bone formation can fill the porous scaffolds in an equivalent manner and cause a comparable increase in fatigue strength, and a comprehensive assessment of fatigue life based on the bone ingrowth and its characteristics is very complex and time-consuming [196]. In addition, the fatigue strength required for a scaffold will greatly depend on its location and the loads it withstands, which are patient and injury specific. Therefore, numerical and analytical tools have to be developed to study the fatigue life of porous scaffolds in specific bone sites. In the case of load bearing applications, the 10% stiffness loss criterion presented in **Paper B** as well as the modelled failure surface can be useful to determine the suitability of different scaffolds as porous biomaterials.

All things considered, the proposed structures can be used in orthopedic implants and bone tissue engineering by adjusting the material properties, the topology of the structures, and their relative density, to create scaffolds suitable for different bone sites. Nonetheless, more research is still necessary to obtain optimal designs that consider quasi-static and fatigue mechanical properties on the long term, as well as variables like the permeability and the osseointegration capabilities of the structures.

Chapter 6

Conclusions

The main goal of this work is to expand the set of tools available to create lattice structures that are suitable to be implemented in orthopedic implants. Thus, the main contributions of this work regarding their applicability are as follows:

Analytical models to design lattice structures to be applied in orthopedic implants

The analytical model of the effective stiffness matrix was obtained for FCCm and VFCCBCC unit cells, including design variables that enable a more flexible design of the structures to match the mechanical properties of bone. These models can be implemented in optimization algorithms to design implants with graded properties and adjusted to each patient. The analysis of the FCCm lattice structure shows that it is suitable to be used in orthopedic implants due to its stiffness level, which is in the range of trabecular bone. Furthermore, the strength of the structure is higher compared to different bone sites.

On the other hand, stretch dominated structures with high connectivity of struts can be designed to have macroscopic elastic transverse isotropy, enabling to align the main load of bone with the principal direction of the structure to improve osseointegration of the implant. Furthermore, the semi-analytical model can be used to match stiffness values of bone sites with high anisotropy. The anisotropy of the manufactured VFCCBCC structure has a variable accuracy, which underlines the importance of manufacturing deviations. Apart from the VFCCBCC structure, a set of possible unit cell designs are proposed to create transversely isotropic structures.

Characterization of the fatigue behavior of lattice structures

A set of tools was developed for an improved prediction of fatigue life of lattice structures, and a more restrictive fatigue failure criterion was established for load bearing applications based on the stiffness loss of the structures. The analytical model based on local tensile stress was adjusted to implement it in a wide range of relative densities. Furthermore, a failure surface was proposed for fatigue life prediction of the structures. These tools enable a easier implementation of fatigue constraints in the design of lattice structures for orthopedic implants.

Effect of manufacturing imperfections

The manufacturing deviations have a very important effect on the final mechanical properties of the structures, and severely limit the predictive capabilities of analytical and numerical models based on

designed geometries. Apart from decreasing the absolute stiffness and strength values, the imperfections have a clear directionality, and they also affect the anisotropy of the structures. Thus, a procedure to predict such anisotropy changes was implemented in a diamond structure, showing good correlation with experimental values.

6.1 Future work

Despite the potential benefits of using lattice structures in orthopedic implants to prevent stress shielding while enhancing osseointegration, their complex nature and the uncertainties regarding some of their properties are still a barrier for the widespread adoption of lattice structures in the medical field. Even if this work has been devoted to shed some light on the mechanical complexities of the structures, some important aspects are still unknown, and should be further studied for a more comprehensive understanding of the nature of lattice structures:

- The discrepancies between the analytical or numerical models of FCCm and VFCCBCC structures with their experimental values should be addressed to safely design and use them in implant applications. This can be achieved by analyzing the actual manufactured structures, and by controlling the whole workflow from design, manufacture, defect analysis and testing, so that the models and defects can be iteratively adjusted.
- This work is limited to compressive loads, while bending or shear loads may also arise in many bone sites. The behavior of lattice structures under those types of loads (or their combinations) is still not very well understood, and studying the quasi-static as well as the fatigue properties under such loads is required.
- A study of bone ingrowth within the FCCm and VFCCBCC structures needs to be carried out before introducing them in an implant design. More generally, bone ingrowth has a very positive impact on the stability of the implant, and more extensive research, with in vitro and in vivo studies are needed to solve some of the discrepancies between different studies regarding optimum pore size, shape, porosity and permeability.
- The effect of bone ingrowth in the mechanical characteristics of the implant-bone ensemble was not considered in this work. As bone grows within the implant, load carrying capacity is increased, as well as its fatigue strength. This increases the available design possibilities, and biodegradable porous implants can be considered in cases where bone is capable of healing completely.

Chapter 7

Bibliography

[1] L. J. Gibson and M. F. Ashby, *Cellular solids structure and properties*. Pergamon Press, 1997.

[2] T. M. Ryan and A. Walker, "Trabecular Bone Structure in the Humeral and Femoral Heads of Anthropoid Primates," *The Anatomical Record: Advances in Integrative Anatomy and Evolutionary Biology*, vol. 293, pp. 719–729, apr 2010.

[3] I. Miranda, J. Gominho, and H. Pereira, "Cellular structure and chemical composition of cork from the Chinese cork oak (Quercus variabilis)," *Journal of Wood Science*, vol. 59, pp. 1–9, oct 2012.

[4] "Additive Manufacturing–General Principles–Terminology," iso/astm 52900, International Organization for Standardization, Geneva, CH, 2015.

[5] A. A. Zadpoor, "Mechanical performance of additively manufactured meta-biomaterials," *Acta Biomaterialia*, vol. 85, pp. 41–59, feb 2019.

[6] S. Babaee, J. Shim, J. C. Weaver, E. R. Chen, N. Patel, and K. Bertoldi, "3D Soft Metamaterials with Negative Poisson's Ratio," *Advanced Materials*, vol. 25, pp. 5044–5049, sep 2013.

[7] W. Wu, P. Liu, and Z. Kang, "A novel mechanical metamaterial with simultaneous stretching- and compression-expanding property," *Materials & Design*, vol. 208, p. 109930, oct 2021.

[8] C. S. Ha, M. E. Plesha, and R. S. Lakes, "Chiral three-dimensional isotropic lattices with negative Poisson's ratio," *physica status solidi (b)*, vol. 253, pp. 1243–1251, jul 2016.

[9] X. L. Peng and S. Bargmann, "Tunable auxeticity and isotropic negative thermal expansion in three-dimensional lattice structures of cubic symmetry," *Extreme Mechanics Letters*, vol. 43, p. 101201, feb 2021.

[10] Q. Wang, J. A. Jackson, Q. Ge, J. B. Hopkins, C. M. Spadaccini, and N. X. Fang, "Lightweight Mechanical Metamaterials with Tunable Negative Thermal Expansion," *Physical Review Letters*, vol. 117, p. 175901, oct 2016.

[11] C. Han, Y. Li, Q. Wang, S. Wen, Q. Wei, C. Yan, L. Hao, J. Liu, and Y. Shi, "Continuous functionally graded porous titanium scaffolds manufactured by selective laser melting for bone implants," *Journal of the Mechanical Behavior of Biomedical Materials*, vol. 80, pp. 119–127, apr 2018.

[12] D. S. Al-Saedi, S. Masood, M. Faizan-Ur-Rab, A. Alomarah, and P. Ponnusamy, "Mechanical properties and energy absorption capability of functionally graded F2BCC lattice fabricated by SLM," *Materials & Design*, vol. 144, pp. 32–44, apr 2018.

[13] T. Maconachie, M. Leary, B. Lozanovski, X. Zhang, M. Qian, O. Faruque, and M. Brandt, "SLM lattice structures: Properties, performance, applications and challenges," *Materials & Design*, vol. 183, p. 108137, dec 2019.

[14] "A 63% lighter titanium aerospace part." `https://www.materialise.com/en/cases/a-63-lighter-titanium-aerospace-part`. Accessed: 2022-03-28.

[15] R. O'Hara and M. Vlahinos, "Unlock breakthrough heat exchanger designs with gyroids." `https://www.ansys.com/blog/heat-exchanger-designs-gyroids`. Accessed: 2022-03-28.

[16] "Is 3d printing going to replace the most manufacturing methods in the next 10-20 years?." `https://www.quora.com/Is-3D-printing-going-to-replace-the-most-manufacturing-methods-in-the-next-10-20-years`. Accessed: 2022-03-29.

[17] J. Wu, W. Wang, and X. Gao, "Design and Optimization of Conforming Lattice Structures," *IEEE Transactions on Visualization and Computer Graphics*, vol. 27, no. 1, pp. 43–56, 2021.

[18] A. Panesar, M. Abdi, D. Hickman, and I. Ashcroft, "Strategies for functionally graded lattice structures derived using topology optimisation for Additive Manufacturing," *Additive Manufacturing*, vol. 19, pp. 81–94, 2018.

[19] C. Bonatti and D. Mohr, "Smooth-shell metamaterials of cubic symmetry: Anisotropic elasticity, yield strength and specific energy absorption," *Acta Materialia*, vol. 164, pp. 301–321, feb 2019.

[20] T. Tancogne-Dejean, M. Diamantopoulou, M. B. Gorji, C. Bonatti, and D. Mohr, "3d plate-lattices: An emerging class of low-density metamaterial exhibiting optimal isotropic stiffness," *Advanced Materials*, vol. 30, p. 1803334, 11 2018.

[21] E. Alabort, D. Barba, and R. C. Reed, "Design of metallic bone by additive manufacturing," *Scripta Materialia*, vol. 164, pp. 110–114, 4 2019.

[22] O. Al-Ketan, R. Rowshan, and R. K. Abu Al-Rub, "Topology-mechanical property relationship of 3D printed strut, skeletal, and sheet based periodic metallic cellular materials," *Additive Manufacturing*, vol. 19, pp. 167–183, jan 2018.

[23] X. Cao, Y. Jiang, T. Zhao, P. Wang, Y. Wang, Z. Chen, Y. Li, D. Xiao, and D. Fang, "Compression experiment and numerical evaluation on mechanical responses of the lattice structures with stochastic geometric defects originated from additive-manufacturing," *Composites Part B: Engineering*, vol. 194, p. 108030, aug 2020.

[24] S. M. Ahmadi, R. Hedayati, Y. Li, K. Lietaert, N. Tümer, A. Fatemi, C. D. Rans, B. Pouran, H. Weinans, and A. A. Zadpoor, "Fatigue performance of additively manufactured meta-biomaterials: The effects of topology and material type," *Acta Biomaterialia*, vol. 65, pp. 292–304, 2018.

[25] B. Lozanovski, *Computational modelling of defects in additively manufactured lattice structures*. PhD thesis, RMIT University, 2020.

[26] I. Gibson, D. W. Rosen, and B. Stucker, "The use of multiple materials in additive manufacturing," in *Additive manufacturing technologies*, pp. 436–449, Springer, 2010.

[27] M. Leary, *Design for additive manufacturing*. Elsevier, 2019.

[28] A. du Plessis, S. M. J. Razavi, M. Benedetti, S. Murchio, M. Leary, M. Watson, D. Bhate, and F. Berto, "Properties and applications of additively manufactured metallic cellular materials: A review," *Progress in Materials Science*, vol. 125, p. 100918, 4 2022.

[29] M. Li, W. Du, A. Elwany, Z. Pei, and C. Ma, "Metal binder jetting additive manufacturing: A literature review," *Journal of Manufacturing Science and Engineering, Transactions of the ASME*, vol. 142, sep 2020.

[30] M. Ziaee and N. B. Crane, "Binder jetting: A review of process, materials, and methods," *Additive Manufacturing*, vol. 28, pp. 781–801, aug 2019.

[31] J.-P. Kruth, P. Mercelis, J. Van Vaerenbergh, L. Froyen, and M. Rombouts, "Binding mechanisms in selective laser sintering and selective laser melting," *Rapid Prototyping Journal*, vol. 11, 2005.

[32] J. Oliveira, A. LaLonde, and J. Ma, "Processing parameters in laser powder bed fusion metal additive manufacturing," *Materials & Design*, vol. 193, p. 108762, 2020.

[33] D. Herzog, V. Seyda, E. Wycisk, and C. Emmelmann, "Additive manufacturing of metals," *Acta Materialia*, vol. 117, pp. 371–392, sep 2016.

[34] Q. Chen and G. A. Thouas, "Metallic implant biomaterials," *Materials Science and Engineering: R: Reports*, vol. 87, pp. 1–57, jan 2015.

[35] K. Yang, C. Zhou, H. Fan, Y. Fan, Q. Jiang, P. Song, H. Fan, Y. Chen, and X. Zhang, "Bio-functional design, application and trends in metallic biomaterials," *International Journal of Molecular Sciences 2018, Vol. 19, Page 24*, vol. 19, p. 24, 12 2017.

[36] Y. Li, H. Jahr, J. Zhou, and A. A. Zadpoor, "Additively manufactured biodegradable porous metals," *Acta Biomaterialia*, aug 2020.

[37] L. Murr, "Open-cellular metal implant design and fabrication for biomechanical compatibility with bone using electron beam melting," *Journal of the mechanical behavior of biomedical materials*, vol. 76, pp. 164–177, 2017.

[38] A. A. Zadpoor and J. Malda, "Additive Manufacturing of Biomaterials, Tissues, and Organs," *Annals of Biomedical Engineering*, vol. 45, pp. 1–11, jan 2017.

[39] I. Echeta, X. Feng, B. Dutton, R. Leach, and S. Piano, "Review of defects in lattice structures manufactured by powder bed fusion," *The International Journal of Advanced Manufacturing Technology 2019 106:5*, vol. 106, pp. 2649–2668, dec 2019.

[40] Y. J. Liu, S. J. Li, H. L. Wang, W. T. Hou, Y. L. Hao, R. Yang, T. B. Sercombe, and L. C. Zhang, "Microstructure, defects and mechanical behavior of beta-type titanium porous structures manufactured by electron beam melting and selective laser melting," *Acta Materialia*, vol. 113, pp. 56–67, jul 2016.

[41] W. J. Sames, F. A. List, S. Pannala, R. R. Dehoff, and S. S. Babu, "The metallurgy and processing science of metal additive manufacturing," *International Materials Reviews*, vol. 61, no. 5, pp. 315–360, 2016.

[42] Y. Amani, S. Dancette, P. Delroisse, A. Simar, and E. Maire, "Compression behavior of lattice structures produced by selective laser melting: X-ray tomography based experimental and finite element approaches," *Acta Materialia*, vol. 159, pp. 395–407, 2018.

[43] A. Charles, A. Elkaseer, L. Thijs, V. Hagenmeyer, and S. Scholz, "Effect of process parameters on the generated surface roughness of down-facing surfaces in selective laser melting," *Applied Sciences (Switzerland)*, vol. 9, no. 6, pp. 1–13, 2019.

[44] S. Arabnejad, R. Burnett Johnston, J. A. Pura, B. Singh, M. Tanzer, and D. Pasini, "High-strength porous biomaterials for bone replacement: A strategy to assess the interplay between cell morphology, mechanical properties, bone ingrowth and manufacturing constraints," *Acta Biomaterialia*, vol. 30, pp. 345–356, jan 2016.

[45] S. Y. Choy, C. N. Sun, K. F. Leong, and J. Wei, "Compressive properties of functionally graded lattice structures manufactured by selective laser melting," *Materials & Design*, vol. 131, pp. 112–120, oct 2017.

[46] A. Cuadrado, A. Yánez, O. Martel, S. Deviaene, and D. Monopoli, "Influence of load orientation and of types of loads on the mechanical properties of porous Ti6Al4V biomaterials," *Materials & Design*, vol. 135, pp. 309–318, dec 2017.

[47] M. Leary, M. Mazur, H. Williams, E. Yang, A. Alghamdi, B. Lozanovski, X. Zhang, D. Shidid, L. Farahbod-Sternahl, G. Witt, I. Kelbassa, P. Choong, M. Qian, and M. Brandt, "Inconel 625 lattice structures manufactured by selective laser melting (SLM): Mechanical properties, deformation and failure modes," *Materials & Design*, vol. 157, pp. 179–199, nov 2018.

[48] L. Liu, P. Kamm, F. García-Moreno, J. Banhart, and D. Pasini, "Elastic and failure response of imperfect three-dimensional metallic lattices: the role of geometric defects induced by Selective Laser Melting," *Journal of the Mechanics and Physics of Solids*, vol. 107, pp. 160–184, oct 2017.

[49] U. Hossain, S. Ghouse, K. Nai, and J. R. Jeffers, "Mechanical and morphological properties of additively manufactured SS316L and Ti6Al4V micro-struts as a function of build angle," *Additive Manufacturing*, vol. 46, p. 102050, oct 2021.

[50] S. Murchio, M. Dallago, F. Zanini, S. Carmignato, G. Zappini, F. Berto, D. Maniglio, and M. Benedetti, "Additively manufactured Ti-6Al-4V thin struts via laser powder bed fusion: Effect of building orientation on geometrical accuracy and mechanical properties," *Journal of the Mechanical Behavior of Biomedical Materials*, vol. 119, p. 104495, jul 2021.

[51] D. Melancon, Z. Bagheri, R. Johnston, L. Liu, M. Tanzer, and D. Pasini, "Mechanical characterization of structurally porous biomaterials built via additive manufacturing: experiments, predictive models, and design maps for load-bearing bone replacement implants," *Acta Biomaterialia*, vol. 63, pp. 350–368, nov 2017.

[52] M. Mazur, M. Leary, S. Sun, M. Vcelka, D. Shidid, and M. Brandt, "Deformation and failure behaviour of ti-6al-4v lattice structures manufactured by selective laser melting (slm)," *The International Journal of Advanced Manufacturing Technology*, vol. 84, pp. 1391–1411, 2016.

[53] M. Dallago, B. Winiarski, F. Zanini, S. Carmignato, and M. Benedetti, "On the effect of geometrical imperfections and defects on the fatigue strength of cellular lattice structures additively manufactured via Selective Laser Melting," *International Journal of Fatigue*, vol. 124, pp. 348–360, jul 2019.

[54] X. Yan, Q. Li, S. Yin, Z. Chen, R. Jenkins, C. Chen, J. Wang, W. Ma, R. Bolot, R. Lupoi, Z. Ren, H. Liao, and M. Liu, "Mechanical and inÂ vitro study of an isotropic ti6al4v lattice structure fabricated using selective laser melting," *Journal of Alloys and Compounds*, vol. 782, pp. 209–223, 2019.

[55] S. Arabnejad and D. Pasini, "Mechanical properties of lattice materials via asymptotic homogenization and comparison with alternative homogenization methods," *International Journal of Mechanical Sciences*, vol. 77, pp. 249–262, 2013.

[56] T. J. Horn, O. L. A. Harrysson, D. J. Marcellin-Little, H. A. West, B. D. X. Lascelles, and R. Aman, "Flexural properties of Ti6Al4V rhombic dodecahedron open cellular structures fabricated with electron beam melting," *Additive Manufacturing*, vol. 1, pp. 2–11, 2014.

[57] N. Korshunova, G. Alaimo, S. B. Hosseini, M. Carraturo, A. Reali, J. Niiranen, F. Auricchio, E. Rank, and S. Kollmannsberger, "Bending behavior of octet-truss lattice structures: Modelling options, numerical characterization and experimental validation," *Materials & Design*, vol. 205, p. 109693, 7 2021.

[58] P. Köhnen, C. Haase, J. Bültmann, S. Ziegler, J. H. Schleifenbaum, and W. Bleck, "Mechanical properties and deformation behavior of additively manufactured lattice structures of stainless steel," *Materials & Design*, vol. 145, pp. 205–217, may 2018.

[59] S. Drücker, M. Schulze, H. Ipsen, L. Bandegani, H. Hoch, M. Kluge, and B. Fiedler, "Experimental and numerical mechanical characterization of additively manufactured ti6al4v lattice structures considering progressive damage," *International Journal of Mechanical Sciences*, vol. 189, p. 105986, 1 2021.

[60] A. Herrera, A. Yánez, O. Martel, H. Afonso, and D. Monopoli, "Computational study and experimental validation of porous structures fabricated by electron beam melting: A challenge to avoid stress shielding," *Materials Science and Engineering C*, vol. 45, pp. 89–93, 2014.

[61] J. Kadkhodapour, H. Montazerian, A. C. Darabi, A. P. Anaraki, S. M. Ahmadi, A. A. Zadpoor, and S. Schmauder, "Failure mechanisms of additively manufactured porous biomaterials: Effects of porosity and type of unit cell," *Journal of the Mechanical Behavior of Biomedical Materials*, vol. 50, pp. 180–191, 2015.

[62] Y. Li, H. Jahr, P. Pavanram, F. Bobbert, U. Puggi, X.-Y. Zhang, B. Pouran, M. Leeflang, H. Weinans, J. Zhou, and A. Zadpoor, "Additively manufactured functionally graded biodegradable porous iron," *Acta Biomaterialia*, jul 2019.

[63] A. Cutolo, B. Engelen, W. Desmet, and B. Van Hooreweder, "Mechanical properties of diamond lattice Ti–6Al–4V structures produced by laser powder bed fusion: On the effect of the load direction," *Journal of the Mechanical Behavior of Biomedical Materials*, vol. 104, p. 103656, apr 2020.

[64] "Mechanical testing of metals-ductility testing-compression test for porous and cellular metals," iso 13314:2011, International Organization for Standardization, Geneva, CH, 2011.

[65] S. Ghouse, S. Babu, R. J. Van Arkel, K. Nai, P. A. Hooper, and J. R. Jeffers, "The influence of laser parameters and scanning strategies on the mechanical properties of a stochastic porous material," *Materials & Design*, vol. 131, pp. 498–508, 2017.

[66] S. Amin Yavari, R. Wauthle, J. Van Der Stok, A. C. Riemslag, M. Janssen, M. Mulier, J. P. Kruth, J. Schrooten, H. Weinans, and A. A. Zadpoor, "Fatigue behavior of porous biomaterials manufactured using selective laser melting," *Materials Science and Engineering C*, vol. 33, pp. 4849–4858, dec 2013.

[67] S. M. Ahmadi, G. Campoli, S. Amin Yavari, B. Sajadi, R. Wauthle, J. Schrooten, H. Weinans, and A. A. Zadpoor, "Mechanical behavior of regular open-cell porous biomaterials made of diamond lattice unit cells," *Journal of the Mechanical Behavior of Biomedical Materials*, vol. 34, pp. 106–115, 2014.

[68] R. Wauthle, J. Van Der Stok, S. Amin Yavari, J. V. Humbeeck, J.-P. Kruth, A. Abbas Zadpoor, H. Weinans, M. Mulier, and J. Schrooten, "Additively manufactured porous tantalum implants," *Acta Biomaterialia*, vol. 14, pp. 217–225, 2015.

[69] R. Hedayati, S. Ahmadi, K. Lietaert, B. Pouran, Y. Li, H. Weinans, C. Rans, and A. Zadpoor, "Isolated and modulated effects of topology and material type on the mechanical properties of additively manufactured porous biomaterials," *Journal of the Mechanical Behavior of Biomedical Materials*, vol. 79, pp. 254–263, mar 2018.

[70] L. Zhang, B. Song, L. Yang, and Y. Shi, "Tailored mechanical response and mass transport characteristic of selective laser melted porous metallic biomaterials for bone scaffolds," *Acta Biomaterialia*, vol. 112, pp. 298–315, 2020.

[71] M. Munford, U. Hossain, S. Ghouse, and J. R. Jeffers, "Prediction of anisotropic mechanical properties for lattice structures," *Additive Manufacturing*, vol. 32, p. 101041, mar 2020.

[72] S. M. Ahmadi, S. A. Yavari, R. Wauthle, B. Pouran, J. Schrooten, H. Weinans, and A. A. Zadpoor, "Additively manufactured open-cell porous biomaterials made from six different space-filling unit cells: The mechanical and morphological properties," *Materials*, vol. 8, no. 4, pp. 1871–1896, 2015.

[73] J. C. Maxwell, "On the calculation of the equilibrium and stiffness of frames," *The London, Edinburgh, and Dublin Philosophical Magazine and Journal of Science*, vol. 27, no. 182, pp. 294–299, 1864.

[74] Z. Hashin and S. Shtrikman, "A variational approach to the theory of the elastic behaviour of multiphase materials," *Journal of the Mechanics and Physics of Solids*, vol. 11, no. 2, pp. 127–140, 1963.

[75] K. Ushijima, W. Cantwell, and D. Chen, "Prediction of the mechanical properties of micro-lattice structures subjected to multi-axial loading," *International Journal of Mechanical Sciences*, vol. 68, pp. 47–55, mar 2013.

[76] V. S. Deshpande, N. A. Fleck, and M. F. Ashby, "Effective properties of the octet-truss lattice material," *Journal of the Mechanics and Physics of Solids*, vol. 49, pp. 1747–1769, 2001.

[77] B. Hanks, J. Berthel, M. Frecker, and T. W. Simpson, "Mechanical properties of additively manufactured metal lattice structures: Data review and design interface," *Additive Manufacturing*, vol. 35, p. 101301, oct 2020.

[78] S. Xu, J. Shen, S. Zhou, X. Huang, and Y. M. Xie, "Design of lattice structures with controlled anisotropy," *Materials & Design*, vol. 93, pp. 443–447, 2016.

[79] M. C. Messner, "Optimal lattice-structured materials," *Journal of the Mechanics and Physics of Solids*, vol. 96, pp. 162–183, 2016.

[80] U. Hossain, S. Ghouse, K. Nai, and J. R. Jeffers, "Controlling and testing anisotropy in additively manufactured stochastic structures," *Additive Manufacturing*, vol. 39, p. 101849, 3 2021.

[81] T. Tancogne-Dejean and D. Mohr, "Elastically-isotropic truss lattice materials of reduced plastic anisotropy," *International Journal of Solids and Structures*, vol. 138, pp. 24–39, 5 2018.

[82] S. Bernard, Q. Grimal, and P. Laugier, "Accurate measurement of cortical bone elasticity tensor with resonant ultrasound spectroscopy," *Journal of the Mechanical Behavior of Biomedical Materials*, 2012.

[83] G. Maquer, S. N. Musy, J. Wandel, T. Gross, and P. K. Zysset, "Bone volume fraction and fabric anisotropy are better determinants of trabecular bone stiffness than other morphological variables," *Journal of Bone and Mineral Research*, vol. 30, pp. 1000–1008, 6 2015.

[84] M. Silva, E. F. Shepherd, W. O. Jackson, F. J. Dorey, and T. P. Schmalzried, "Average patient walking activity approaches 2 million cycles per year: Pedometers under-record walking activity," *The Journal of Arthroplasty*, vol. 17, pp. 693–697, 9 2002.

[85] C. N. Kelly, N. T. Evans, C. W. Irvin, S. C. Chapman, K. Gall, and D. L. Safranski, "The effect of surface topography and porosity on the tensile fatigue of 3d printed ti–6al–4v fabricated by selective laser melting," *Materials Science and Engineering: C*, vol. 98, pp. 726–736, 5 2019.

[86] M. Speirs, B. V. Hooreweder, J. V. Humbeeck, and J. P. Kruth, "Fatigue behaviour of niti shape memory alloy scaffolds produced by slm, a unit cell design comparison," *Journal of the Mechanical Behavior of Biomedical Materials*, vol. 70, pp. 53–59, 6 2017.

[87] S. M. Ahmadi, R. Kumar, E. V. Borisov, R. Petrov, S. Leeflang, Y. Li, N. Tümer, R. Huizenga, C. Ayas, A. A. Zadpoor, and V. A. Popovich, "From microstructural design to surface engineering: A tailored approach for improving fatigue life of additively manufactured meta-biomaterials," *Acta Biomaterialia*, vol. 83, pp. 153–166, jan 2019.

[88] S. Amin Yavari, S. M. Ahmadi, R. Wauthle, B. Pouran, J. Schrooten, H. Weinans, and A. A. Zadpoor, "Relationship between unit cell type and porosity and the fatigue behavior of selective laser melted meta-biomaterials," *Journal of the Mechanical Behavior of Biomedical Materials*, vol. 43, pp. 91–100, 2015.

[89] S. Zhao, S. Li, W. Hou, Y. Hao, R. Yang, and R. Misra, "The influence of cell morphology on the compressive fatigue behavior of Ti-6Al-4V meshes fabricated by electron beam melting," *Journal of the Mechanical Behavior of Biomedical Materials*, vol. 59, pp. 251–264, jun 2016.

[90] L. Yang, C. Yan, W. Cao, Z. Liu, B. Song, S. Wen, C. Zhang, Y. Shi, and S. Yang, "Compression–compression fatigue behaviour of gyroid-type triply periodic minimal surface porous structures fabricated by selective laser melting," *Acta Materialia*, vol. 181, pp. 49–66, dec 2019.

[91] A. Cutolo, B. Neirinck, K. Lietaert, C. de Formanoir, and B. Van Hooreweder, "Influence of layer thickness and post-process treatments on the fatigue properties of CoCr scaffolds produced by laser powder bed fusion," *Additive Manufacturing*, vol. 23, pp. 498–504, oct 2018.

[92] L. Boniotti, S. Beretta, L. Patriarca, L. Rigoni, and S. Foletti, "Experimental and numerical investigation on compressive fatigue strength of lattice structures of AlSi7Mg manufactured by SLM," *International Journal of Fatigue*, vol. 128, p. 105181, nov 2019.

[93] H. Kolken, A. F. Garcia, A. Du Plessis, C. Rans, M. Mirzaali, and A. Zadpoor, "Fatigue performance of auxetic meta-biomaterials," *Acta Biomaterialia*, vol. 126, pp. 511–523, may 2021.

[94] J. de Krijger, C. Rans, B. Van Hooreweder, K. Lietaert, B. Pouran, and A. A. Zadpoor, "Effects of applied stress ratio on the fatigue behavior of additively manufactured porous biomaterials under compressive loading," *Journal of the Mechanical Behavior of Biomedical Materials*, vol. 70, pp. 7–16, jun 2017.

[95] M. W. Wu, J. K. Chen, B. H. Lin, and P. H. Chiang, "Improved fatigue endurance ratio of additive manufactured Ti-6Al-4V lattice by hot isostatic pressing," *Materials & Design*, vol. 134, pp. 163–170, nov 2017.

[96] D. Ren, S. Li, H. Wang, W. Hou, Y. Hao, W. Jin, R. Yang, R. D. K. Misra, and L. E. Murr, "Fatigue behavior of Ti-6Al-4V cellular structures fabricated by additive manufacturing technique," *Journal of Materials Science and Technology*, vol. 35, pp. 285–294, feb 2019.

[97] J. Schijve, "Fatigue of structures and materials in the 20th century and the state of the art," *International Journal of Fatigue*, vol. 25, pp. 679–702, 8 2003.

[98] D. Kujawski and F. Ellyin, "A fatigue crack growth model with load ratio effects," *Engineering Fracture Mechanics*, vol. 28, pp. 367–378, 1 1987.

[99] B. Van Hooreweder and J. P. Kruth, "Advanced fatigue analysis of metal lattice structures produced by Selective Laser Melting," *CIRP Annals - Manufacturing Technology*, vol. 66, no. 1, pp. 221–224, 2017.

[100] K. Lietaert, A. Cutolo, and B. Van Hooreweder, "Fatigue life of additively manufactured Ti6Al4V scaffolds under tension-tension, tension-compression and compression-compression fatigue load OPEN," *Scientific REPORTS*, vol. 8, p. 4957, 2018.

[101] R. Molaei, A. Fatemi, N. Sanaei, J. Pegues, N. Shamsaei, S. Shao, P. Li, D. H. Warner, and N. Phan, "Fatigue of additive manufactured Ti-6Al-4V, Part II: The relationship between microstructure, material cyclic properties, and component performance," *International Journal of Fatigue*, vol. 132, p. 105363, mar 2020.

[102] X. Y. Zhang, G. Fang, S. Leeflang, A. J. BÃ¶ttger, A. A. Zadpoor, and J. Zhou, "Effect of subtransus heat treatment on the microstructure and mechanical properties of additively manufactured ti-6al-4v alloy," *Journal of Alloys and Compounds*, vol. 735, pp. 1562–1575, 2 2018.

[103] M. Benedetti, A. du Plessis, R. O. Ritchie, M. Dallago, S. M. Razavi, and F. Berto, "Architected cellular materials: A review on their mechanical properties towards fatigue-tolerant design and fabrication," apr 2021.

[104] J. Haan, M. Asseln, M. Zivcec, J. Eschweiler, R. Radermacher, and C. Broeckmann, "Effect of subsequent hot isostatic pressing on mechanical properties of astm f75 alloy produced by selective laser melting," *http://dx.doi.org/10.1179/0032589915Z.000000000236*, vol. 58, pp. 161–165, 7 2015.

[105] R. Wauthle, S. M. Ahmadi, S. Amin Yavari, M. Mulier, A. A. Zadpoor, H. Weinans, J. Van Humbeeck, J. P. Kruth, and J. Schrooten, "Revival of pure titanium for dynamically loaded porous implants using additive manufacturing," *Materials Science and Engineering: C*, vol. 54, pp. 94–100, sep 2015.

[106] M. J. Mahtabi, N. Shamsaei, and M. R. Mitchell, "Fatigue of Nitinol: The state-of-the-art and ongoing challenges," *Journal of the Mechanical Behavior of Biomedical Materials*, vol. 50, pp. 228–254, oct 2015.

[107] L. Yang, C. Yan, H. Fan, Z. Li, C. Cai, P. Chen, Y. Shi, and S. Yang, "Investigation on the orientation dependence of elastic response in Gyroid cellular structures," *Journal of the Mechanical Behavior of Biomedical Materials*, vol. 90, pp. 73–85, feb 2019.

[108] G. Pyka, A. Burakowski, G. Kerckhofs, M. Moesen, S. V. Bael, J. Schrooten, and M. Wevers, "Surface modification of ti6al4v open porous structures produced by additive manufacturing," *Advanced Engineering Materials*, vol. 14, pp. 363–370, 6 2012.

[109] K. Karami, A. Blok, L. Weber, S. M. Ahmadi, R. Petrov, K. Nikolic, E. V. Borisov, S. Leeflang, C. Ayas, A. A. Zadpoor, M. Mehdipour, E. Reinton, and V. A. Popovich, "Continuous and pulsed selective laser melting of Ti6Al4V lattice structures: Effect of post-processing on microstructural anisotropy and fatigue behaviour," *Additive Manufacturing*, vol. 36, p. 101433, dec 2020.

[110] A. A. Zadpoor and R. Hedayati, "Analytical relationships for prediction of the mechanical properties of additively manufactured porous biomaterials," *Journal of Biomedical Materials Research - Part A*, vol. 104, no. 12, pp. 3164–3174, 2016.

[111] K. Ushijima, W. J. Cantwell, and D. H. Chen, "Estimation of the compressive and shear responses of three-dimensional micro-lattice structures," *Procedia Engineering*, vol. 10, pp. 2441–2446, 2011.

[112] S. Babaee, H. Jahromi, A. Ajdari, H. Nayeb-Hashemi, and A. Vaziri, "Mechanical properties of open-cell rhombic dodecahedron cellular structures," *Acta Materialia*, vol. 60, pp. 2873–2885, 2012.

[113] R. Hedayati, M. Sadighi, M. Mohammadi-Aghdam, and A. A. Zadpoor, "Mechanical behavior of additively manufactured porous biomaterials made from truncated cuboctahedron unit cells," *International Journal of Mechanical Sciences*, vol. 106, pp. 19–38, 2016.

[114] R. Hedayati, M. Sadighi, M. Mohammadi-Aghdam, and A. A. Zadpoor, "Mechanical properties of regular porous biomaterials made from truncated cube repeating unit cells: Analytical solutions and computational models," *Materials Science & Engineering C*, vol. 60, pp. 163–183, 2016.

[115] T. Tancogne-Dejean and D. Mohr, "Stiffness and specific energy absorption of additively-manufactured metallic BCC metamaterials composed of tapered beams," *International Journal of Mechanical Sciences*, vol. 141, pp. 101–116, jun 2018.

[116] M. Zhang, Z. Yang, Z. Lu, B. Liao, and X. He, "Effective elastic properties and initial yield surfaces of two 3D lattice structures," *International Journal of Mechanical Sciences*, vol. 138-139@ar, pp. 146–158, apr 2018.

[117] M. C. Messner, M. I. Barham, M. Kumar, and N. R. Barton, "Wave propagation in equivalent continuums representing truss lattice materials," *International Journal of Solids and Structures*, vol. 73-74, pp. 55–66, nov 2015.

[118] M. H. Luxner, J. Stampfl, and H. E. Pettermann, "Finite element modeling concepts and linear analyses of 3D regular open cell structures," *Journal of Materials Science*, vol. 40, pp. 5859–5866, 2005.

[119] L. Xiao and W. Song, "Additively-manufactured functionally graded Ti-6Al-4V lattice structures with high strength under static and dynamic loading: Experiments," *International Journal of Impact Engineering*, vol. 111, pp. 255–272, jan 2018.

[120] T. Maconachie, M. Leary, P. Tran, J. Harris, Q. Liu, G. Lu, D. Ruan, O. Faruque, and M. Brandt, "The effect of topology on the quasi-static and dynamic behaviour of slm alsi10mg lattice structures," *The International Journal of Advanced Manufacturing Technology*, pp. 1–20, 10 2021.

[121] V. Crupi, E. Kara, G. Epasto, E. Guglielmino, and H. Aykul, "Static behavior of lattice structures produced via direct metal laser sintering technology," *Materials & Design*, vol. 135, pp. 246–256, 2017.

[122] M. Smith, Z. Guan, and W. J. Cantwell, "Finite element modelling of the compressive response of lattice structures manufactured using the selective laser melting technique," *International Journal of Mechanical Sciences*, 2013.

[123] H. Guo, A. Takezawa, M. Honda, C. Kawamura, and M. Kitamura, "Finite element simulation of the compressive response of additively manufactured lattice structures with large diameters," *Computational Materials Science*, vol. 175, p. 109610, 4 2020.

[124] H. Lei, C. Li, J. Meng, H. Zhou, Y. Liu, X. Zhang, P. Wang, and D. Fang, "Evaluation of compressive properties of slm-fabricated multi-layer lattice structures by experimental test and μ-ct-based finite element analysis," *Materials & Design*, vol. 169, p. 107685, 5 2019.

[125] G. Campoli, M. S. Borleffs, S. Amin Yavari, R. Wauthle, H. Weinans, and A. A. Zadpoor, "Mechanical properties of open-cell metallic biomaterials manufactured using additive manufacturing," *Materials & Design*, vol. 49, pp. 957–965, 2013.

[126] M. R. K. Ravari, M. Kadkhodaei, M. Badrossamay, and R. Rezaei, "Numerical investigation on mechanical properties of cellular lattice structures fabricated by fused deposition modeling," *International Journal of Mechanical Sciences*, vol. 88, pp. 154–161, 2014.

[127] R. Hedayati, H. Hosseini-Toudeshky, M. Sadighi, M. Mohammadi-Aghdam, and A. A. Zadpoor, "Computational prediction of the fatigue behavior of additively manufactured porous metallic biomaterials," *International Journal of Fatigue*, vol. 84, pp. 67–79, 3 2016.

[128] A. Zargarian, M. Esfahanian, J. Kadkhodapour, S. Ziaei-Rad, and D. Zamani, "On the fatigue behavior of additive manufactured lattice structures," *Theoretical and Applied Fracture Mechanics*, vol. 100, pp. 225–232, apr 2019.

[129] C. Han, C. Yan, S. Wen, T. Xu, S. Li, J. Liu, Q. Wei, and Y. Shi, "Effects of the unit cell topology on the compression properties of porous Co-Cr scaffolds fabricated via selective laser melting ," *Rapid Prototyping Journal*, vol. 23, no. 1, pp. 7–15, 2017.

[130] S. Ruiz de Galarreta, J. R. Jeffers, and S. Ghouse, "A validated finite element analysis procedure for porous structures," *Materials & Design*, vol. 189, p. 108546, apr 2020.

[131] F. J. Quevedo González and N. Nuño, "Finite element modelling approaches for well-ordered porous metallic materials for orthopaedic applications: cost effectiveness and geometrical considerations," *Computer Methods in Biomechanics and Biomedical Engineering*, vol. 19, pp. 845–854, jun 2016.

[132] S. L. Omairey, P. D. Dunning, and S. Sriramula, "Development of an ABAQUS plugin tool for periodic RVE homogenisation," *Engineering with Computers*, vol. 35, no. 2, pp. 567–577, 2018.

[133] J. Kang, E. Dong, D. Li, S. Dong, C. Zhang, and L. Wang, "Anisotropy characteristics of microstructures for bone substitutes and porous implants with application of additive manufacturing in orthopaedic," *Materials & Design*, vol. 191, p. 108608, jun 2020.

[134] M. Leary, M. Mazur, J. Elambasseril, M. Mcmillan, T. Chirent, Y. Sun, M. Qian, M. Easton, and M. Brandt, "Selective laser melting (SLM) of AlSi12Mg lattice structures," *Materials & Design*, vol. 98, pp. 344–357, 2016.

[135] J. Kadkhodapour, H. Montazerian, A. C. Darabi, A. Zargarian, and S. Schmauder, "The relationships between deformation mechanisms and mechanical properties of additively manufactured porous biomaterials," *Journal of the Mechanical Behavior of Biomedical Materials*, vol. 70, pp. 28–42, jun 2017.

[136] N. Korshunova, G. Alaimo, S. B. Hosseini, M. Carraturo, A. Reali, J. Niiranen, F. Auricchio, E. Rank, and S. Kollmannsberger, "Image-based numerical characterization and experimental validation of tensile behavior of octet-truss lattice structures," *Additive Manufacturing*, vol. 41, p. 101949, 5 2021.

[137] Z. Yang, M. Ruess, S. Kollmannsberger, A. DÃ¼ster, and E. Rank, "An efficient integration technique for the voxel-based finite cell method," *International Journal for Numerical Methods in Engineering*, vol. 91, pp. 457–471, 8 2012.

[138] B. Lozanovski, M. Leary, P. Tran, D. Shidid, M. Qian, P. Choong, and M. Brandt, "Computational modelling of strut defects in SLM manufactured lattice structures," *Materials & Design*, vol. 171, jun 2019.

[139] M. Doroszko, A. Falkowska, and A. Seweryn, "Image–based numerical modeling of the tensile deformation behavior and mechanical properties of additive manufactured ti–6al–4v diamond lattice structures," *Materials Science and Engineering: A*, vol. 818, p. 141362, 6 2021.

[140] P. Li, Z. Wang, N. Petrinic, and C. R. Siviour, "Deformation behaviour of stainless steel microlattice structures by selective laser melting," *Materials Science and Engineering: A*, vol. 614, pp. 116–121, 9 2014.

[141] R. Gümrük and R. A. W. Mines, "Compressive behaviour of stainless steel micro-lattice structures," *International Journal of Mechanical Sciences*, vol. 68, pp. 125–139, 2013.

[142] S. Bandyopadhyay-Ghosh, "Bone as a collagen-hydroxyapatite composite and its repair," *Trends in Biomaterials and Artificial Organs*, vol. 22, no. 2, pp. 112–121, 2008.

[143] X. Wang, S. Xu, S. Zhou, W. Xu, M. Leary, P. Choong, M. Qian, M. Brandt, and Y. M. Xie, "Topological design and additive manufacturing of porous metals for bone scaffolds and orthopaedic implants: A review," *Biomaterials*, vol. 83, pp. 127–141, 2016.

[144] J. M. García-Aznar, M. J. Gómez-Benito, M. Á. Pérez, and M. Doblaré, "Mechanobiological Models for Bone Tissue. Applications to Implant Design," in *Biomechanics of Hard Tissues: Modeling, Testing, and Materials* (A. 'Ochsner and W. Ahmed, eds.), ch. 4, pp. 123–143, John Wiley & Sons, Ltd, 2010.

[145] R. Huiskes, R. Ruimerman, G. H. van Lenthe, and J. D. Janssen, "Effects of mechanical forces on maintenance and adaptation of form in trabecular bone," *Nature 2000 405:6787*, vol. 405, pp. 704–706, jun 2000.

[146] E. Ozcivici, Y. K. Luu, B. Adler, Y.-X. Qin, J. Rubin, S. Judex, and C. T. Rubin, "Mechanical signals as anabolic agents in bone," *Nature Reviews Rheumatology 2010 6:1*, vol. 6, pp. 50–59, jan 2010.

[147] S. L. Teitelbaum, "Bone resorption by osteoclasts," *Science*, vol. 289, pp. 1504–1508, sep 2000.

[148] R. Oftadeh, M. Perez-Viloria, J. C. Villa-Camacho, A. Vaziri, and A. Nazarian, "Biomechanics and mechanobiology of trabecular bone: A review," *Journal of Biomechanical Engineering*, vol. 137, 1 2015.

[149] E. F. Morgan and T. M. Keaveny, "Dependence of yield strain of human trabecular bone on anatomic site," *Journal of Biomechanics*, vol. 34, pp. 569–577, may 2001.

[150] S. Dendorfer, H. J. Maier, D. Taylor, and J. Hammer, "Anisotropy of the fatigue behaviour of cancellous bone," *Journal of Biomechanics*, vol. 41, pp. 636–641, jan 2008.

[151] A. K. Aiyangar, J. Vivanco, A. G. Au, P. A. Anderson, E. L. Smith, and H. L. Ploeg, "Dependence of anisotropy of human lumbar vertebral trabecular bone on quantitative computed tomography-based apparent density," *Journal of Biomechanical Engineering*, vol. 136, no. 9, 2014.

[152] P. Augat, T. Link, T. F. Lang, J. C. Lin, S. Majumdar, and H. K. Genant, "Anisotropy of the elastic modulus of trabecular bone specimens from different anatomical locations," *Medical Engineering & Physics*, vol. 20, pp. 124–131, mar 1998.

[153] T. M. Keaveny, E. F. Morgan, G. L. Niebur, and O. C. Yeh, "Biomechanics of trabecular bone," *Annual review of biomedical engineering*, vol. 3, no. 1, pp. 307–333, 2001.

[154] S. Bernard, Q. Grimal, and P. Laugier, "Accurate measurement of cortical bone elasticity tensor with resonant ultrasound spectroscopy," *Journal of the Mechanical Behavior of Biomedical Materials*, vol. 18, pp. 12–19, 2013.

[155] D. T. Reilly and A. H. Burstein, "The elastic and ultimate properties of compact bone tissue," *Journal of Biomechanics*, vol. 8, pp. 393–405, jan 1975.

[156] J. Y. Rho, R. B. Ashman, and C. H. Turner, "Young's modulus of trabecular and cortical bone material: Ultrasonic and microtensile measurements," *Journal of Biomechanics*, vol. 26, pp. 111–119, feb 1993.

[157] Y.-c. Fung, *Biomechanics: mechanical properties of living tissues*. Springer Science & Business Media, 1993.

[158] J. C. Lotz, T. N. Gerhart, and W. C. Hayes, "Mechanical properties of metaphyseal bone in the proximal femur," *Journal of Biomechanics*, vol. 24, no. 5, 1991.

[159] F. G. Evans and R. Vincentelli, "Relations of the compressive properties of human cortical bone to histological structure and calcification," *Journal of Biomechanics*, vol. 7, pp. 1–10, jan 1974.

[160] I. Sevostianov and M. Kachanov, "Impact of the porous microstructure on the overall elastic properties of the osteonal cortical bone," *Journal of Biomechanics*, vol. 33, pp. 881–888, jul 2000.

[161] A. Nauth, M. D. McKee, T. A. Einhorn, J. T. Watson, R. Li, and E. H. Schemitsch, "Managing bone defects," *Journal of Orthopaedic Trauma*, vol. 25, pp. 462–466, aug 2011.

[162] E. H. Schemitsch, "Size Matters: Defining Critical in Bone Defect Size!," *Journal of Orthopaedic Trauma*, vol. 31, pp. S20–S22, oct 2017.

[163] V. Viateau, G. Guillemin, V. Bousson, K. Oudina, D. Hannouche, L. Sedel, D. Logeart-Avramoglou, and H. Petite, "Long-bone critical-size defects treated with tissue-engineered grafts: A study on sheep," *Journal of Orthopaedic Research*, vol. 25, pp. 741–749, jun 2007.

[164] M. Z. Ibrahim, A. A. Sarhan, F. Yusuf, and M. Hamdi, "Biomedical materials and techniques to improve the tribological, mechanical and biomedical properties of orthopedic implants – A review article," *Journal of Alloys and Compounds*, vol. 714, pp. 636–667, aug 2017.

[165] L. Bai, C. Gong, X. Chen, Y. Sun, J. Zhang, L. Cai, S. Zhu, and S. Q. Xie, "Additive Manufacturing of Customized Metallic Orthopedic Implants: Materials, Structures, and Surface Modifications," *Metals 2019, Vol. 9, Page 1004*, vol. 9, p. 1004, sep 2019.

[166] S. Amin Yavari, J. van der Stok, S. M. Ahmadi, R. Wauthle, J. Schrooten, H. Weinans, and A. A. Zadpoor, "Mechanical analysis of a rodent segmental bone defect model: The effects of internal fixation and implant stiffness on load transfer," *Journal of Biomechanics*, vol. 47, pp. 2700–2708, aug 2014.

[167] J. Yang, H. Cai, J. Lv, K. Zhang, H. Leng, C. Sun, Z. Wang, and Z. Liu, "In vivo study of a self-stabilizing artificial vertebral body fabricated by electron beam melting," *Spine*, vol. 39, pp. E486–E492, apr 2014.

[168] W. Luo, L. Huang, H. Liu, W. Qu, X. Zhao, C. Wang, C. Li, T. Yu, Q. Han, J. Wang, and Y. Qin, "Customized Knee Prosthesis in Treatment of Giant Cell Tumors of the Proximal Tibia: Application of 3-Dimensional Printing Technology in Surgical Design," *Medical Science Monitor : International Medical Journal of Experimental and Clinical Research*, vol. 23, p. 1691, apr 2017.

[169] S. Wu, X. Liu, K. W. Yeung, C. Liu, and X. Yang, "Biomimetic porous scaffolds for bone tissue engineering," *Materials Science and Engineering: R: Reports*, vol. 80, pp. 1–36, 2014.

[170] D. R. Sumner, "Long-term implant fixation and stress-shielding in total hip replacement," *Journal of Biomechanics*, vol. 48, pp. 797–800, mar 2015.

[171] N. Reznikov, O. R. Boughton, S. Ghouse, A. E. Weston, L. Collinson, G. W. Blunn, J. R. Jeffers, J. P. Cobb, and M. M. Stevens, "Individual response variations in scaffold-guided bone regeneration are determined by independent strain- and injury-induced mechanisms," *Biomaterials*, vol. 194, pp. 183–194, feb 2019.

[172] D. Barba, E. Alabort, and R. C. Reed, "Synthetic bone: Design by additive manufacturing," *Acta Biomaterialia*, vol. 97, pp. 637–656, oct 2019.

[173] O. L. Harrysson, O. Cansizoglu, D. J. Marcellin-Little, D. R. Cormier, and H. A. West, "Direct metal fabrication of titanium implants with tailored materials and mechanical properties using electron beam melting technology," *Materials Science and Engineering C*, vol. 28, no. 3, pp. 366–373, 2008.

[174] C. Rivière, G. Grappiolo, C. A. E. Jr, J.-P. Vidalain, A.-F. Chen, N. Boehler, J. Matta, and P.-A. Vendittoli, "Long-term bone remodelling around "legendary" cementless femoral stems," *EFORT open reviews*, vol. 3, pp. 45–57, feb 2018.

[175] F. S. Bobbert, K. Lietaert, A. A. Eftekhari, B. Pouran, S. M. Ahmadi, H. Weinans, and A. A. Zadpoor, "Additively manufactured metallic porous biomaterials based on minimal surfaces: A unique combination of topological, mechanical, and mass transport properties," *Acta Biomaterialia*, vol. 53, pp. 572–584, apr 2017.

[176] N. Taniguchi, S. Fujibayashi, M. Takemoto, K. Sasaki, B. Otsuki, T. Nakamura, T. Matsushita, T. Kokubo, and S. Matsuda, "Effect of pore size on bone ingrowth into porous titanium implants fabricated by additive manufacturing: An in vivo experiment," *Materials Science and Engineering C*, vol. 59, pp. 690–701, 2016.

[177] S. Van Bael, Y. C. Chai, S. Truscello, M. Moesen, G. Kerckhofs, H. Van Oosterwyck, J. P. Kruth, and J. Schrooten, "The effect of pore geometry on the in vitro biological behavior of

human periosteum-derived cells seeded on selective laser-melted Ti6Al4V bone scaffolds," *Acta Biomaterialia*, vol. 8, no. 7, pp. 2824–2834, 2012.

[178] A. Fukuda, M. Takemoto, T. Saito, S. Fujibayashi, M. Neo, D. K. Pattanayak, T. Matsushita, K. Sasaki, N. Nishida, T. Kokubo, and T. Nakamura, "Osteoinduction of porous ti implants with a channel structure fabricated by selective laser melting," *Acta Biomaterialia*, vol. 7, pp. 2327–2336, 5 2011.

[179] V. Karageorgiou and D. Kaplan, "Porosity of 3d biomaterial scaffolds and osteogenesis," *Biomaterials*, vol. 26, pp. 5474–5491, 9 2005.

[180] C. Boyle and I. Y. Kim, "Comparison of different hip prosthesis shapes considering micro-level bone remodeling and stress-shielding criteria using three-dimensional design space topology optimization," *Journal of Biomechanics*, vol. 44, pp. 1722–1728, 6 2011.

[181] S. Ghouse, N. Reznikov, O. R. Boughton, S. Babu, K. C. Ng, G. Blunn, J. P. Cobb, M. M. Stevens, and J. R. Jeffers, "The design and in vivo testing of a locally stiffness-matched porous scaffold," *Applied Materials Today*, vol. 15, pp. 377–388, jun 2019.

[182] C. Pabinger and A. Geissler, "Utilization rates of hip arthroplasty in OECD countries," *Osteoarthritis and Cartilage*, vol. 22, pp. 734–741, jun 2014.

[183] A. J. Price, A. Alvand, A. Troelsen, J. N. Katz, G. Hooper, A. Gray, A. Carr, and D. Beard, "Knee replacement," *The Lancet*, vol. 392, pp. 1672–1682, nov 2018.

[184] C. Pabinger, H. Lothaller, and A. Geissler, "Utilization rates of knee-arthroplasty in OECD countries," *Osteoarthritis and Cartilage*, vol. 23, pp. 1664–1673, oct 2015.

[185] C. Pabinger, H. Lothaller, N. Portner, and A. Geissler, "Projections of hip arthroplasty in OECD countries up to 2050," *HIP International*, vol. 28, pp. 498–506, sep 2018.

[186] R. Hedayati, M. Sadighi, M. Mohammadi-Aghdam, and A. A. Zadpoor, "Analytical relationships for the mechanical properties of additively manufactured porous biomaterials based on octahedral unit cells," *Applied Mathematical Modelling*, vol. 46, pp. 408–422, 2017.

[187] X. Cao, S. Duan, J. Liang, W. Wen, and D. Fang, "Mechanical properties of an improved 3D-printed rhombic dodecahedron stainless steel lattice structure of variable cross section," *International Journal of Mechanical Sciences*, vol. 145, pp. 53–63, sep 2018.

[188] K. Ushijima, W. J. Cantwell, R. A. Mines, S. Tsopanos, and M. Smith, "An investigation into the compressive properties of stainless steel micro-lattice structures," *Journal of Sandwich Structures and Materials*, vol. 13, no. 3, pp. 303–329, 2011.

[189] R. Asbai-Ghoudan, S. Ruiz de Galarreta, and N. Rodriguez-Florez, "Analytical model for the prediction of permeability of triply periodic minimal surfaces," *Journal of the Mechanical Behavior of Biomedical Materials*, vol. 124, p. 104804, dec 2021.

[190] A. Entezari, I. Roohani, G. Li, C. R. Dunstan, P. Rognon, Q. Li, X. Jiang, and H. Zreiqat, "Architectural Design of 3D Printed Scaffolds Controls the Volume and Functionality of Newly Formed Bone," *Advanced Healthcare Materials*, vol. 8, jan 2019.

[191] H. M. Kolken, K. Lietaert, T. van der Sloten, B. Pouran, A. Meynen, G. Van Loock, H. Weinans, L. Scheys, and A. A. Zadpoor, "Mechanical performance of auxetic meta-biomaterials," *Journal of the Mechanical Behavior of Biomedical Materials*, vol. 104, p. 103658, apr 2020.

[192] A. M. Arefin, N. R. Khatri, N. Kulkarni, and P. F. Egan, "Polymer 3D Printing Review: Materials, Process, and Design Strategies for Medical Applications," *Polymers 2021, Vol. 13, Page 1499*, vol. 13, p. 1499, may 2021.

[193] D. L. Kopperdahl and T. M. Keaveny, "Yield strain behavior of trabecular bone," *Journal of Biomechanics*, vol. 31, pp. 601–608, jul 1998.

[194] V. S. Nikolaou, N. Efstathopoulos, G. Kontakis, N. K. Kanakaris, and P. V. Giannoudis, "The influence of osteoporosis in femoral fracture healing time," *Injury*, vol. 40, pp. 663–668, jun 2009.

[195] A. Yánez, M. P. Fiorucci, A. Cuadrado, O. Martel, and D. Monopoli, "Surface roughness effects on the fatigue behaviour of gyroid cellular structures obtained by additive manufacturing," *International Journal of Fatigue*, vol. 138, sep 2020.

[196] R. Hedayati, S. Janbaz, M. Sadighi, M. Mohammadi-Aghdam, and A. A. Zadpoor, "How does tissue regeneration influence the mechanical behavior of additively manufactured porous biomaterials?," *Journal of the Mechanical Behavior of Biomedical Materials*, vol. 65, pp. 831–841, jan 2017.

Appendix A

Publications

The following section presents the main contributions of this thesis. These are the papers published and already included:

- Alaña, M., Lopez-Arancibia, A., Pradera-Mallabiabarrena A., Ruiz de Galarreta, S. (2019). Analytical modelof the elastic behavior of a modified face-centered cubic lattice structure. Journal of the Mechanical Behavior of Biomedical Materials, 98, 357-368. (DOI: 10.1016/j.jmbbm.2019.05.043).
- Alaña, M., Cutolo, A., Probst, G., Ruiz de Galarreta, S., Van Hooreweder, B. (2020). Understanding elastic anisotropy in diamond based lattice structures produced by laser powder bed fusion: Effect of manufacturing deviations. Materials and Design, 195, 108971. (DOI: 10.1016/j.matdes.2020.108971).
- Alaña, M., Cutolo, A., Ruiz de Galarreta, S., Van Hooreweder, B. (2021). Influence of relative density on quasi-static and fatigue failure of lattice structures in Ti6Al4V produced by laser powder bed fusion. Scientific Reports, 11, 19314. (DOI: 10.1038/s41598-021-98631-3).
- Alaña, M., Lopez-Arancibia, A., Ghouse, S., Rodriguez-Florez, N., Ruiz de Galarreta, S. Additively manufactured lattice structures with controlled transverse isotropy for orthopedic porous implants. *Submitted to* Computers in Biology and Medicine.

In addition, two conference presentations were also a contribution from the present work:

- Alaña, M., Puerta, I., Rodriguez-Florez, N., Lopez-Arancibia, A., López, A., Ruiz de Galarreta, S. (2021). Lattice structures under combined stress states for scaffolds in orthopedic implant applications. 26th Conference of the European Society of Biomechanics.
- Alaña, M., Ruiz de Galarreta, S., Lopez-Arancibia, A. (2021). Fabrikazio aditibo bidezko sare egituren eredu analitikoa zeharkako isotropiarako. IV. Ikergazte. Nazioarteko ikerketa euskaraz. Kongresuko artikulu bilduma. Ingeniaritza eta Arkitektura. (DOI: 10.26876/ikergazte.iv.03.12).